US Army Corps of Engineers
Waterways Experiment Station

Technical Report SL-97-5
August 1997

Experimental Comparison of Prototype and 1:5-Scale Model Wicket Gates

by *Mostafiz R. Chowdhury, Douglas G. Ross, Robert L. Hall*

WES

Prepared for Headquarters, U.S. Army Corps of Engineers
and U.S. Army Engineer District, Louisville

Technical Report SL-97-5
August 1997

Experimental Comparison of Prototype and 1:5-Scale Model Wicket Gates

by Mostafiz R. Chowdhury, Douglas G. Ross, Robert L. Hall

U.S. Army Corps of Engineers
Waterways Experiment Station
3909 Halls Ferry Road
Vicksburg, MS 39180-6199

Final report

Prepared for Headquarters, U.S. Army Corps of Engineers
Washington, DC 20314-1000

Under U.S. Army Engineer District, Louisville
P.O. Box 59
Louisville, KY 40201-0059

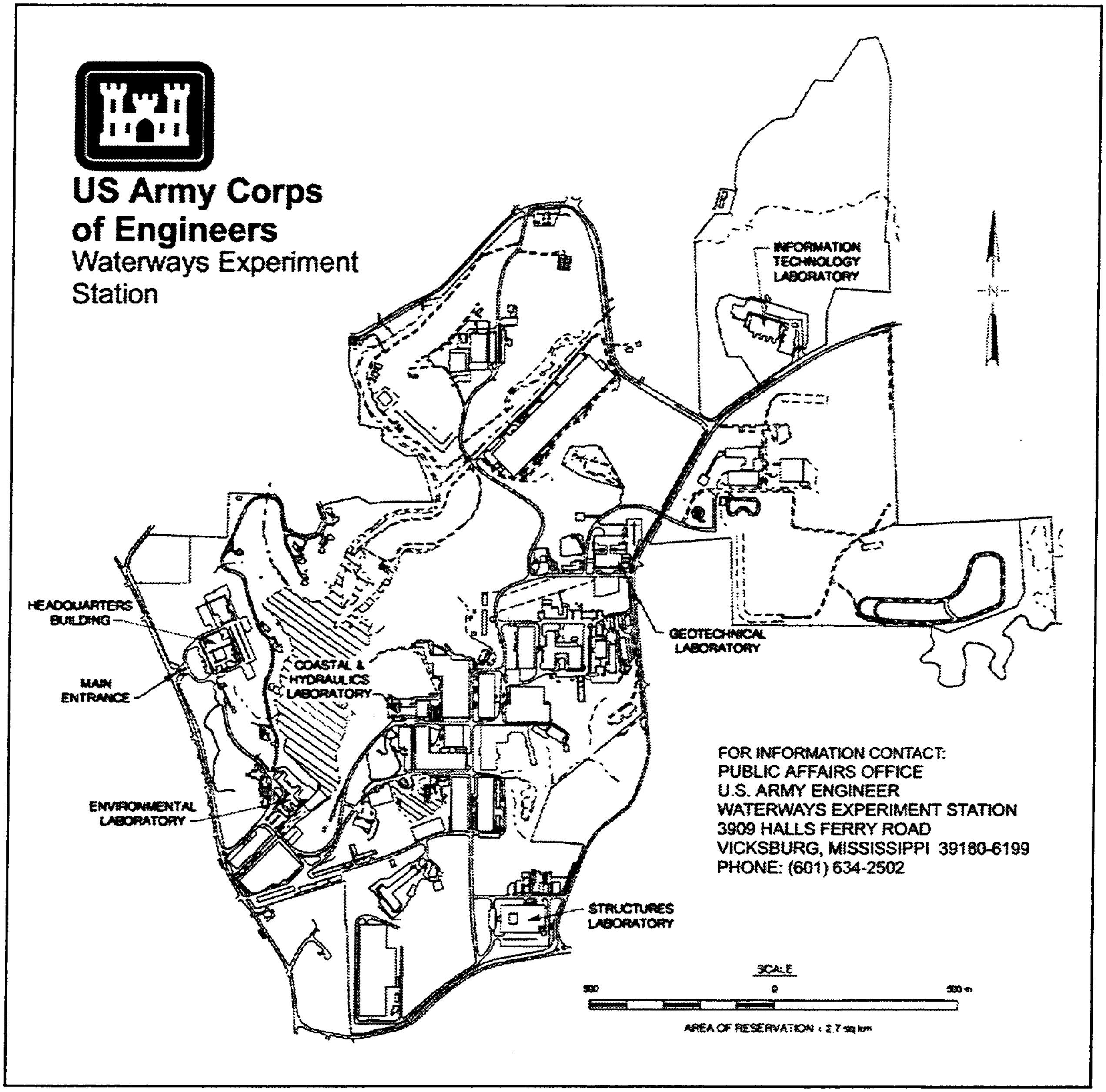

Waterways Experiment Station Cataloging-in-Publication Data

Chowdhury, Mostafiz R.

Experimental comparison of prototype and 1:5-scale model wicket gates / by Mostafiz R. Chowdhury, Douglas G. Ross, Robert L. Hall ; prepared for Headquarters, U.S. Army Corps of Engineers under U.S. Army Engineer District, Louisville.

232 p. : ill. ; 28 cm. — (Technical report ; SL-97-5)

1. Hydraulic gates — Models — Evaluation. 2. Gates — Models — Design and construction. I. Ross, Douglas G. II. Hall, Robert L. III. United States. Army. Corps of Engineers. Louisville District. IV. U.S. Army Engineer Waterways Experiment Station. V. Structures Laboratory (U.S. Army Engineer Waterways Experiment Station) VI. Title. VII. Series: Technical report (U.S. Army Engineer Waterways Experiment Station) ; SL-97-5.

TA7 W34 no.SL-97-5

Contents

List of Figures

List of Tables

Preface

The research reported herein was sponsored by the U.S. Army Engineer District, Louisville, in support of the Olmsted Navigational Model Study program. Mr. Rick Schultz was the Program Monitor for the physical model studies and Mrs. Anjana Chudgar was the technical monitor for the structural performance evaluation of the Olmsted wickets. Mr. Ralph Snowberger provided the structural design guidance, and Mr. Gordon Lance, U. S. Army Engineer Division, Ohio River, contributed to the hydraulic design aspect of the Olmsted project.

All work was carried out by Dr. Mostafiz R. Chowdhury, Dr. Robert L. Hall, and 1st LT Douglas G. Ross, Structural Mechanics Division (SMD), Structures Laboratory (SL), U.S. Army Engineer Waterways Experiment Station (WES), under the general supervision of Mr. Bryant Mather, Director, SL; Mr. John Ehrgott, Assistant Director, SL; and Dr. Reed Mosher, Chief, SMD. The work was conducted during August 1995 through June 1996.

Mr. Joe Ables, Information Technology laboratory (ITL), was responsible for instrumentation and operation of the prototype and model during tests. Mr. Terry Warren, ITL, wrote the program for data acquisition, and Mr. Homer Greer, ITL, was responsible for coordinating instrumentation and data acquisition tasks. Mr. Ken Vitaya-udom, SL, prepared the model shop drawings. Ms. Vicky Smith, SMD, provided technical assistance for the preparation of the report.

At the time of publication of this report, Director of WES was Dr. Robert W. Whalin. Commander was COL Bruce K. Howard, EN.

Conversion Factors, Non-SI to SI Units of Measurement

Non-SI units of measurement used in this report can be converted to SI units as follows:

Multiply	By	To Obtain
degrees (angle)	0.01745329	radians
feet	0.3048	metres
inches	0.0254	metres
ksi (kips per square in.)	6.894757	megapascals
pounds (force)	4.4484	newtons
pounds (mass)	0.4535924	kilograms
pounds (force) per square inch	0.006894757	megapascals
g (standard acceleration of free fall)	9.80665	metres per second squared

1 Introduction

Background

Olmsted Locks and Dam is one of the largest civil works projects undertaken by the U.S. Army Corps of Engineers to modernize navigational facilities for the twenty-first century. Maintaining a robust navigational infrastructure to meet the demand for ever-increasing barge traffic through our nation's waterways is vital to our economy. Transportation of bulk commodities via our vast inland waterways not only provides the most economic mode of conveyance but also helps to conserve energy resources. In this regard, the Corps' continuing effort to improve the navigational facilities using the latest technology is essential. Several research and development phases were initiated and coordinated by the U.S. Army Engineer District, Louisville (ORL), to accomplish this monumental navigational upgrade on the Ohio river.

The principal focus of this research scheme was to determine the most appropriate type of wicket for the new Olmsted Locks and Dam project. In January 1990, a wicket-gate model study was initiated to support the design of the prototype structure to be constructed at Smithland Dam. In a relentless effort to better understand the performance of these unprecedented hydraulically lifted wickets under variable operating conditions, a series of models was subsequently developed and tested by the U.S. Army Engineer Waterways Experiment Station (WES) (March and Elder 1992; Chowdhury, Hall, and Pesantes in preparation). In the final phase of this model program, a 1:5-scale model was studied at WES. Experimental feedback from such physical models was provided to the designers at the Louisville District to improve the design of the hydraulically operated Olmsted wickets. Subsequently, after a series of interactive design changes, a final version of the prototype wicket was adapted for further data collection and verification at the Smithland facility. Because of the limitations of the prototype facility, the broad range of operating conditions necessary for determining the dynamic performance of the wickets was investigated in a 1:5-scale physical model at WES.

This data report is in response to the WES proposal to the Louisville District to instrument, test, and analyze the prototype wicket gates at the Smithland, KY, test facility. Originally, it was intended to instrument and test the prototype wickets by an independent contractor outside the Corps of Engineers. Teledyne Brown Engineering of Marion, MA, was contracted by the ORL to develop the instrumentation specifications and drawings for component testing at the Olmsted Dam prototype. Two fully instrumented prototype gates with 160 sensors were planned in agreement with the instrumentation design for the 1:5-scale physical model (Teledyne Engineering Services 1993). Modification of the original design philosophy of the wickets from using hydraulically lifting mechanism prompted the ORL to scale down the number of sensors and reduce the scope of the test plan. In response to this new directive, WES prepared a revised instrumentation, test, and analysis plan for the prototype wickets. This plan called for a total of 40 sensors (28 in the steel gate and 12 in the composite gate) for measuring the flow-induced dynamic responses of the prototype wickets. The prototype dam is full scale but only five gates wide (approximately 50 ft). A composite wicket along with four traditionally coated different steel gates was installed in this facility. A complete geometric description of the steel and composite gates is reported in the literature (Chowdhury, Hall, and Davis in preparation; Chowdhury et al. 1997).

All but the shear pins in the sensor inventory was instrumented and calibrated by WES. Teledyne Brown Engineering was contracted to instrument and calibrate the hinge pins and prop pin for the prototype wickets. Note that the pins supplied by the Teledyne were incorrectly instrumented such that the location of one of the grooves on each pin was misaligned with the bearing. An error occurred due to the use of wrong dimensions during the machining of the grooves by the contractor. As a result of such misalignment, each shear pin acted in single-shear rather than double-shear, even though the shear pins were configured to be sensitive to double-shear. Use of this shear pins, thus, acted with a new sensitivity lower than the original calibration. Recalibration of shear pins, except the left vertical one which was no longer functional during the recalibration process, with single-shear was conducted by Teledyne to correct this measurement error. This pin had been repaired once before by WES to correct the leakage through the protective coatings. These corrective measures, thus, must be considered during the evaluation of the shear pin results presented in this report. Data presented for the shear pins were rescaled by using the new recalibration factor.

This report presents the experimental results of the prototype wickets for a number of available flow and operating configurations. Prototype and 1:5-scale physical model results are compared to determine the effectiveness of the hydraulic and structural similitude relationships. It also contains data plots and comparisons which show the results of flow-induced vibration and shaker-excited modal experiments performed on the prototype steel and composite gates and the 1:5 model. An explanation of the key aspects of each plot is given.

Objective

The objective of this analysis is to correlate respective results between the prototype and 1:5-scale wicket model, to include:

a. Prototype and model mode shape comparisons derived from laser vibrometer data.

b. Time- and frequency-domain comparisons of structural and hydraulic responses under corresponding gate and flow conditions.

c. Effectiveness of the 1:5 model in predicting structural and hydraulic responses of the Olmsted wicket for various gate configurations and flow conditions.

Scope

Several sets of experiments were conducted to compare the responses of the prototype and model gates:

a. Shaker-excited modal test on the prop-supported dry prototype wicket--Performed with a state-of-the-art Scanning Laser Doppler Vibrometer to extract the natural vibration characteristics of the prototype wicket for comparison to the 1:5 model.

b. Full operating range flow-induced vibration tests on the prototype--A full range of experiments conducted at available pool conditions to identify the critical gate configurations.

c. Fixed-gate flow-induced vibration experiment on the prototype--Conducted to identify critical flow conditions at the fixed 65-deg position.

d. Identical full operating range flow-induced vibration experiments on the 1:5 model--Conducted at corresponding prototype pool conditions to compare hinge forces, prop reaction, upstream/downstream pressures and accelerations at selected locations.

e. Identical fixed-gate flow-induced vibration experiment on the model--Conducted to compare forces, pressures, and accelerations at 65 deg.

Time- and frequency-domain comparisons of the respective responses between the systems will be performed to measure the adequacy of the 1:5 physical and numerical models for predicting the prototype response.

2 Modal Analysis

Shaker-Excited Modal Analysis

The Lazon laser data acquisition system was used to perform a shaker-excited modal analysis of the prototype steel, composite, and 1:5 model wicket gates. All gates were prop-supported in a dry configuration. I-DEAS Master Series CAE/CAM software was used to examine the Lazon data for determining the modal vibration characteristics of each gate. A schematic diagram for the laser setup is shown in Figure 1. The laser head was positioned 62 ft down from the prototype gate on a platform, and a MB Modal 50 A Exciter with two added inertia blocks (30 lb each) was used to excite the wicket using

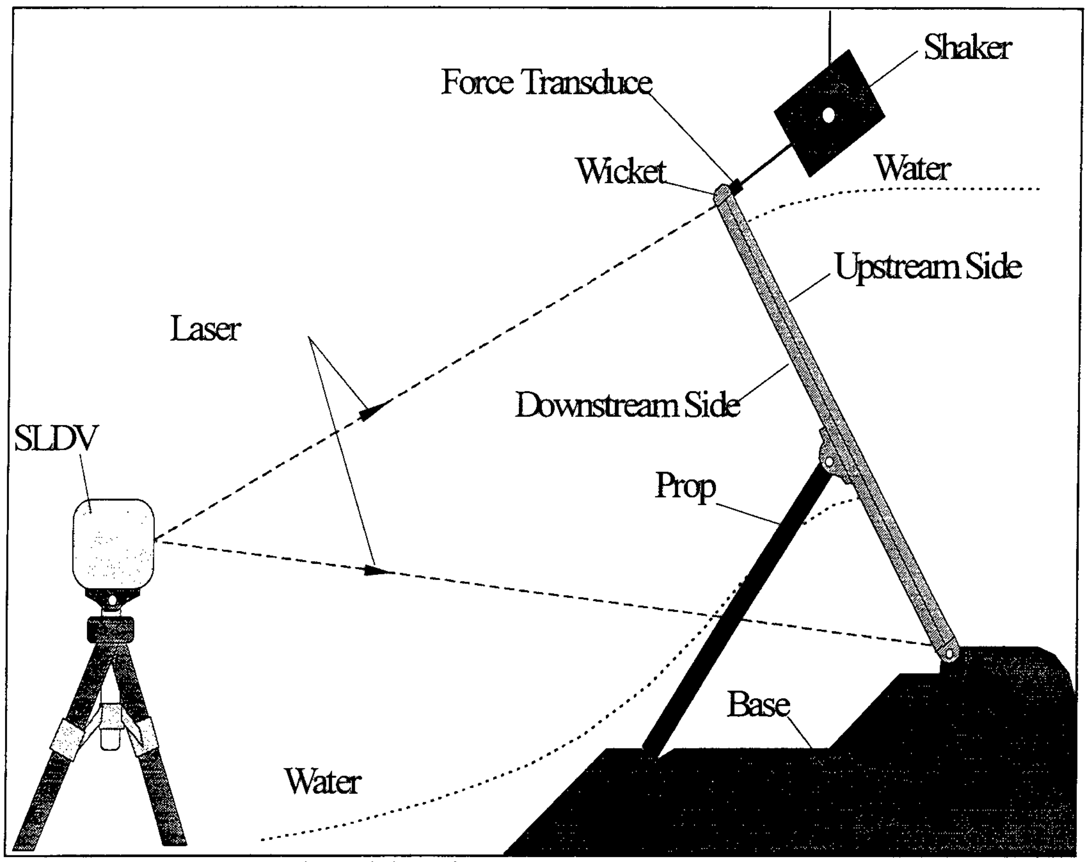

Figure 1. Experimental modal testing setup

a burst random signal. A detailed description of the analysis setup, laser operation, and information on modal analysis is reported in the literature (Chowdhury, Hall, and Davis in preparation; Zonic 1991; Structural Dynamic Research Corporation 1993; and Ewins 1984). The first seven mode shapes for the prototype steel, composite, and 1:5 model wickets are shown in Figure 2.

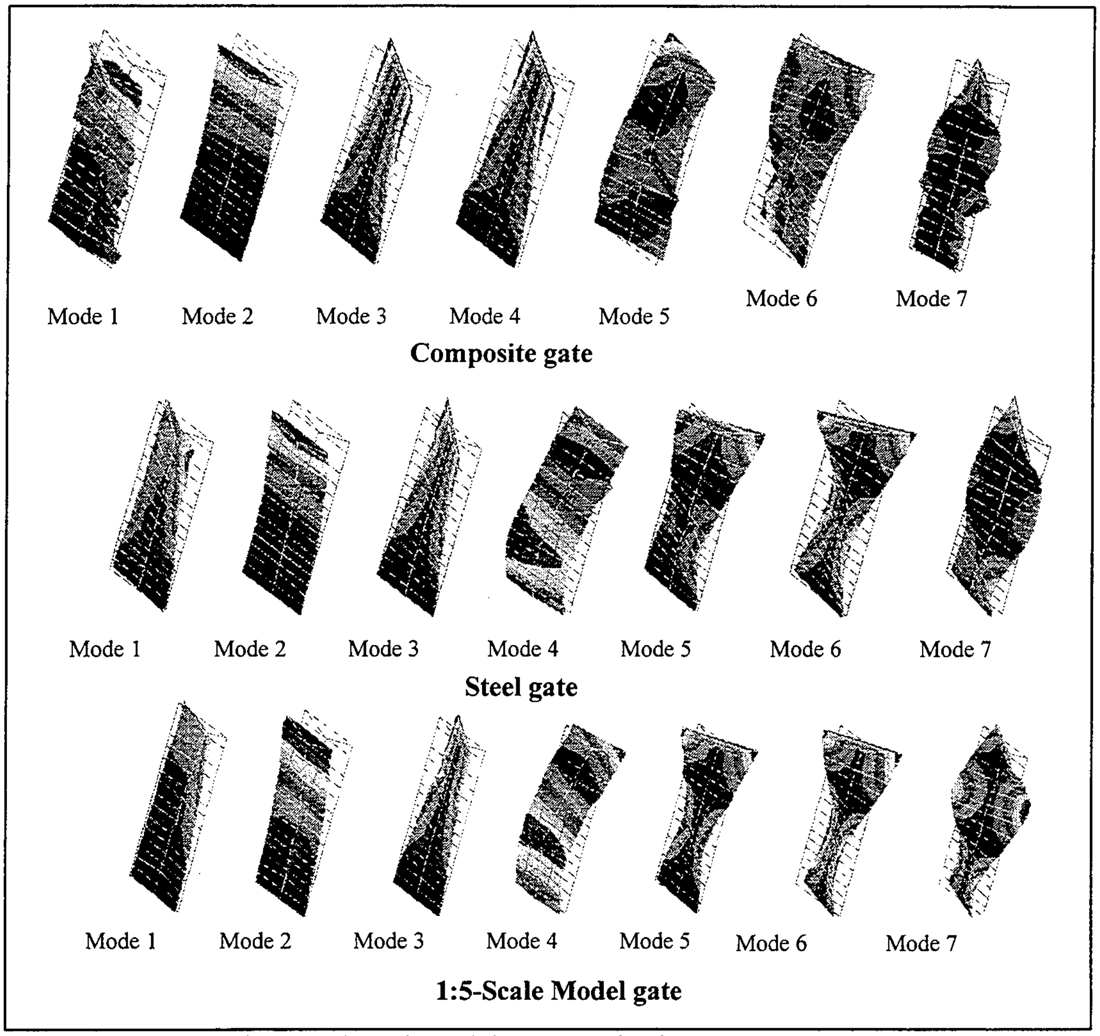

Figure 2. Composite, steel, and model gate mode shapes

Each of these representations of the mode shapes visually agrees, with the exception that modes 4 and 5 for the composite gate appear to be transposed. This is directly due to structural differences between the composite and steel gates.

In comparing the relative stiffness of the steel and composite gates, it was determined that the prototype steel gate had a higher bending and torsional stiffness in all corresponding modes. Since the natural frequency of both systems can be described by the square root of the spring constant divided by mass:

$$\omega = \sqrt{\frac{k}{m}} \tag{1}$$

a relationship between the spring constants for the steel and composite gates was developed such that:

$$\frac{k_s}{k_c} = \frac{(\omega^2 m)_s}{(\omega^2 m)_c} \tag{2}$$

The steel gate weight (22.86 K lb) was determined by summing hinge and prop-rod forces obtained from a dry gate data taken at 65 deg. Substituting frequencies from Table 1 for modes 2 through 5 into the equation above, spring constant ratios were obtained for a range of possible composite gate weights, shown in Table 2. $k_s/k_c > 1$ for each bending and torsion mode at the approximate composite gate weight of 15 K lb. This indicates the steel gate provided a higher relative stiffness for both bending and torsional modes than

Table 1
Experimentally Determined Mode Frequencies for Prototype Composite, Steel, and 1:5 Model Gates

Mode Number	Composite Modes [Hz]	Steel Modes [Hz]	1:5 Model Modes [Hz]	Scaled 1:5 Modes [$\lambda_L = 5$]
1	8.32	8.99	43.1	8.62
2	14.11	15.14	58.0	11.60
3	23.36	20.45	91.4	18.28
4	30.84	32.80	141.2	28.24
5	50.06	45.06	231.6	46.32
6	61.15	64.02	291.9	58.40
7	86.39	92.39	400.8	80.20

the composite gate. As shown in Table 2, if the composite weight was greater than 17.5 K lb, the composite gate would have exhibited a higher relative stiffness for mode 3 (torsion), and greater than 18.5 K lb the composite gate would have exhibited a higher relative stiffness for modes 3 and 5.

Table 2
Calculation of Stiffness Ratio between the Steel and Composite Gates

Composite Weight [K lb]	k_s/k_c Bending #2	Torsion #3	Bending #4	Torsion #5
13.0	2.02	1.35	1.99	1.42
13.5	1.95	1.30	1.92	1.37
14.0	1.88	1.25	1.85	1.32
14.5	1.82	1.21	1.78	1.28
15.0	1.75	1.17	1.72	1.23
15.5	1.70	1.13	1.67	1.19
16.0	1.64	1.09	1.62	1.16
16.5	1.60	1.06	1.57	1.12
17.0	1.55	1.03	1.52	1.09
17.5	1.50	1.00	1.48	1.06
18.0	1.46	0.97	1.44	1.03
18.5	1.42	0.95	1.40	1.00
19.0	1.39	0.92	1.36	0.97
19.5	1.35	0.90	1.33	0.95
20.0	1.32	0.88	1.29	0.93

The experimentally determined modal frequencies for the three gates are shown in Table 1. The first five modal frequencies for the 1:5 model gate compare well with the modal frequencies of the prototype steel and composite gates, which is substantiated later by modal correlation results. The slight deviations in frequency values between the 1:5 and prototype gates can be attributed to small variations in the nominal material sizes which were used to fabricate the gates, as well as the nonlinearity of the system. Figure 3 shows a graphic representation of the modal frequencies for the three gates.

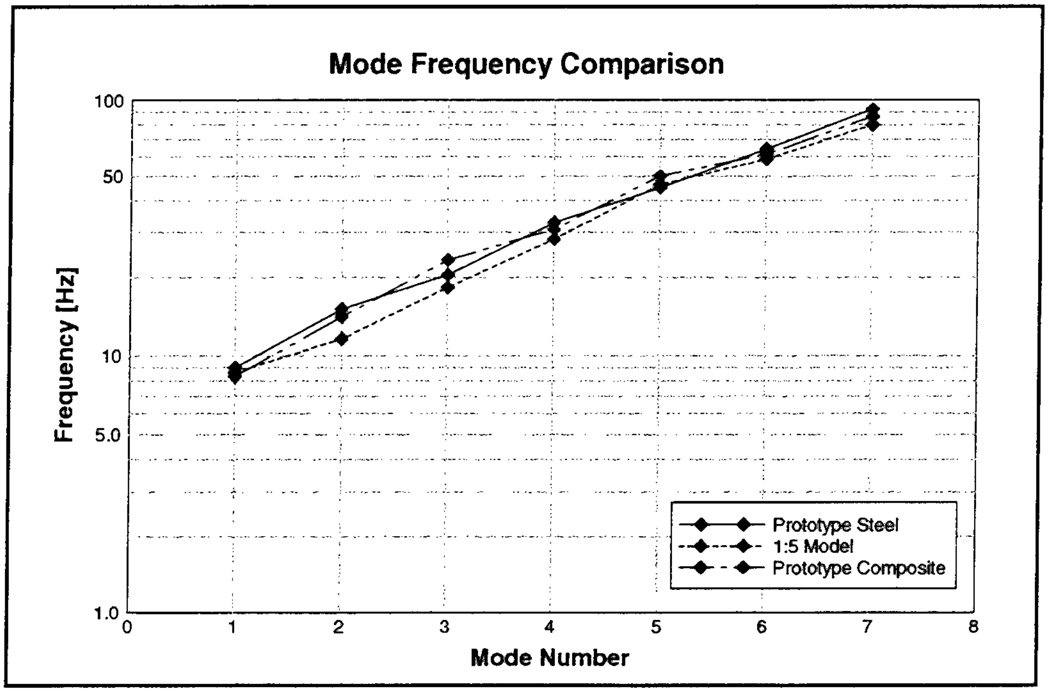

Figure 3. Mode frequency comparison for prototype steel, composite, and 1:5 model

As mentioned, the slight deviations in frequency values between the 1:5 and prototype gates, shown in Table 2, are in part attributed to system nonlinearity. Since the gates are supported by the prop-rod while fixed at 65 deg, the prop-rod contributes to the gate vibration. A modal analysis was performed for the prop-rod, pin-connected at the gate and free at the lower end, and some of the vibration characteristics are shown in Figure 4. The tendency toward extreme movement at the lower end of the prop-rod is not linear and will cause an increase or decrease in the gate modal frequencies for in-phase or out-of-phase prop-rod vibration, respectively. Consideration of the effects of prop-rod vibration may explain some of the modal frequency variance in Table 1.

Another cause of the shift in frequency values is the difference in inertial mass between the prototype steel and 1:5 model gates. The gate and prop-rod weight for the prototype is 22.86 K lb, while the model is 24.06 K lb (scaled by $\lambda_L^3 = 5^3$). Using the stiffness relationship to relate the prototype to model stiffness:

$$\frac{k_s}{k_m} = \frac{(\omega^2 m)_s}{(\omega^2 m)_m} \qquad (3)$$

this represents a 5.3 percent increase in model stiffness. This increase in stiffness causes the modal frequencies for the model to be lower than those of the prototype, which is the case in Table 1.

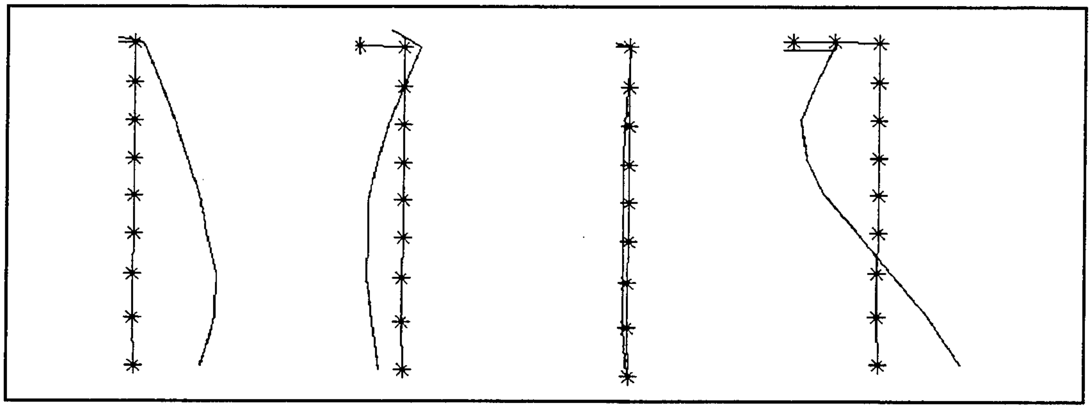

Figure 4. Vibratory characteristics of prop-rod with gate at 65 deg

As a measure of correlation between the prototype and model mode shapes, modal assurance criteria (MAC) plots were performed in I-DEAS (Structural Dynamic Research Corporation 1993). This analysis determines the percentage of correlation between all available mode shapes for two given experiments. Figure 5 shows correlation values above 50 percent for the prototype steel versus 1:5 model gates. This figure shows that the first seven modes of dry operation correspond well, while correlation becomes less distinct for the higher modes. Table 3 shows the same information in matrix format. All torsional modes for the model relate partially with the corresponding prototype bending and torsional modes. This indicates an interaction of the prop-bending tendency with the gate torsion modes. Note that a scaling factor of λ_L (5) is used to predict the prototype frequency from the model results. For the flow-induced motion, this frequency scale factor became $\sqrt{\lambda_L}$ based on the Froude scaling relationship.

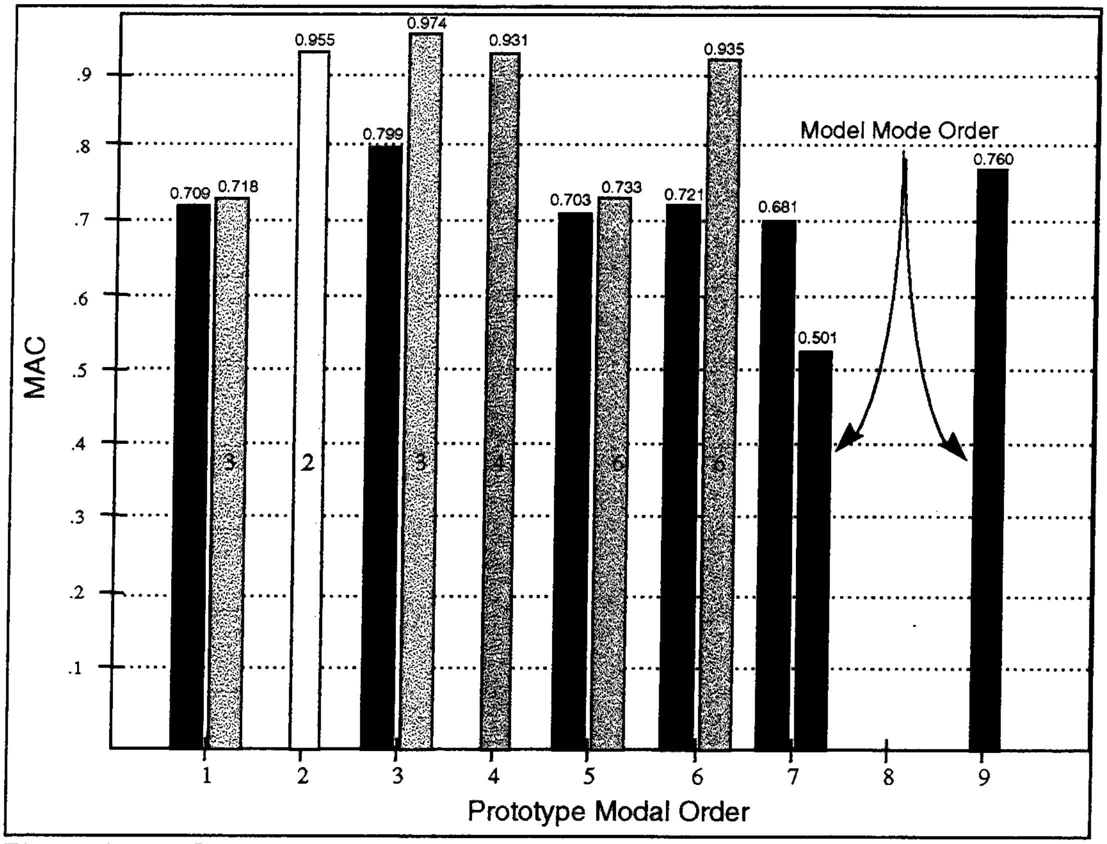

Figure 5. MAC plot for modal comparison of prototype steel and 1:5 model

Table 3
Correlation Matrix for the First 9 Modes between the Model and Prototype Steel Gate

Prototype	Model								
	1	2	3	4	5	6	7	8	9
1	0.709		0.718						
2		0.955							
3	0.799		0.974						
4				0.931					
5					0.703	0.733			
6					0.721	0.935			
7							0.681	0.501	
8									
9								0.76	

Figure 6 shows correlation values above 50 percent for the prototype steel versus composite gates. This figure shows that the first three modes of dry operation correspond well, while correlation becomes less distinct for higher modes. Modal correlation between the composite and steel prototype gates appears to break above the third mode, which is attributed to the localized effects of the geometry. A high degree of correlation between the lower order modes of composite and steel gates indicate that the two gates have a quite similar dynamic characteristics. The difference in higher order vibrational characteristics for these two gates is clearly evident in Figure 6. Table 4 shows the same information in matrix format.

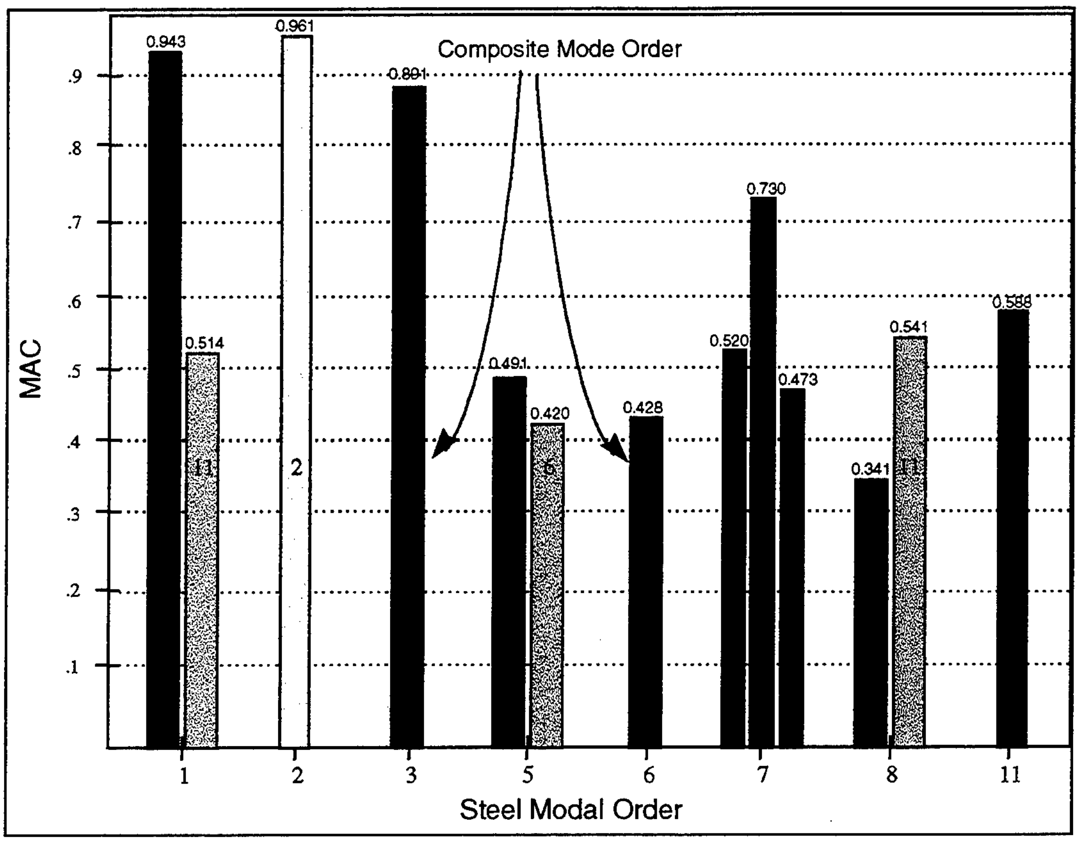

Figure 6. MAC plot for modal comparison of prototype composite and steel gates

Table 4
Correlation Matrix between the Composite and Steel Mode Shapes

Steel	Composite										
	1	2	3	5	6	7	9	10	11	12	13
1	0.943								0.514		0.366
2		0.961									
3		0.891									
4											
5				0.491	0.42						
6						0.428					
7	0.52								0.73		0.473
8	0.341								0.541		

Operating Deflected Shape - Frequency Domain

Acceleration data obtained from the prototype and model gates were used to develop operating deflected shapes (ODS) in the frequency domain. An agreement of the corresponding ODS would indicate the similarity of the flow-induced vibrational pattern of the operational wicket. A detailed discussion on the ODS extraction procedure using I-DEAS Master Series Test module is presented in the literature (Chowdhury, Hall, and Davis in preparation). Accelerometer data for the 1:5 model and prototype gates were imported into I-DEAS Test, and operating deflected shapes for cross-spectral peaks were determined. Modal frequencies determined from shaker excited modal analysis and Fast Fourier Transform analysis were taken into consideration for selecting these peaks, to improve accuracy of mode determination.

Operating deflected shapes for the prototype steel and model gates are shown in Figure 7. Data from the bottom right accelerometer on the composite gate were not properly recorded, which prevented an accurate representation and analysis of the composite gate operating deflected shapes using this method.

Although modes 2 through 5 appear to correlate, it was apparent that nine accelerometers were not enough to conclusively represent these vibrational shapes, and thus a credible correlation was not possible. Comparing deflected shapes in Figure 7 to those obtained by shaker excited modal analysis in Figure 2, significant vibratory motion in portions of the gate not defined by accelerometers is evident. Motion of portions of the gate between the accelerometers had to therefore be interpolated, which led to an increase in deflected shape ambiguity for the more complex mode shapes. Correlation between prototype and model operating deflected shapes by means of the MAC matrix was not as clearly defined as desired, due to the difficulty in defining these deflected shapes.

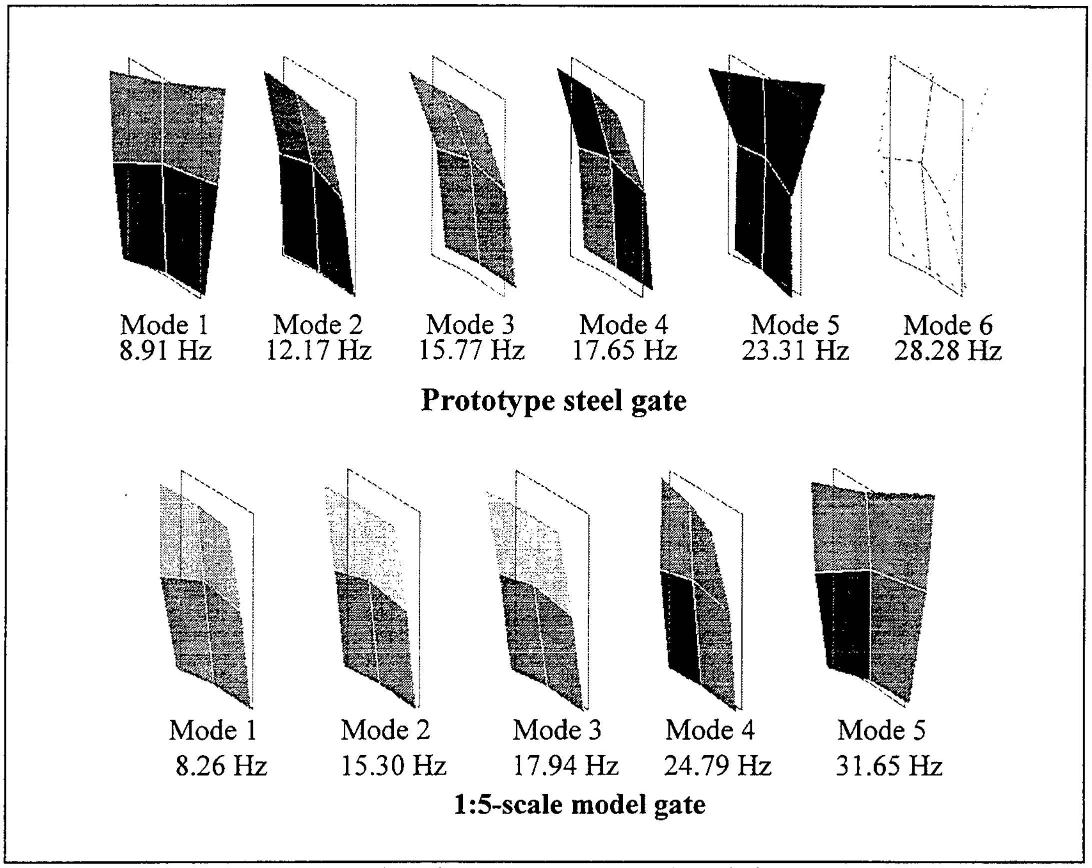

Figure 7. Experimental acceleration-derived operating deflected shapes

Driving-Point Mobility Function

The driving-point mobility function for the composite and steel gates is shown in Figure 8. This figure also shows the coherence plot, which is an indicator of the quality of the measurement. The driving-point mobility plot for the prototype steel and 1:5 model gates is shown in Figure 9.

The peak shifts in the FRFs shown in Figures 8 and 9 indicate that the gate system response was sensitive to the direction of the driving force. Such changes in the peak frequencies resulted primarily due to the nonlinear behavior of the "no-tension" prop-rod supporting mechanisms during wicket excitation. The bottom end of the prop-rod in its locked position provides restraint only along a direction away from the gate. Also the uncertain orientation of the clevis connection at the top end of the prop-rod introduced nonlinearity into the system.

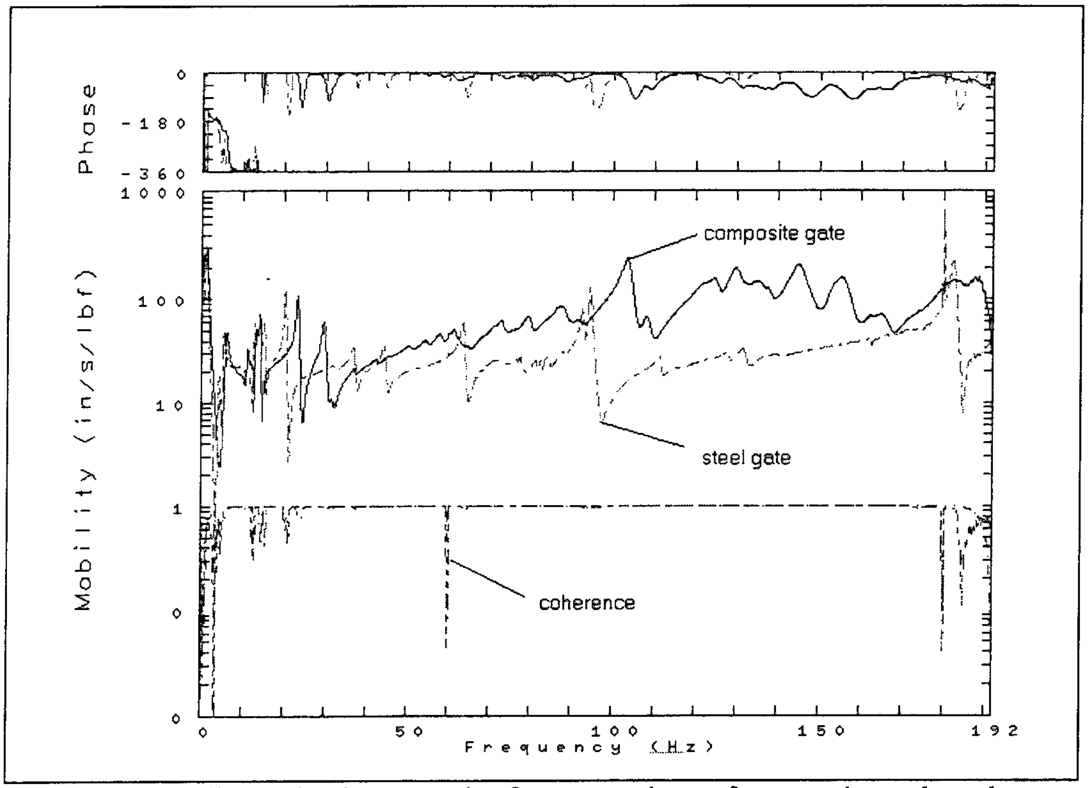

Figure 8. Mobility and coherence plot for comparison of composite and steel prototype gates

Modeling the uncertain orientation of the clevis connection at the top of the prop-rod, however, is beyond the scope of the present research. Such an intrinsic uncertain random behavior could be modeled using the stochastic FE method (Chang 1993).

Analysis of experimental results indicated that the modal density for the prototype and model remained invariant. An investigation of the mode shapes also indicated that the corresponding mode shapes for the model and prototype were identical, although the modal frequencies shifted as shown in Figure 9.

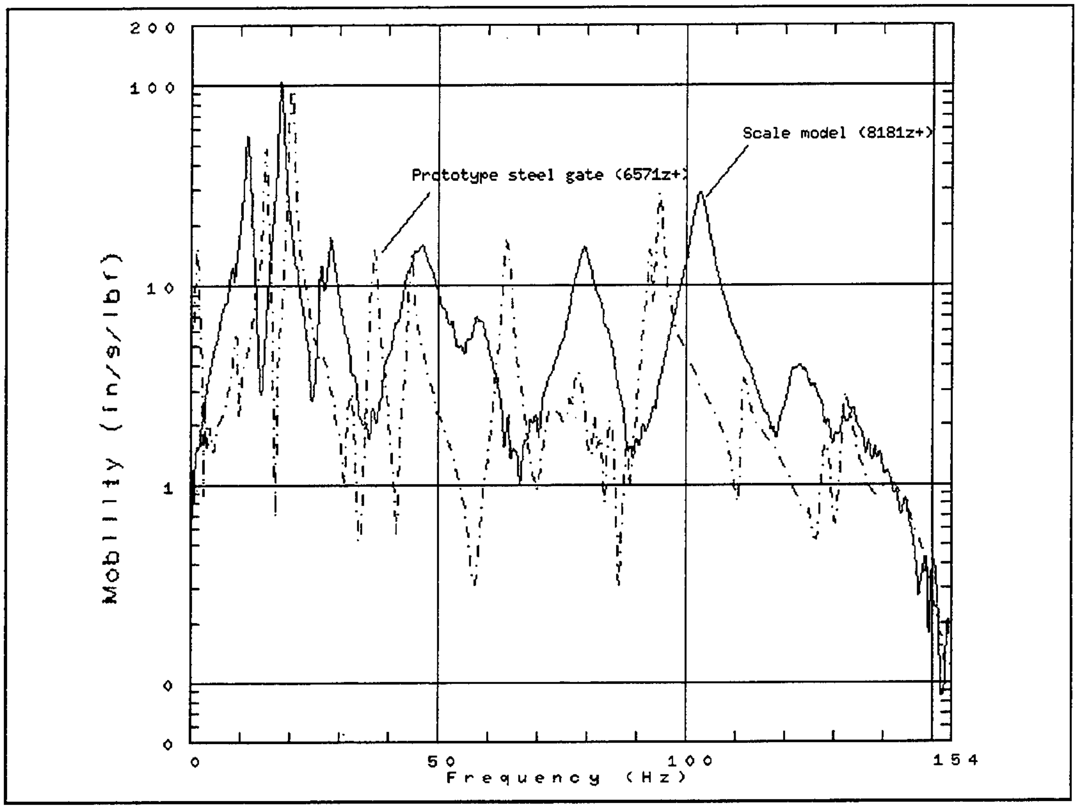

Figure 9. Mobility plot for comparison of 1:5 model and steel prototype gates

3 Flow-Induced 1:5 and Prototype Comparison

Gate Configurations, Flow Conditions

Identical flow-induced experiments were conducted with the 1:5 model corresponding to pool elevations for experiments performed on the prototype steel and composite gates. Fifteen experiment groups were developed to include all critical gate configurations. These included dry and wet configurations fixed at 65 deg, as well as full-range runs to identify the critical gate configuration among the following:

a. 1-gate gap
b. 2-gate gap (test gate as left gate, looking upstream)
c. 2-gate gap (test gate as right gate, looking upstream)
d. 3-gate gap (test gate as lone gate)

The gate numbering scheme is shown in Figures 10 and 11. Figure 10 shows the prototype gates fixed at 65 deg, while Figure 11 shows the model in a 3-gate gap configuration, with the test gate as the lone gate.

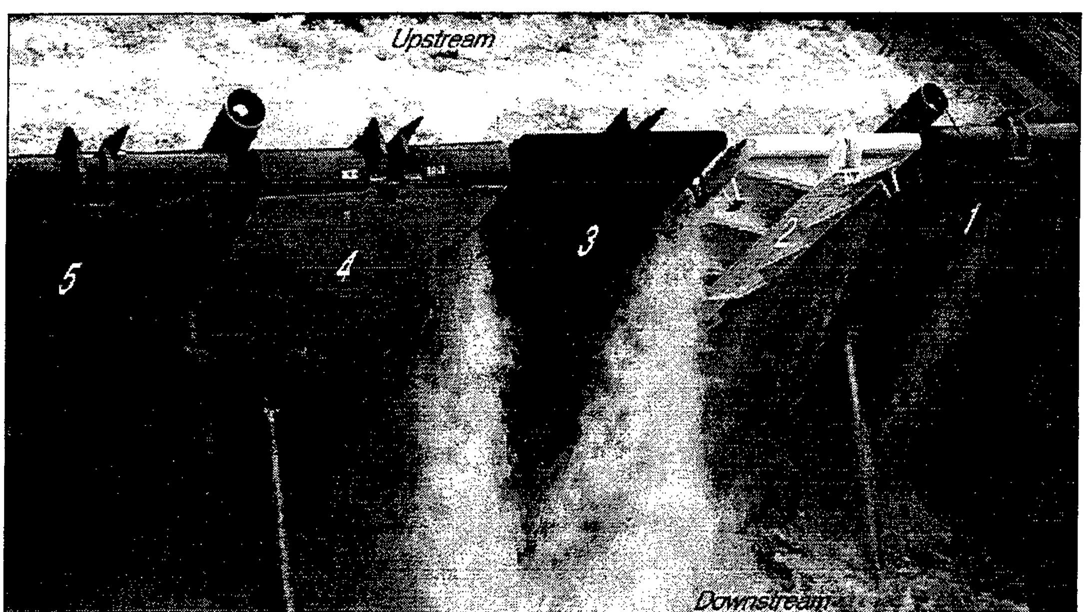

Figure 10. Prototype gates--downstream view

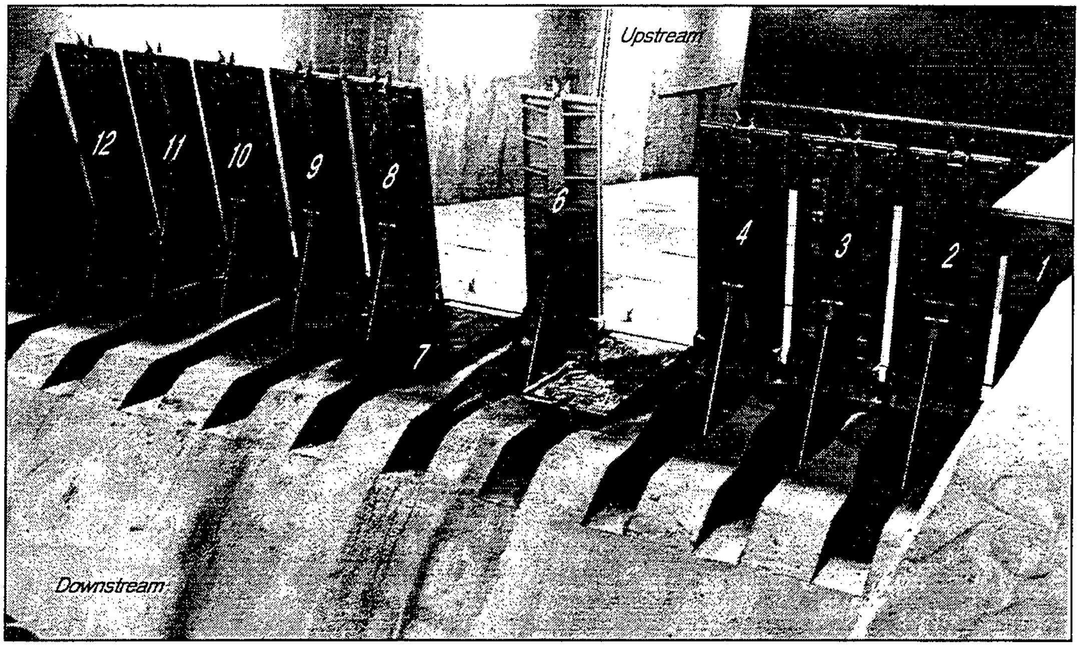

Figure 11. 1:5 Model gates--downstream view

Experiment Setup

The experiment log sheet for 15 test groups is presented in Table 5. This table includes the test group type (as explained in the remarks column), 1:5 model experiment numbers with corresponding prototype experiment numbers (experiments compared are circled), and the run date for each model experiment. Gate configuration is shown, as corresponding to Figures 10 and 11. Head- and tail-water levels for the prototype runs are shown, with those of the model in the next two columns. Head- and tail-water levels for the 1:5 runs were chosen to closely or exactly match those of corresponding prototype configurations. All model water levels were within 0.3 ft of corresponding prototype water levels, with most exactly matching.

The data conversion table, used to scale 1:5 model data to prototype scale and units, is shown in Table 6. All applicable channels of data collected for the prototype steel and composite gates were associated with corresponding channels for the model. Appropriate conversion factors to convert model data to prototype scale are shown. The two CAD drawings in Figures 12 and 13 show the sensor locations for the prototype steel and composite gates.

The instrumented steel gate had 28 sensors and the composite gate had only 12 sensors for recording the response history of the prototype wickets. More sensors were needed for the steel gate since the prototype steel gate response had been used to validate the similitude 1:5-scale model results for identical flow-induced experiments. Although there were fewer prototype sensors than in the scale model, the sensor locations for the prototype gates were kept identical to those of the 1:5-scale model. Selected composite gate responses were recorded to determine the typical response pattern due to available pool elevations. Each of the steel and composite gates had nine uniaxial accelerometers in three columns (two lines on both edges of the skin plate and another in the middle of the gate) to measure gate vibrations in the upstream (U/S)-downstream (D/S) directions. Each of the accelerometers was mounted on the skin plate such that three were installed in the top, three in the middle, and three in the bottom portion of the wickets. Type 4-202 strain gauge accelerometers were used, each with a rated range of ±25 g in the application (Consolidated Electrodynamics 1995b).

The steel gate had six pressure cells at three locations: one pair at the midcenter, one at the bottom left, and another pair at the bottom center on the surface of the wicket. Three of these pressure cells measured upstream pressure while the remaining three measured downstream pressures on the back of the gate. Type 4-312 pressure transducers were used, each with ±13 psi to ±50 psi pressure ranges (Consolidated Electrodynamics 1995a). The pins connecting the gate to the sill were instrumented to determine the reactions of the steel gate. The hinge pins were instrumented by Teledyne Brown Engineering. Two Type 4-312 pressure cells, one at the top surface and another mounted on the back of the gate, measured the pressure; a tiltmeter measured the inclination of the composite wicket gate. Detailed information on the instrumentation for the 1:5-scale physical model is available in the literature (Chowdhury, Hall, and Davis in preparation).

An in-house custom-built data acquisition system consisted of two personal computers, an analog-to-digital converter, signal conditioning amplifiers, and a printer used for recording the wicket response. Signal conditioning included continuous variable gain amplifiers, tracking filters, and anti-alias filters. Custom software was written to automate calibration measurements, data recording during a test, and time-history plotting of the recorded data. Matlab matrix analysis software and IDEAS-Master series test module (Structural Dynamic Research Corporation 1993) were used for postprocessing of the recorded data. More information regarding the measured response, including the transducer locations, calibrations, data acquisition and reduction system, and functional descriptions of the measured response are presented in the literature (Chowdhury, Hall, and Davis in preparation).

Table 5

Experimental Data Comparison Table - 1:5 Model to Prototype

Test Group #	1:5 Test #	1:5 Run Date	Corresponding 1:1 Test #'s	Wicket Gates Up	Wicket Gates Down	Test Gate #	Test Gate Operation	HW Level (Corrected to Olmsted,-25.5)	TW Level (Corrected to Olmsted,-25.5)	HW Level (1:5 Test Conditions)	TW Level (1:5 Test Conditions)	Remarks
1	800	2-8-96					-3 to 65			302.0	302.0	Zero reference test--wet
	801-802	2-8-96	612	1,2,4,5		3	-3 to 65	298.7	280.2	299.2	282.7	
	803	2-8-96	621	1,2,4,5		3	0 to 65	299	282.7	0	0	Zero reference test--dry (for expt. #803 only)
	804-805	2-8-96	623	1,2,4,5		3	0 to 65	299.2	282.7	299.2	282.7	1-GG UP
			625	1,2,4,5		3	0 to 65	299.3	282.8			
2	812-813	2-9-96	610	1,2,4,5		3	65 to -3	299.1	280.5	299.2	282.8	
			620	1,2,4,5		3	65 to 0	299.2	282.7			1-GG Down
			622	1,2,4,5		3	65 to 0	299.2	282.8			
			624	1,2,4,5		3	65 to 0	299.3	282.8			
3	808-809	2-9-96	628	1,5	2,4	3	0 to 65	298.6	283.0	298.6	283.3	
			630	1,5	2,4	3	0 to 65	298.6	283.3			3-GG UP
			632	1,5	2,4	3	0 to 65	298.3	283.4			
			643	1,5	2,4	3	0 to 65	298.6	283.6			
4	810-811	2-9-96	627	1,5	2,4	3	65 to 0	298.8	282.9	298.6	283.3	
			629	1,5	2,4	3	65 to 0	298.8	283.2			3-GG Down
			631	1,5	2,4	3	65 to 0	298.6	283.4			
			642	1,5	2,4	3	65 to 0	298.5	283.4			
			656	1,5	2,4	3	65 to 0	298.4	286.1			
5	814-815	2-9-96	649	1,4,5	2	3	0 to 65	298.6	285.9	298.7	285.9	
			651	1,4,5	2	3	0 to 65	298.8	285.9			2-GG(EL) UP
			653	1,4,5	2	3	0 to 65	298.6	286.0			
6	816-817	2-9-96	648	1,4,5	2	3	65 to 0	298.9	285.8	298.9	285.9	
			652	1,4,5	2	3	65 to 0	298.9	285.9			2-GG(EL) Down
			654	1,4,5	2	3	65 to 0	299.0	286.0			
7	818-819	2-9-96	657	1,2,5	4	3	0 to 65	298.4	286.2	298.7	286.4	2-GG(ER) UP
			669	1,2,5	4	3	0 to 65	299.0	286.6			
8	820-821	2-9-96	614	1-3,5		4	-3 to 65	298.6	280.7	298.6	280.7	
			616	1-3,5		4	-3 to 65	298.5	280.8			1-GG UP
			618	1-3,5		4	-3 to 65	298.6	280.7			
			647	1-3,5		4	-3 to 65	298.8	285.8			
9	822-823	2-12-96	613	1-3,5		4	65 to -3	298.8	280.8	298.8	280.8	1-GG Down
			615	1-3,5		4	65 to -3	298.8	280.9			
			617	1-3,5		4	65 to -3	299.0	280.8			ch. 17 pressure bad, not used
			646	1-3,5		4	65 to -3	299.2	285.8			on composite gate test.
10	824	2-12-96	635	1,2	3,5	4	0 to 65	298.4	283.9	298.5	284.0	
	825	2-13-96	637	1,2	3,5	4	0 to 65	298.5	283.9			3-GG(L) UP
			639	1,2	3,5	4	0 to 65	298.5	284.0			
			641	1,2	3,5	4	0 to 65	298.5	284.0			
11	826-827	2-13-96	634	1,2	3,5	4	65 to 0	298.3	283.8	298.8	283.9	
			636	1,2	3,5	4	65 to 0	298.7	283.8			3-GG(L) Down
			638	1,2	3,5	4	65 to 0	298.8	283.9			
			640	1,2	3,5	4	65 to 0	298.8	284.0			
12	828-829	2-14-96	661	1,2,5	3	4	-3 to 65	298.9	286.3	299.0	286.3	
			664	1,2,5	3	4	-3 to 65	299.2	286.3			2-GG(ER) UP
			666	1,2,5	3	4	-3 to 65	298.8	286.3			
13	830-831	2-14-96	660	1,2,5	3	4	65 to -3	298.9	286.4	299.0	286.4	
			662	1,2,5	3	4	65 to -3	299.1	286.4			2-GG(ER) Down
			663	1,2,5	3	4	65 to -3	299.2	286.5			
			665	1,2,5	3	4	65 to -3	298.8	286.4			
14	832-833	2-24-96	658	1,2,3	5	4	-3 to 65	299.0	286.3	299.0	286.3	
			667	1,2,3	5	4	-3 to 65	299.1	286.3			2-GG(EL) UP
			668	1,2,3	5	4	-3 to 65	298.8	286.5			
15	806	2-8-96	619	1-5		3,4	65	299.1	282.6	299.1	280.2	Fixed--wet
	807	2-8-96	633	1-5		3,4	65	299.1	283.5	0	0	Fixed--dry
			644	1-5		3,4	65	299.1	284.3			
			645	1-5		3,4	65					

NOTE: GATE #3 STEEL GATE, GATE #4 COMPOSITE GATE.
ALL TEST FILTERED AT 250 Hz. AND 500 SPS.

Table 6
Data Conversion Table - Olmsted 1:5 Model to Prototype

1:5 MODEL CH.#	TYPE	MEASUREMENT *	FACTOR =	1:1 STEEL GATE CH.#	TYPE	MEASUREMENT
1	FORCE	RIGHT HINGE PIN VERT. (LB)	125/1000	16	FORCE	RIGHT HINGE PIN VERT. (K LB)
2	FORCE	RIGHT HINGE PIN HORZ. (LB)	125/1000	17	FORCE	RIGHT HINGE PIN HORZ. (K LB)
3	FORCE	LEFT HINGE PIN VERT. (LB)	125/1000	18	FORCE	LEFT HINGLE PIN VERT. (K LB)
4	FORCE	LEFT HINGE PIN HORZ. (LB)	125/1000	19	FORCE	LEFT HINGLE PIN HORZ. (K LB)
7	FORCE	RIGHT TRUNNION @ 65deg (LB)				
			0.671(LT + RT)(125/1000)	20	FORCE	PROP ROD PIN @ 65deg (K LB)
8	FORCE	LEFT TRUNNION @ 65deg (LB)				
14	PRESSURE	5 U/S MIDDLE CENTER (IN. WC)	5/12	10	PRESSURE	U/S MIDDLE CENTER (FT WC)
17	PRESSURE	8 U/S BOTTOM CENTER (IN. WC)	5/12	11	PRESSURE	U/S BOTTOM CENTER (FT WC)
18	PRESSURE	9 U/S BOTTOM LEFT (IN. WC)	5/12	12	PRESSURE	U/S BOTTOM LEFT (FT WC)
23	PRESSURE	14 D/S MIDDLE CENTER (IN. WC)	5/12	13	PRESSURE	D/S MIDDLE CENTER (FT WC)
26	PRESSURE	17 D/S BOTTOM CENTER (IN. WC	5/12	14	PRESSURE	D/S BOTTOM CENTER (FT WC)
27	PRESSURE	18 D/S BOTTOM LEFT (IN. WC)	5/12	15	PRESSURE	D/S BOTTOM LEFT (FT WC)
28	PRESSURE	CYLINDER #6 (UPPER) (IN. WC)	5/12			
29	PRESSURE	CYLINDER #6 (LOWER) (IN. WC)	5/12			
32	ACCELER	1Z TOP-RIGHT (g.)	1	1	ACCELER	TOP RIGHT (g.)
33	ACCELER	2 TOP-CENTER (g.)	1	2	ACCELER	TOP CENTER (g.)
36	ACCELER	3Z TOP-LEFT (g.)	1	3	ACCELER	TOP LEFT (g.)
37	ACCELER	4 MIDDLE-RIGHT (g.)	1	4	ACCELER	MIDDLE RIGHT (g.)
40	ACCELER	5Z MIDDLE-CENTER (g.)	1	5	ACCELER	MIDDLE CENTER (g.)
41	ACCELER	6 MIDDLE-LEFT (g.)	1	6	ACCELER	MIDDLE LEFT (g.)
42	ACCELER	7 BOTTOM-RIGHT (g.)	1	7	ACCELER	BOTTOM RIGHT (g.)
43	ACCELER	8 BOTTOM-CENTER (g.)	1	8	ACCELER	BOTTOM CENTER (g.)
44	ACCELER	9 BOTTOM-LEFT (g.)	1	9	ACCELER	BOTTOM LEFT (g.)
47	TILTMETER	GATE ANGLE (DEG.)	1	27	TILTMETER	GATE ANGLE, STEEL (DEG.)
50	POSITION	ACTUATOR #6 (IN.)				
51	ELEVATION	HEADWATER (FT.)				
52	ELEVATION	TAILWATER (FT.)				
53	PRESSURE	BAROMETRIC (IN. WC)	1/12	28	PRESSURE	BAROMETRIC (FT WC)

1:5 MODEL CH.#	TYPE	MEASUREMENT *	FACTOR =	1:1 COMPOSITE GATE CH.#	TYPE	MEASUREMENT
32	ACCELER	1Z TOP-RIGHT (g.)	1	29	ACCELER	1 TOP RIGHT (g.)
33	ACCELER	2 TOP-CENTER (g.)	1	30	ACCELER	2 TOP CENTER (g.)
36	ACCELER	3Z TOP-LEFT (g.)	1	31	ACCELER	3 TOP LEFT (g.)
37	ACCELER	4 MIDDLE-RIGHT (g.)	1	32	ACCELER	4 MIDDLE RIGHT (g.)
40	ACCELER	5Z MIDDLE-CENTER (g.)	1	33	ACCELER	5 MIDDLE CENTER (g.)
41	ACCELER	6 MIDDLE-LEFT (g.)	1	34	ACCELER	6 MIDDLE LEFT (g.)
42	ACCELER	7 BOTTOM-RIGHT (g.)	1	35	ACCELER	7 BOTTOM RIGHT (g.)
43	ACCELER	8 BOTTOM-CENTER (g.)	1	36	ACCELER	8 BOTTOM CENTER (g.)
44	ACCELER	9 BOTTOM-LEFT (g.)	1	37	ACCELER	9 BOTTOM LEFT (g.)
18	PRESSURE	U/S BOTTOM LEFT (IN. WC)	5/12	38	PRESSURE	U/S BOTTOM LEFT (FT WC)
27	PRESSURE	D/S BOTTOM LEFT (IN. WC)	5/12	39	PRESSURE	D/S BOTTOM LEFT (FT WC)
47	TILTMETER	GATE ANGLE (DEG.)	1	40	TILTMETER	GATE ANGLE, COMPOSIT (DEG.)

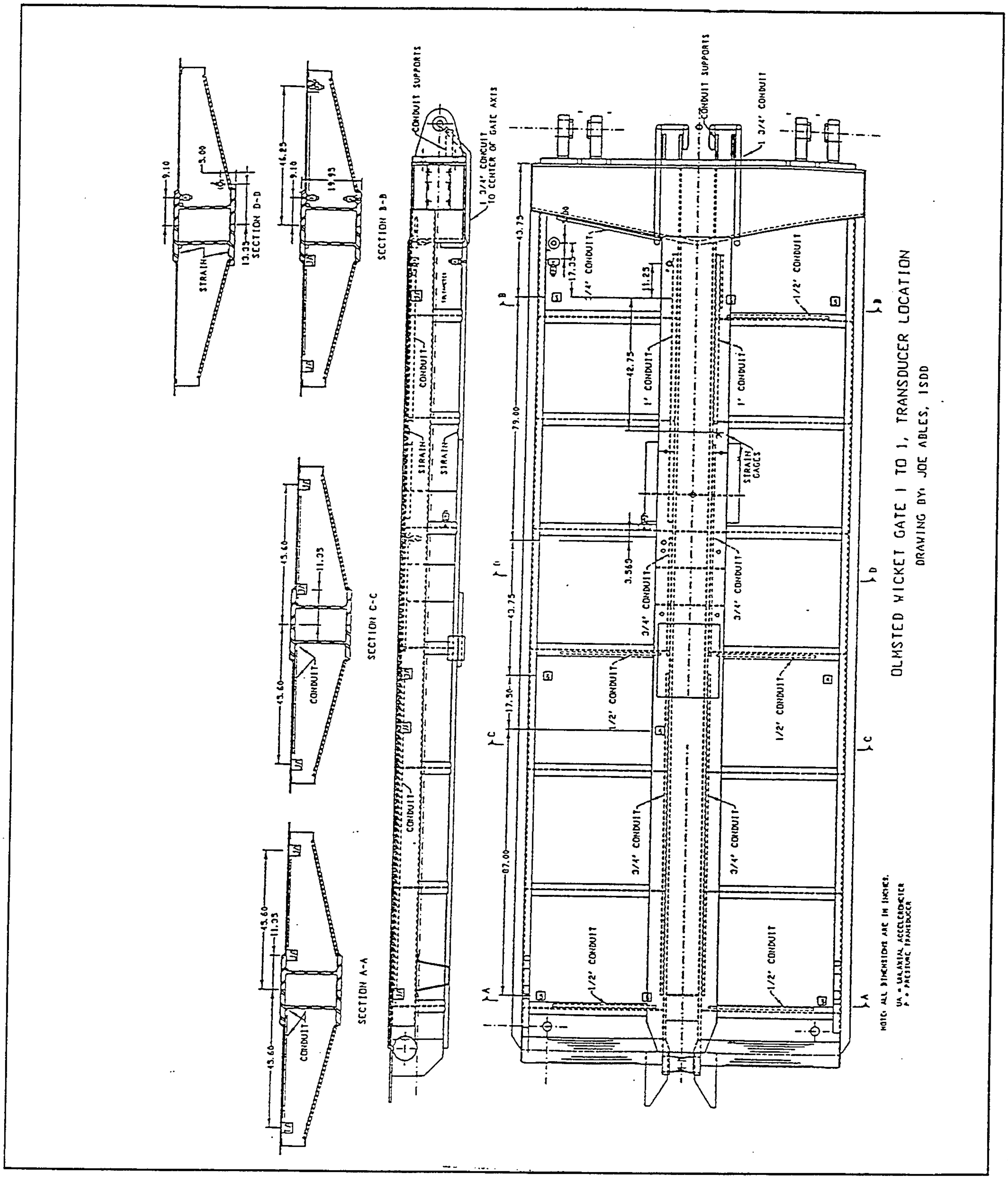

Figure 12. Prototype steel gate transducer locations

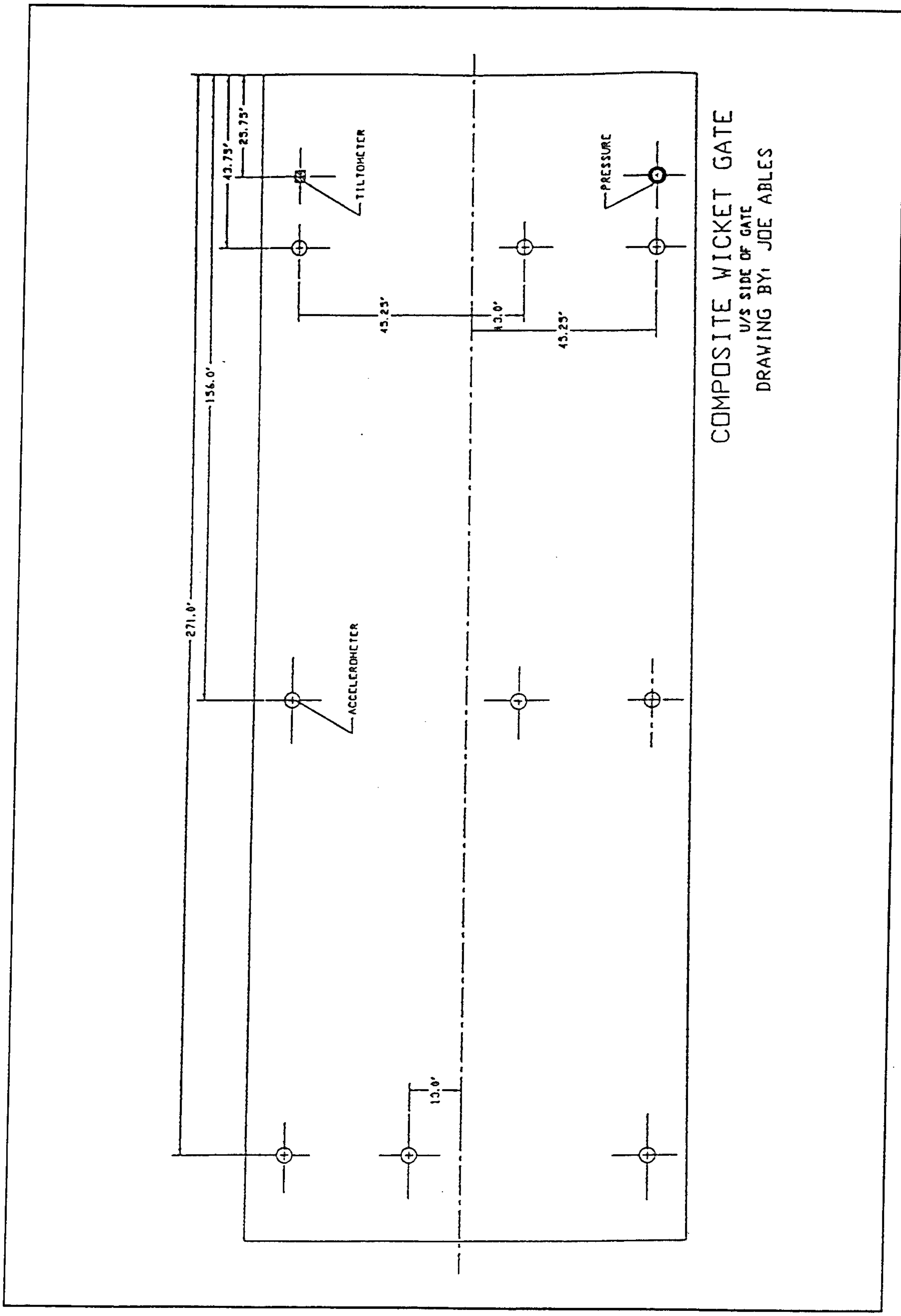

Figure 13. Prototype composite gate transducer locations

Time-Scaling Factor

The Olmsted wicket gate lock and dam system may be characterized as an open-channel flow with varying surface levels. Thus, achieving complete similitude between the Olmsted prototype and 1:5 model requires both Reynolds number and Froude number similarity. The three desired types of similarity are:

a. Geometric Similarity - length-scale ratio.
b. Kinematic Similarity - length-scale ratio, time-scale ratio.
c. Dynamic Similarity - length-scale ratio, time-scale ratio, force-scale ratio.

The Olmsted prototype and 1:5 model will be *geometrically* similar if and only if all body dimensions in all three coordinates have the same linear-scale ratio (White 1986). Geometric similarity between the prototype and 1:5 model was fairly well achieved, since all physical model dimensions were accurately scaled by 5 to include the nominal material sizes used in the model construction, and all hinges and other fasteners were accurately scaled. The only factor not accurately modeled was surface roughness, since this was not deemed significant for the scope of this hydraulic analysis. Fabrication cost would have been significantly higher in attempting to achieve a surface smooth enough to satisfy the requirement for Manning's roughness constant (Lindeburg 1992):

$$n_{ratio} = (L_{ratio})^{1/6} \quad (4)$$

The motions of the Olmsted prototype and 1:5 model will be *kinematically* similar if "homologous particles lie at homologous points at homologous times" (White 1986). To achieve kinematic similarity, all gate motion must be appropriately scaled. There are two significant areas where kinematic similarity is not achieved in the 1:5 model, both of which are due to variance in gate angular velocity between the prototype and model.

Differences in the prototype and model hydraulic systems caused a slight deviance in gate angle during the course of the tests. The prototype used a constant pressure hydraulic system, while the model used a constant angular velocity hydraulic system. This meant that as the prototype gate was raised from -3 to 65 deg, its angular velocity decreased as the load increased, while the model gate maintained a constant angular velocity throughout the same range. Thus, the prototype gate angular velocity is inversely related to total gate load, while the model gate angular velocity and gate load are approximately independent. This phenomenon is illustrated in Figure 14:

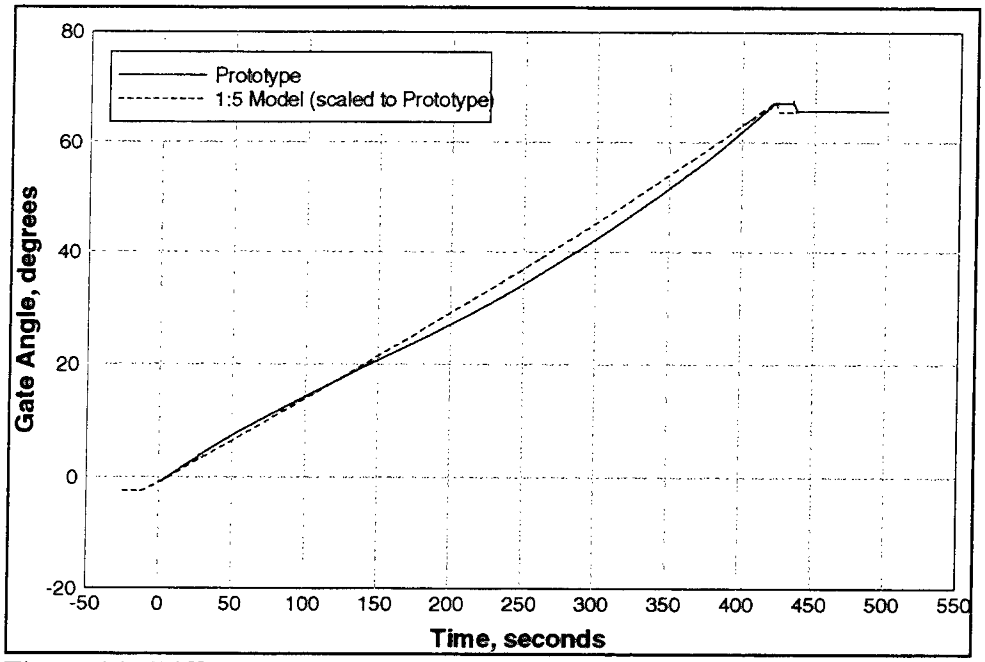

Figure 14. Difference in prototype and model gate angular velocity

Application of a correction factor for this phenomenon would involve determining a third- or fourth-order function to approximate the prototype curve, and then adjusting all time-dependent model data by this functional factor. After analysis of results for several comparison tests, it was decided that the deviance in gate angle versus time between the prototype and model would not significantly affect the data under consideration.

Because of differences in hydraulic system capabilities and other factors, the model gate was not raised at the appropriate angular velocity to permit correct scaling to the prototype. The correct time-scaling factor, derived from Froude similitude, takes the form:

$$T_p = \sqrt{\lambda_L} \cdot T_m \tag{5}$$

where $\sqrt{\lambda_L} = \sqrt{5}$

Scaling of time (and hence angular velocity) by $\sqrt{5}$ was not appropriate for comparison of the 1:5 model and prototype gates, as shown in Figure 15. To permit proper correlation with the prototype angular velocity, an adjusted scaling factor was

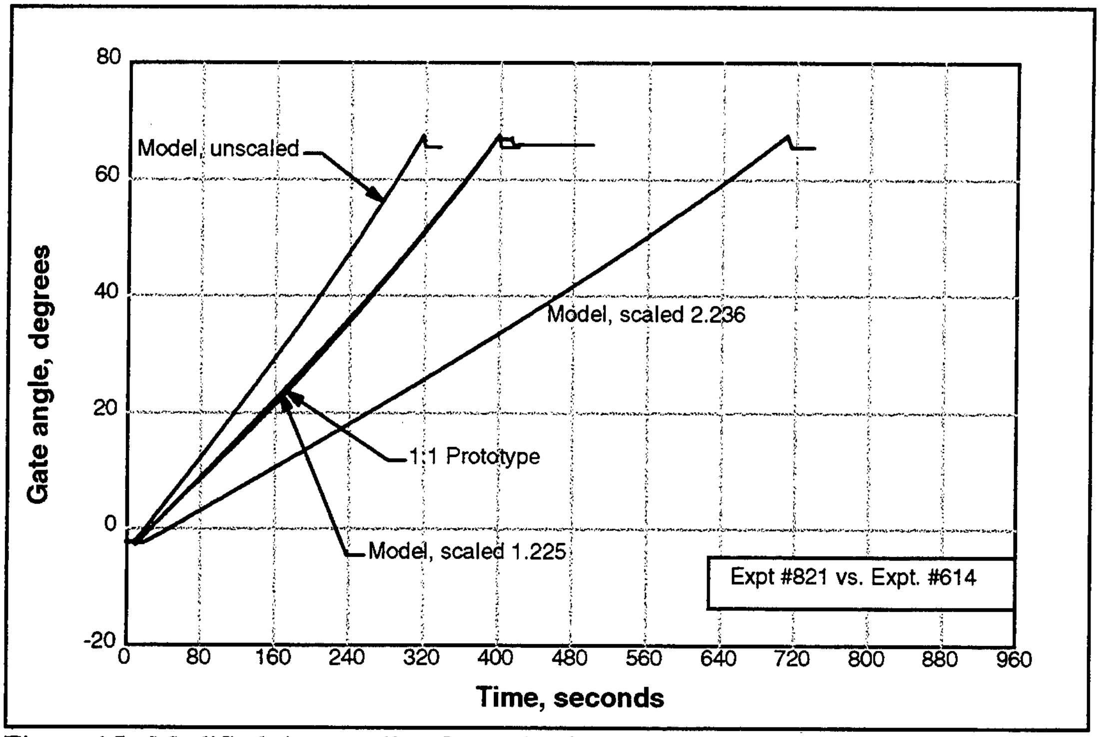

Figure 15. Modified time-scaling factor for 821 vs. 614

determined, which aligned the model gate angle curve to that of the prototype at two locations: 0 and 65 deg. This is essentially a scaling factor which equates gate travel time for the model and prototype and aligns the model gate to the prototype gate for any given position in (prototype) time. Use of this adjusted time-scale factor allows the model to meet the kinematic similarity requirement of "homologous particles located at homologous points at homologous times" (White 1986), even though it does not follow traditional Froude scaling requirements. Figure 15 also shows the closer correlation of model and prototype using the adjusted correction factor (1.225) for Experiment #821 versus Experiment #614.

Determination of a unique time-scaling factor for each comparison was required for two reasons. The first and primary reason was due to the constant pressure hydraulic shaft installed on the prototype. The load-dependent hydraulic system made it impossible to achieve equal travel times from -3 to 65 deg for the various prototype gate configurations. Since each gate configuration produced a unique loading pattern throughout the range of motion due to varying water flow patterns, plots of angular velocity were different for each configuration. A second, and less important, reason requiring unique time-scaling factors was due to unavoidable variances in the testing procedures. Part way through prototype testing, the foot on the prototype gate was damaged, which limited its operational range to 0 to 65 deg. Data collected from the model -3 to 65 deg range had to be shifted to align at 0 deg with the prototype for these comparisons. Additionally, the data abscissa also had to be shifted to align the gate rotation start times, since the start times for data sampling and gate rotation were never the same (to ensure the integrity of data during gate rotation). (Adjusting the abscissa does not distort the data in any way but merely aligns the start times for data acquisition to a known start point.) Thus, accurate correlation of prototype and model gate position versus time required a time-scaling factor unique to each comparison.

Table 7 shows some of the adjusted time-scale factors that were determined for specific test comparisons from plots of gate angle versus time. Determining the required ordinate shift (scale factor) for time was critical to achieving proper correlation of gate acceleration data in the frequency domain and is the primary focus of this discussion.

Table 7
Time-Scale Factors Obtained from Gate Angle Correlation

Test Type	Tests Compared	Similitude Scale Factor $\sqrt{\lambda_L}$	Modified Scale Factor	Abscissa Shift [seconds]
1-Gate Gap (up)	804, 621	$\sqrt{5}$	1.265	-24.2
3-Gate Gap (up)	808, 630	$\sqrt{5}$	1.395	-16.0
3-Gate Gap (down)	810, 631	$\sqrt{5}$	1.860	-5.8
2-Gate Gap (End Left) (up)	815, 649	$\sqrt{5}$	1.273	-24.89
2-Gate Gap (End Right) (up)	818, 657	$\sqrt{5}$	1.236	-3.34
1-Gate Gap (up-Composite)	821, 614	$\sqrt{5}$	1.225	0.0

The primary reason for determining corrected time-scale factors was to perform accurate Fast Fourier Transform (FFT) comparisons on prototype and model acceleration data. Determination of appropriate time-scale factors was crucial to showing modal alignment between the prototype and model. As shown in Figures 16 and 17, use of the adjusted time-scaling factor provides a much better correlation of frequency data. The model data scaled by 1.395 in Figure 16 shows the clearly defined peak alignment at frequencies of 15, 37, 43, 65, 112, and 150 Hz, while the model data scaled by the Froude factor of $\sqrt{5}$ do not show as clear of a correlation to peaks in the prototype data.

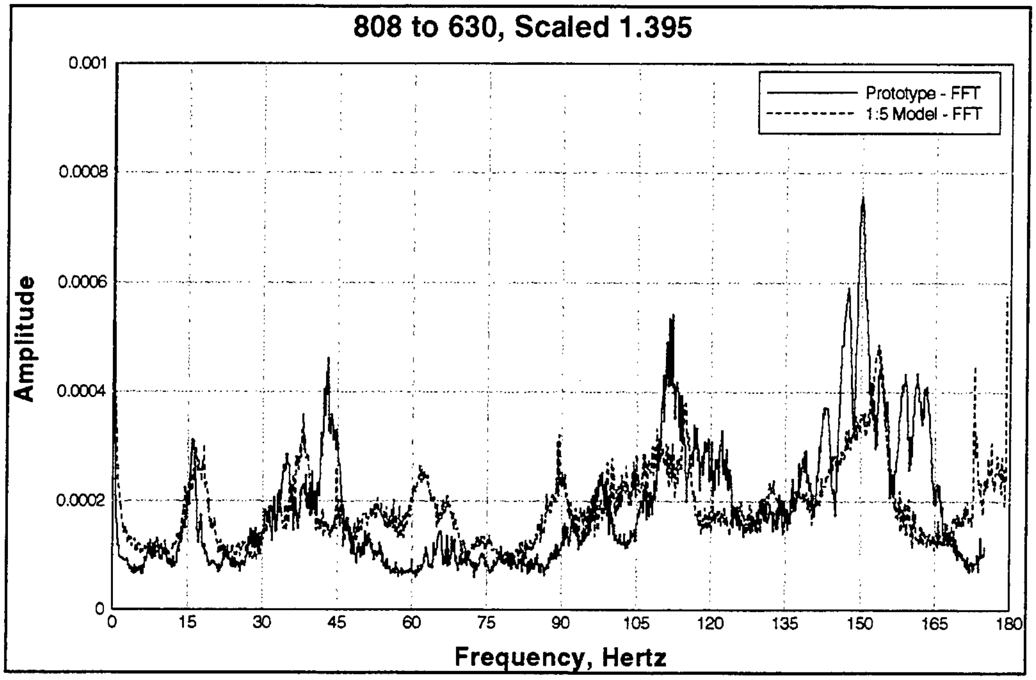

Figure 16. Acceleration FFT scaled by modified time-scale factor

If force, pressure, or acceleration measurements made on the prototype and model gates are compared as a function of time, this time-scale factor must be applied to achieve a valid comparison. All time-domain comparisons, however, were made as a function of gate angle, which inherently produced kinematic similarity. Only the frequency-domain comparisons (FFTs of acceleration and pressure) required plotting versus time, and so these were the primary data to which the adjusted time-scale factor was applied.

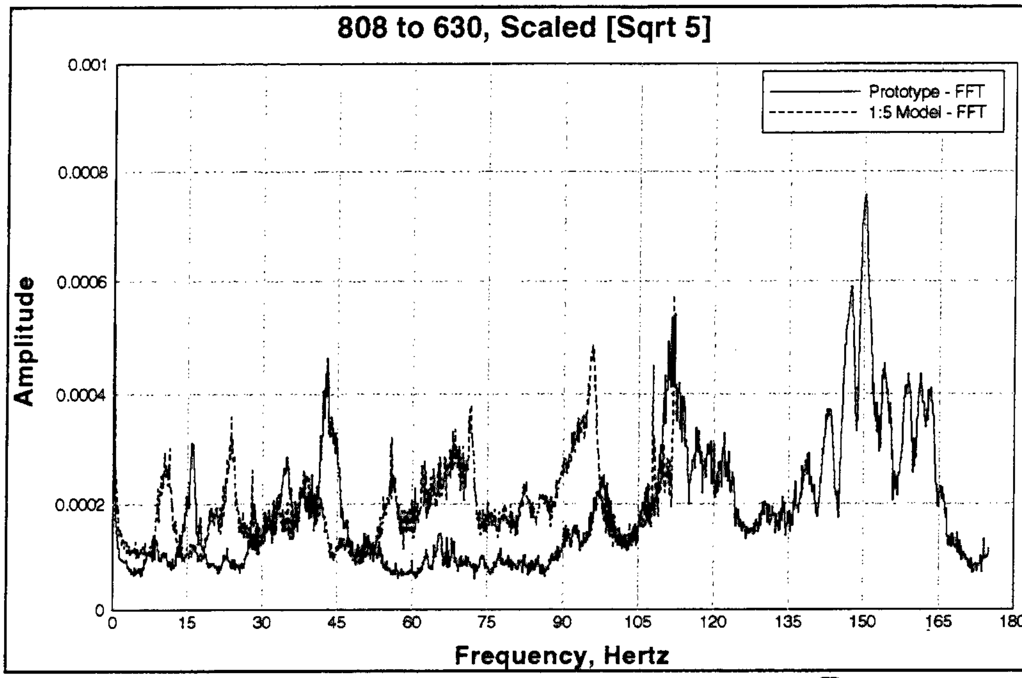

Figure 17. Acceleration FFT scaled by Froude scale factor of $\sqrt{5}$

Dynamic similarity will exist between the Olmsted prototype and 1:5 model when their force and pressure coefficients are identical (White 1986). Since dynamic similarity requires the prototype and model to have the same length-scale, time-scale, and force-scale (mass-scale) ratios, its only difference from kinematic similarity is the addition of the force-scale ratio requirement. For free surface flow, this translates to the requirement that prototype and model Reynolds numbers, Weber numbers, Strouhl numbers, and Cavitation (Euler) numbers be correspondingly equal. For these flow conditions, the Weber and Cavitation numbers are not necessary, which leaves Reynolds number equality as the only additional requirement. It has already been stated that surface friction was not a construction priority for the 1:5 model and that obtaining equal Reynolds numbers for the prototype and model was not of primary concern for the scope of the study (nor would it have been easily obtainable or economically feasible).

Thus, with the determination of a modified time-scale factor, the inventory of required scaling relationships is complete. Model data can be scaled to prototype units for comparison, or the model may be used to predict behavior of the prototype under additional flow conditions.

Damping

Table 8 shows a comparison of experimentally determined damping, natural frequency, and periods for several model and prototype flow configurations. This table shows an expected increase in damping factors from dry to wet operating conditions for both the prototype and model gates.

Table 8
Damping Comparison of Prototype Steel and 1:5 Model Gates

Experiment Type		Experiment #	Accel Position	Period [sec]	Frequency [Hz]	Damping Factor (Zeta)
Dry Test	1:5 Model	803	1z (T.R.)	0.0179	351.0	0.0185
			2 (T.C.)	0.018	349.1	0.0162
			3z (T.L.)	0.0177	356.0	0.0188
	Prototype Steel	601	1z (T.R.)	0.0674	93.2	0.0072
			2 (T.C.)	0.0674	93.2	0.0065
			3z (T.L.)	0.0677	92.9	0.00685
1-GG	1:5 Model	804	1z (T.R.)	0.0194	323.7	0.025
			2 (T.C.)	0.0192	327.5	0.023
			3z (T.L.)	0.0195	321.7	0.0235
	Prototype Steel	621	1z (T.R.)	--	--	--
			2 (T.C.)	--	--	--
			3z (T.L.)	--	--	--
3-GG	1:5 Model	808	1z (T.R.)	0.0187	336.0	0.0772
			2 (T.C.)	0.0186	337.8	0.0273
			3z (T.L.)	0.0184	341.5	0.0426
	Prototype Steel	630	1z (T.R.)	0.080	78.54	0.0411
			2 (T.C.)	0.0812	77.38	0.0489
			3z (T.L.)	0.0812	77.38	0.043

T.R. = top right
T.C. = top center
T.L. = top left

Data were obtained by considering a portion of accelerometer data immediately after a significant driving force input caused a vibratory motion in the gate. One such force was caused when the prop-rod settled against its stop; the momentum of the gate induced a transient vibration which exhibited the damping effects shown in the plots. Figures 18 and 19 identify the transient response of the gate as the prop-rod is placed on the hurter recess.

When feasible, the period and frequency were determined by the logarithmic decrement method (measuring the amplitudes of successive peaks):

$$\delta = \ln \frac{X_n}{X_{n+1}} \tag{6}$$

with the damping factor, zeta, determined by:

$$\zeta = \frac{\delta}{\sqrt{(2\pi)^2 + \delta^2}} \tag{7}$$

In other instances it was necessary to perform a curve fit (illustrated in Figures 20 and 21) to obtain the best-matched decaying exponential curve,

$$x(t) = Xe^{-\zeta \omega t} \tag{8}$$

which permitted an accurate determination of the damping factor (Hutton 1981). The decaying exponential curve is the damped portion of the equation of motion:

$$\mathrm{x(t)} = \mathrm{Xe}^{-\zeta \omega t} \sin(\omega_d t + \phi) \tag{9}$$

ω_d was determined from the period of the system, τ, and the natural frequency, ω, with the following:

$$\omega = \frac{2\pi}{\tau} \tag{10}$$

$$\omega_d = \sqrt{1-\zeta^2}\,\omega \tag{11}$$

Examples of decaying exponential curve fits, as well as plots of the natural vibratory decay for wet and dry gate operation, are shown in Appendix A, Figures A1 through A18.

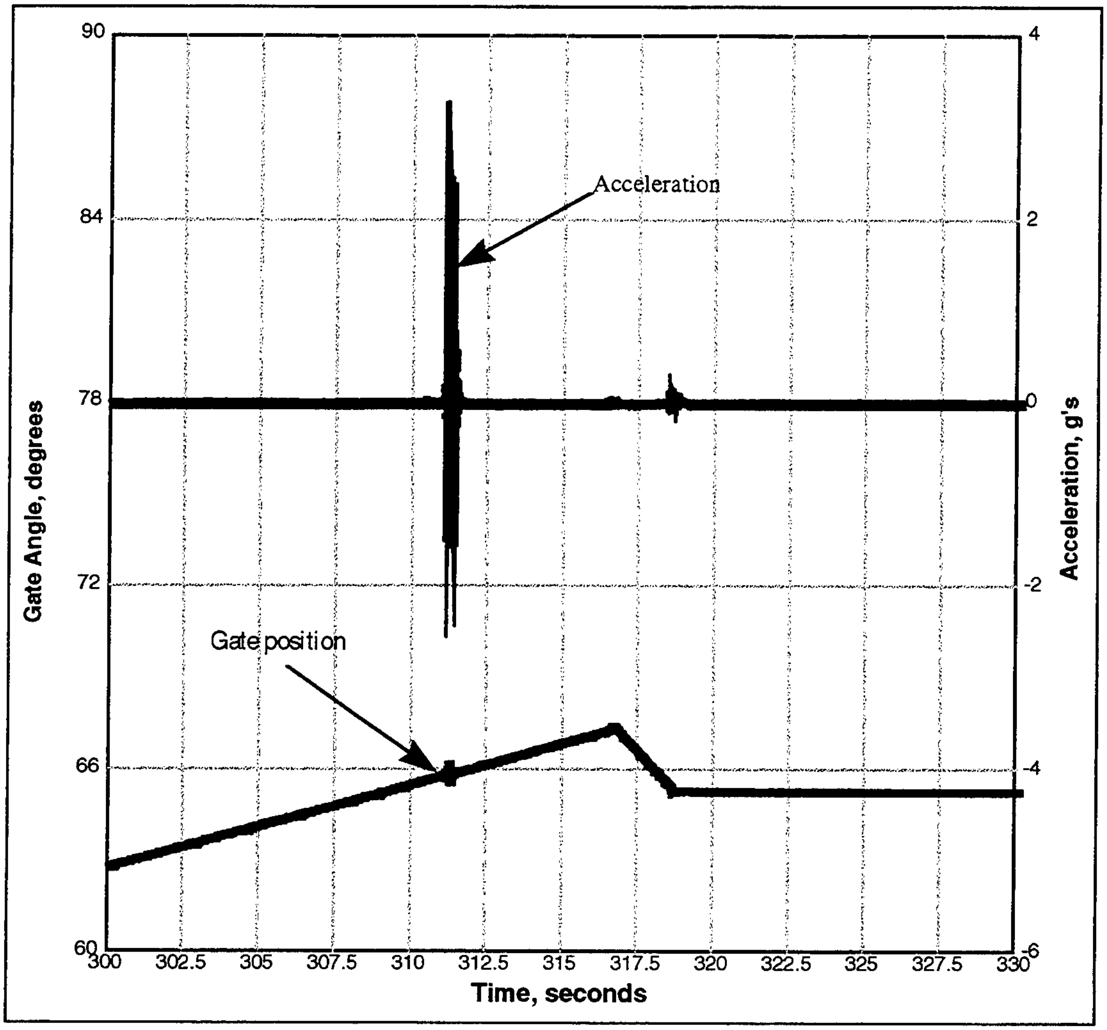

Figure 18. Gate angle/acceleration vs. time (Experiment # 803)

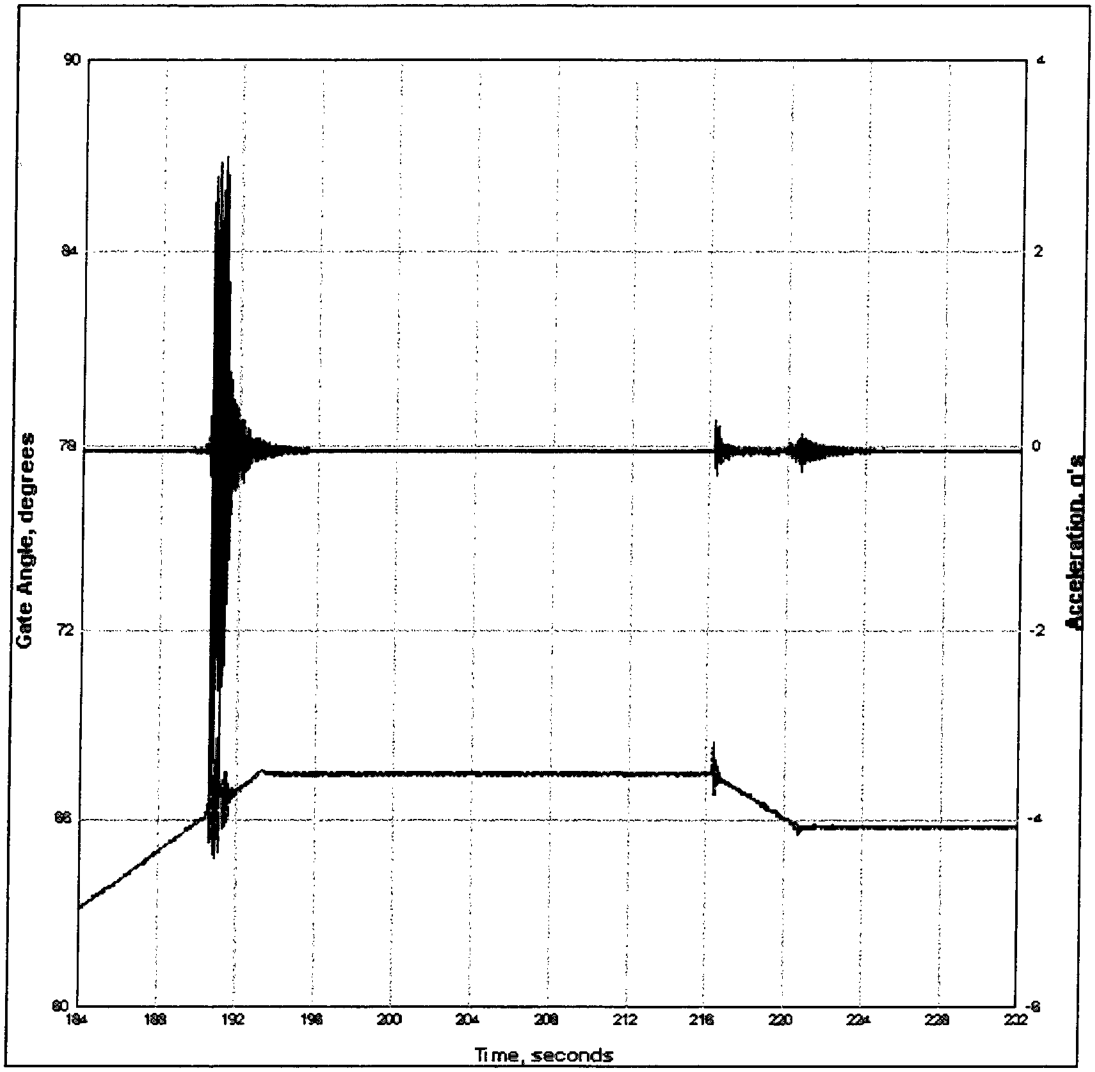

Figure 19. Gate angle/acceleration vs. time (Experiment #601)

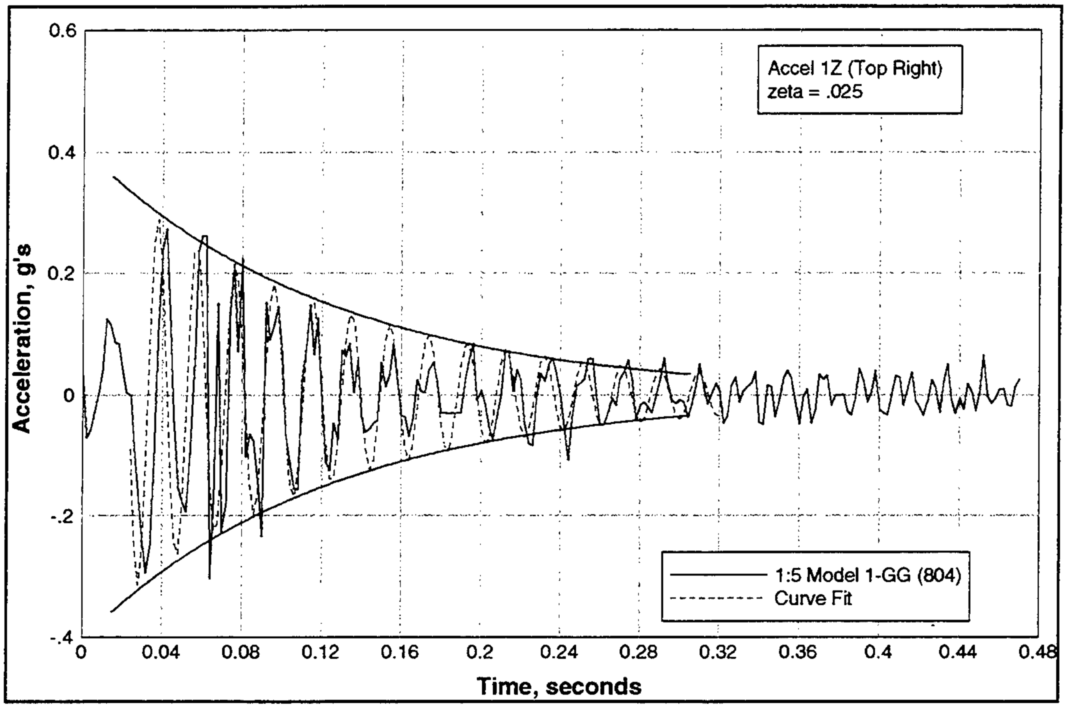

Figure 20. Decaying exponential curve fit: 1-gate gap

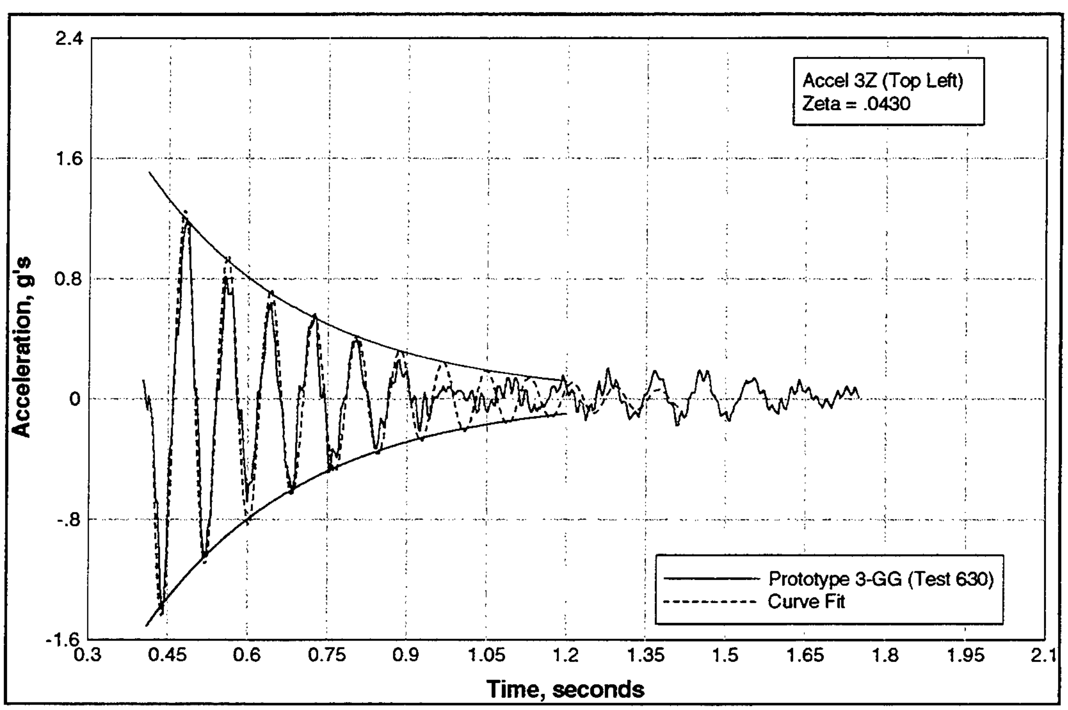

Figure 21. Decaying exponential curve fit: 3-gate gap

Frequency-Domain and FFT Plots

In Appendix B, Figures B1 through B84 show Fast Fourier Transforms of pressure and acceleration, with corresponding plots versus time for three identical-flow comparisons between the prototype steel and 1:5 model gates. For proper correlation, the model data were scaled by time-scale factors discussed earlier. Since the prototype used strain-gauge accelerometers to record both static and dynamic accelerations and the model used piezoelectric accelerometers to record only dynamic accelerations, it was necessary to subtract the static portion of the prototype data. This was accomplished by subtracting the acceleration offset due to the gate rotation:

$$\text{Acceleration}_{(\text{dynamic})} = \text{Acceleration}_{(\text{total})} - \text{Cosine(gate angle)} \qquad (12)$$

The static portion of acceleration is represented by the cosine of the gate angle, and in data collection the static acceleration was -1 at $\theta = 0$, and 0 at $\theta = 90$. Subtraction of static acceleration from prototype data is represented in Figure 22.

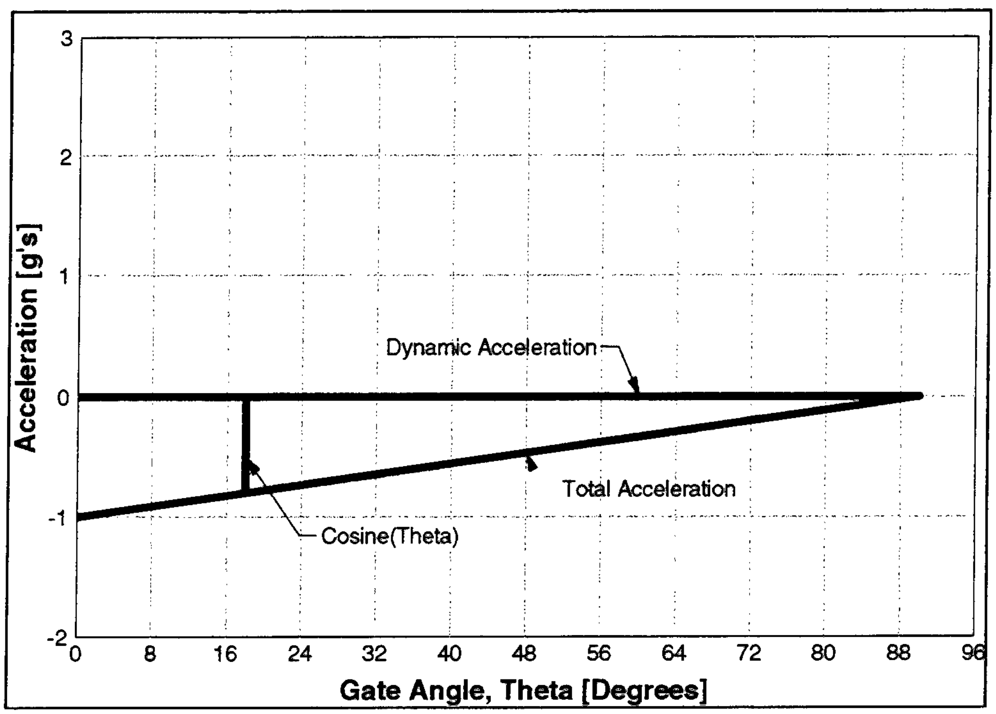

Figure 22. Representation of method for subtracting static acceleration from prototype data

The time-domain plots of acceleration in Appendix B (Figures B1 through B84) show the dynamic acceleration for the prototype and model gates. Figures B81 through B84 show comparison plots before the static acceleration was subtracted from the prototype data.

As seen in these plots, upstream and downstream power spectra agreed well for the prototype and the model. The frequency plots, particularly those generated from accelerations, show reasonable correspondence between modal peaks for the prototype and model. For example, Figure 23 shows the peak alignment at the top left accelerometer location. Peaks at 15, 39, 62, 110, and 155 Hz correlate well, while there is a slight deviance between the peaks for the prototype at 83 Hz and the model at 90 Hz.

Resonant peaks below 15 Hz for the top accelerometers in the prototype wicket did not appear in the model. These low-frequency peaks were associated with the rigid body translational and rotational motion of the operating wicket. A difference in the

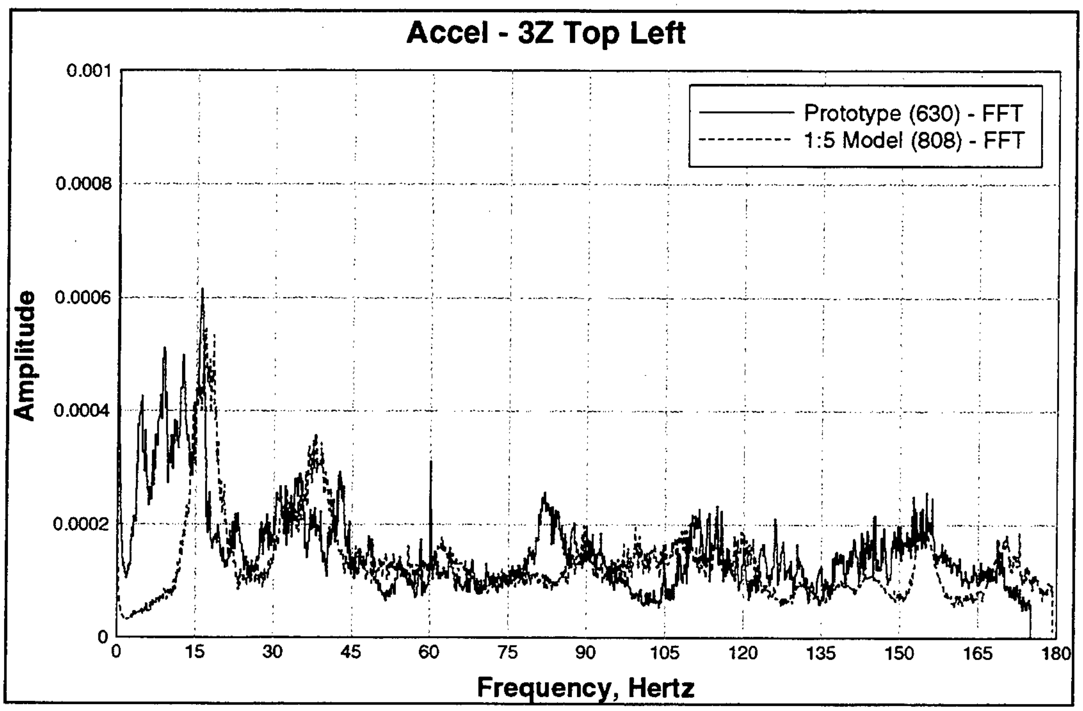

Figure 23. FFT of acceleration, 3Z top left for 1:5 model 808 to prototype 630

frequency distribution is the result of satisfying the Froude model scaling relations for the first structural mode of vibrations as discussed in the 1:5-scale model report (Chowdhury, Hall, and Davis in preparation). Despite the difference in the frequency spectra, the dominating modes contributing the most to the vibration of the prototype wicket were well reproduced in the model. A companion analytical study of the model indicates that the first three modes excluding the rigid body contributed significantly to the dynamic response of the wet wicket (Chowdhury, Garner, Seda, and Hall 1997). Frequency plots were developed for all pressure and acceleration data, which included:

1:5 Model Channel #	Prototype Channel #	Type	Measurement
1	16	Force	Right hinge pin vert.
2	17	Force	Right hinge pin horz.
3	18	Force	Left hinge pin vert.
4	19	Force	Left hinge pin horz.
14	10	Pressure	U/S middle center
17	11	Pressure	U/S bottom center
18	12	Pressure	U/S bottom left
23	13	Pressure	D/S middle center
26	14	Pressure	D/S bottom center
27	15	Pressure	D/S bottom left
32	1	Acceleration	1z top right
33	2	Acceleration	2 top center
36	3	Acceleration	3z top left
37	4	Acceleration	4 middle right
40	5	Acceleration	5z middle center
41	6	Acceleration	6 middle left
42	7	Acceleration	7 bottom right
43	8	Acceleration	8 bottom center
44	9	Acceleration	9 bottom left

Time-Domain Plots

In Appendix C, Figures C1 through C54 show time-domain comparisons between the prototype and model gates for all appropriate data listed in the Data Conversion Table (Table 6). All plots are functions of gate angle in degrees, which eliminates the need to apply a time-scaling factor.

A comparison of both hinge reactions for different flow configurations are presented in Figures 24 and 25. Total vertical and horizontal forces exerted on the hinges due to flow-induced motion for the indicated flow configurations are shown in Figure 26. Sensitive axes of the shear transducer were fixed with the local axes of the gate such that one axis was normal to the gate surface (vertical) and another was parallel to its longitudinal axis (horizontal). Thus, a positive horizontal force results due to the pulling of the gate away from the sill, and a positive vertical reaction resists the downward motion of the gate. A comparison of right and left reaction indicates that the reaction forces for both hinges are asymmetrically distributed and their directions are reversed as the gate is raised from down to the up position. This type of reverse loading at the bottom hinges may exhibit fatigue distress due to long-term loading. An observation of the test results indicates that the peak response is attained right at or about the moment when the

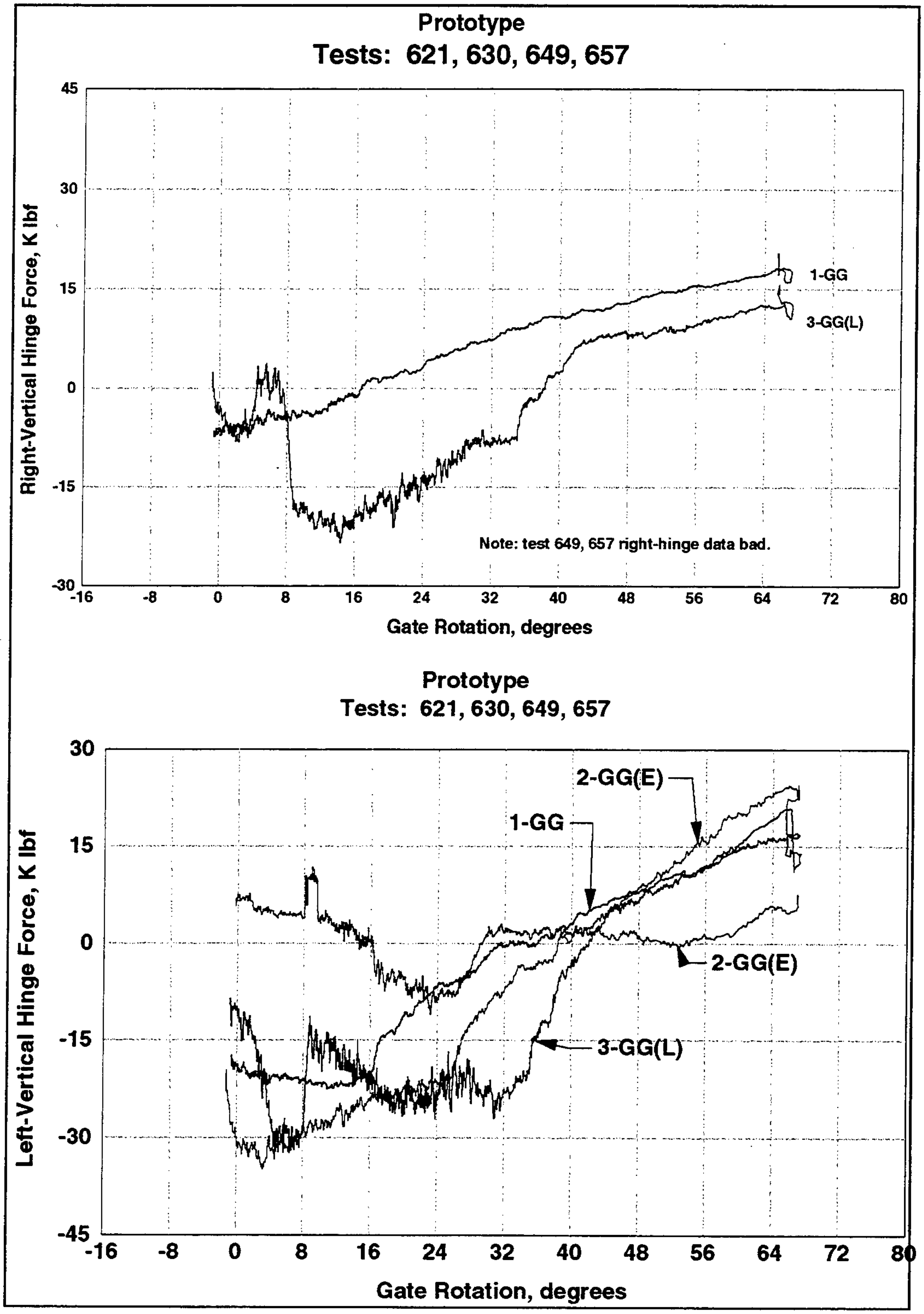

Figure 24. Prototype vertical reactions for different flow conditions

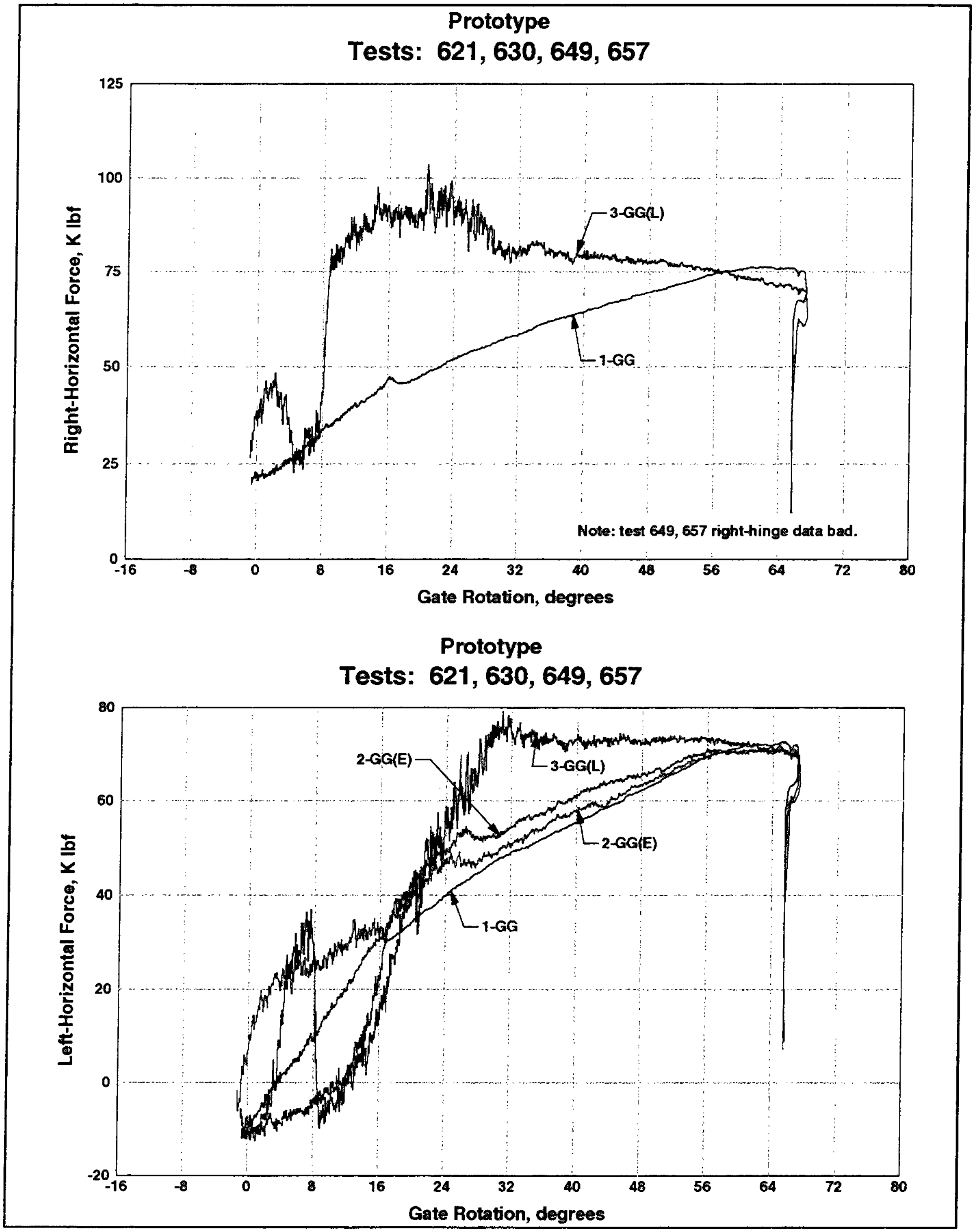

Figure 25. Prototype horizontal reactions for different flow conditions

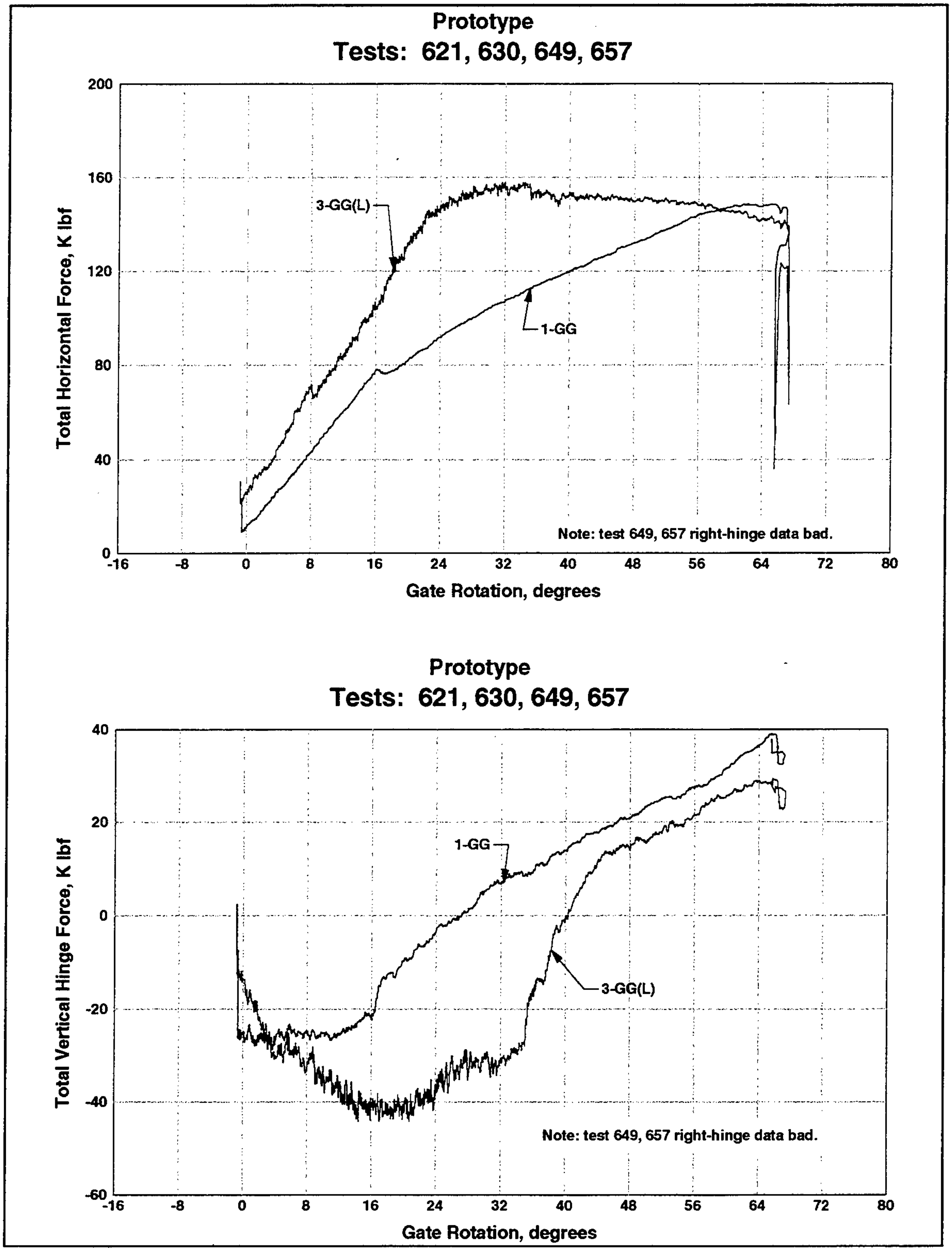

Figure 26. Prototype total hinge reactions for different flow conditions

downstream air bubble (vacuum) beneath the gate pops up. The same phenomenon was observed during the 1:5-scale tests which showed that a three-gate gap (lone condition) is the critical configuration regardless of head difference in the pool condition. This critical position for the 3GG(L) case was at about 16 to 24 deg.

Recalibration of the prototype gate hinge force transducers was necessary to account for incorrect strain gauge positioning during fabrication of the hinge pins by the Teledyne Brown Engineering. Initially, the hinge-force transducers were calibrated based on correct sensor and hinge pin groove alignment, which would have permitted a double-shear measurement effect. Since one groove on each pin was offset from correct alignment, a new set of calibration tables was developed to account for this incorrect alignment. The hinge-force plots in Appendix C reflect these recalibration data. Recalibration of hinge force data was performed by adjusting the measured force, F_m, by the new y-intercept, α_n, and slope, β_n, values for each of the four transducers to obtain the actual force, F_a. The calibration equation for the sensor output can be obtained using the equation: $F_m = \alpha_o + \beta_o V$, in which V is the sensor analog output in mV/V. Sensor output based on the original calibration factor then becomes:

$$\frac{F_m - \alpha_o}{\beta_o} = V \tag{13}$$

Therefore, the actual force based on the correct recalibration factor is:

$$\left(\frac{F_m - \alpha_o}{\beta_o}\right)\beta_n + \alpha_n = \alpha_n + \beta_n V \tag{14}$$

Since $F_a = \alpha_n + \beta_n V$, we have:

$$F_a = \alpha_n + \frac{\beta_n}{\beta_o}\left(F_m - \alpha_o\right) \tag{15}$$

Subscripts 'o' and 'n' correspond to old and new y-intercept and slope values, respectively.

Values used to recalibrate the prototype steel gate hinge force data are shown in Table 9. The left vertical transducer was nonfunctional during recalibration, making it impossible to obtain new calibration factors. A drift effect during both prototype and model data acquisition caused a shift in magnitude recorded in the experiments. This offset in recorded data from actual values was a result of differences in sensor initialization between the prototype and model experimental environments. A wet-zero reference condition test required sensor initialization under static zero head difference pool conditions, which could not be attained in the nature-dependent prototype facility. Thus, the experimental data presented in this report were measured with reference to the dry initial condition of the sensors instead of the preferred wet-zero reference condition. As a result of this dry initialization, the recorded data depended upon the uncertain thermal and mechanical drifting of the analog transducers during the data acquisition.

Two experiments were conducted in the 1:5-scale model to determine the effects of these different initialization methods. Flow-induced experimental results recorded from dry and wet initialization schemes indicated that the reaction forces based on the dry zero reference test could vary up to 37 percent from that of the wet-based result. Therefore, the results presented in this report may fall short of the absolute value of the operating response, caused by a linear shift produced by drift in the analog transducers. Base hinge reactions presented in Appendix C were corrected for such thermal linear drift by shifting the model data upward to match the starting points of the responses under comparison.

Acceleration plots compared in Appendix B show such a linear drift between the prototype and model responses. Neglecting the drift in the acceleration record, both predicted and actual prototype maximum accelerometer responses were generally within 20 percent of each other. Model data for the right horizontal hinge force were shifted up by 45 kips to match the force trends to the prototype data and to ensure a conservative estimate of hinge force data were provided. Due to this drift effect, the magnitudes of the hinge force data may not reflect actual values for hinge forces, but the force trends accurately represent those of the operating conditions.

Table 9
Prototype Steel Gate Hinge-Force Recalibration Factors

	Old Intercept α_o	New Intercept α_n	Old Slope β_o	New Slope β_n
Right Vertical	-3.63	1.98	287	357
Right Horizontal	-3.27	1.88	295	359
Left Vertical	n/a	n/a	300	n/a
Left Horizontal	0.71	0.58	299	388

The right hinge prototype reactions agreed very well (within 12 percent of each other) with the corresponding model predicted responses, with slightly higher differences in the turbulent flow region. Significant deviations were noted in the left horizontal force plots in Appendix C (C4, C13, C22, C31, C38, C44, and C50). Although this large deviation is attributed to thermal, mechanical, and electrical inconsistencies during experimentation, analysis of these data indicated that an ordinate scaling factor of 0.485 brings the prototype data into very close alignment with the model data. During the time from initial placement of left vertical transducer to the time of experiment, the left vertical sensor was damaged and could not be recalibrated. The left pin had also been repaired prior to the experimental data acquisition by WES, which could affect the original calibration factor for the repaired pin. Reassembling of the left pin was needed to correct the water leakage through the protective coatings of the strain-gauge bridges. Because of such multitudes of problems in the left pin, the data presented here can only be used to indicate trends which compare favorably with the 1:5-scale physical response.

Pressure data showed an excellent correlation, except for the model U/S bottom-center pressure (channel 17), which was nonoperational during the postexperiment inspection. The prototype vertical and horizontal right hinge sensors and the U/S middle-center and bottom-center pressure transducers provided bad data on 21 Dec 95 and were discarded. Inaccurate pressure data for channel 17 were discarded and not compared in this report. In general, the upstream prototype pressure deviation from that of the model prediction was less than 15 percent. The general trend in the downstream pressure envelop was identical for both prototype and model. Except at the most turbulent region, in most cases the downstream pressure for the prototype did not deviate more than 10 percent from that of the model prediction. Close agreement between the respective predicted and actual prototype response suggests the strength of the similitude model in reproducing the flow-induced dynamic behavior of the Olmsted dam.

In Appendix D, Figures D1 through D62 show comparisons between the prototype composite and model gates. Two pressure sensors were placed on the composite gate: upstream (U/S) bottom left and downstream (D/S) bottom left. Additionally, nine accelerometers were placed on the gate, in locations shown in Figure 13. Composite accelerometer channel 35 (bottom right) did not record properly, and this comparison was discarded. The composite gate has a much greater vibratory response than the prototype steel gate under similar operating conditions.

In general, model and prototype data corresponded very well, except for those cases noted above. Note the correlation of data throughout the gate rotational range in Figure 27.

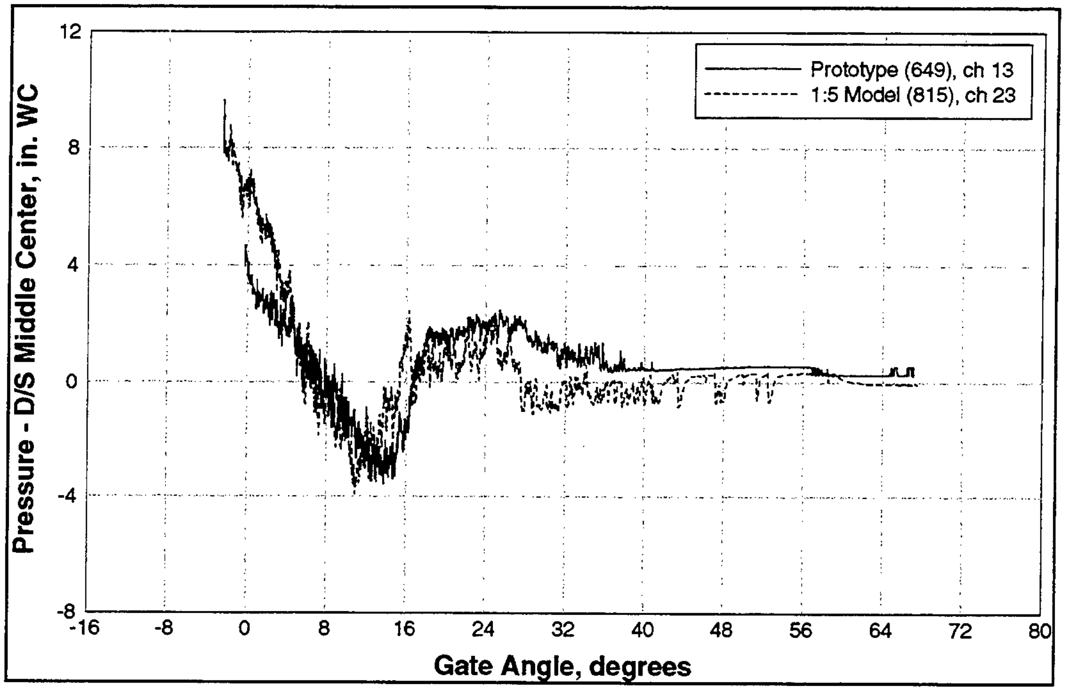

Figure 27. D/S middle center pressure for prototype 649 vs. model 815

Prop-Rod Force

The prop-rod force had to be calculated for the 1:5 model based on total trunnion force, since the 1:5 model prop-rod sensor was damaged during operation. Table 10 shows a comparison of prototype prop-rod force to total model trunnion force for selected configurations. In Appendix E, Figure E1 shows the hinge-force comparisons between the prop-supported prototype and model gates. Apparent difference in the hinge reactions resulted due to thermal drift in the respective sensors, as discussed above, for dry-zero reference initialization during the experiments. Due to incorrect alignment of prop-rod hinge pin sensors, the full load along the direction of the prop-rod was used for comparison. The calculated model prop-rod force agrees well with the prototype prop-rod force operating under the same conditions.

The weight of the prototype steel gate was not obtained prior to installation, thus its dry weight had to be determined from sensor data to be used in the calculation. Plots used to determine the required model trunnion force values for the above calculations are shown in Appendix F, Figures F1 through F3. The top plot shows the angular position of the gate as a function of time, permitting determination of the prop-rod force at the required gate angle.

Table 10 Prototype Prop-Rod Force vs. Total Model Trunnion Force @ 65°		
Gate Condition	Experiment #	Force [K lbf]
1-GG	804 (Model)	149.8
	621 (Prototype)	147.2
3-GG	808 (Model)	122.8
	630 (Prototype)	127.1
Dry Test	803 (Model)	12
	601 (Prototype)	14

Stress/Strain

In Appendix G, Figure G1 shows the strain-gauge orientation, while Figures G2 through G31 show principal stresses, strains, and planes plots for the prototype steel gate in all operating configurations. These plots show σ_1, σ_2, ε_1, ε_2, and the principal planes through which these act versus prototype gate angle. These were determined from:

$$\sigma_1, \sigma_2 = \frac{E}{2}\left[\frac{\varepsilon_a + \varepsilon_c}{1-\nu} \pm \frac{1}{1+\nu}\sqrt{2(\varepsilon_a - \varepsilon_b)^2 + 2(\varepsilon_b - \varepsilon_c)^2}\right] \quad (16)$$

$$\varepsilon_1, \varepsilon_2 = \frac{1}{2}\left[\varepsilon_a + \varepsilon_c \pm \sqrt{2(\varepsilon_a - \varepsilon_b)^2 + 2(\varepsilon_b - \varepsilon_c)^2}\right] \quad (17)$$

$$\tan 2\theta = \frac{2\varepsilon_b - \varepsilon_a - \varepsilon_c}{\varepsilon_a - \varepsilon_c} \quad (18)$$

when, $\boldsymbol{\varepsilon_b \succ \frac{\varepsilon_a + \varepsilon_c}{2}}$ ***and*** $\mathbf{0 \prec \theta \prec +90^0}$ (Beckwith and Marangoni 1990)

The strain-gauge rosettes were located at the highest possible stress level in the gate as determined by finite element analyses of the Olmsted wicket. Maximum stress was approximately 7 ksi for Prototype Experiment # 630, 3-GG(L). Data obtained from axial strain transducers mounted on the 1:5-scale gate were used for comparison to confirm the validity of prototype stress and strain data.

Flow-induced strain data were obtained from the 1:5-scale wicket gate from four axial transducers mounted longitudinally 16 in. from the base of the gate. Two transducers were mounted on the top skin plate on the upstream side, and two were mounted on the bottom flanges on the downstream side. The axial strain for the 21-ft head difference, 3-gate gap configuration is shown in Figure 28. As indicated in the figure, the bottom transducers showed a reversal in strain level due to raising the gate, while the top locations showed a decrease in strain as the gate was lifted from the down to up position. This figure also shows the click marks which relate the time and the gate position during the experimentation. Maximum strain for the two U/S transducers is 60 to 70 μ. Multiplying by 3 by 10^7 psi (modulus of elasticity) and by 5 (stress scaling factor), a maximum longitudinal stress of 9 to 11.25 ksi is obtained.

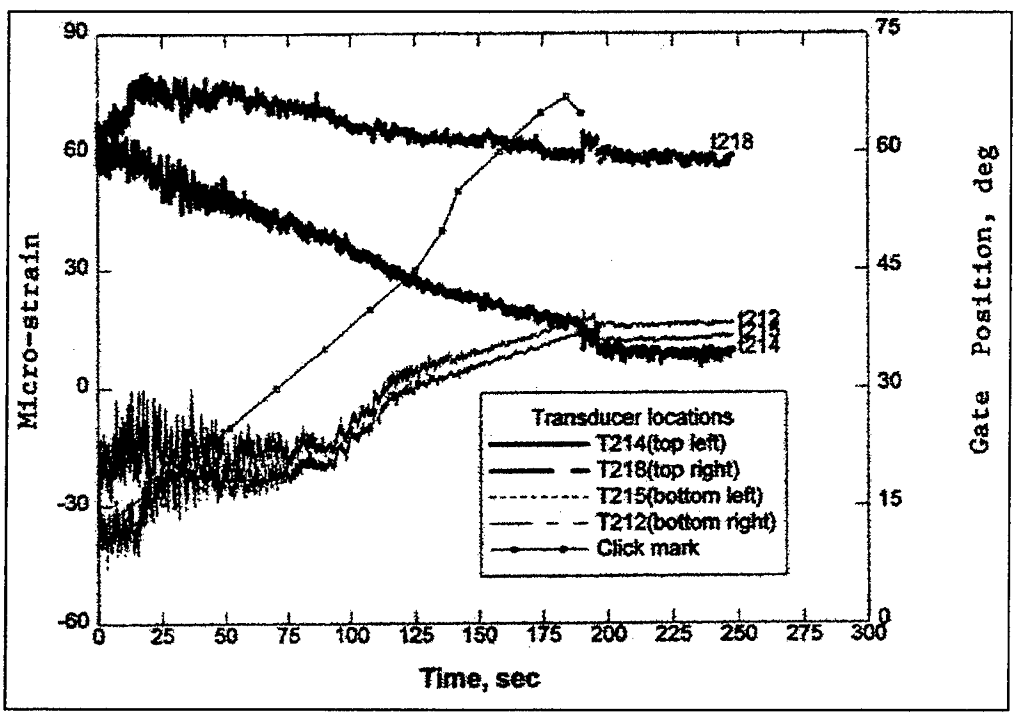

Figure 28. Flow-induced strain response for 1:5 wicket, 3-gate gap configuration (+ tension, - compression)

This is in range with prototype data for maximum stress for the same gate configuration. The D/S water level was lower for the model than for the prototype, and this added U/S water pressure on the model would increase the stress and strain measured by the transducers. Additionally, strain-gauge rosettes were used on the prototype, while axial strain gauges were used on the model, causing both systems to provide data in slightly different formats. The axial transducers used in the model may not have been precisely oriented along the plane of principal strain, while the strain-gauge rosettes on the prototype permitted accurate determination of principal planes. Despite these differences, the primary reason for this comparison was to ensure the prototype data were within an acceptable range, which was validated.

Analytical and experimental results of the Olmsted wicket indicate that the proposed flow and operating conditions do not pose any vibrational threat due to the flow-induced motion of the wicket (Chowdhury, Hall, and Davis in preparation and Chowdhury Garner, Seda, and Hall 1997). For the proposed reasonably low cycle of gate operation and a low anticipated strain level (an absolute maximum stress level of 11,250 psi is estimated from the model for the most critical flow configuration), such an applied stress does not pose a fatigue threat for the structural components unless environmental effects have harshly deteriorated the mechanical performance of the gate material. Moreover, the maximum strain level occurs only during the transitional phase of operation and lasts for a short duration. The strain level for the prop-supported gate, most active position during the course of operation, is significantly low compared to the maximum stress at the critical configuration.

4 Conclusion

Comparison of experimental results for the prototype and 1:5-scale physical model validates the effectiveness of the scaled similitude model in predicting the structural and hydraulic responses of the Olmsted wicket. A close agreement between the respective predicted and actual prototype response suggests the strength of the similitude model in reproducing the flow-induced dynamic behavior of the Olmsted dam. Results obtained from the comparison affirm:

a. A very good correlation (MAC values over 70 percent for the respective first six modes) between the corresponding mode shapes for the prototype steel and 1:5 model gates validates the structural similarity of the prototype and scaled model. Mode shapes 4 and 5 for the composite gate appeared to be transposed, which was attributed to differences in its internal support structure.

b. The prototype steel gate provided a higher relative stiffness for both bending and torsional modes than the composite gate. If the composite gate weight were increased above 17.5 or 18.5 K lb, the composite gate would exhibit greater torsional stiffness than the steel gate in one or two modes, respectively.

c. A time-scale factor was computed to adjust the kinematic dissimilarity of the prototype wicket. By adjusting the time scale in the flow-induced response spectra, the resonant peaks in the acceleration power spectra between the prototype and scaled model correlated well with each other, although peak alignment on some plots was difficult to observe. Low-frequency resonant peaks, below 15 Hz, associated with the forced motion of the wicket in the prototype did not appear in the model. A difference in the frequency distribution resulted due to the modeling distortion of the Froude model in not meeting the criteria of the elastic-mass similitude relationship. Despite the difference in the frequency spectra in the lower frequency range, the dominating modes contributing the most to the vibration of the prototype wicket were well reproduced in the model. As a result of the similarity of the first few elastic operating shapes, the model predicted dynamic response differed less than 20 percent from that of the prototype response.

d. Comparison of U/S and D/S power spectra agreed well for the prototype and the model. Time-domain pressure data showed an excellent correlation, except for the model U/S bottom center pressure (channel 17), which was found nonoperational during the postexperiment inspection. In general, the U/S prototype pressure deviation from that of the model prediction was less than 15 percent. The general trend in the D/S pressure envelop was identical for both prototype and model. Except at the most turbulent region, the D/S pressure for the prototype did not deviate more than 10 percent than that of the model prediction for all cases except one.

e. Time-domain right hinge prototype and model reactions had less than 12 percent difference for most cases. Inconsistencies were noted in left hinge-force data which resulted from improper calibration of the left shear pins. The left vertical transducer was nonfunctional during recalibration, thus making it impossible to obtain new calibration factors for correction.

f. The composite gate has a much greater vibratory response than the prototype steel gate under similar operating conditions, as evinced in comparisons of time-domain plots of acceleration for each gate.

g. Analysis of the damping phenomenon noted in pressure and acceleration data demonstrated an expected increase in damping from dry to wet operating conditions.

h. Calculated model prop rod force had less than 5 percent difference from that of the prototype response operating under the same flow conditions.

i. Maximum stress was approximately 7 ksi for prototype critical flow configuration. Prototype stress was obtained from strain-gauge rosettes mounted on the prototype wicket. Using a different type of removable externally mounted axial transducer, the model predicted a maximum stress of 10.5 ksi for the identical critical flow-configuration. This difference is attributed to the variance in orientation of transducers, very low sensor output, and a slightly different D/S pool elevation during the prototype and model experiments. Despite the difference, this comparison ensures that the prototype stress was within an acceptable range of the predicted value.

References

Beckwith, T. G., and Marangoni, R. D. (1990). *Mechanical measurements.* 4th ed., Addison-Wesley Publishing Company, Reading, MA.

Chang, T. P. (1993). "Dynamic finite element analysis of a beam on random foundation," *Computers & Structures* 48(4), 583-589.

Chowdhury, M. R., Hall, R. L., and Pesantes, E. (1997). "Flow-induced vibrational test results for a 1:25 flat wicket gate," Technical Report SL-97-04, U.S. Army Engineer Waterways Experiment Station, Vicksburg, MS.

Chowdhury, M. R., Hall, R. L., Davis, G. W. "Flow-induced structural response of a 1:5-scale Olmsted Wicket Model," (technical report in preparation), U.S. Army Engineer Waterways Experiment Station, Vicksburg, MS.

Chowdhury, M. R., Hall, R. L., Hoffman, P., McClellan, B., Mundolch, J. (1997). "Composite wicket gate development at the Olmsted prototype dam," The Composite Institute of the Society of the Plastics Industry, International Composite Expo, Nashville, TN.

Chowdhury, M. R., Garner S., Seda-Sanabria, Y., and Hall, R. L. (1997). "A finite-element model for the Olmsted Wicket," Technical Report SL-97-06, U.S. Army Engineer Waterways Experiment Station, Vicksburg, MS.

Consolidated Electrodynamics. (1995a). "Bulletin 4312/667: CEC/transducer products," Monrovia, CA.

__________. (1995b). "Bulletin 4202B/766: CEC/transducer products," Monrovia, CA.

Ewins, D. J. (1984). *Modal testing: Theory and practice.* Research Studies Press Ltd., Letchworth, England.

Hutton, D. V. (1981). *Applied mechanical vibrations.* McGraw-Hill, New York.

Lindeburg, M. R. (1992). *Engineer-in-training reference manual.* 8th ed., Professional Publications, Inc., San Carlos, CA.

March, T. A., and Elder, R. A. (1992). "Review of the 1:25-scale hydraulic model Olmsted Wicket Dam," U.S. Army Engineer Division, Ohio River, Contract # DACW55-92-0187, Cincinnati, OH.

Structural Dynamic Research Corporation. (1993). "I-DEAS master series 2.0," Milford, OH.

Teledyne Engineering Services (1993). "Olmsted prototype instrumentation and measurement plan," Technical Report -21323-1, U.S. Army Engineer District, Louisville, Louisville, KY.

White, F. M. (1986). *Fluid mechanics.* 2nd ed., McGraw-Hill, New York.

Zonic Corporation. (1991). *Workstation 7000 users manual*, Milford, OH.

Appendix A Natural Vibration Decay Plots

Free-vibrational responses of the 1:5-scale model and prototype gates for dry and wet conditions are plotted in this appendix. Top right corner of each plot shows the experimental conditions. Three accelerometer responses for each test condition were used to compute the damping factors, zeta. As an example, Figures A1 to A3 show the transient response for the dry 1:5-scale model.

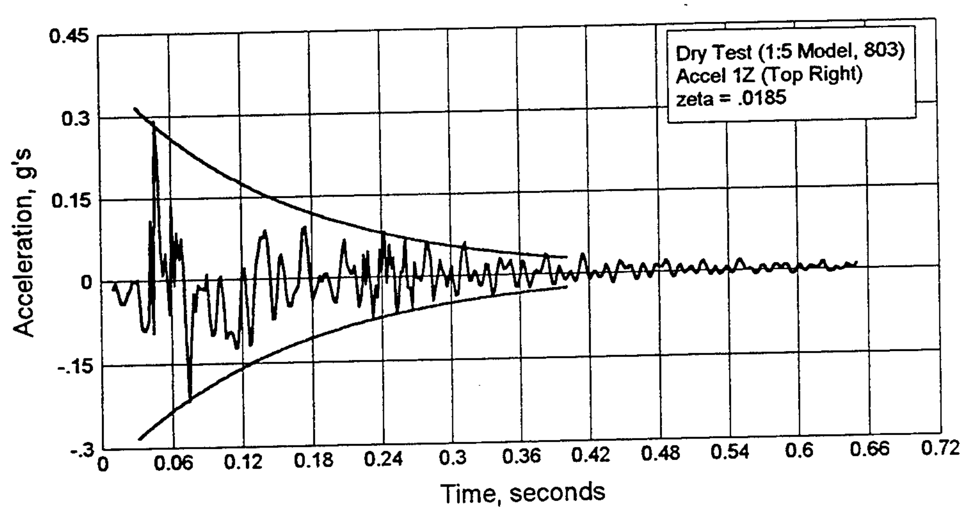

Figure A1. Accerleration 1Z curve fit for dry model (Experiment 803)

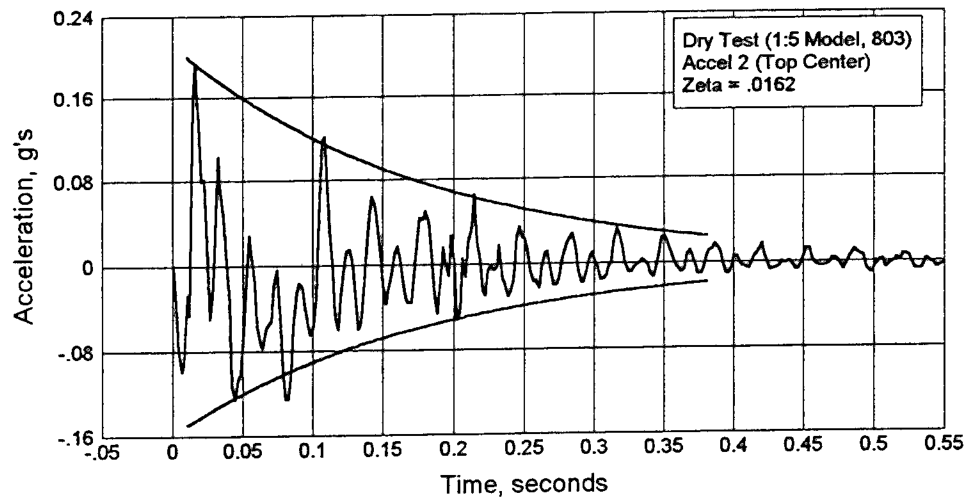

Figure A2. Acceleration 2 curve fit for dry model (Experiment 803)

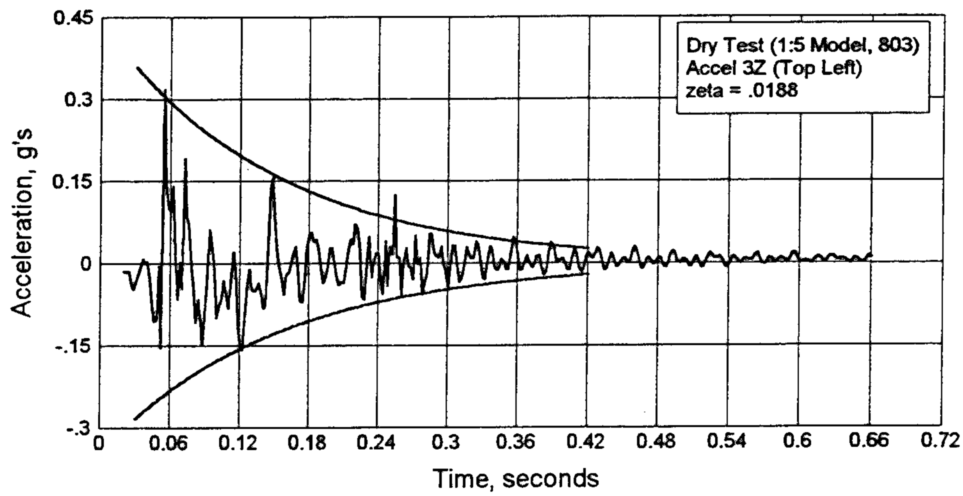

Figure A3. Acceleration 3Z curve fit for dry model (Experiment 803)

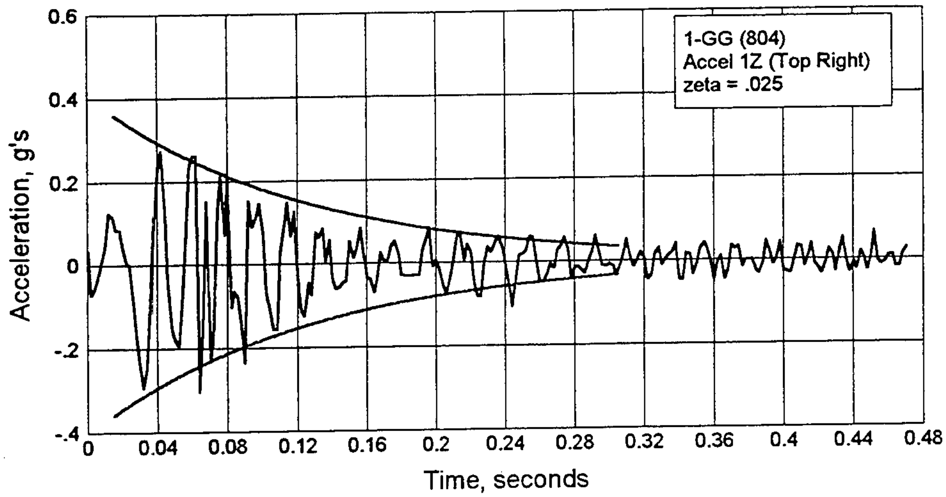

Figure A4. Acceleration 1Z curve fit for 1-GG up condition (Model 804)

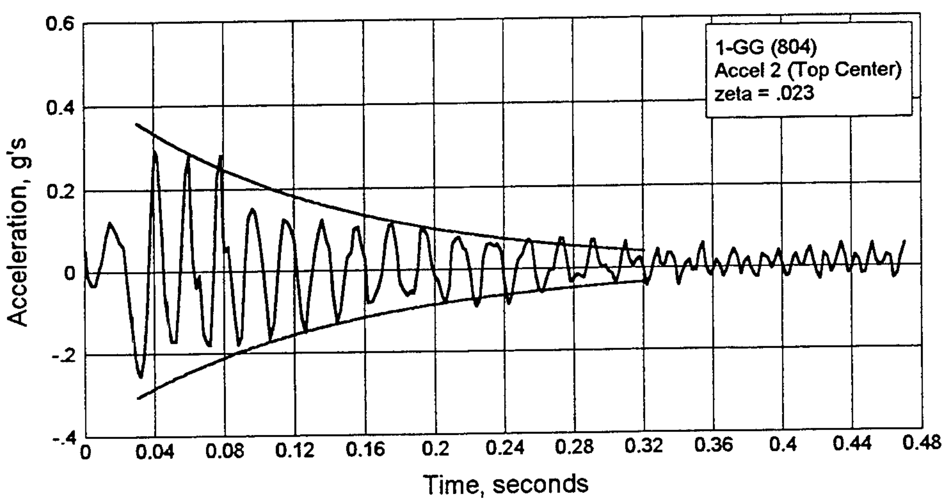

Figure A5. Acceleration 2 curve fit for 1-GG up condition (Model 804)

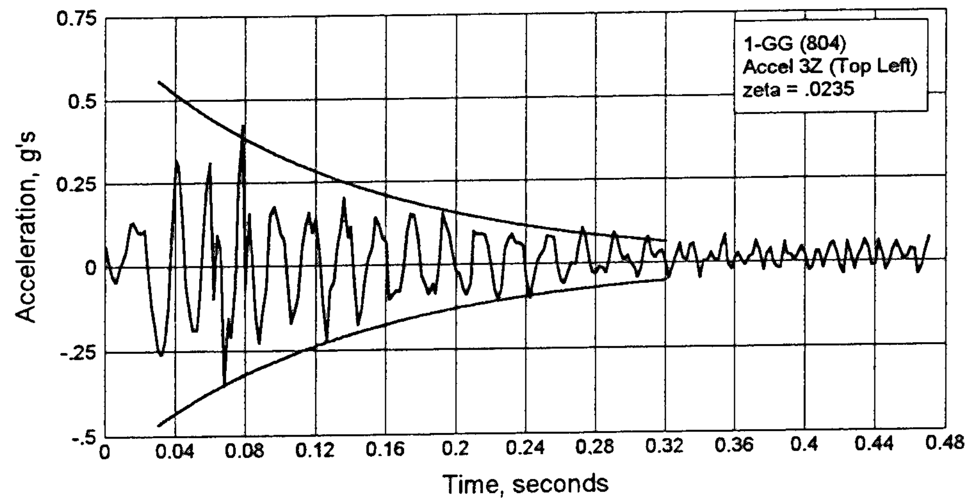

Figure A6. Acceleration 3Z curve fit for 1-GG up condition (Model 804)

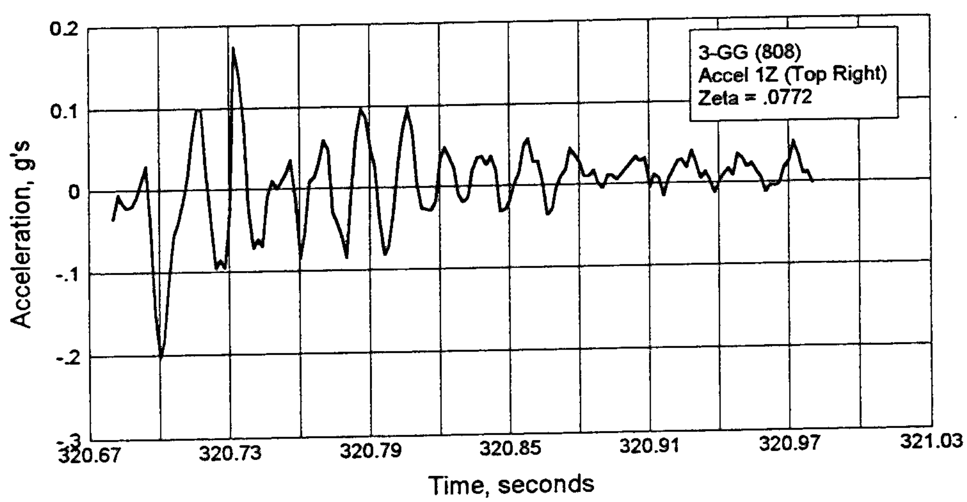

Figure A7. Acceleration 1Z curve fit for 3-GG up condition (Model 808)

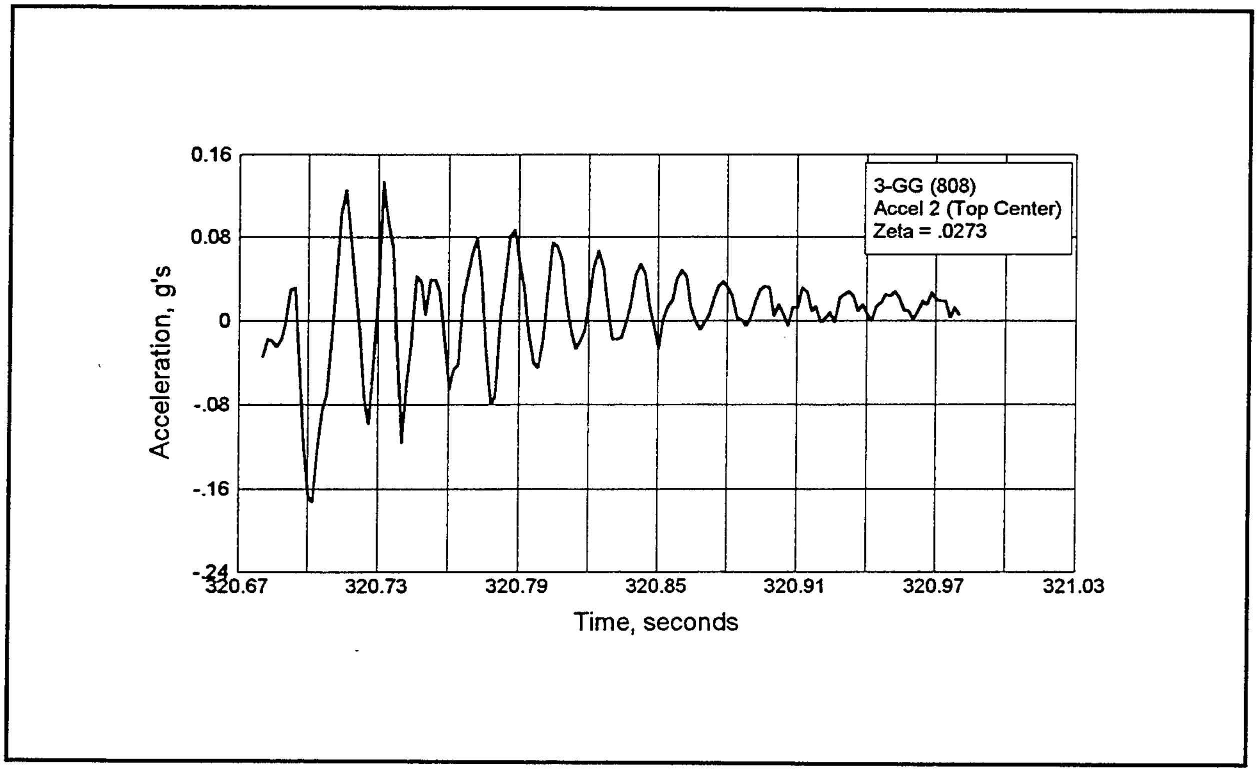

Figure A8. Acceleration 2 curve fit for 3-GG up condition (Model 808)

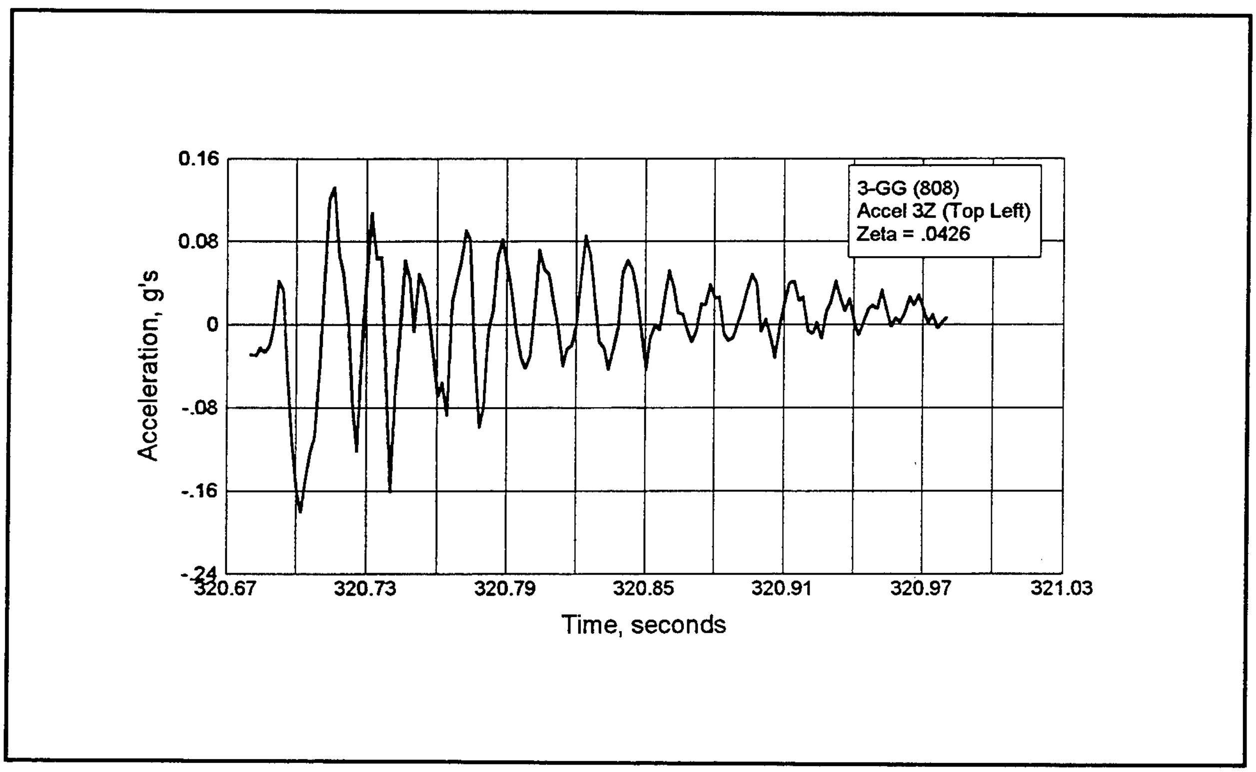

Figure A9. Acceleration 3Z curve fit for 3-GG up condition (Model 808)

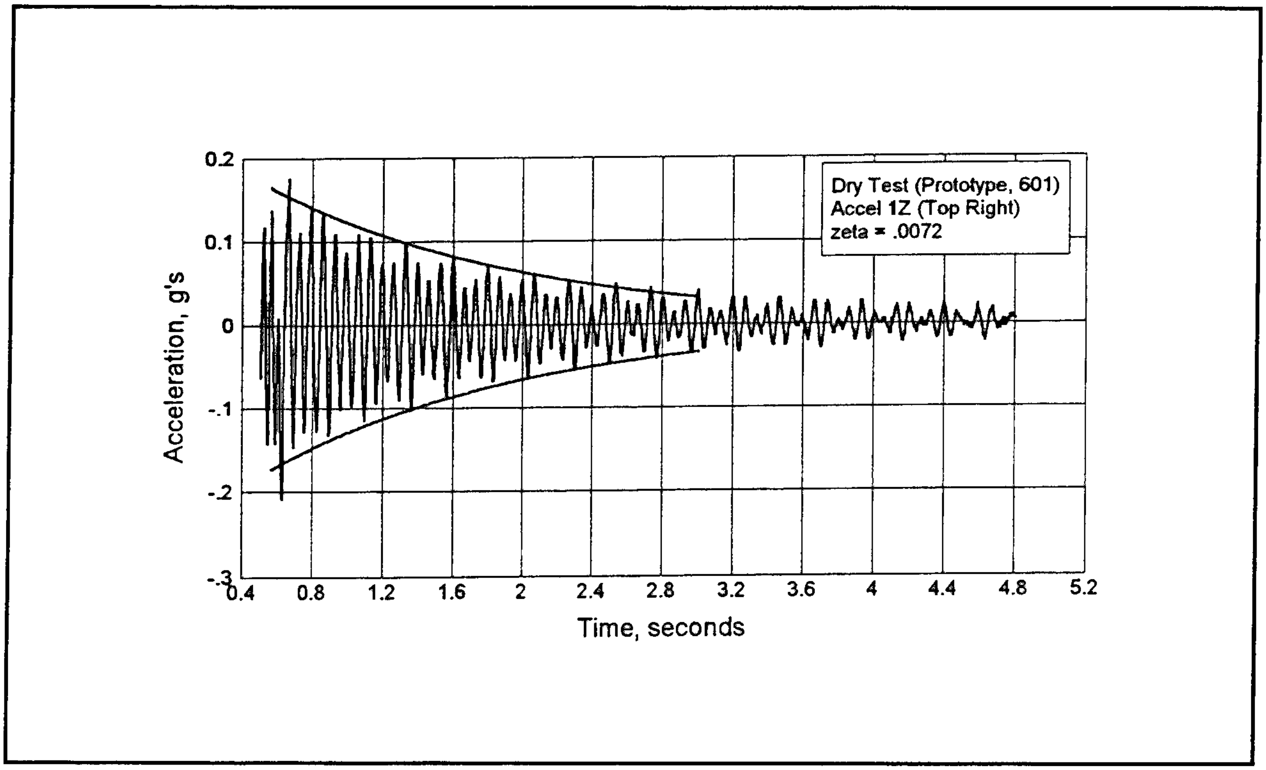

Figure A10. Acceleration 1Z curve fit for dry gate (Prototype 601)

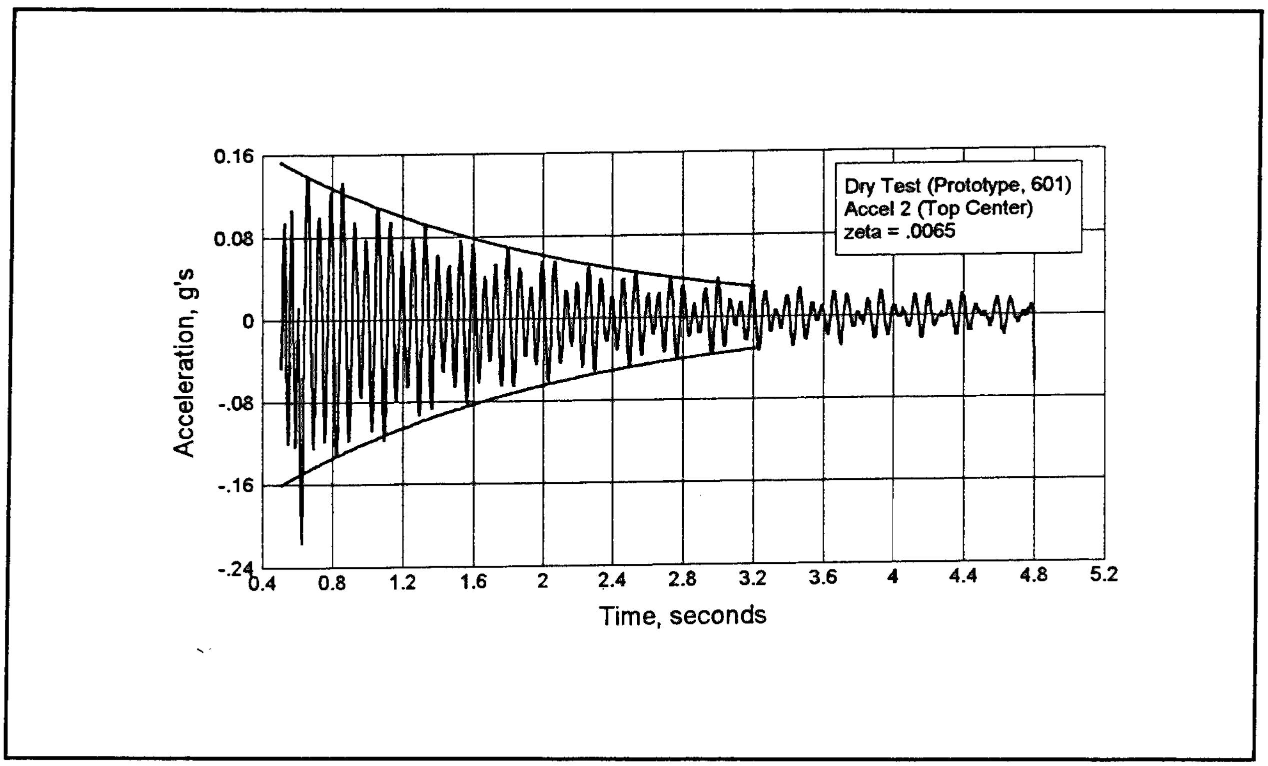

Figure A11. Acceleration 2 curve fit for dry gate (Prototype 601)

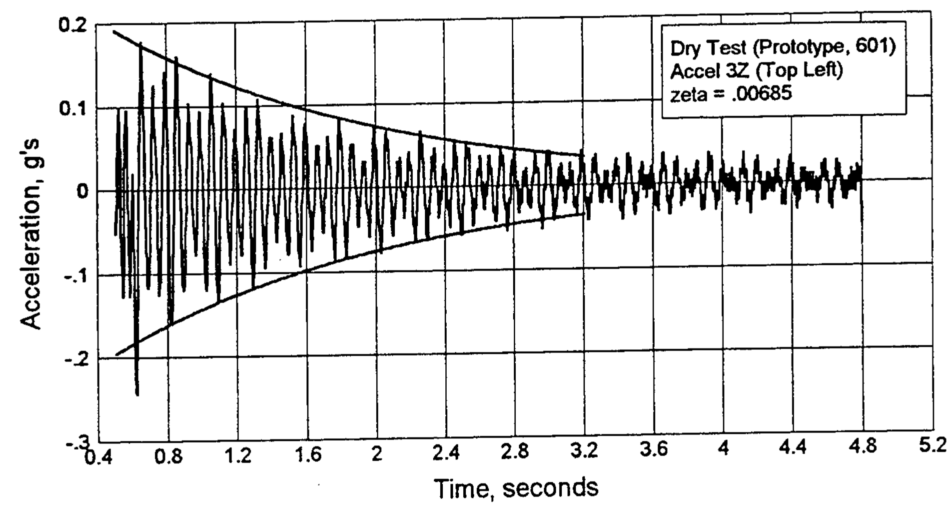

Figure A12. Acceleration 3Z curve fit for dry gate (Prototype 601)

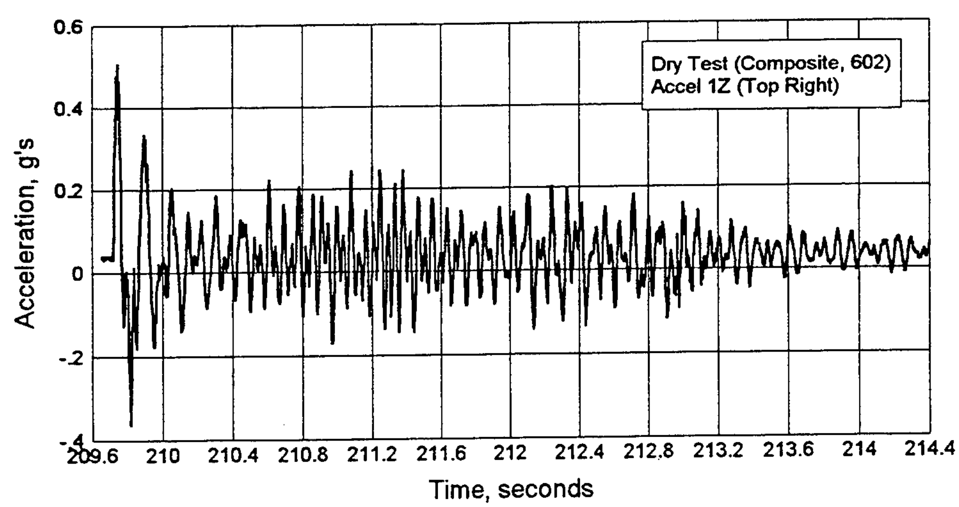

Figure A13. Acceleration 1Z curve fit for dry composite gate (Prototype 602)

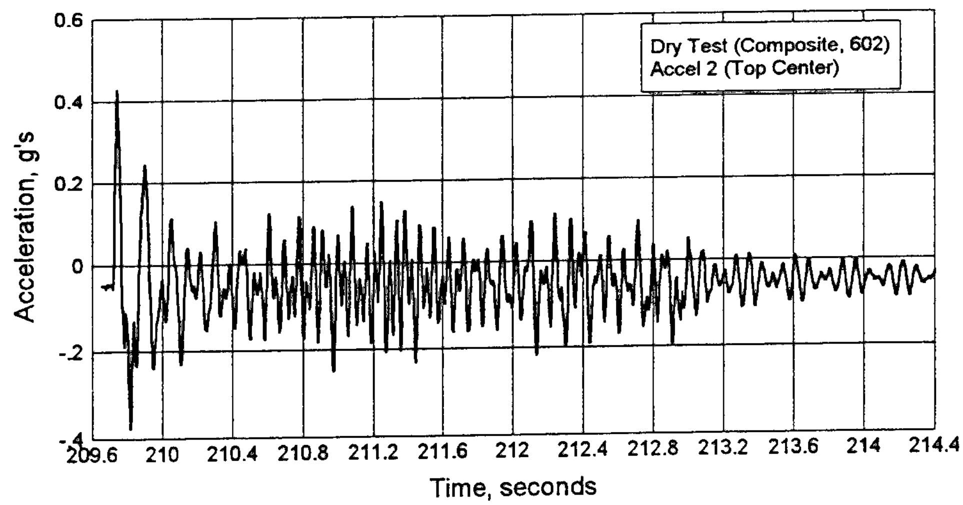

Figure A14. Acceleration 2 curve fit for dry composite gate (Prototype 602)

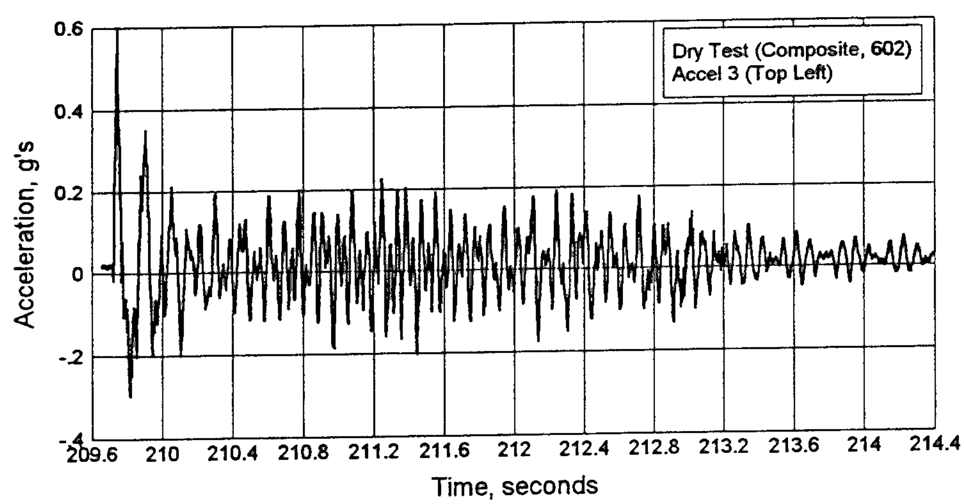

Figure A15. Acceleration 3 curve fit for dry composite gate (Prototype 602)

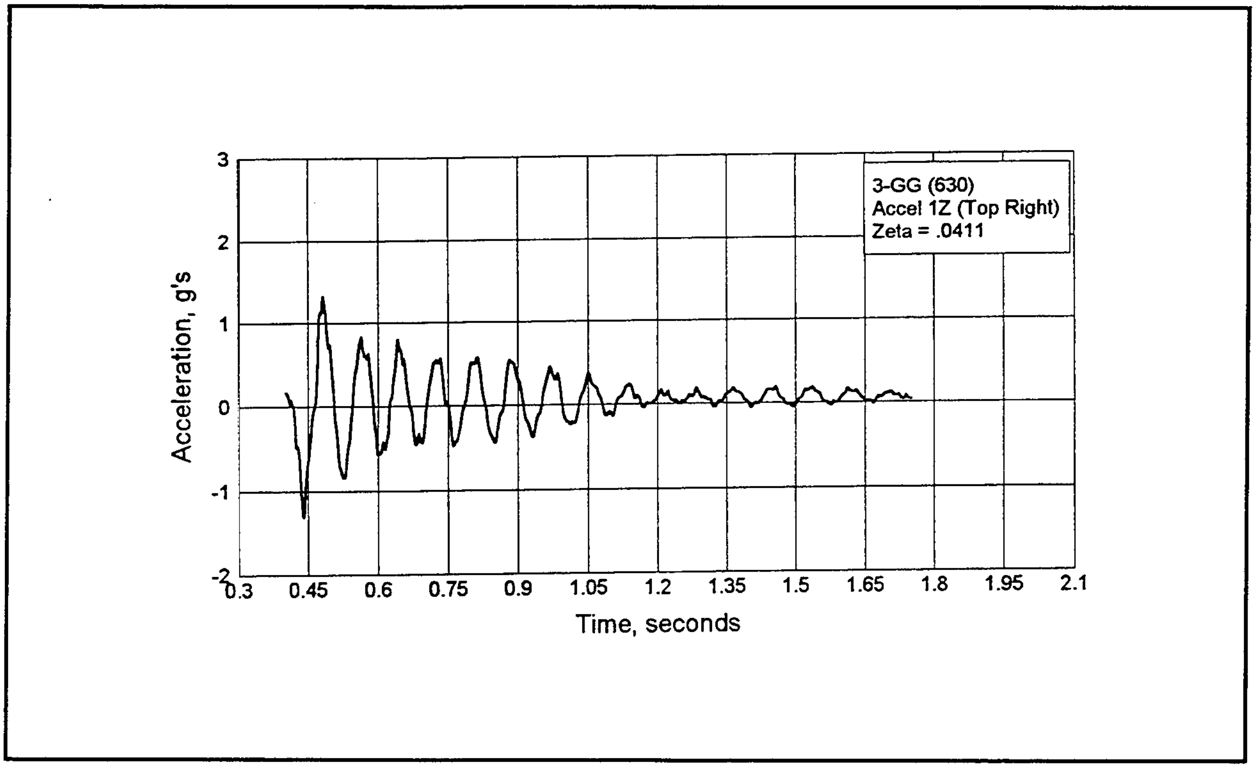

Figure A16. Acceleration 1Z curve fit for 3-GG up condition (Prototype 630)

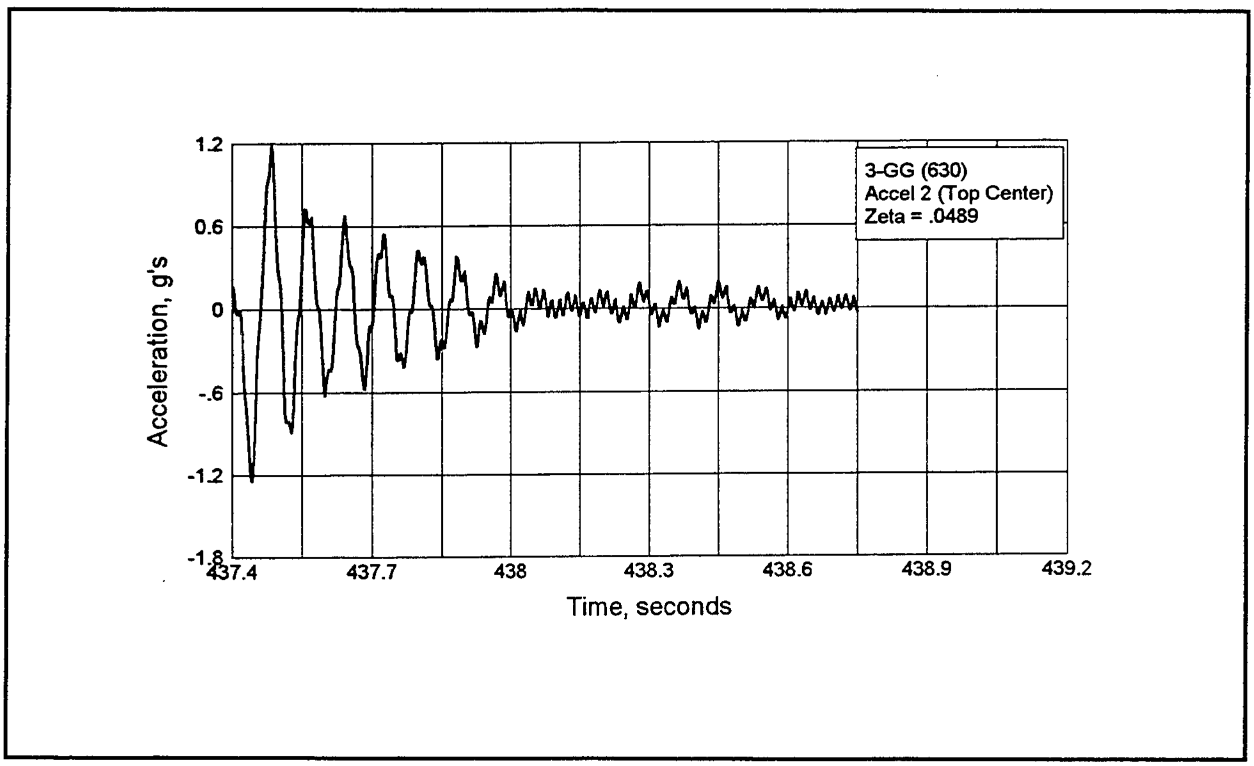

Figure A17. Acceleration 2 curve fit for 3-GG up condition (Prototype 630)

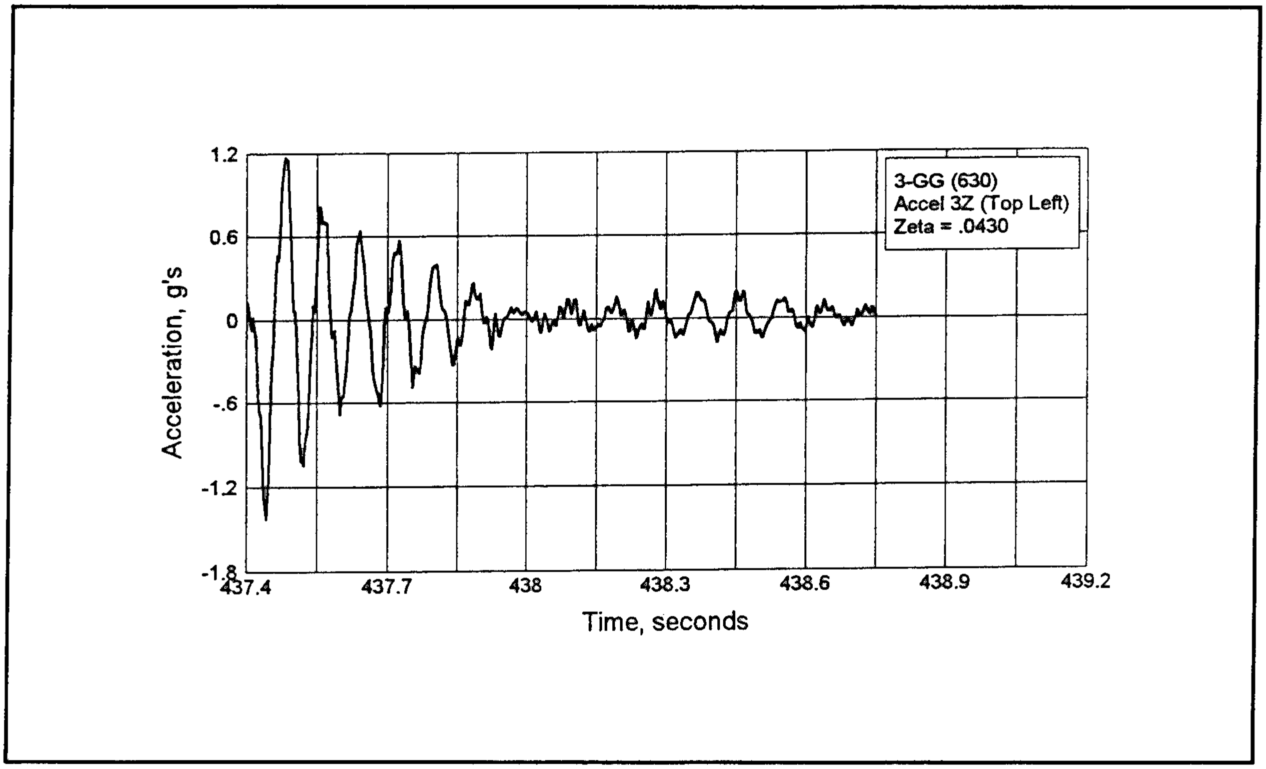

Figure A18. Acceleration 3Z curve fit for 3-GG up condition (Prototype 630)

Appendix B
Time- and Frequency-Domain Comparisons of Pressure and Acceleration Data

Selected flow-induced pressure and accelerometer responses for prototype (solid line) and 1:5-scale model (dashed line) wickets are compared in this appendix (Figures B1 through B80). In these plots, model responses were converted to the prototype scale. Each page contains a time-and frequency-domain comparison of respective response for one of the three flow configurations used in this study. Flow-configurations include a one-gate gap (Test No. 804 vs 621), a two-gate gap (Test No. 808 vs 630), and a three-gate gap (Test No. 815 vs 649).

Time-domain data show the variation of gate response as the wicket is raised from the down to the up position. A linear drift in the compared responses (see the acceleration plots) is the result of the mechanical and thermal drifting of the analog transducers during the data acquisition (see text for further explanation of the drifting problem). A difference in the data initializations also explains the reason for having this drift in the compared responses. Note that the prototype acceleration data compared in these figures were corrected to eliminate the static acceleration of the strain-gauge accelerometers as mentioned in the text. Prototype acceleration, even after correction, shows a static offset from the zero position. Thus, in the acceleration plots presented here, any shifted acceleration from the origin, if any, represent prototype response. Note that the acceleration reported here is the gate response normal to its surface. Figures B81 to B84 show comparison plots before the static acceleration was subtracted from the prototype raw data. A deviation in the measured prototype acceleration resulted due to the static motion of the wicket recorded by the prototype strain-gauge accelerometers.

Peaks in the accelerometer PSDs correspond to the governing frequencies of the operating wicket. These are the major frequencies at which the gate is forced to vibrate during the flow conditions used for the experiment. An operating shape corresponding to each peaks may define the operating deflected shape of the wicket.

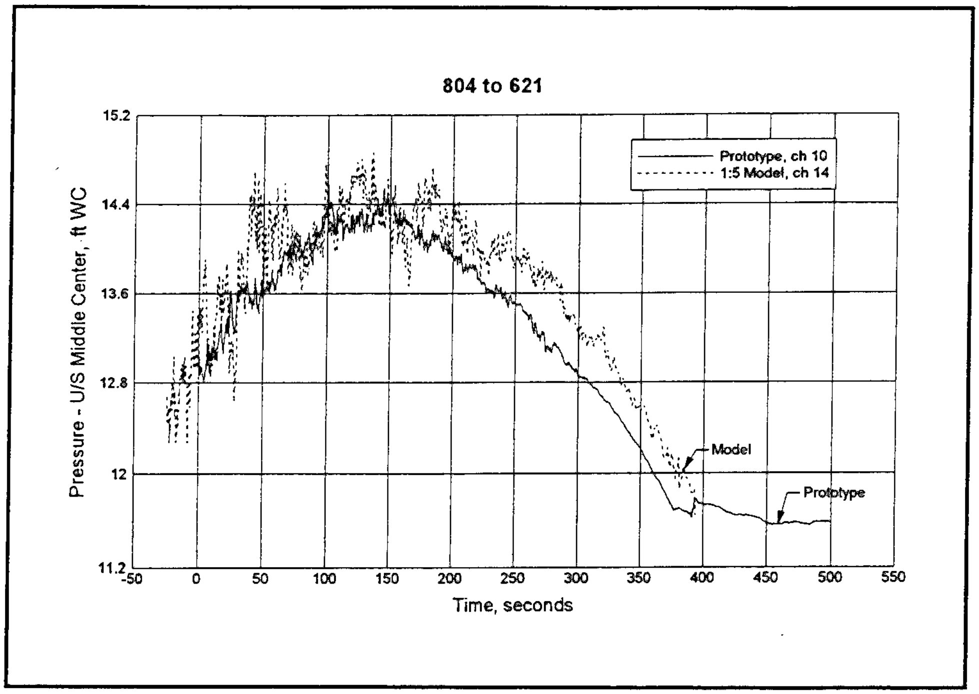

Figure B1. Upstream middle center pressure versus time for 1-GG up condition

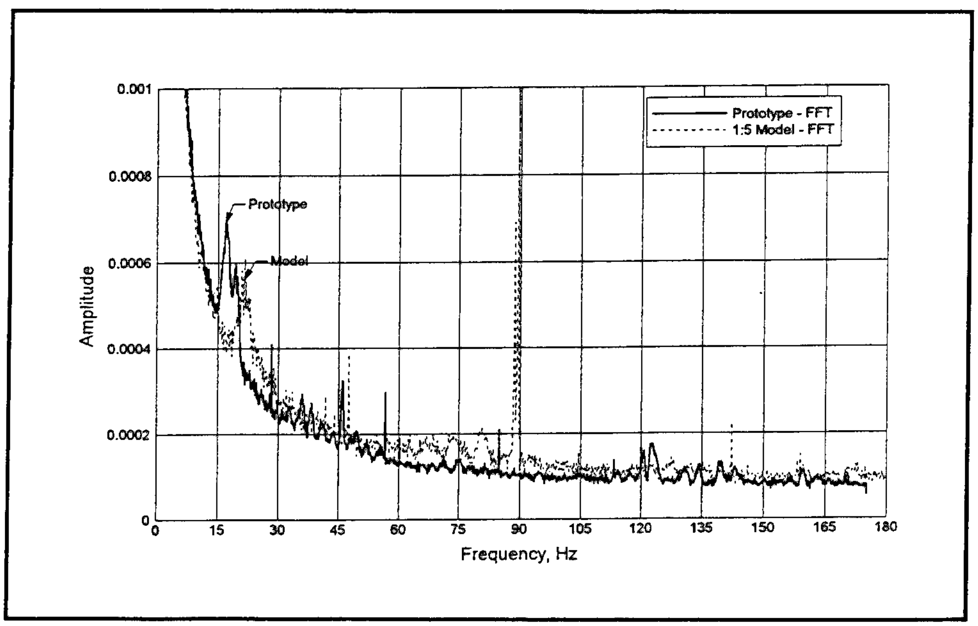

Figure B2. Upstream middle center pressure FFT for 1-GG up condition

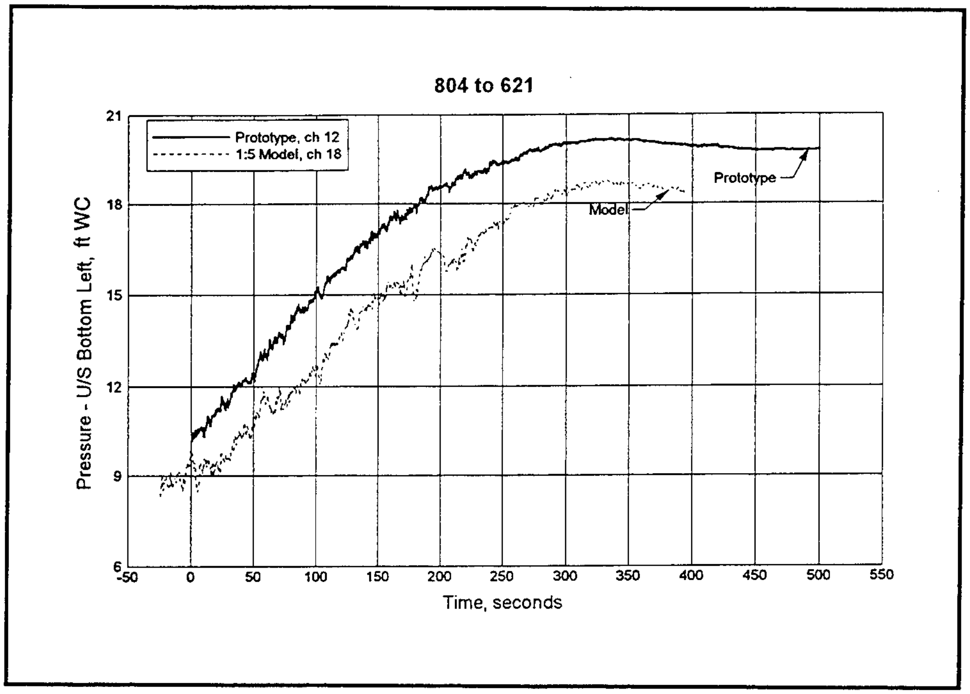

Figure B3. Upstream bottom left pressure versus time for 1-GG up condition

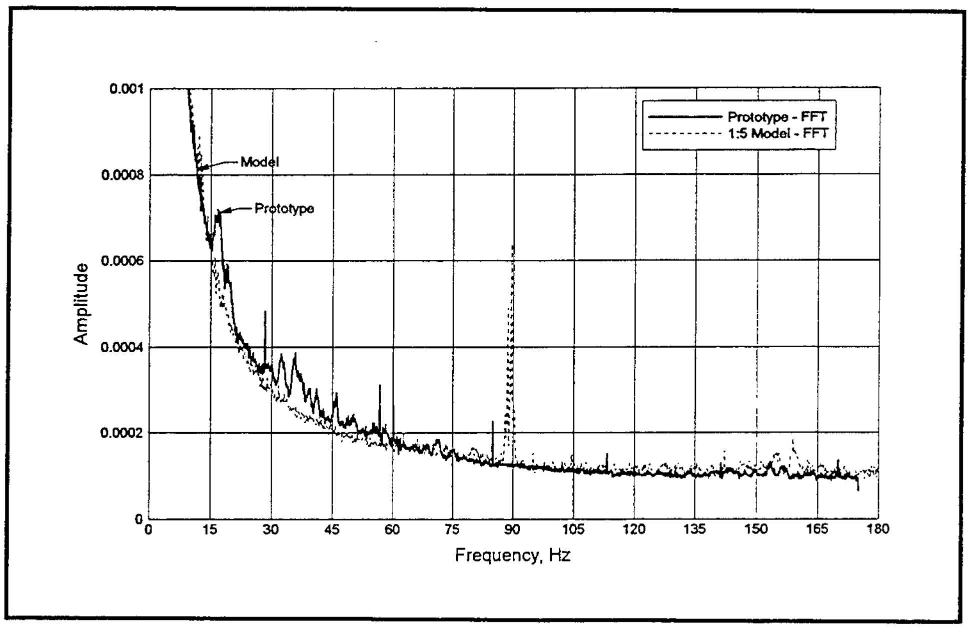

Figure B4. Upstream bottom left pressure FFT for 1-GG up condition

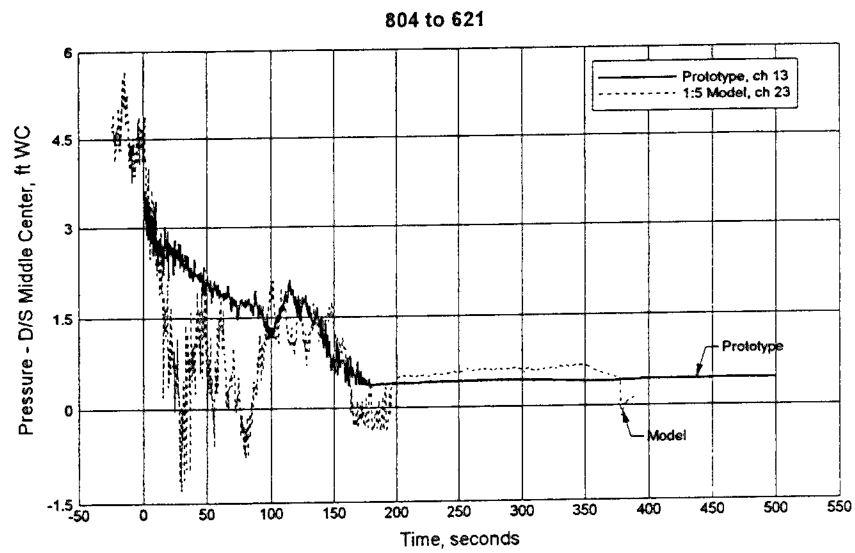

Figure B5. Downstream middle center pressure versus time for 1-GG up condition

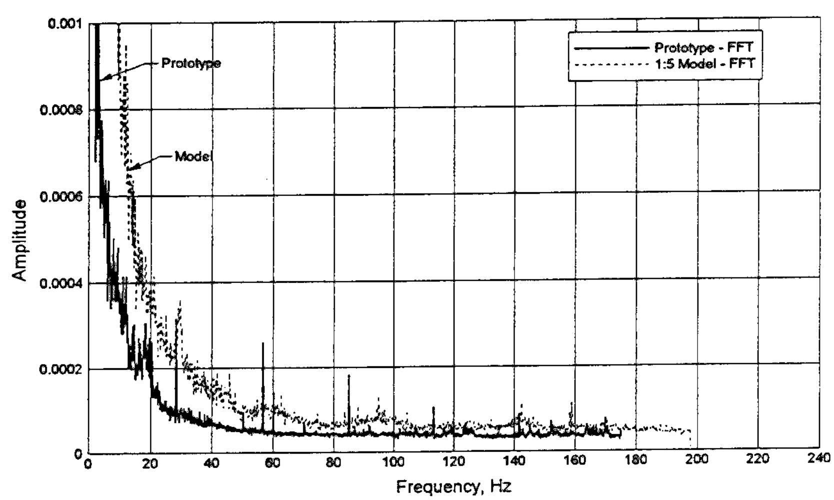

Figure B6. Downstream middle center pressure FFT for 1-GG up condition

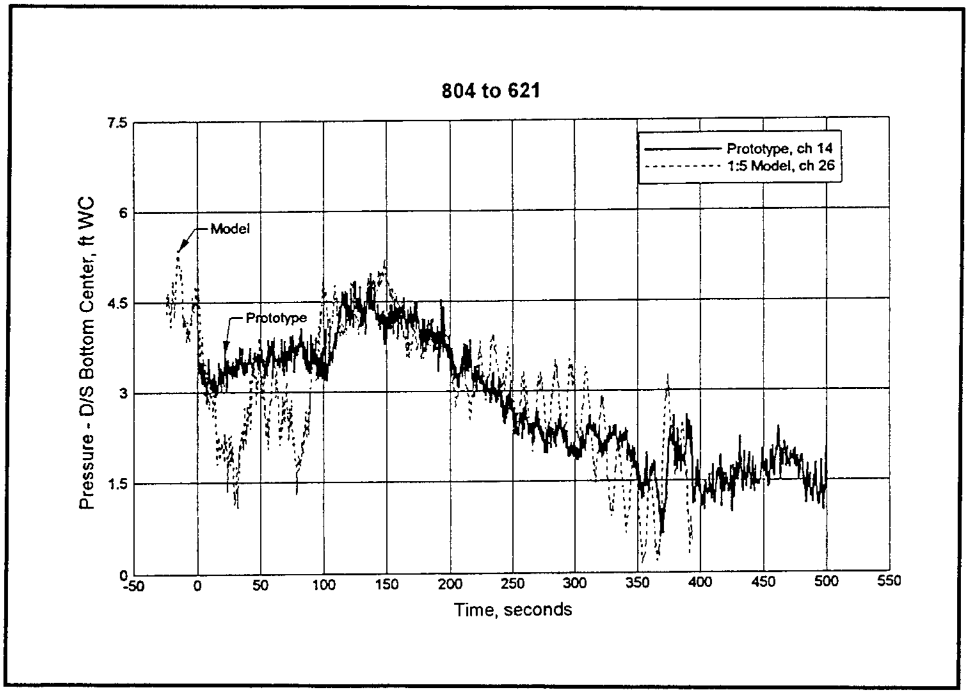

Figure B7. Downstream bottom center pressure versus time for 1-GG up condition

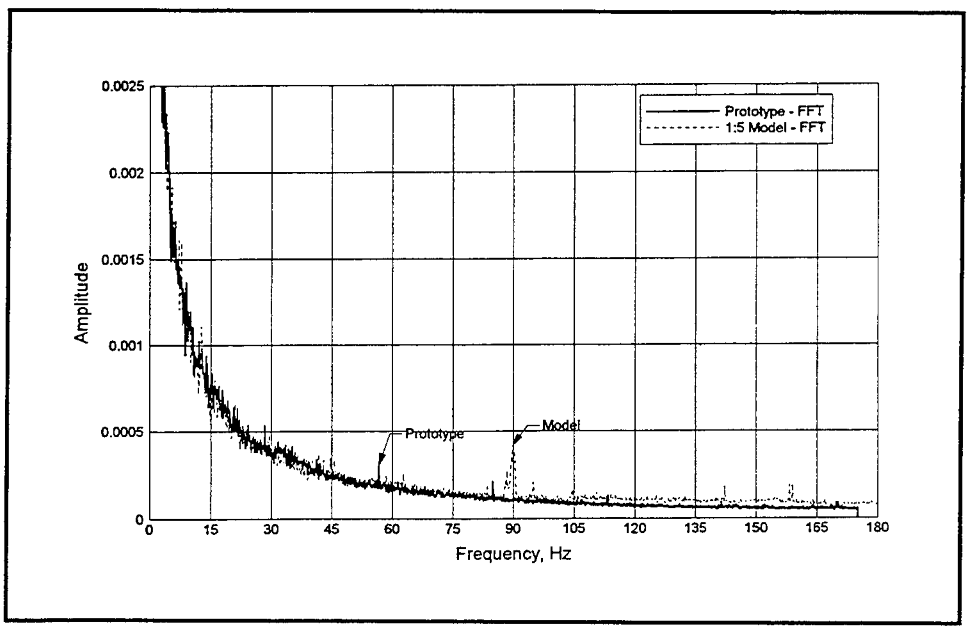

Figure B8. Downstream bottom center pressure FFT for 1-GG up condition

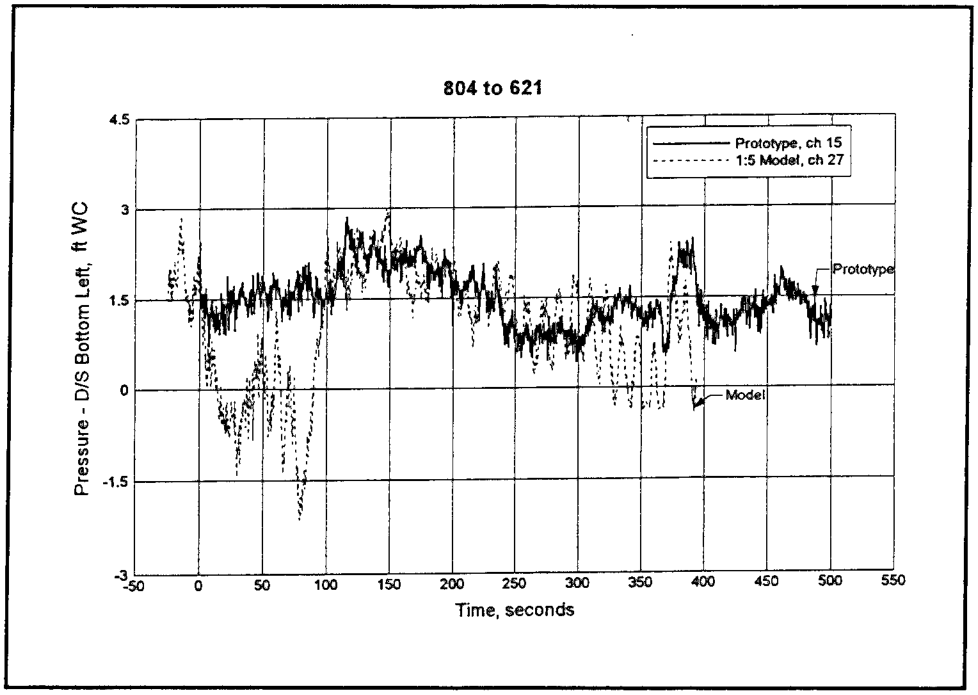

Figure B9. Downstream bottom left pressure versus time for 1-GG up condition

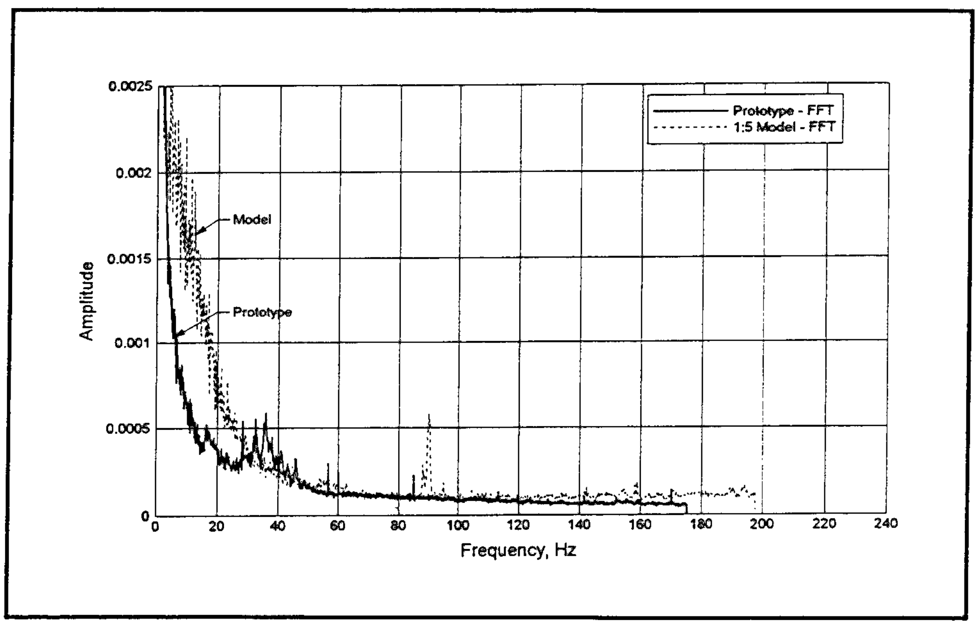

Figure B10. Downstream bottom left pressure FFT for 1-GG up condition

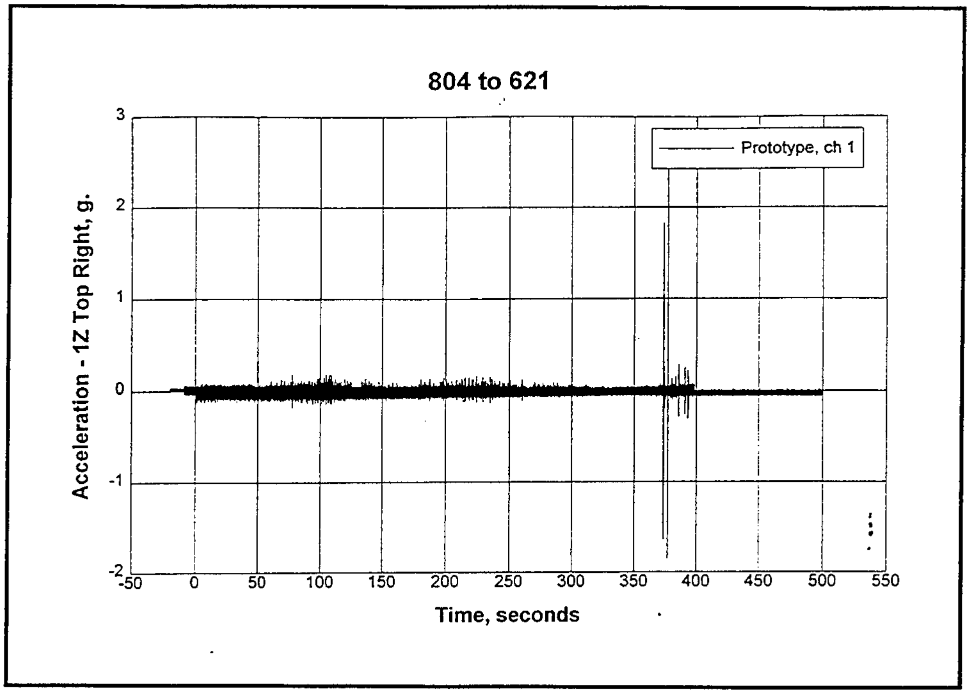

Figure B11. 1Z top right acceleration versus time 1-GG up condition

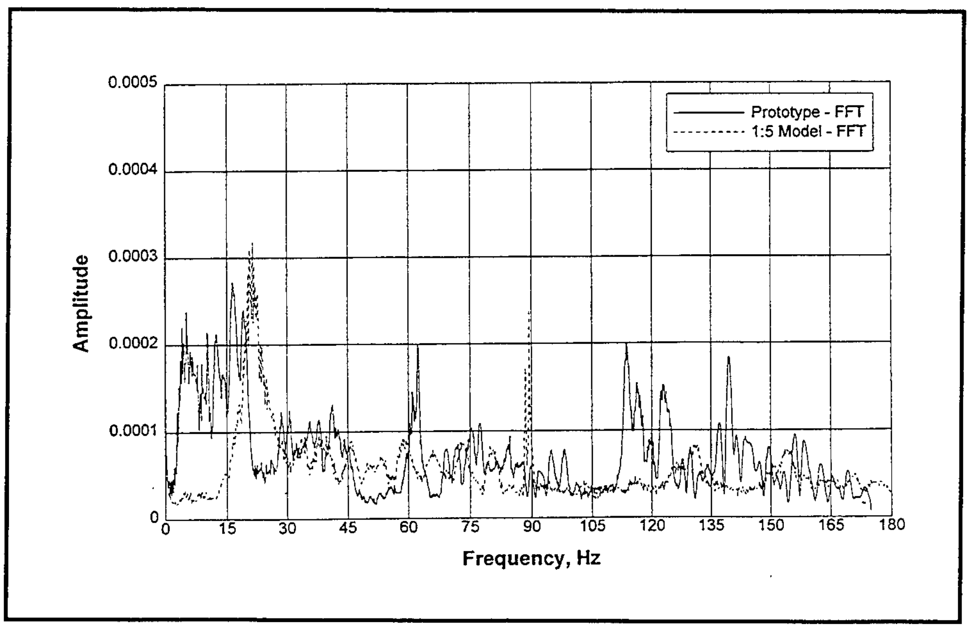

Figure B12. 1Z top right acceleration FFT for 1-GG up condition

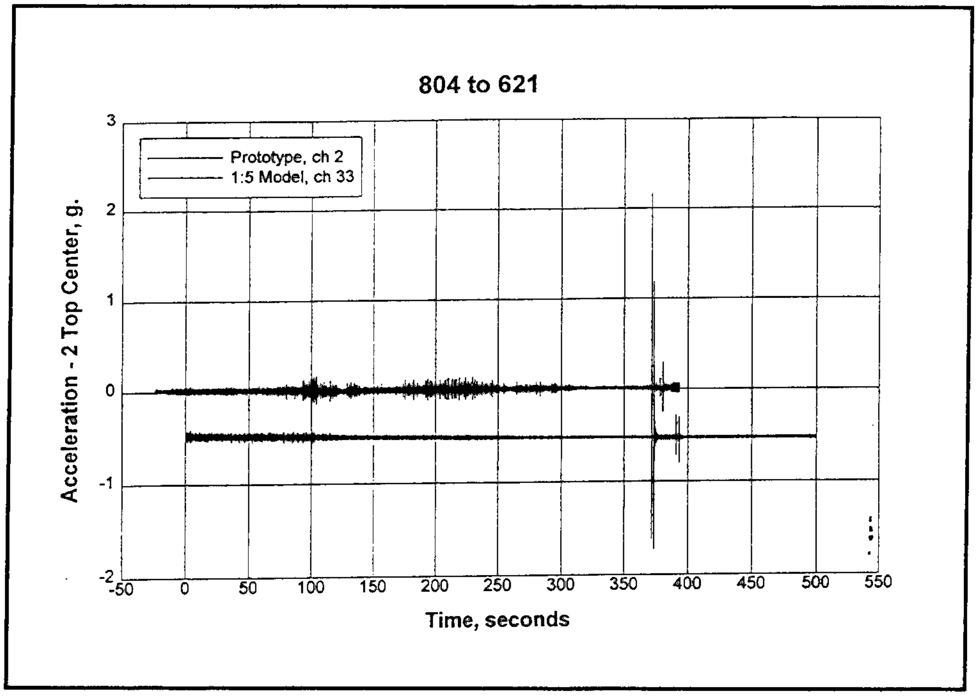

Figure B13. 2 top center acceleration versus time for 1-GG up condition

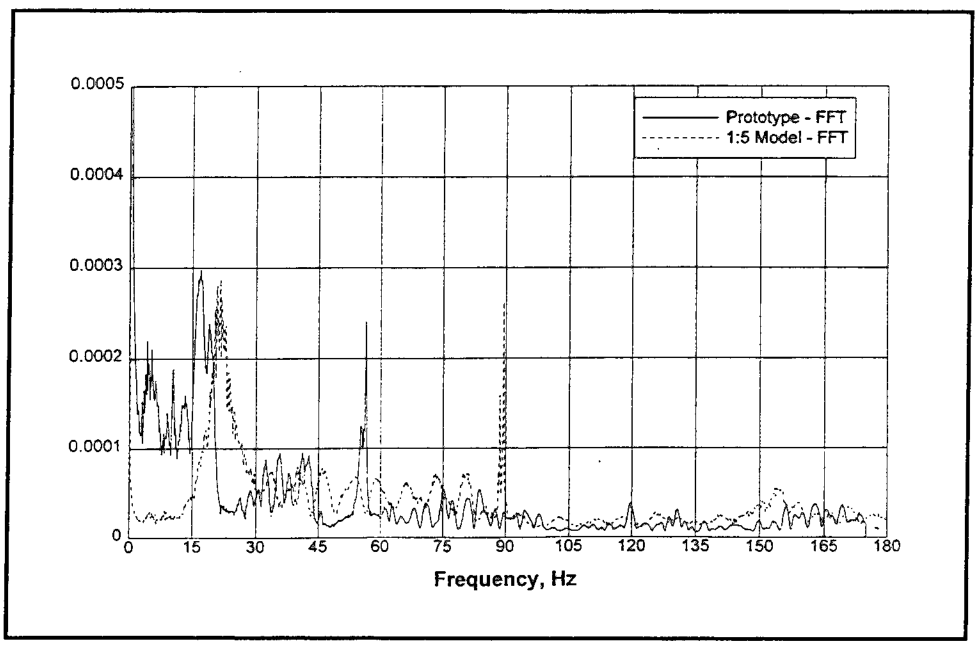

Figure B14. 2 top center acceleration FFT time for 1-GG up condition

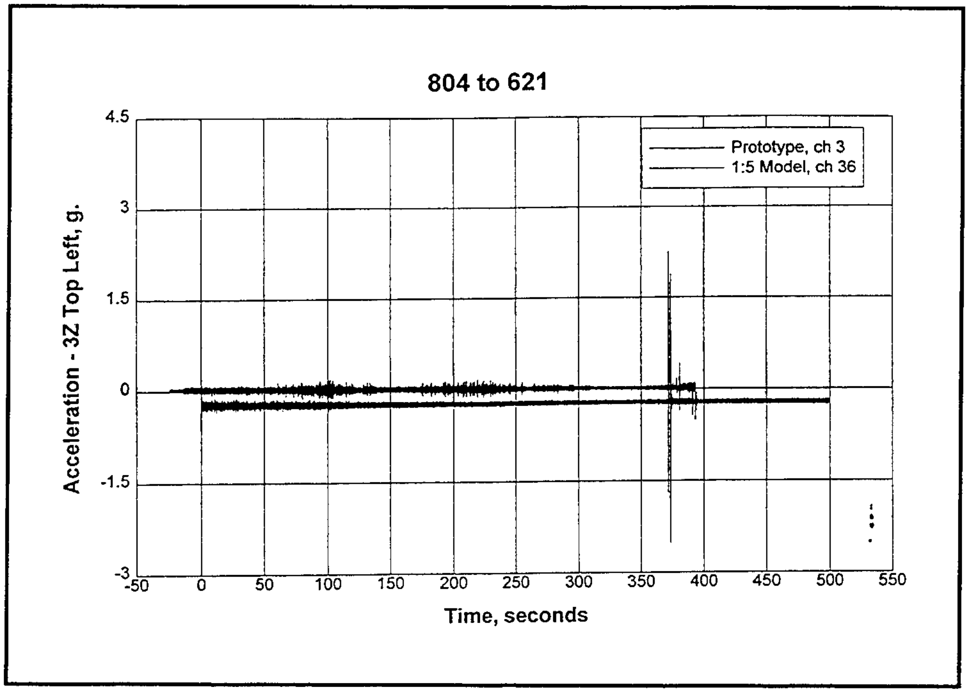

Figure B15. 3Z top left acceleration versus time for 1-GG up condition

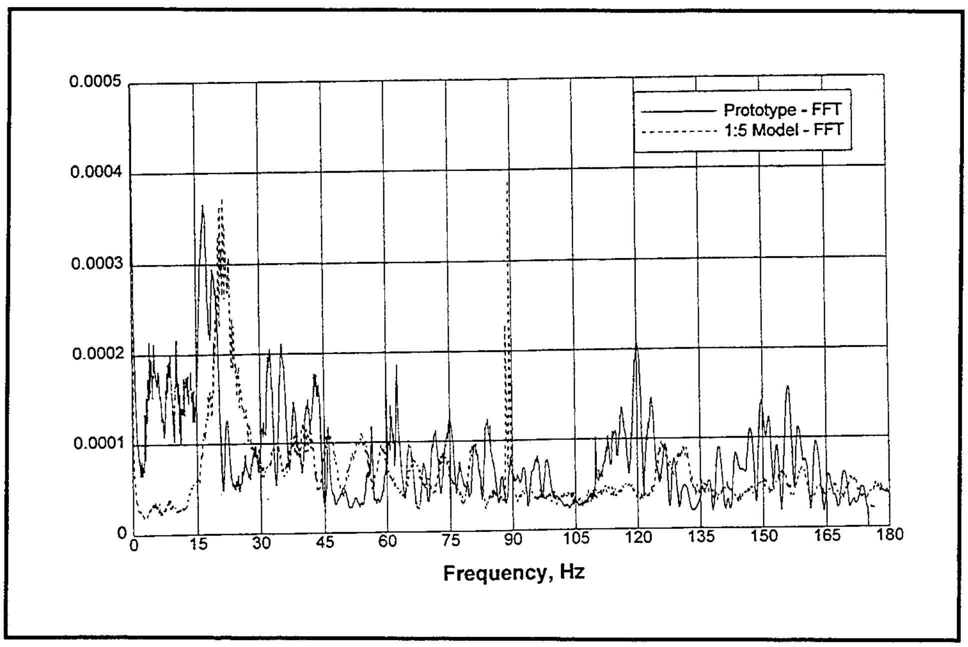

Figure B16. 3Z top left acceleration FFT for 1-GG up condition

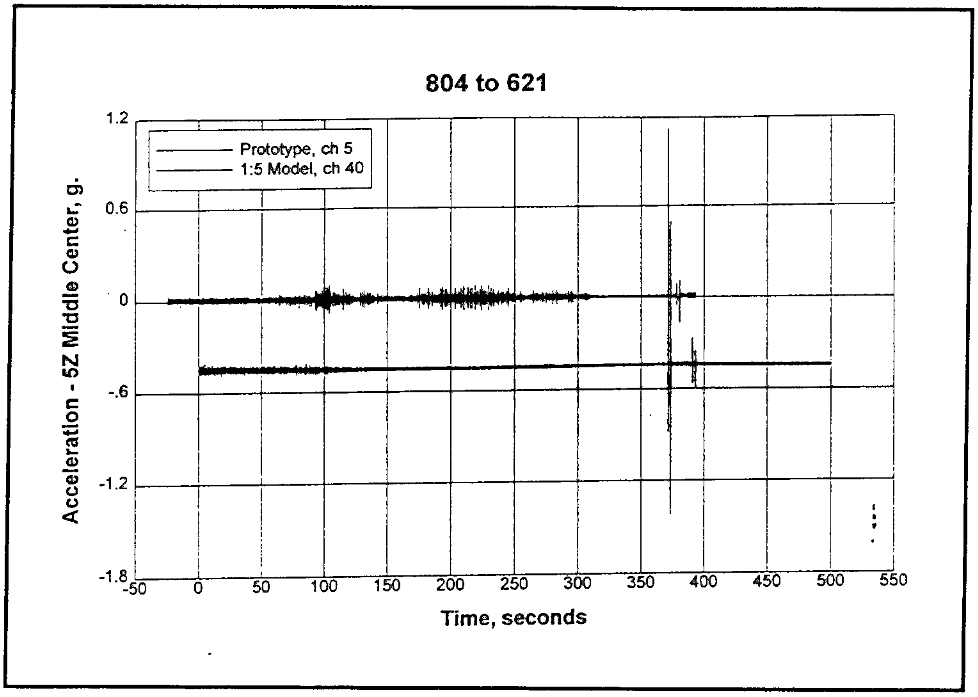

Figure B17. 5Z middle center acceleration versus time for 1-GG up condition

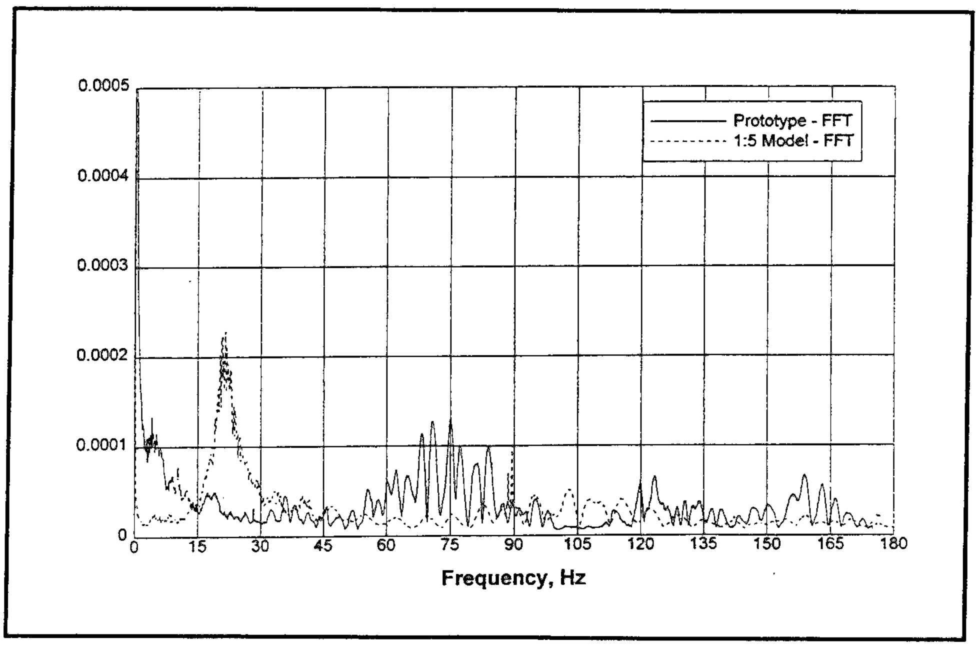

Figure B18. 5Z middle center acceleration FFT for 1-GG up condition

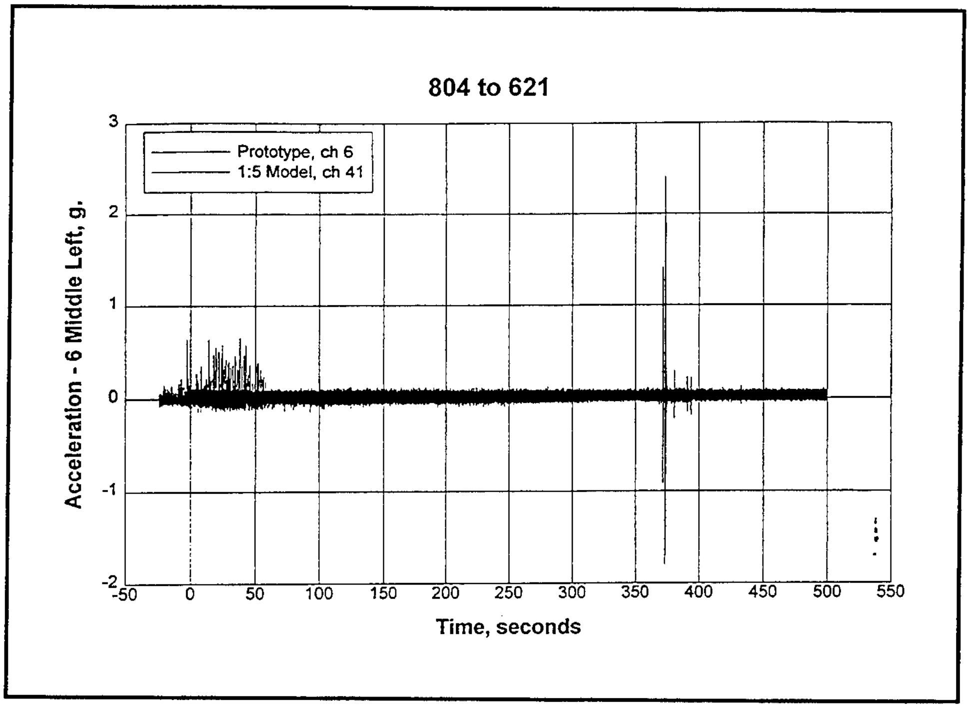

Figure B19. 6 middle left acceleration versus time for 1-GG up condition

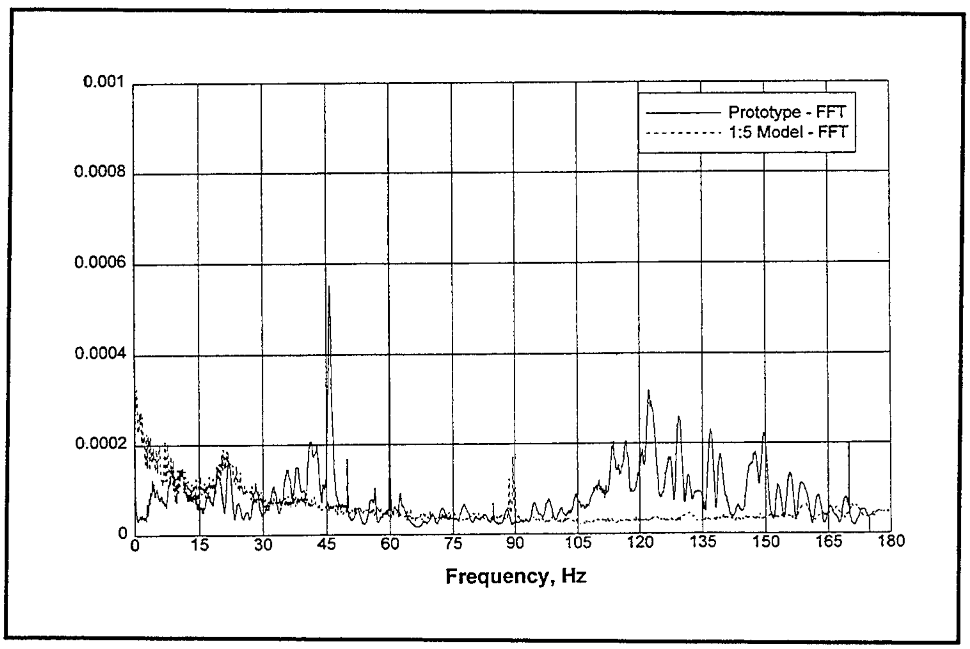

Figure B20. 6 middle left acceleration FFT for 1-GG up condition

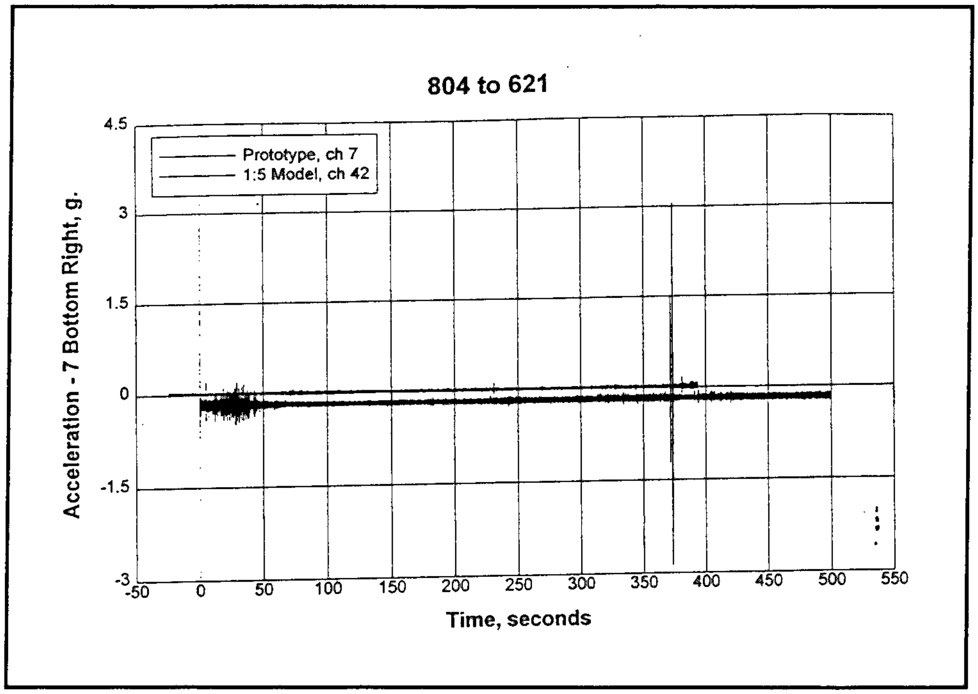

Figure B21. 7 bottom right acceleration versus time for 1-GG up condition

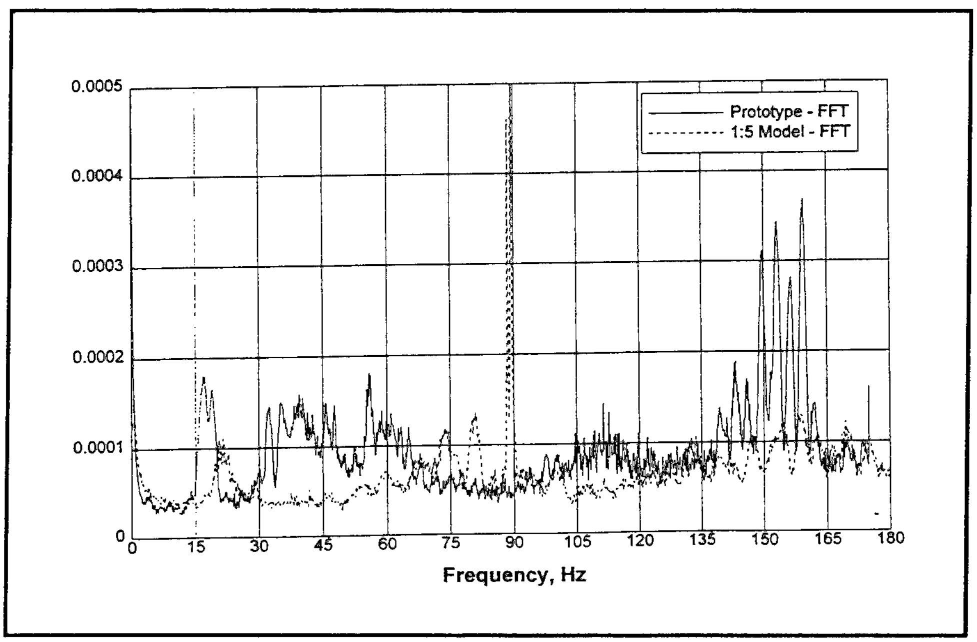

Figure B22. 7 bottom right acceleration FFT for 1-GG up condition

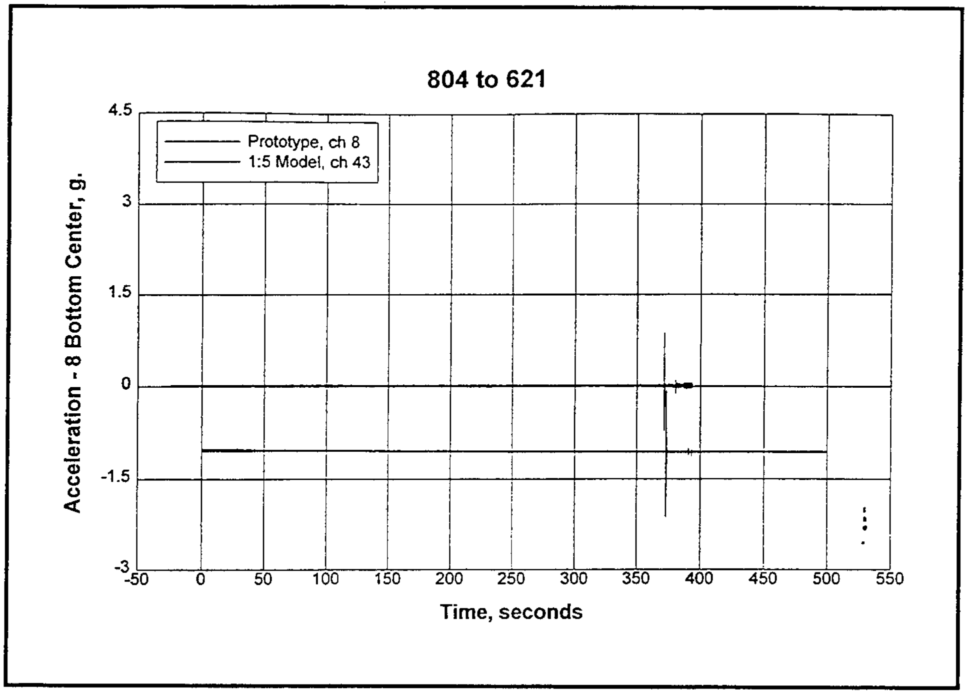

Figure B23. 8 bottom center acceleration versus time for 1-GG up condition

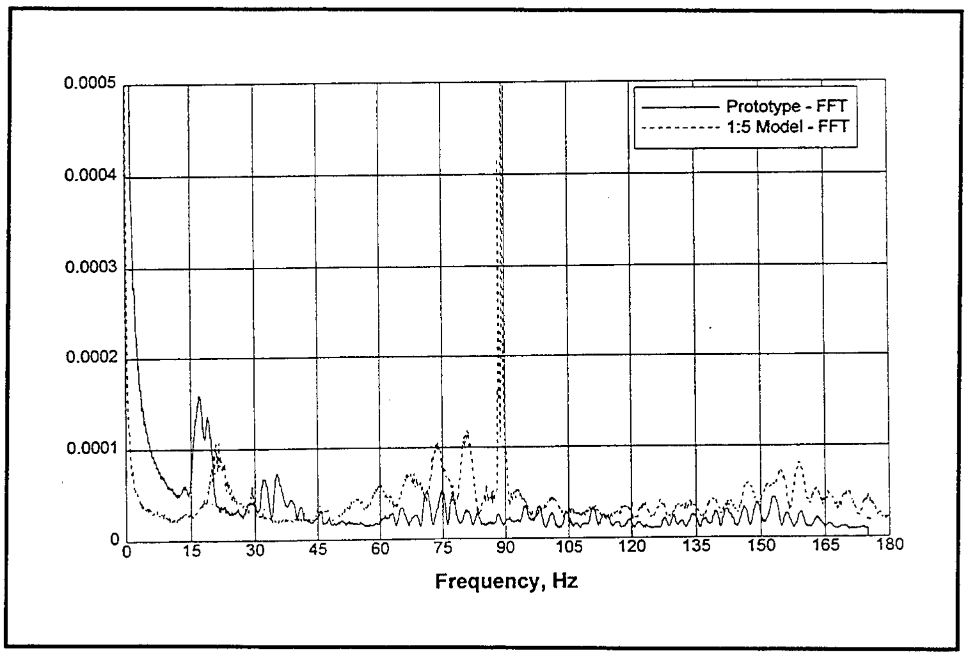

Figure B24. 8 bottom center acceleration FFT for 1-GG up condition

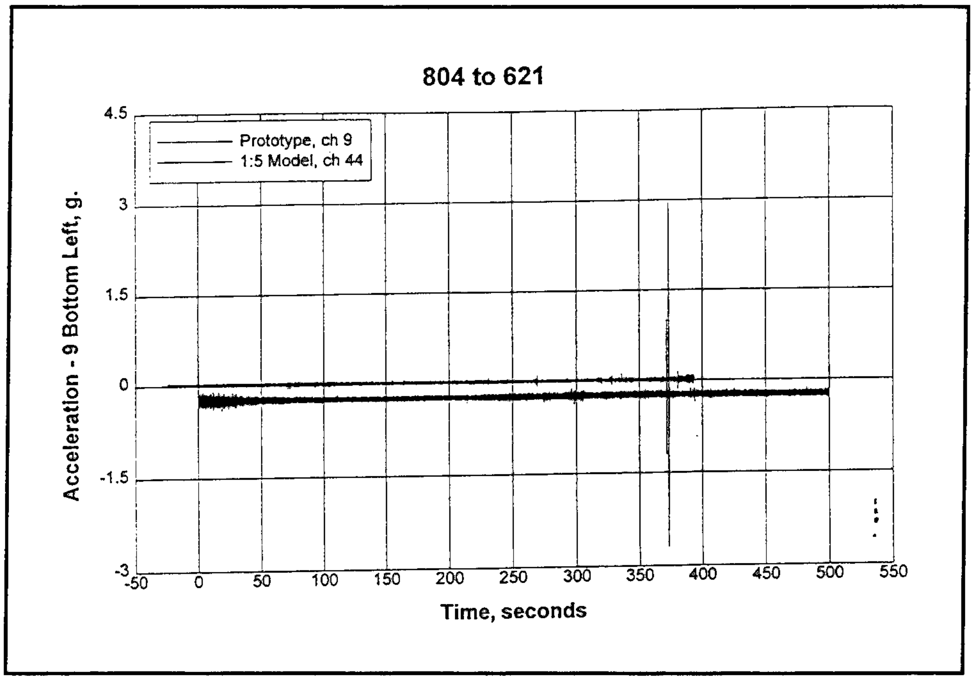

Figure B25. 9 bottom left acceleration versus time for 1-GG up condition

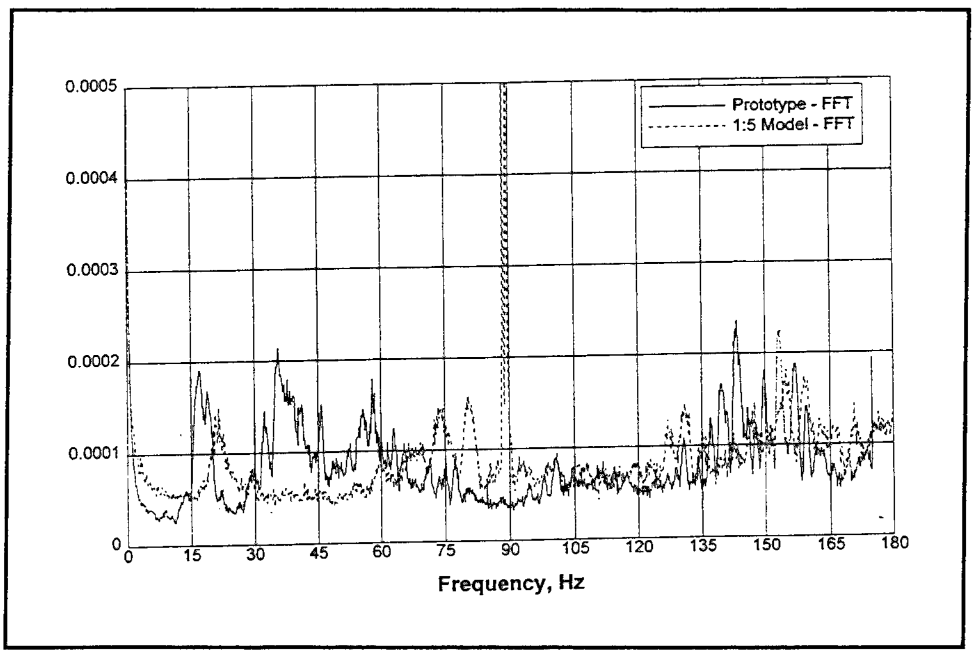

Figure B26. 9 bottom left acceleration FFT for 1-GG up condition

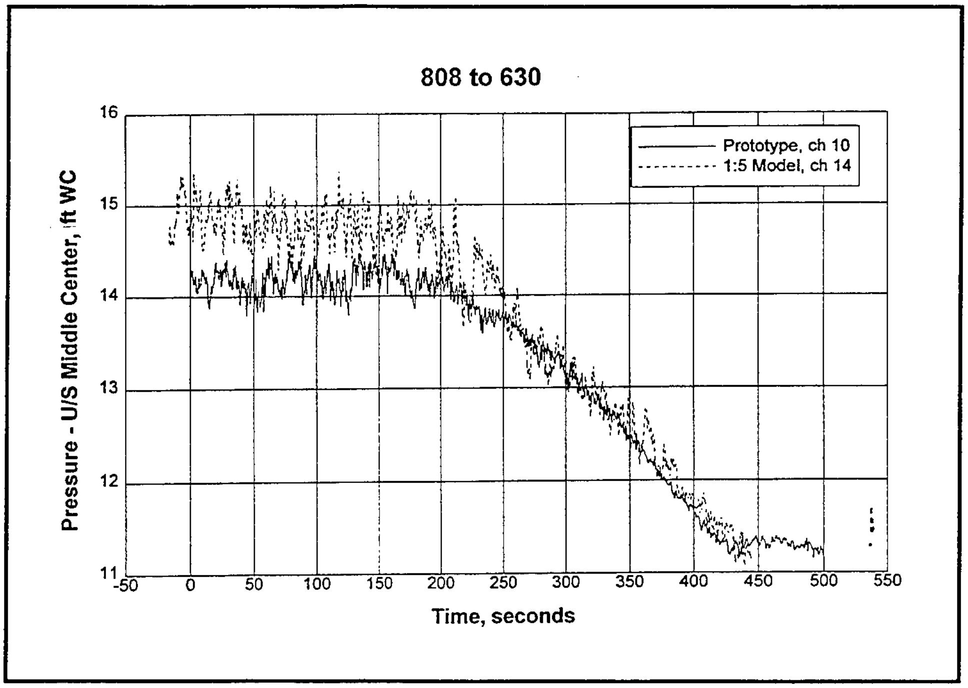

Figure B27. Upstream middle center pressure vs time for 3-GG up condition

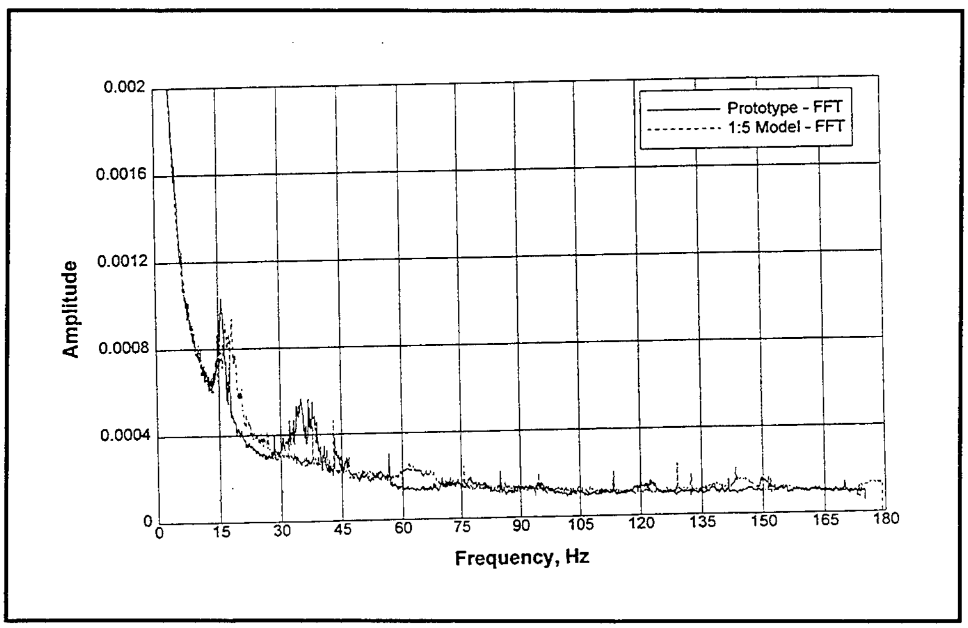

Figure B28. Upstream middle center pressure FFT for 3-GG up condition

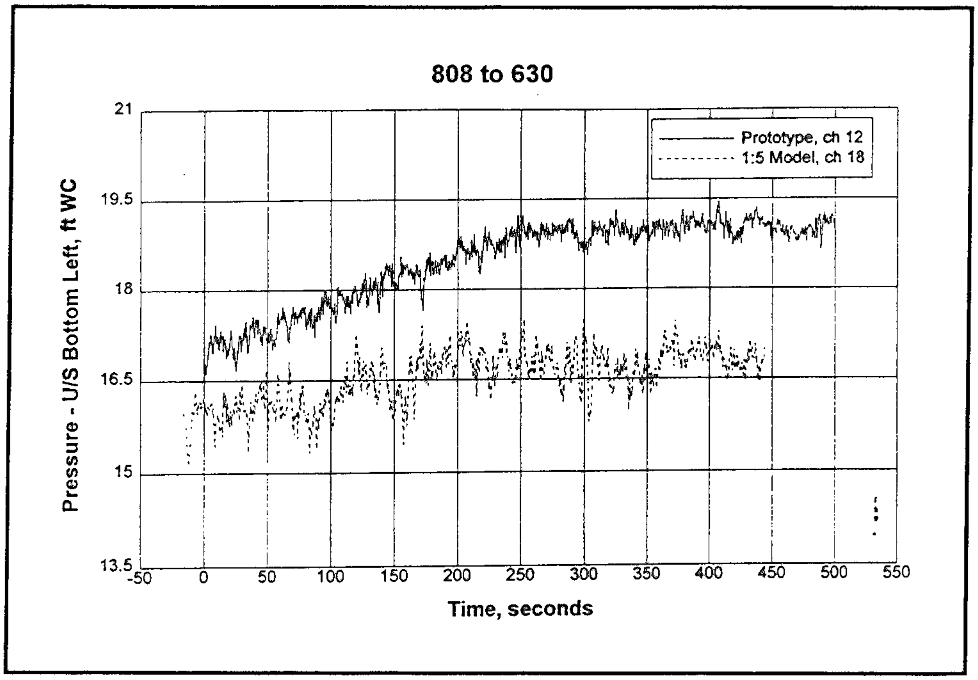

Figure B29. Upstream bottom left pressure vs time for 3-GG up condition

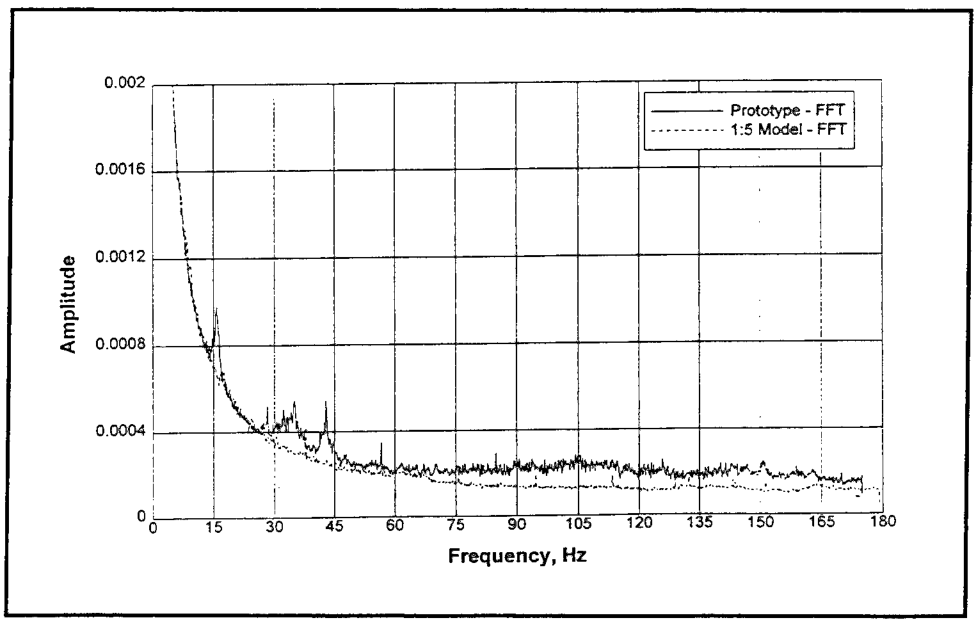

Figure B30. Upstream bottom left pressure FFT for 3-GG up condition

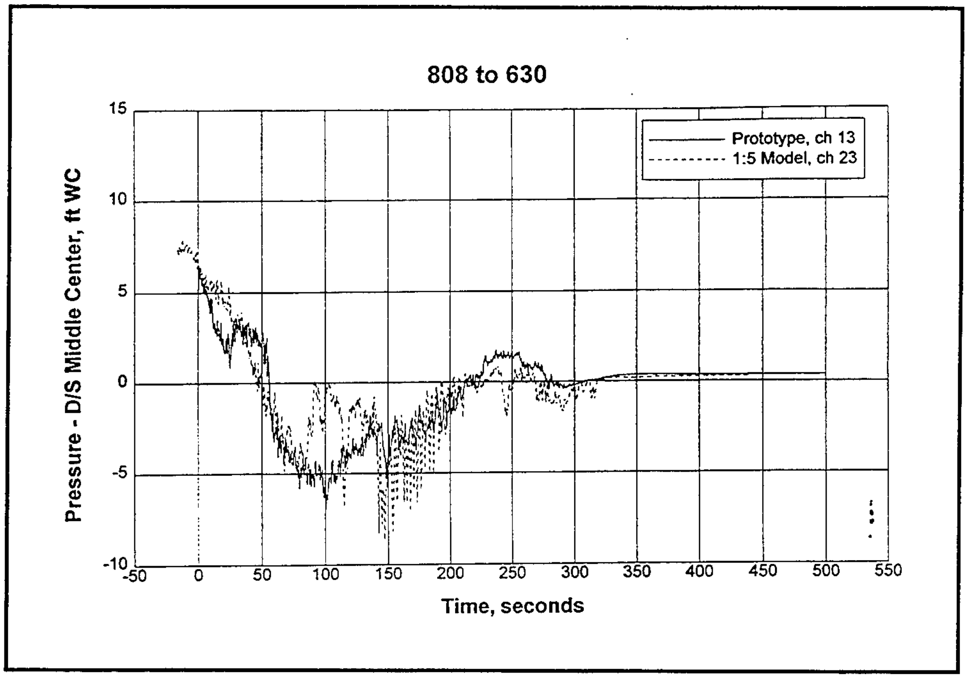

Figure B31. Downstream middle center pressure vs time for 3-GG up condition

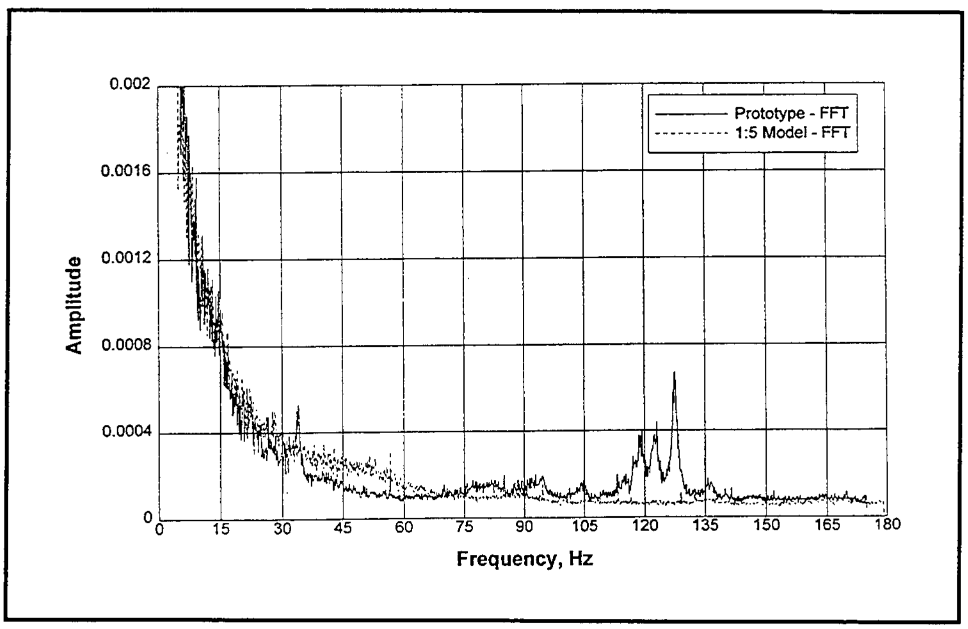

Figure B32. Downstream middle center pressure FFT for 3-GG up condition

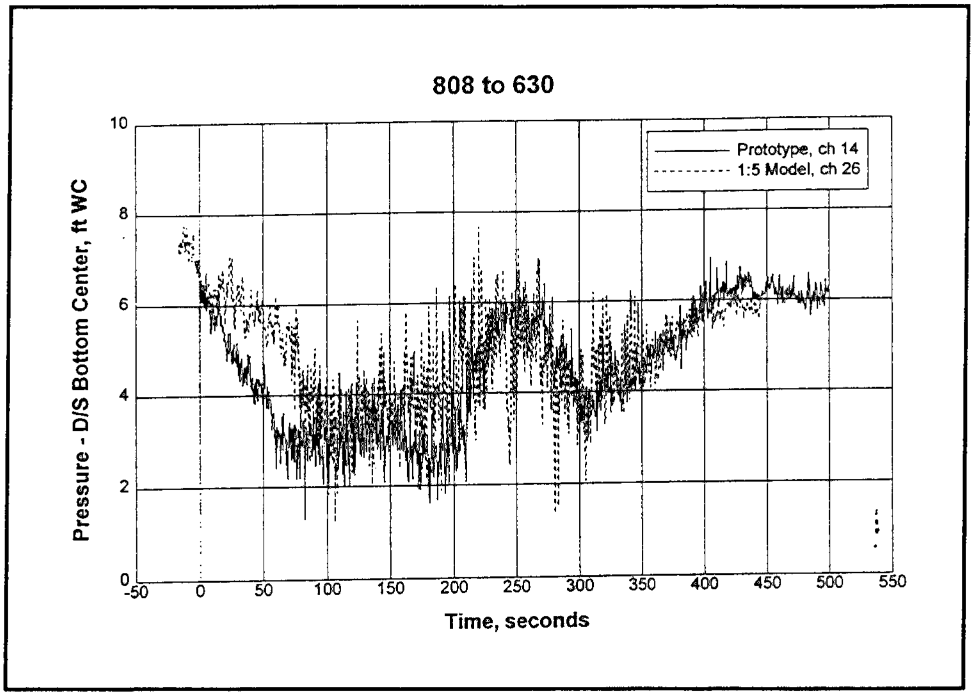

Figure B33. Downstream bottom center pressure vs time for 3-GG up condition

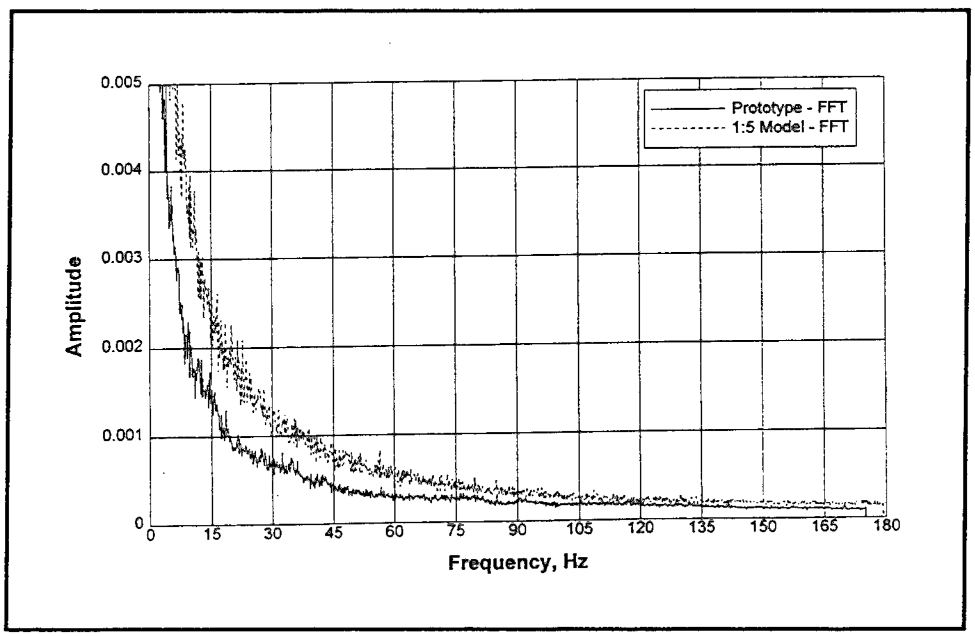

Figure B34. Downstream bottom center pressure FFT for 3-GG up condition

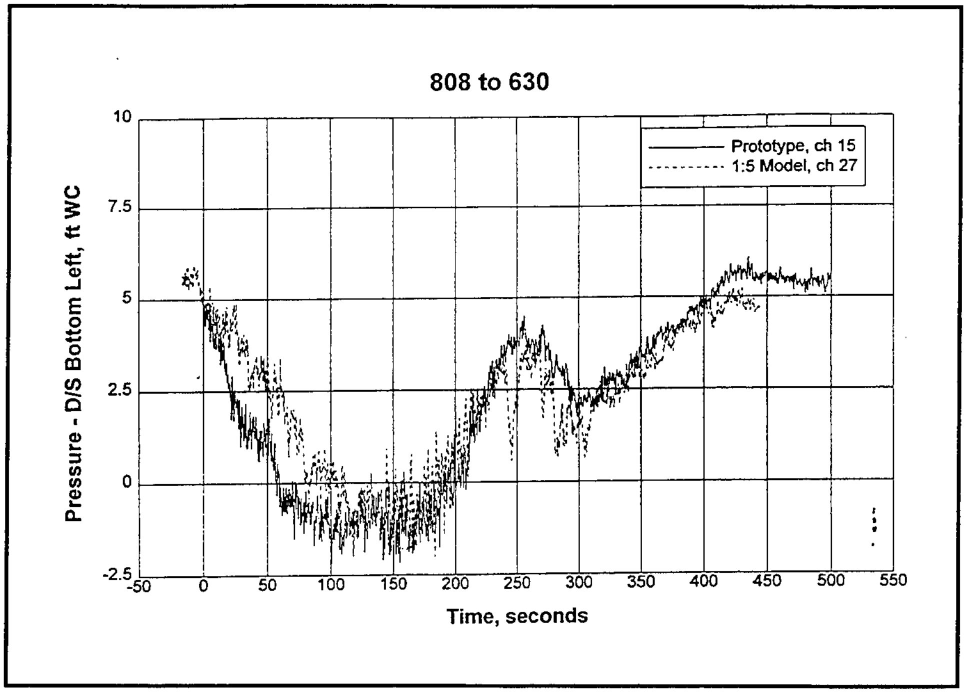

Figure B35. Downstream bottom left pressure vs time for 3-GG up condition

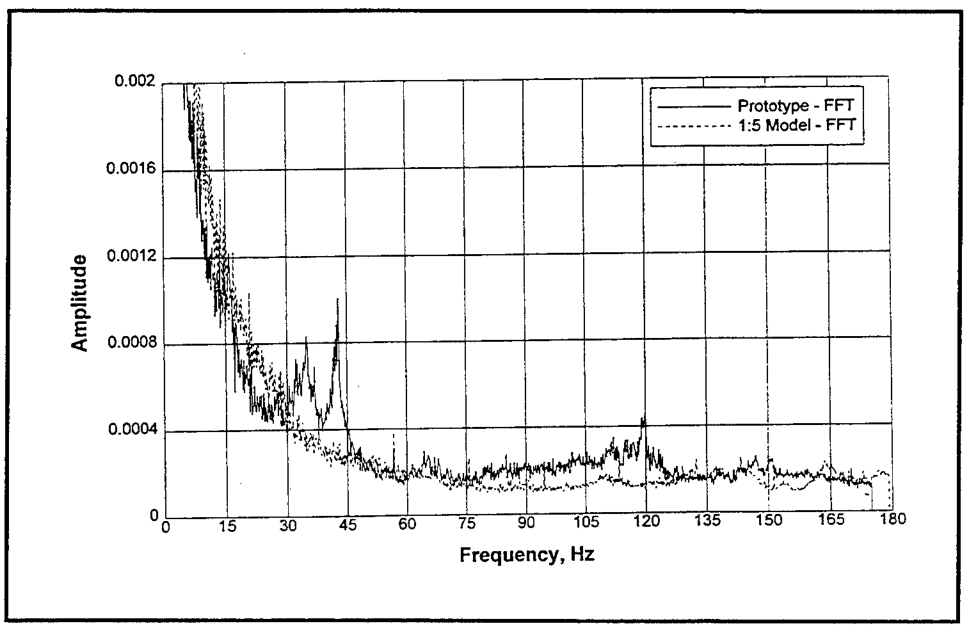

Figure B36. Downstream bottom left pressure FFT for 3-GG up condition

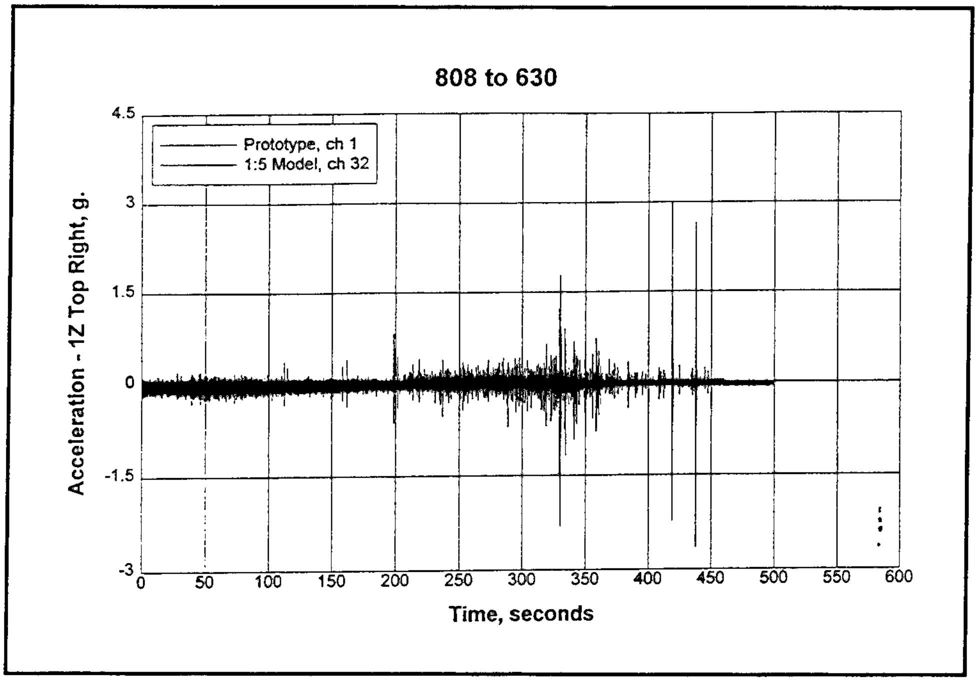

Figure B37. 1Z top right acceleration vs time for 3-GG up condition

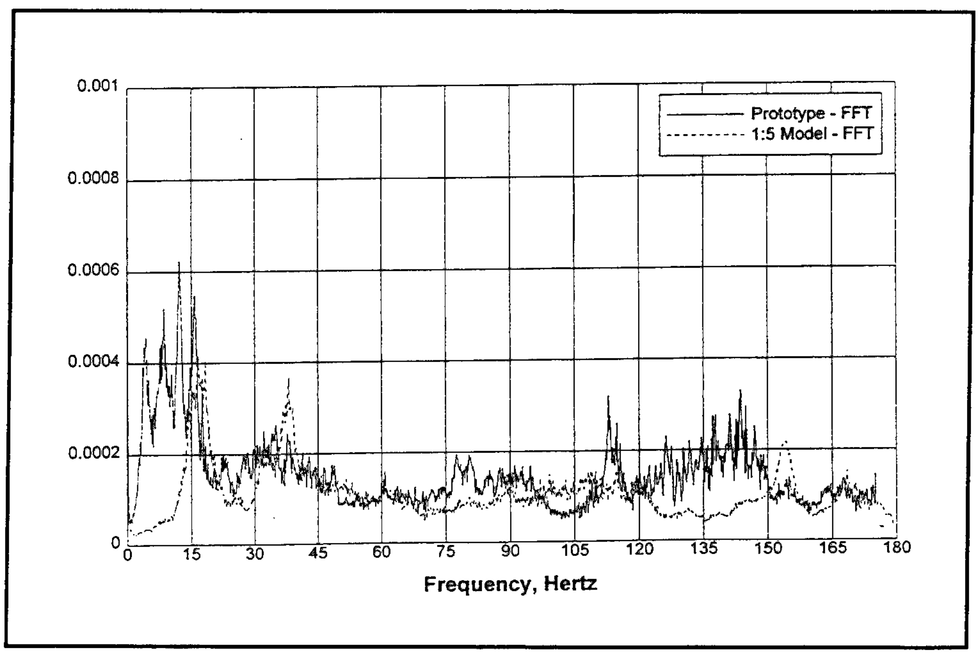

Figure B38. 1Z top right acceleration FFT for 3-GG up condition

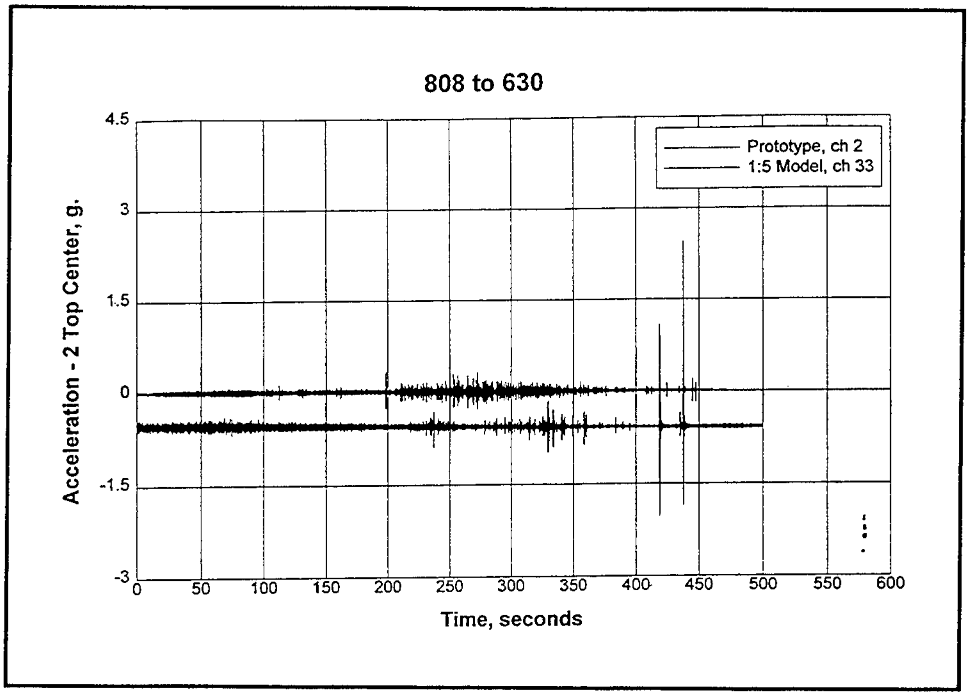

Figure B39. 2 top center acceleration vs time for 3-GG up condition

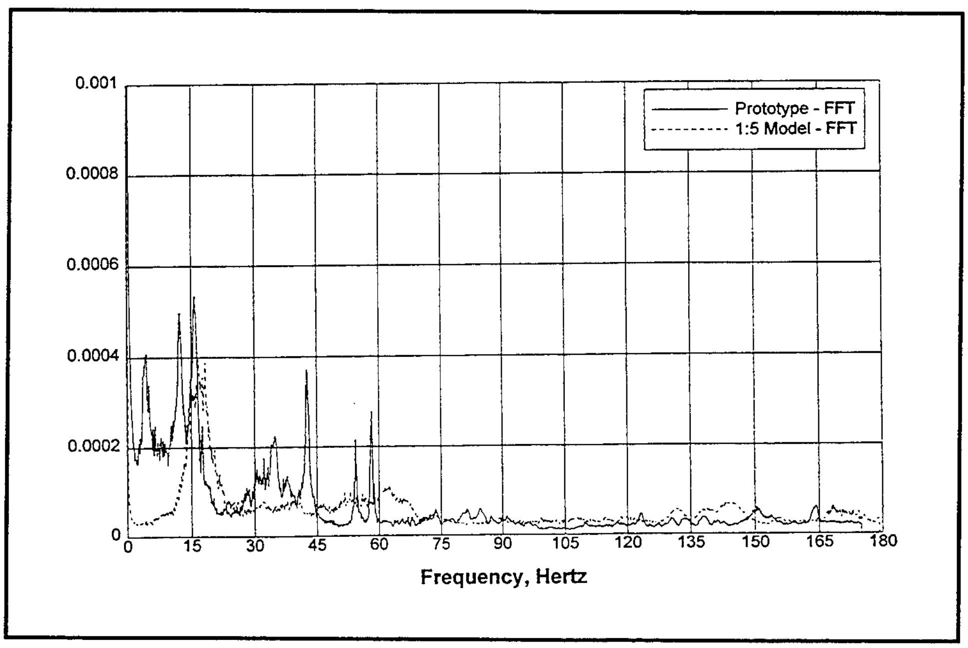

Figure B40. 2 top center acceleration FFT for 3-GG up condition

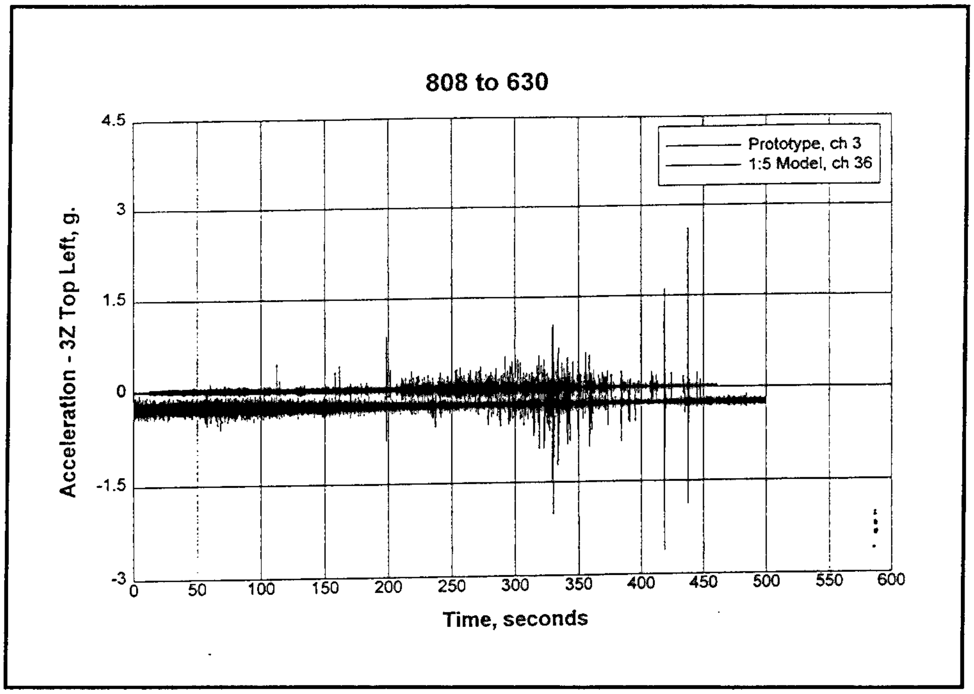

Figure B41. 3Z top left acceleration vs time for 3-GG up condition

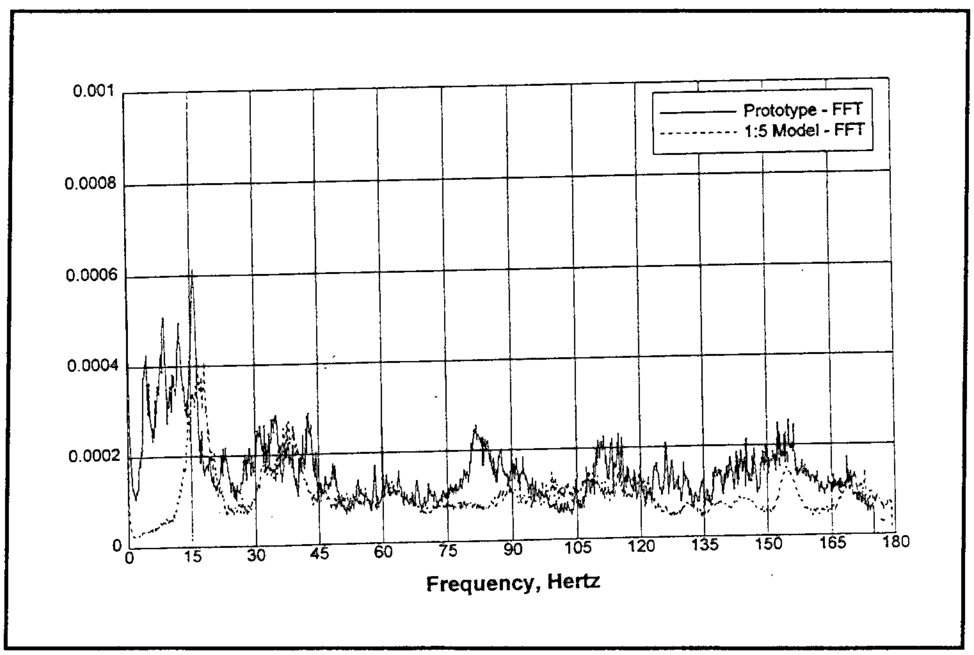

Figure B42. 3Z top left acceleration FFT for 3-GG up condition

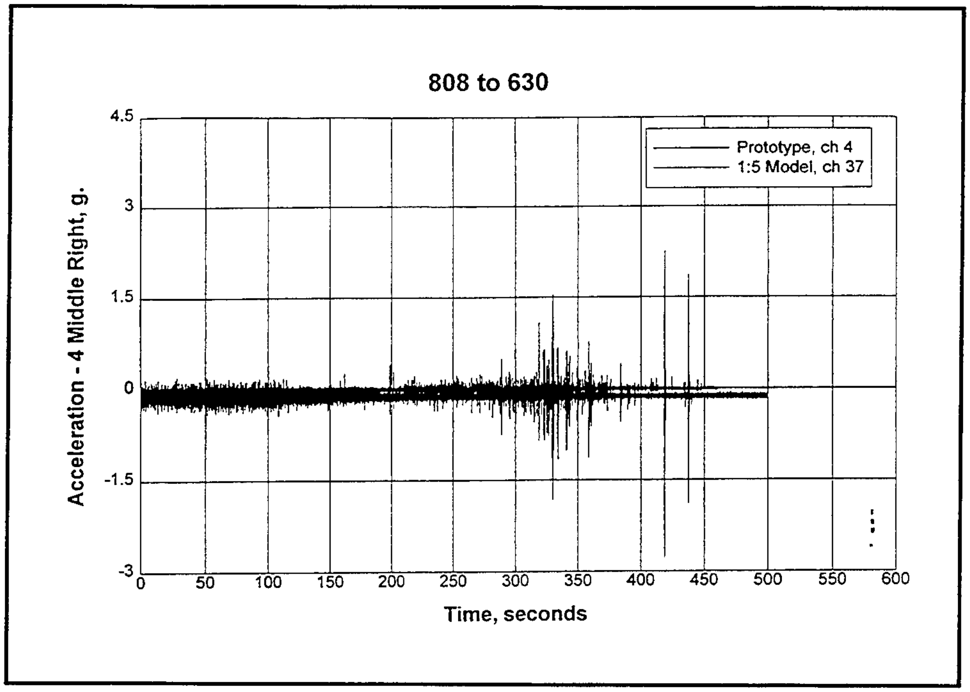

Figure B43. 4 middle right acceleration vs time for 3-GG up condition

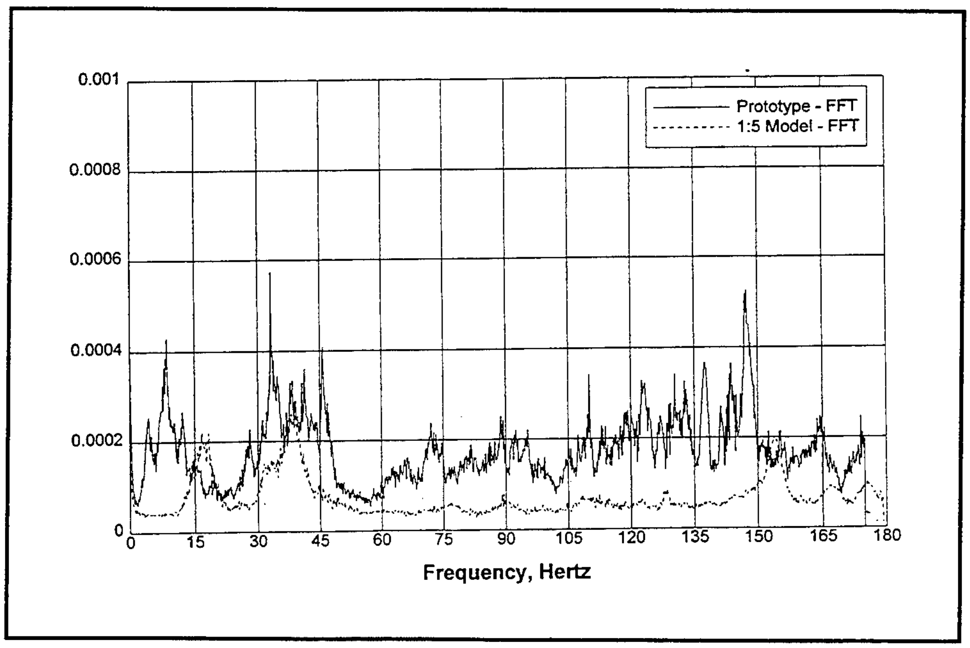

Figure B44. 4 middle right acceleration FFT for 3-GG up condition

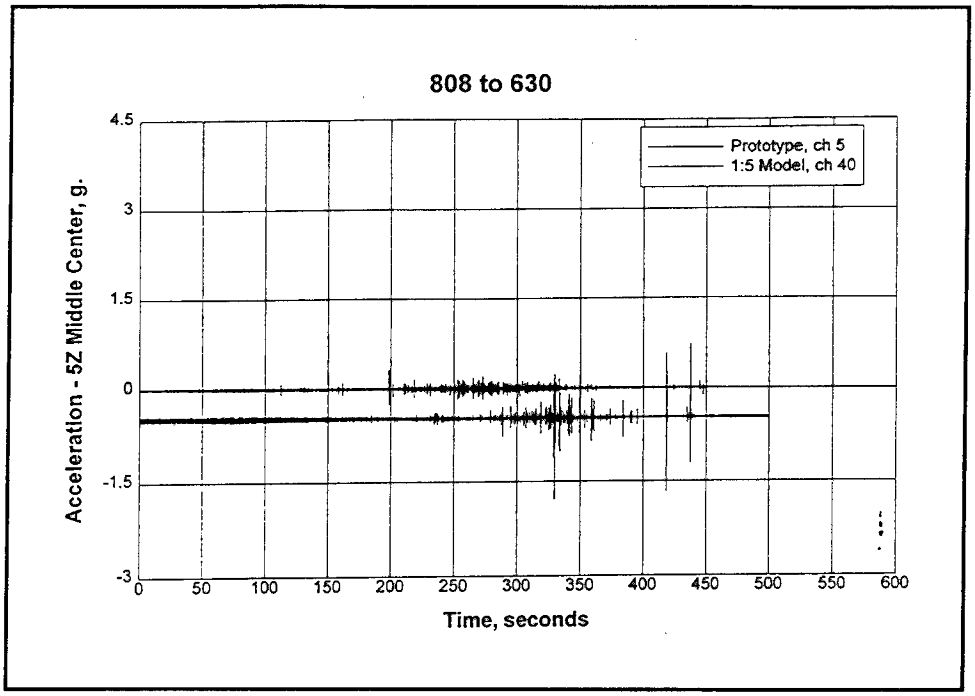

Figure B45. 5Z middle center acceleration vs time for 3-GG up condition

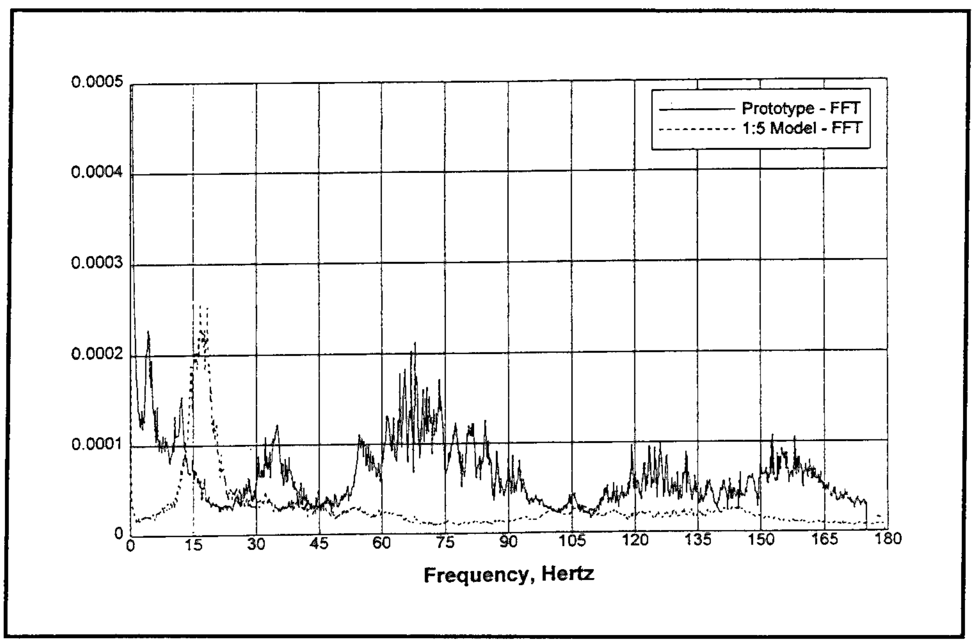

Figure B46. 5Z middle center acceleration FFT for 3-GG up condition

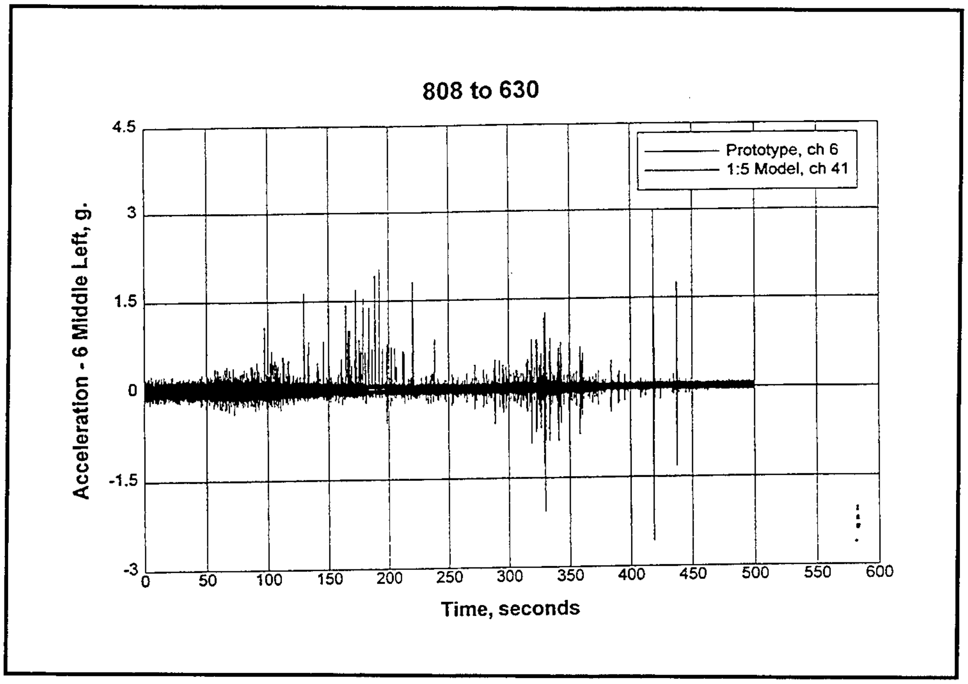

Figure B47. 6 middle left acceleration vs time for 3-GG up condition

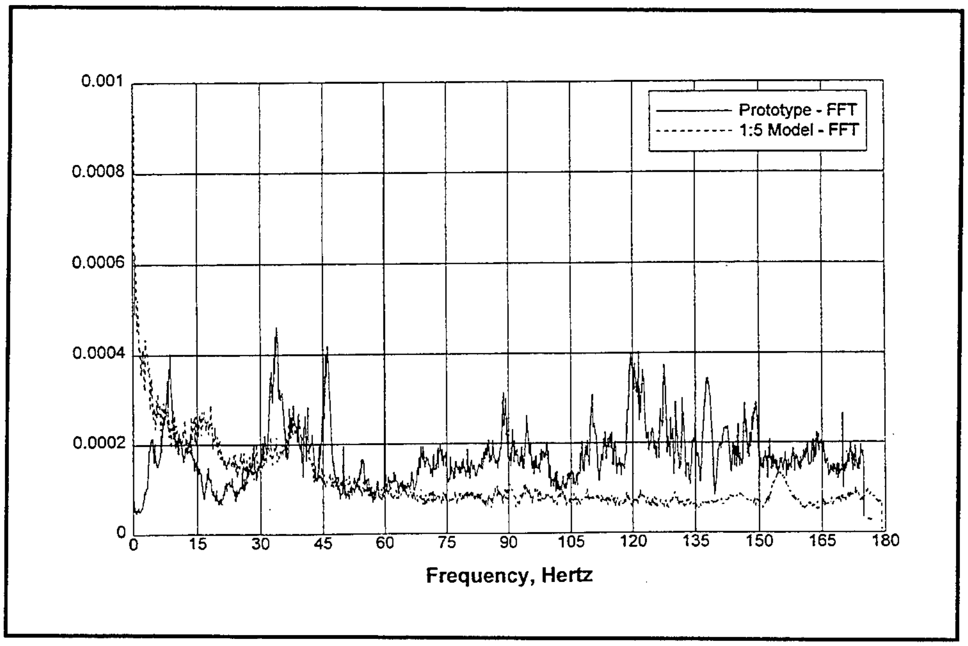

Figure B48. 6 middle left acceleration FFT for 3-GG up condition

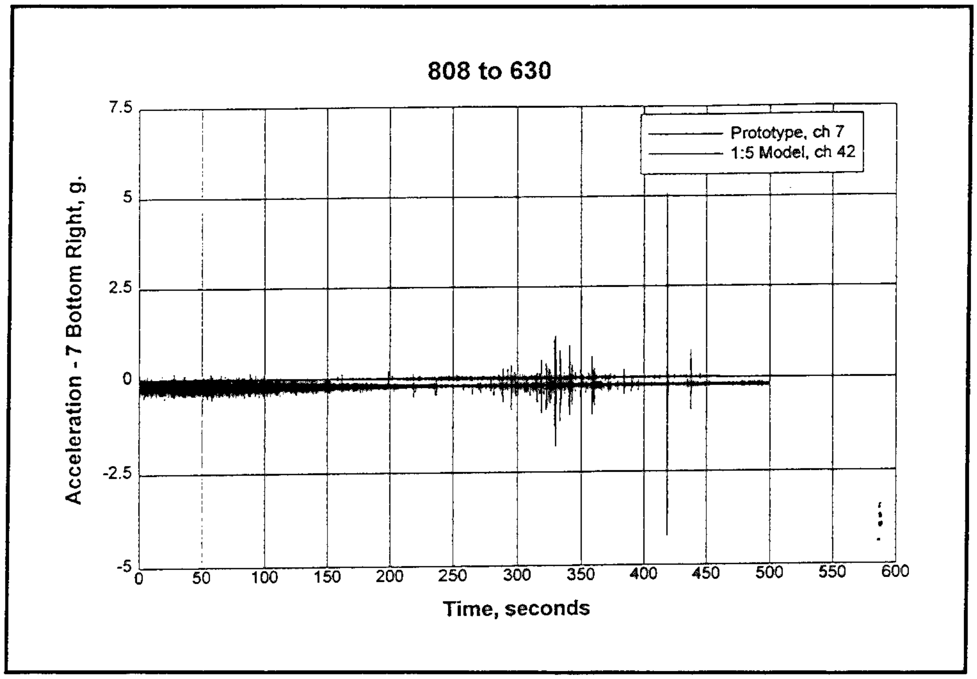

Figure B49. 7 bottom right acceleration vs time for 3-GG up condition

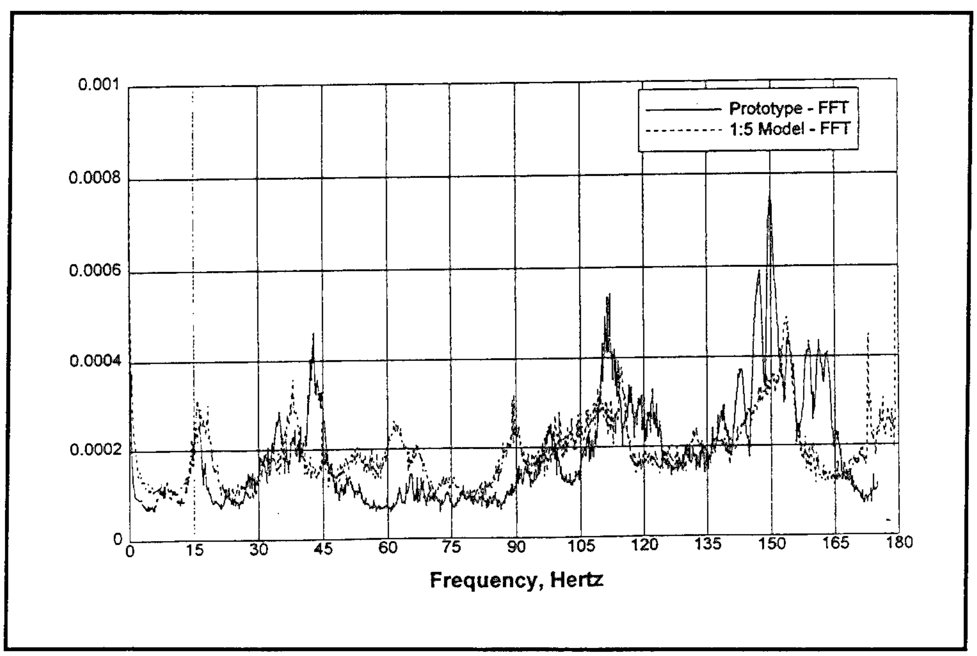

Figure B50. 7 bottom right acceleration FFT for 3-GG up condition

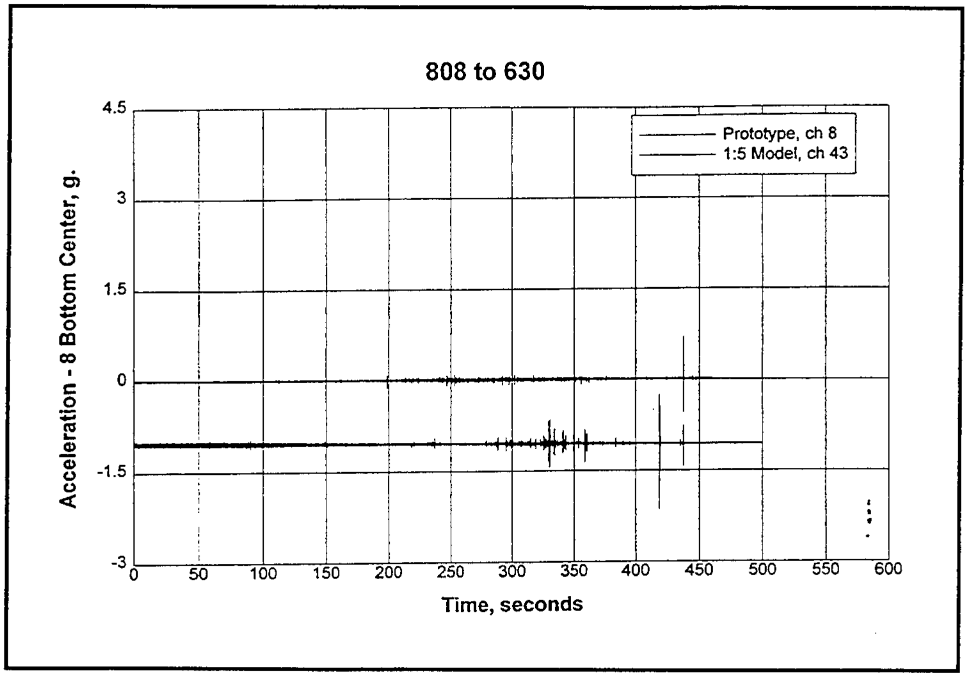

Figure B51. 8 bottom center acceleration vs time for 3-GG up condition

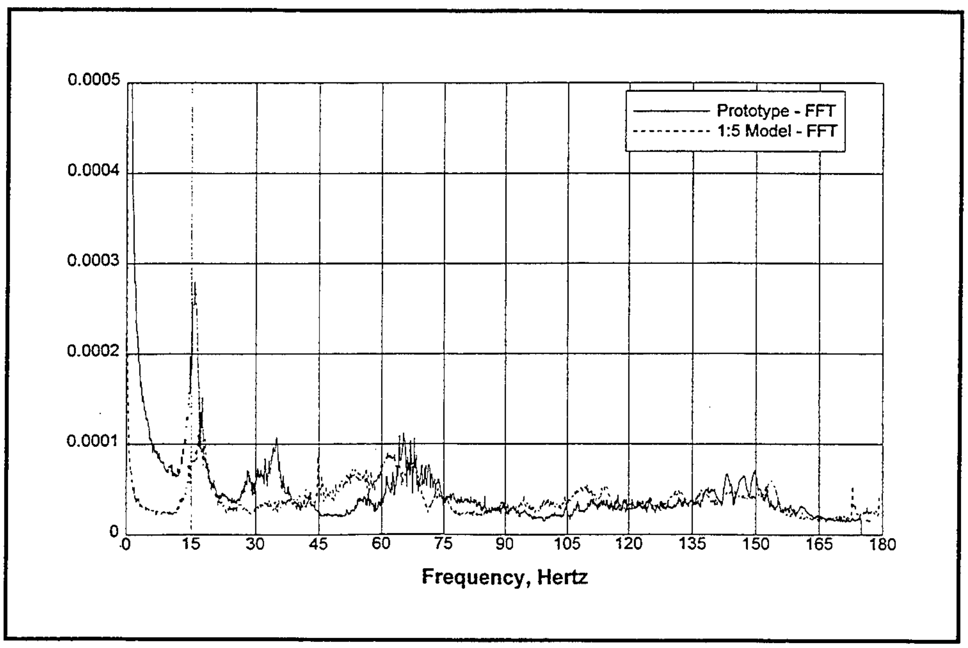

Figure B52. 8 bottom center acceleration FFT for 3-GG up condition

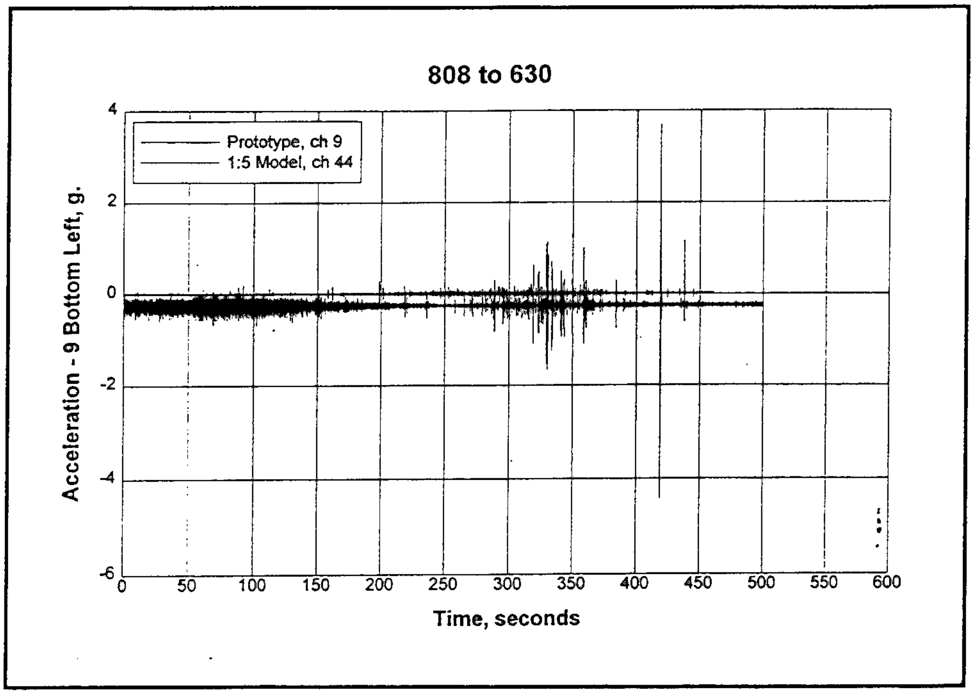

Figure B53. 9 bottom left acceleration vs time for 3-GG up condition

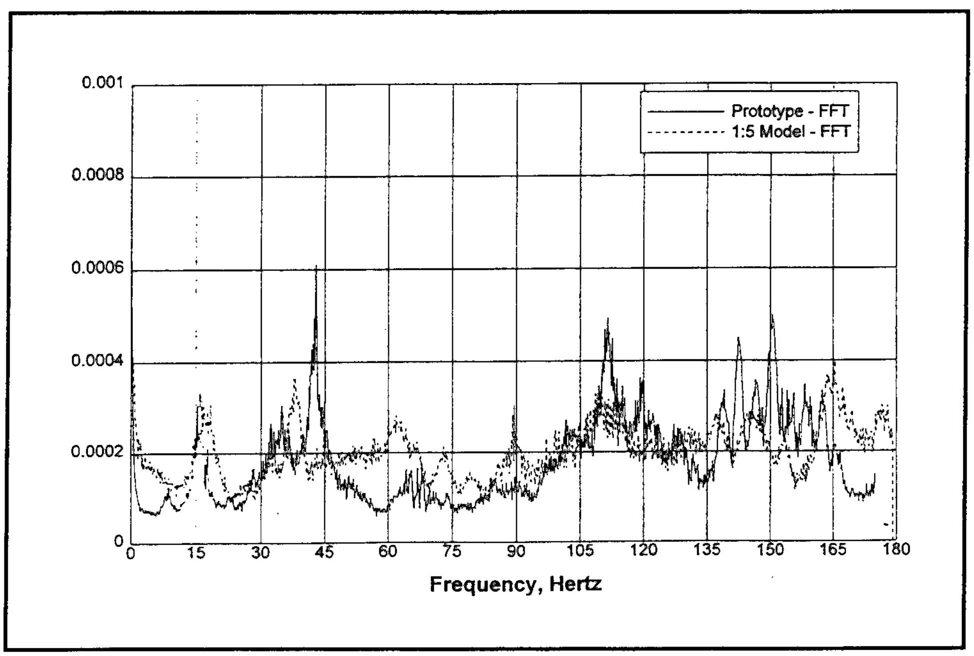

Figure B54. 9 bottom left acceleration FFT for 3-GG up condition

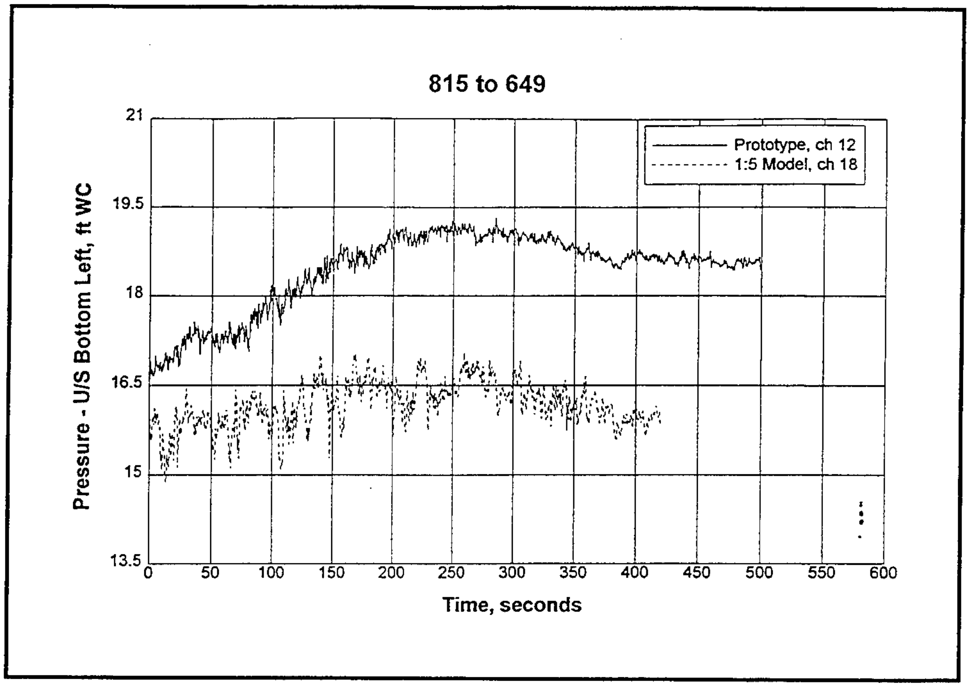

Figure B55. Upstream bottom left pressure vs time for 2-GG (EL) condition

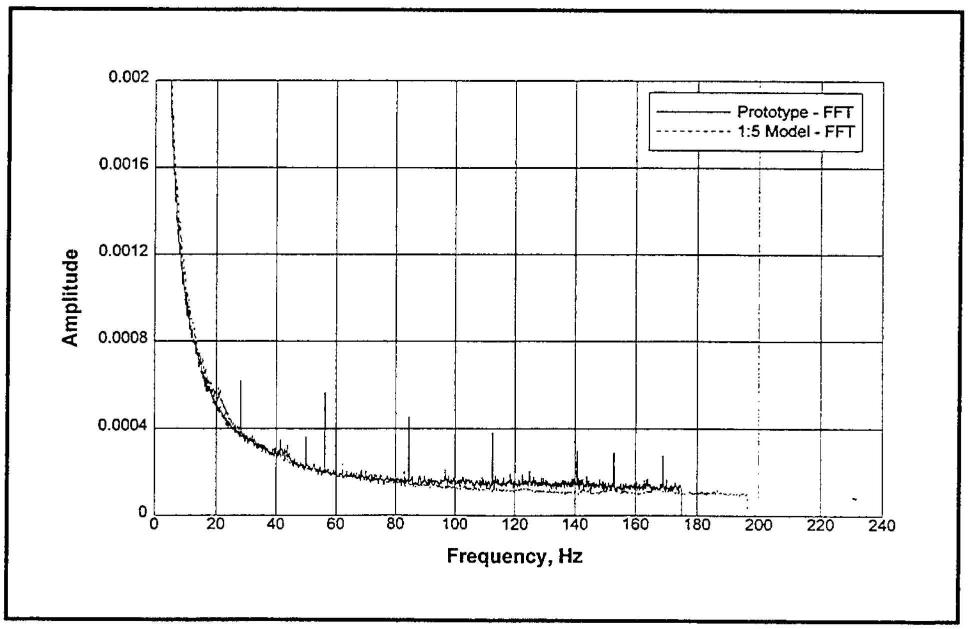

Figure B56. Upstream bottom left pressure FFT for 2-GG (EL) condition

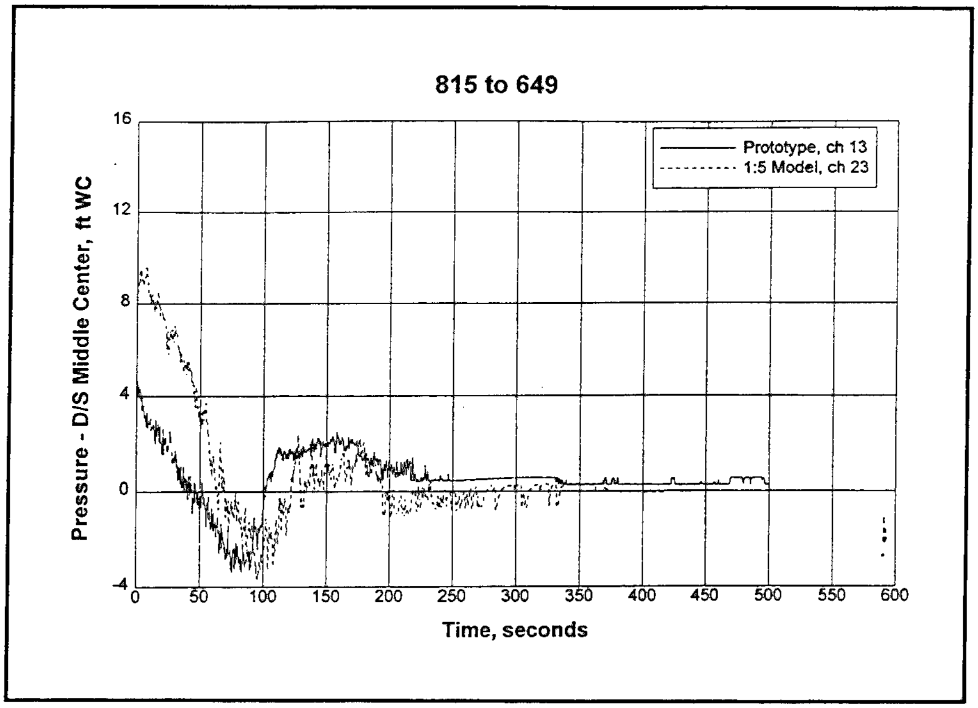

Figure B57. Downstream middle center pressure vs time for 2-GG (EL) condition

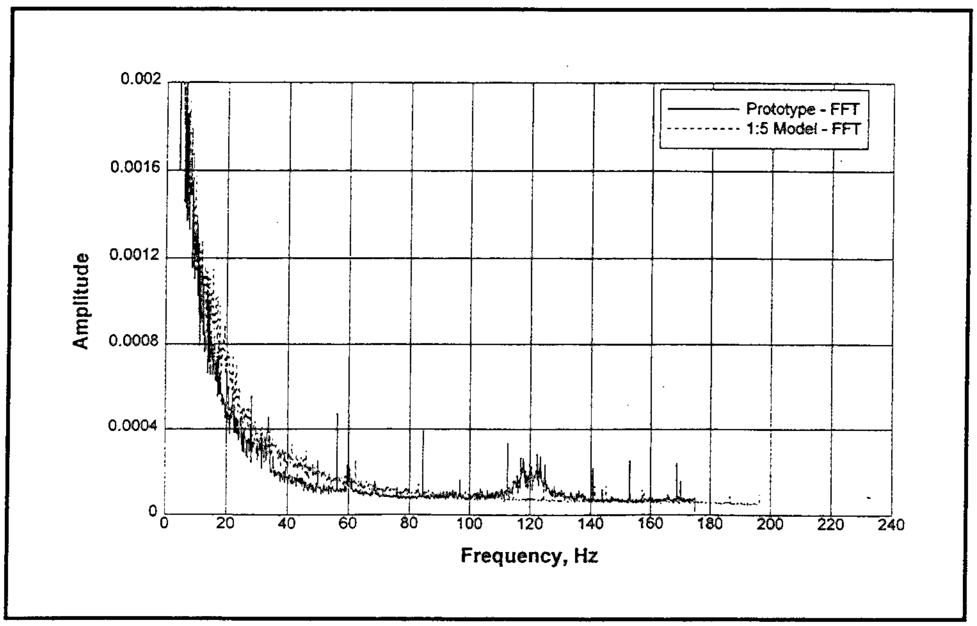

Figure B58. Downstream middle center pressure FFT for 2-GG (EL) condition

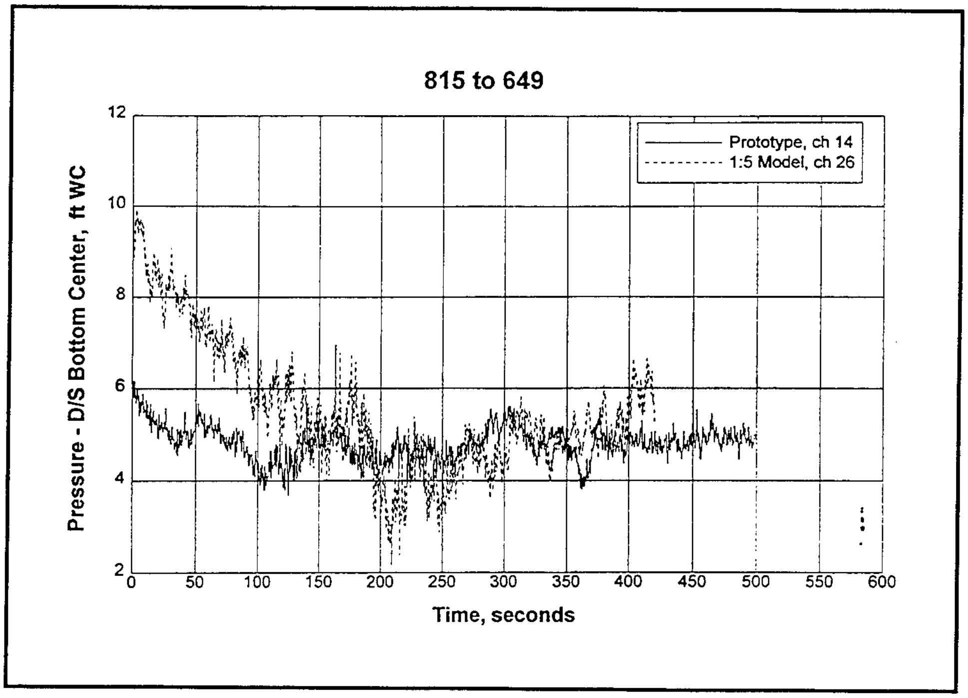

Figure B59. Downstream bottom center pressure vs time for 2-GG (EL) condition

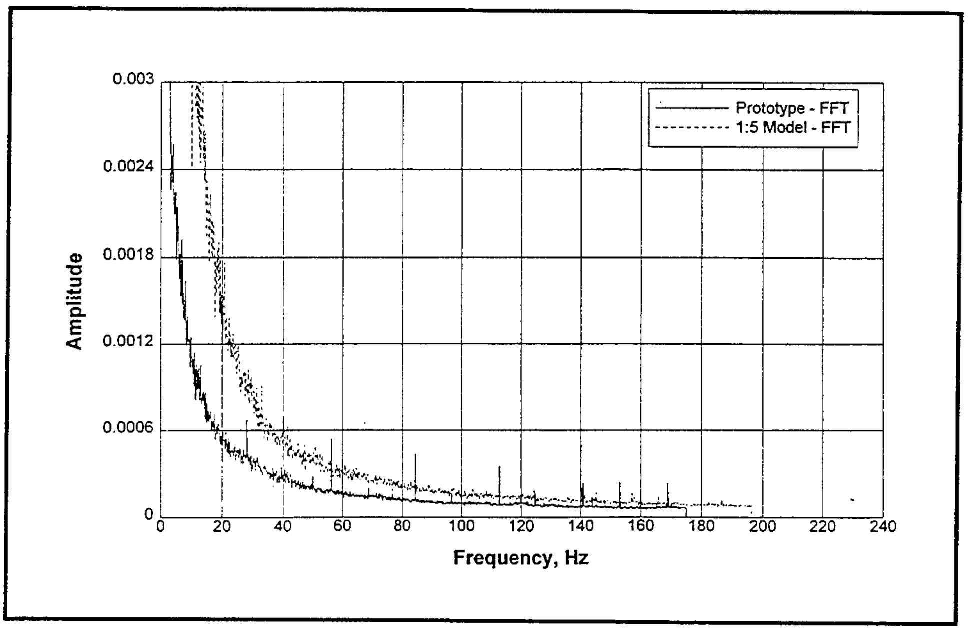

Figure 60. Downstream bottom center pressure FFT for 2-GG (EL) condition

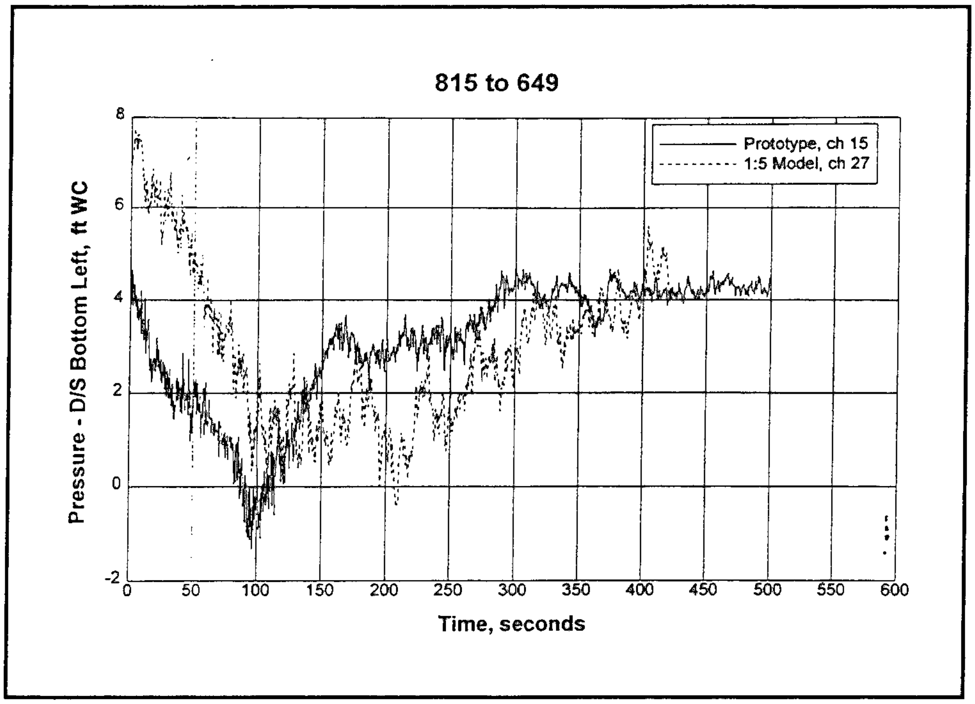

Figure B61. Downstream bottom left pressure vs time for 2-GG (EL) condition

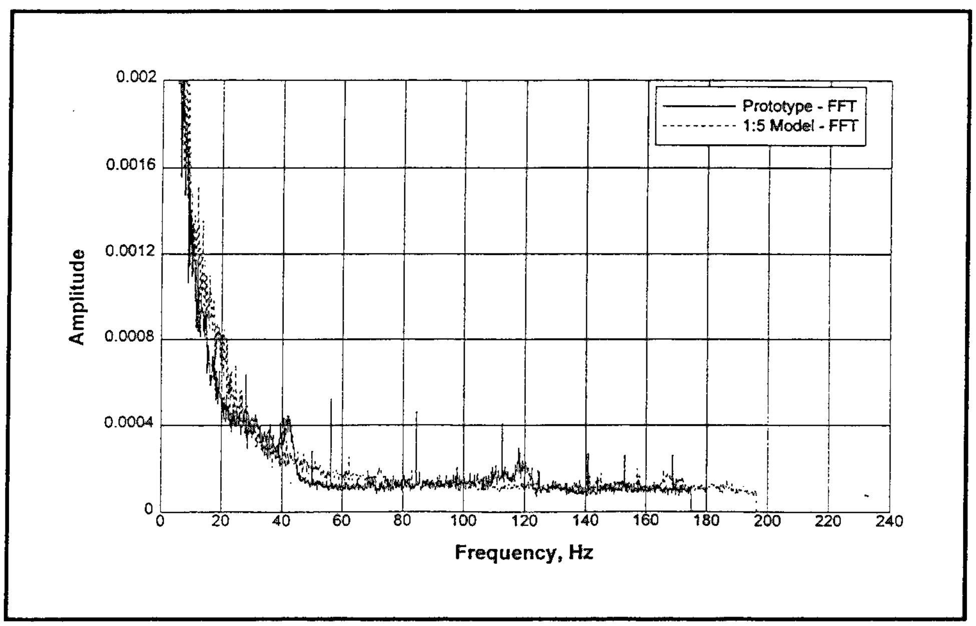

Figure B62. Downstream bottom left pressure FFT for 2-GG (EL) condition

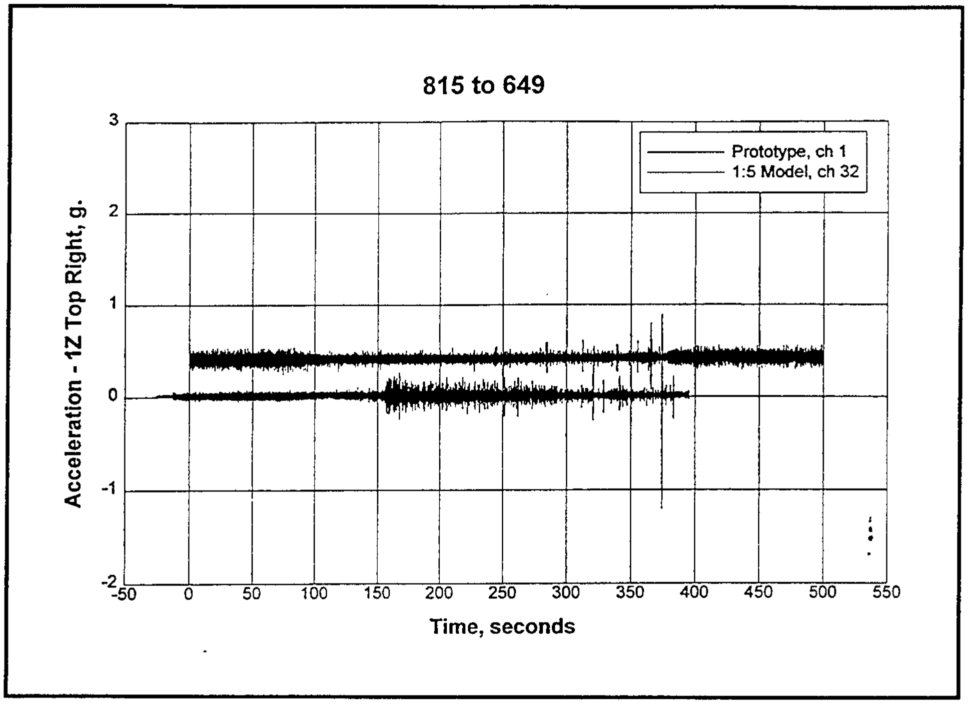

Figure B63. 1Z top right acceleration vs time for 2-GG (EL) condition

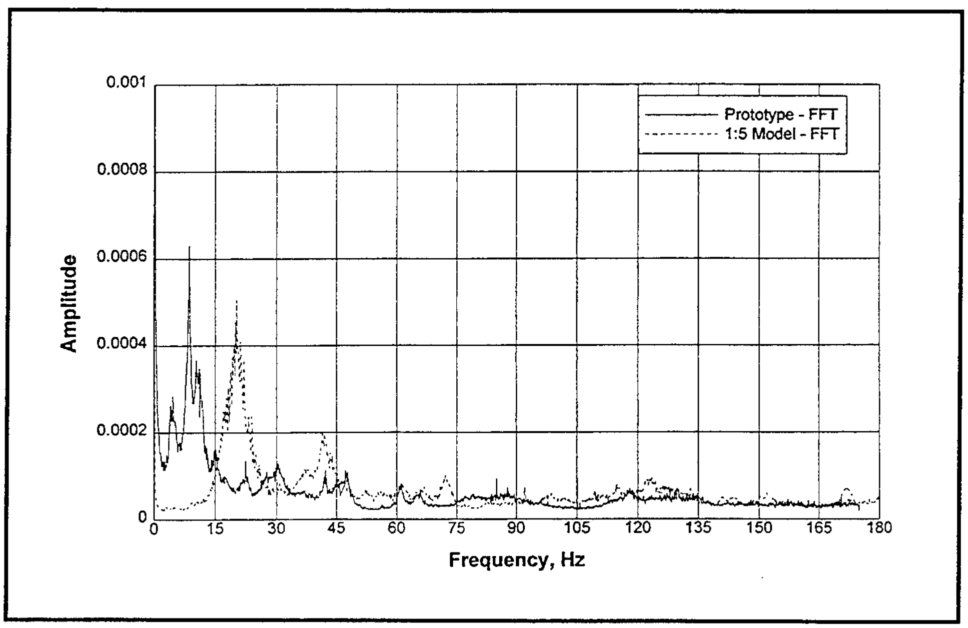

Figure B64. 1Z top right acceleration FFT for 2-GG (EL) condition

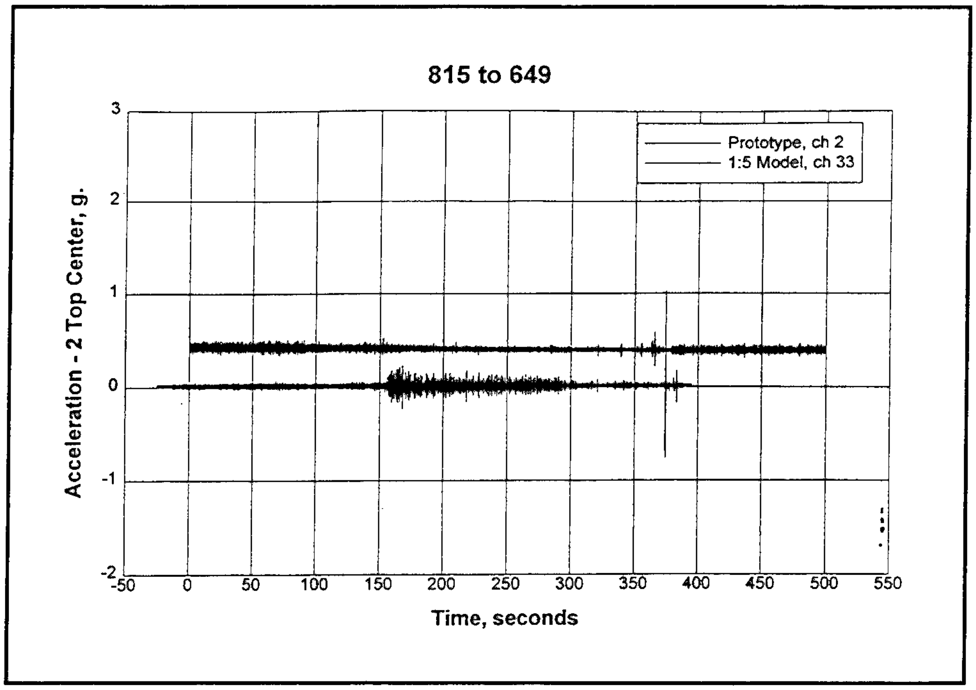

Figure B65. 2 top center acceleration vs time for 2-GG (EL) condition

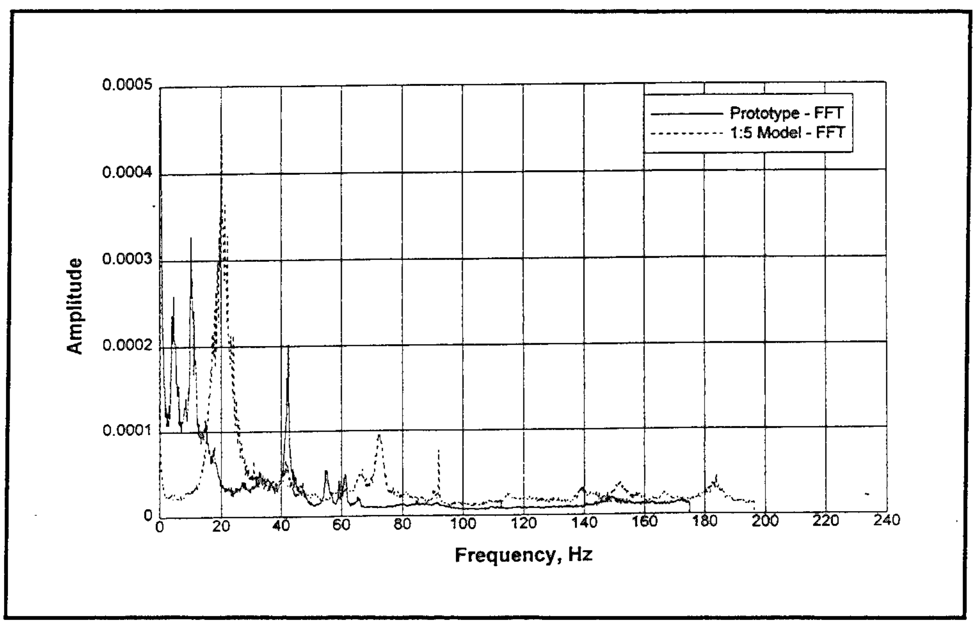

Figure B66. 2 top center acceleration FFT for 2-GG (EL) condition

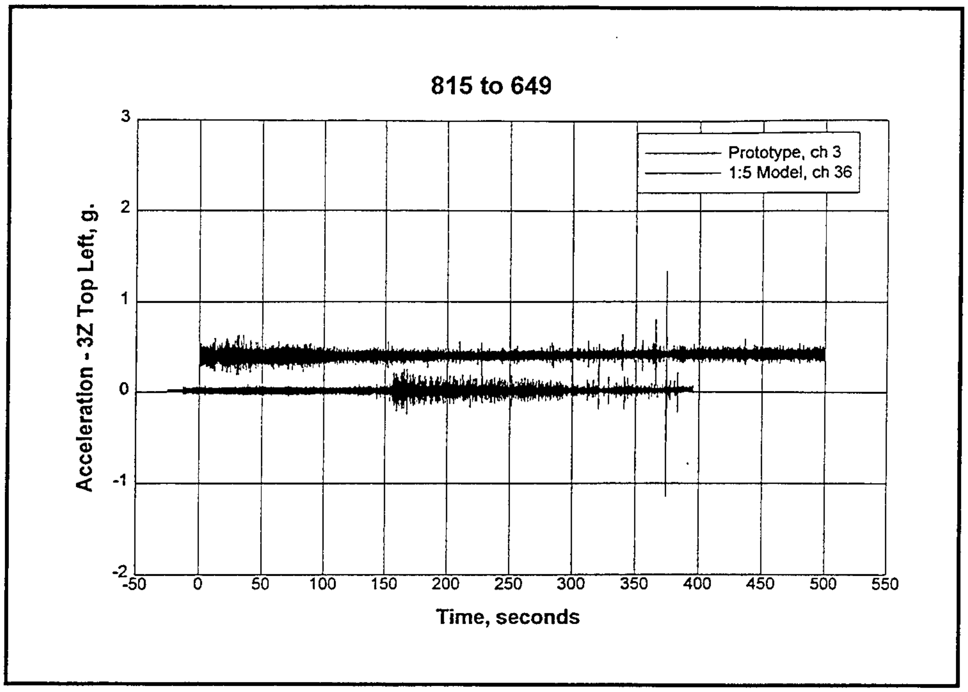

Figure B67. 3Z top left acceleration vs time for 2-GG (EL) condition

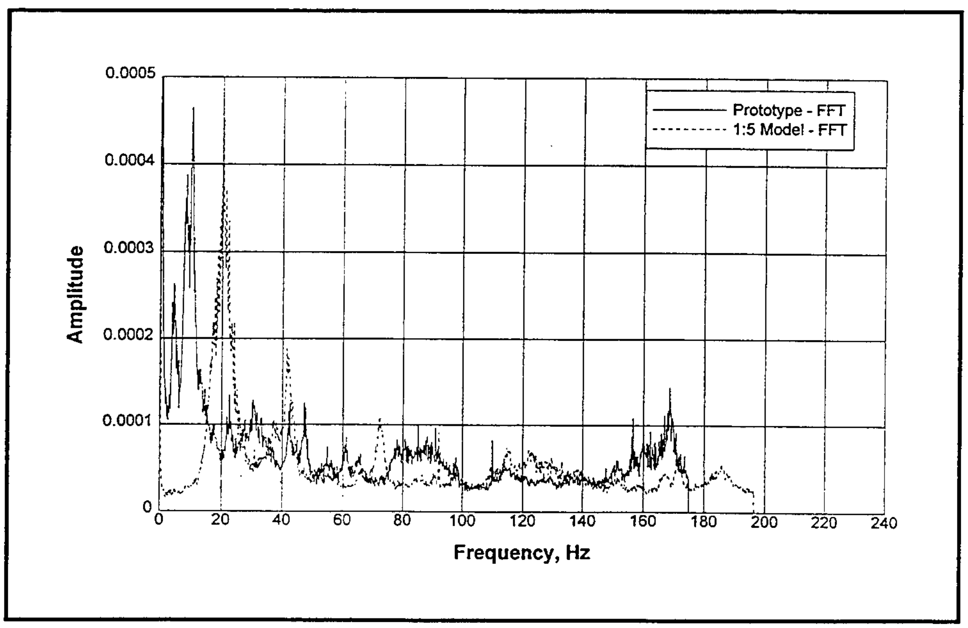

Figure B68. 3Z top left acceleration FFT for 2-GG (EL) condition

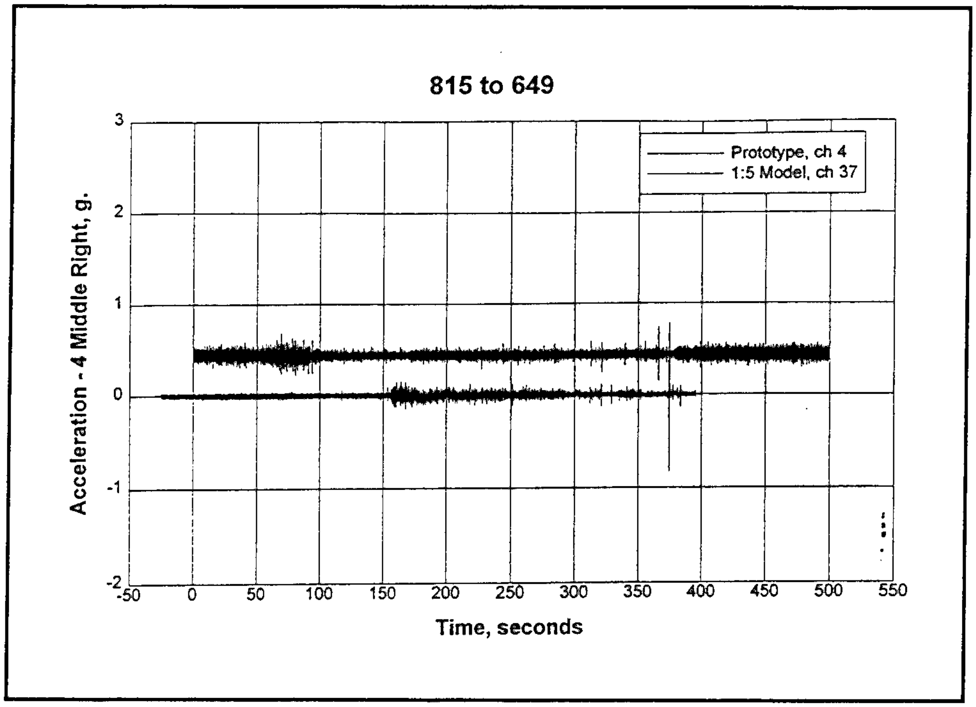

Figure B69. 4 middle right acceleration vs time for 2-GG (EL) condition

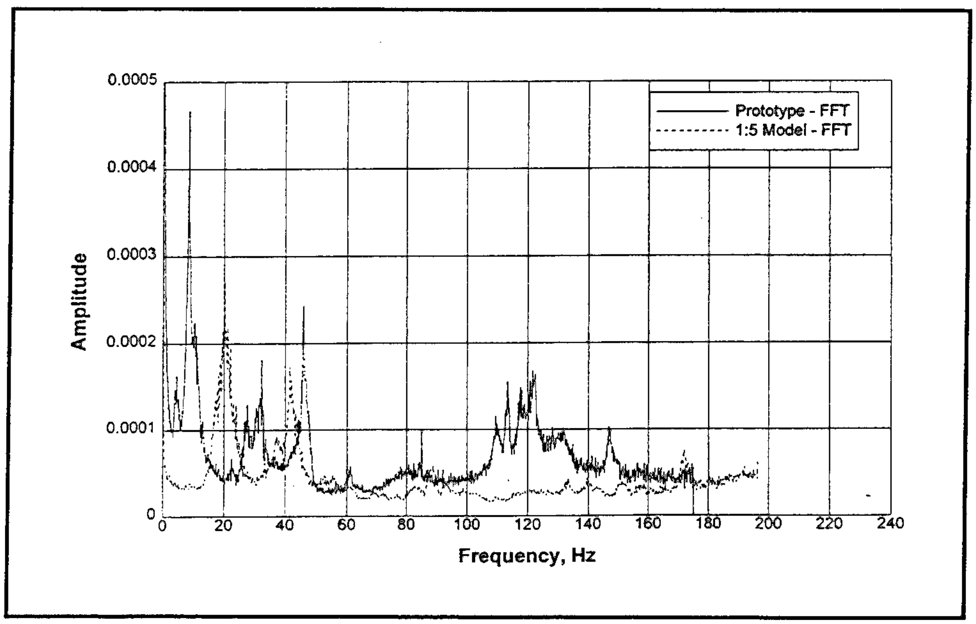

Figure B70. 4 middle right acceleration FFT for 2-GG (EL) condition

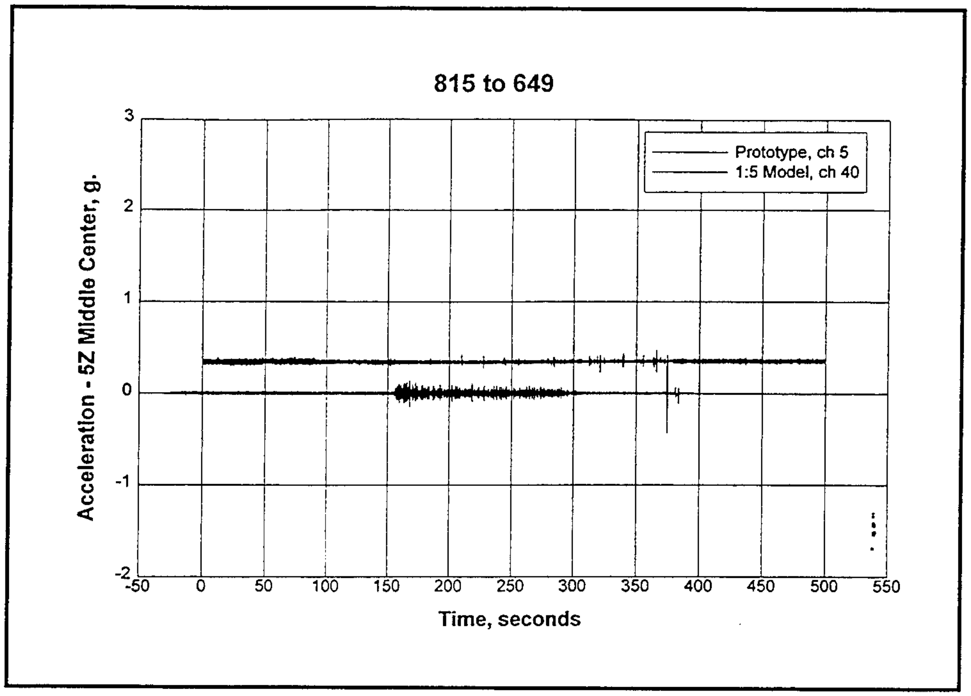

Figure B71. 5Z middle center acceleration vs time for 2-GG (EL) condition

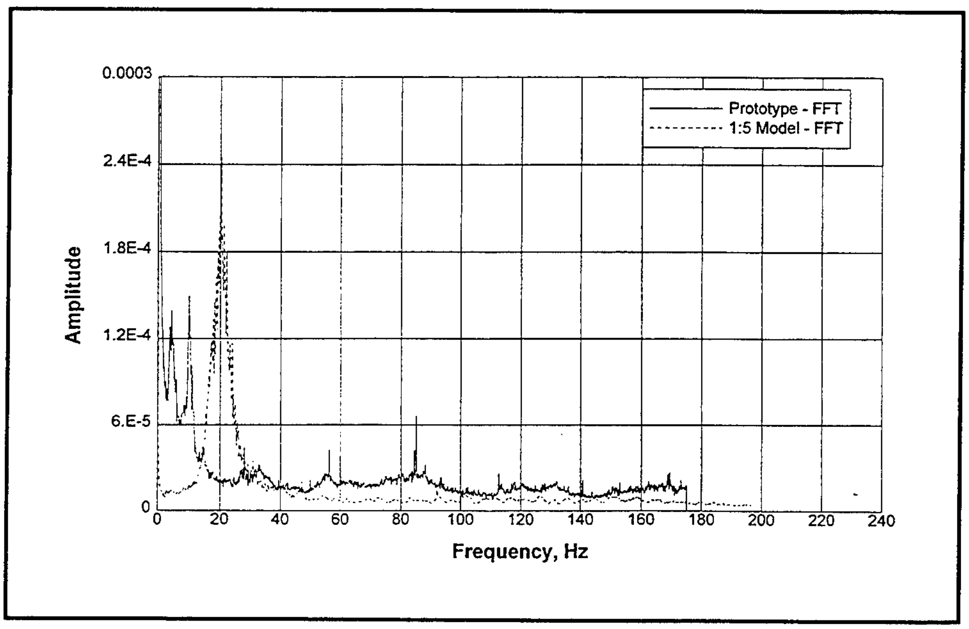

Figure B72. 5Z middle center acceleration FFT for 2-GG (EL) condition

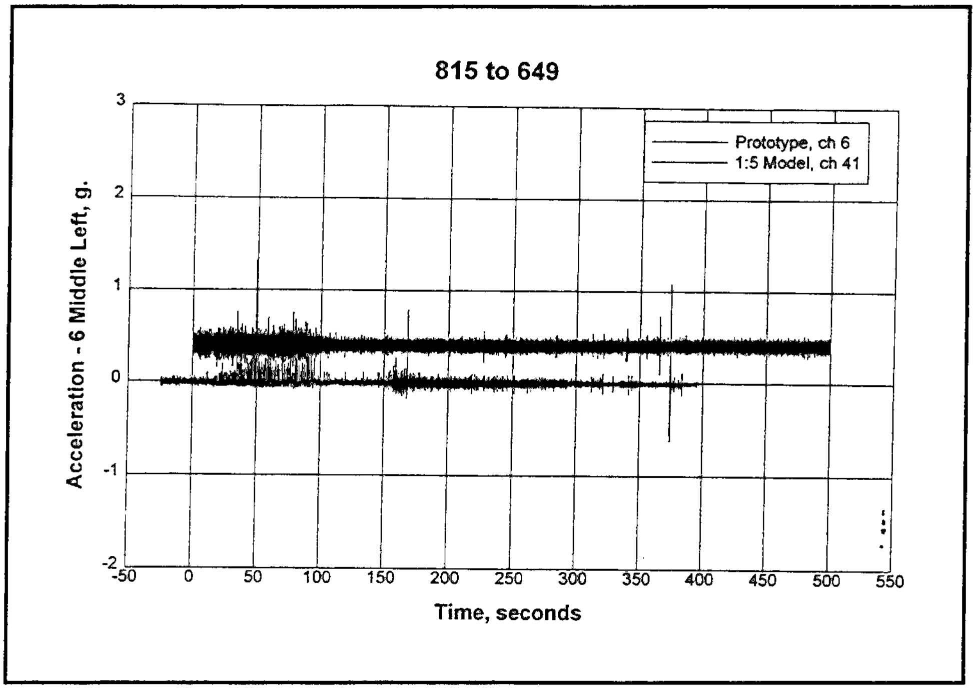

Figure B73. 6 middle left acceleration vs time for 2-GG (EL) condition

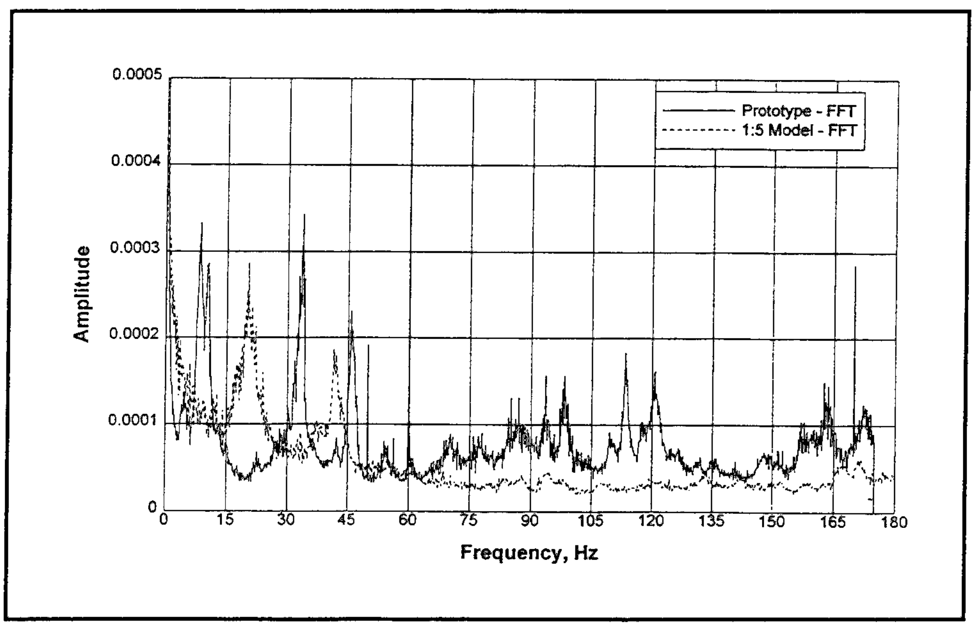

Figure B74. 6 middle left acceleration FFT for 2-GG (EL) condition

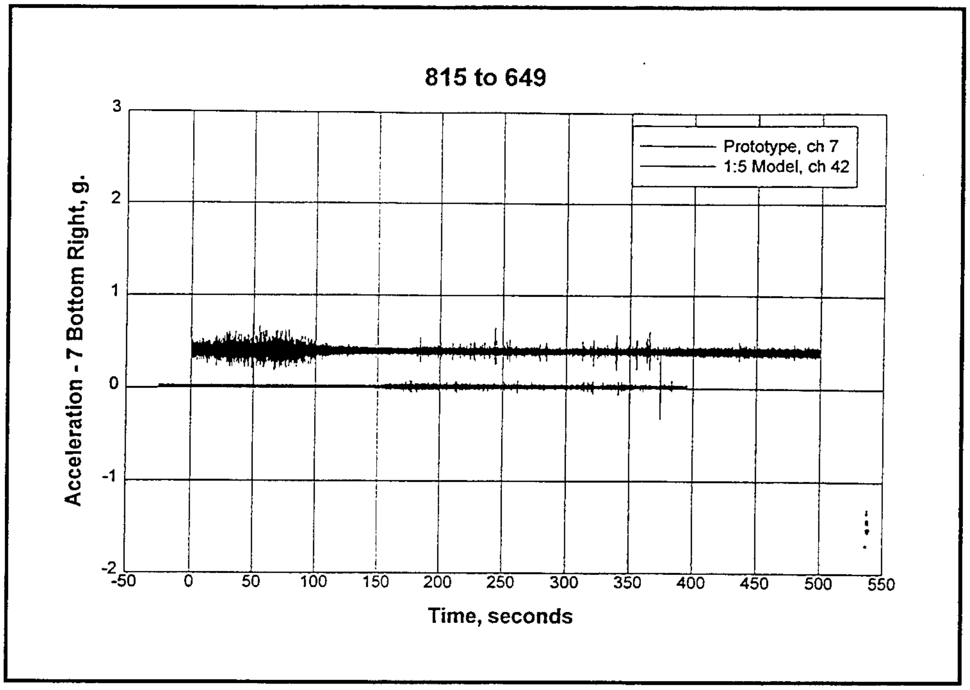

Figure B75. 7 bottom right acceleration FFT for 2-GG (EL) condition

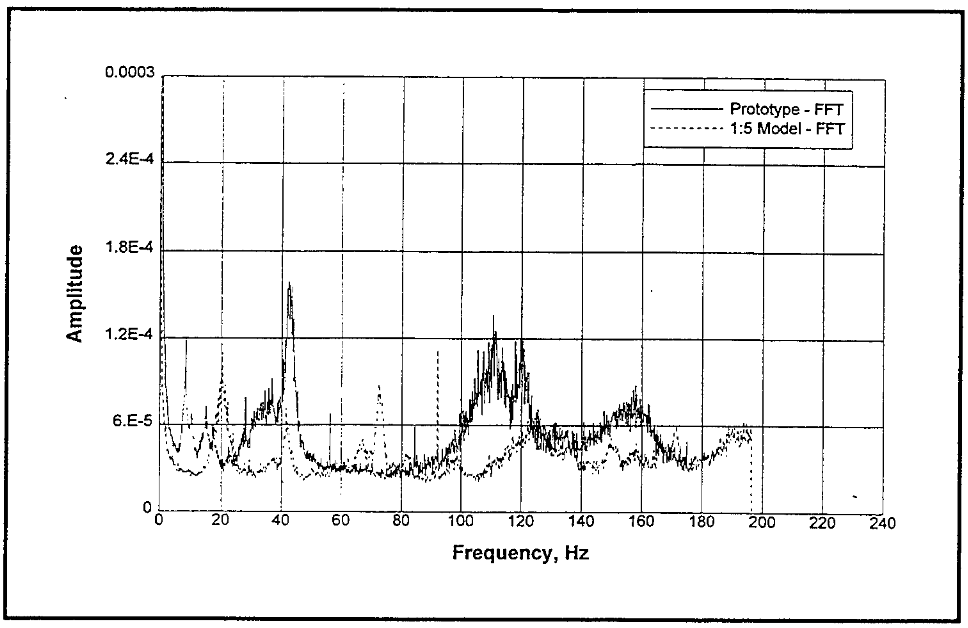

Figure B76. 7 bottom right acceleration FFT for 2-GG (EL) condition

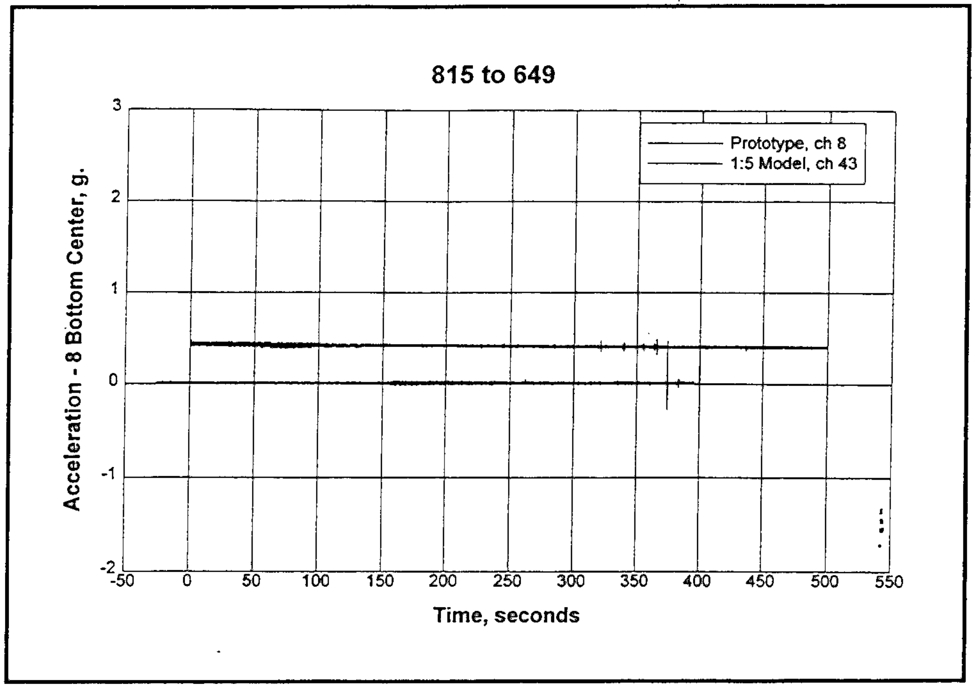

Figure B77. 8 bottom center acceleration vs time for 2-GG (EL) condition

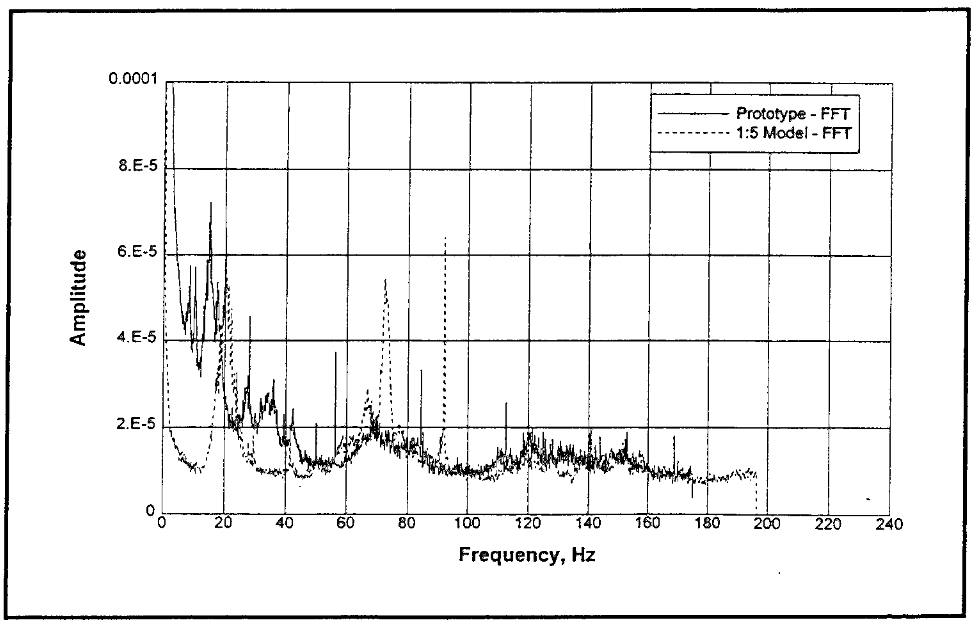

Figure B78. 8 bottom center acceleration FFT for 2-GG (EL) condition

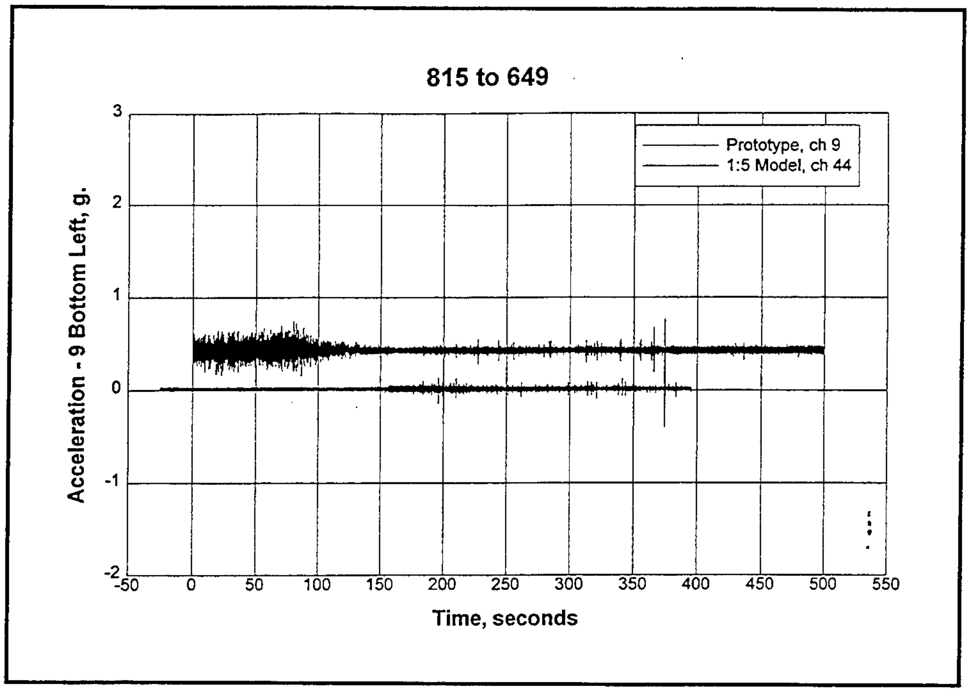

Figure B79. 9 bottom left acceleration vs time for 2-GG (EL) condition

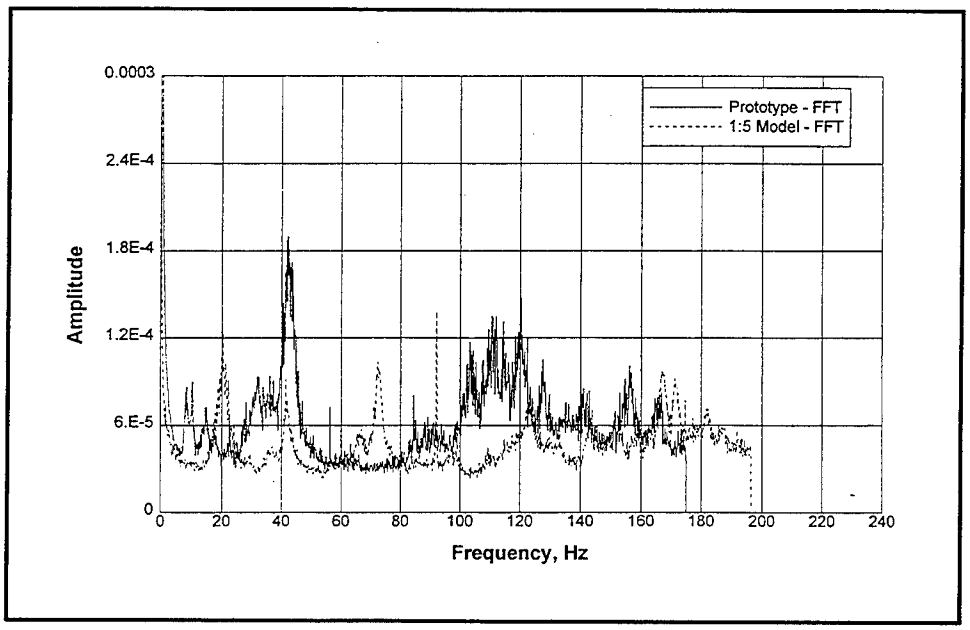

Figure B80. 9 bottom left acceleration FFT for 2-GG (EL) condition

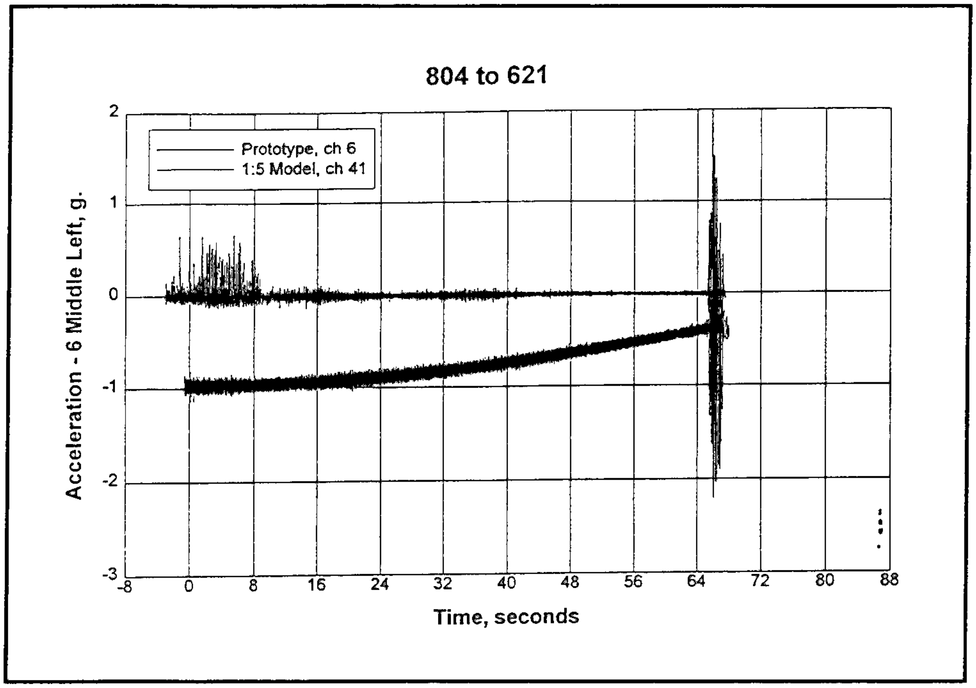

Figure B81. Effects of strain-gauge accelerometer 6 on the prototype response (drifted) for 1-GG up condition

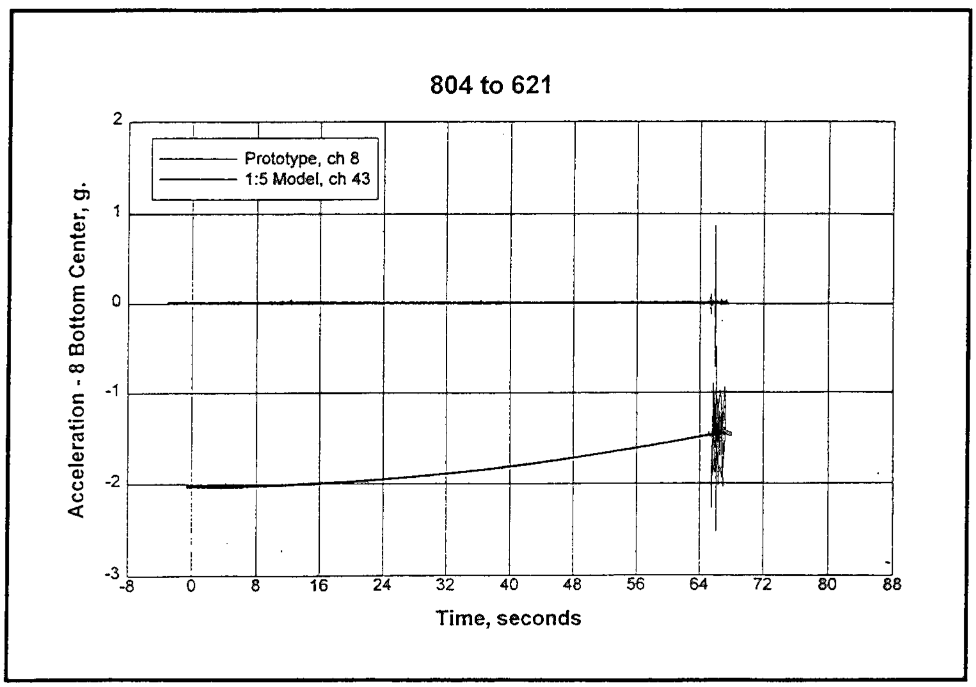

Figure B82. Effects of strain-gauge accelerometer 8 on the prototype response (drifted) for 1-GG up condition

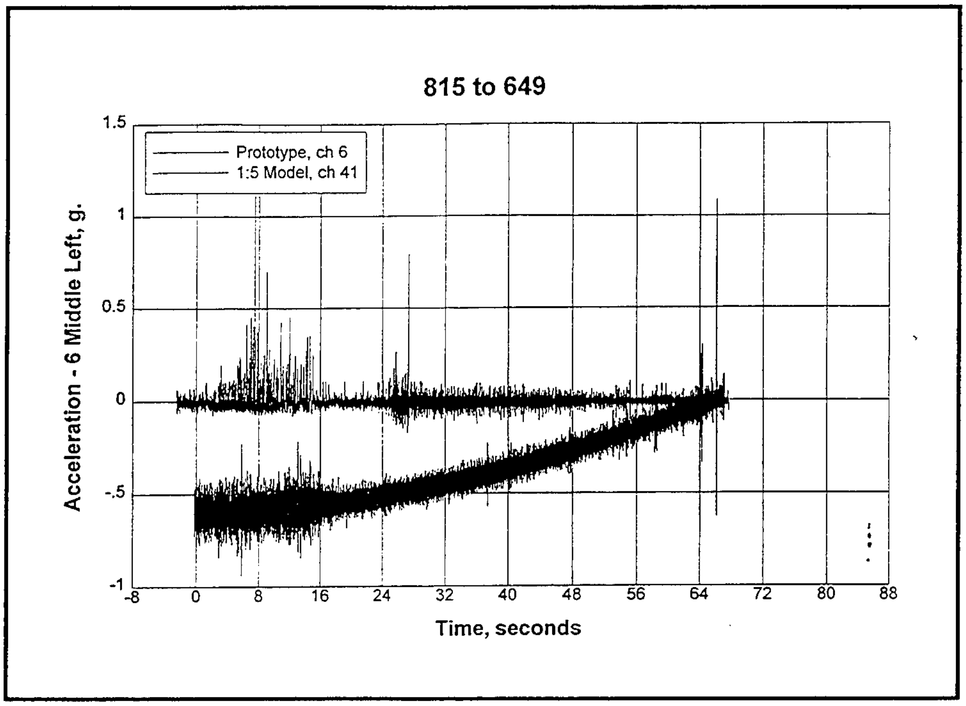

Figure B83. Effects on strain-gauge accelerometer 6 on the prototype response (drifted) for 2-GG (EL) up condition

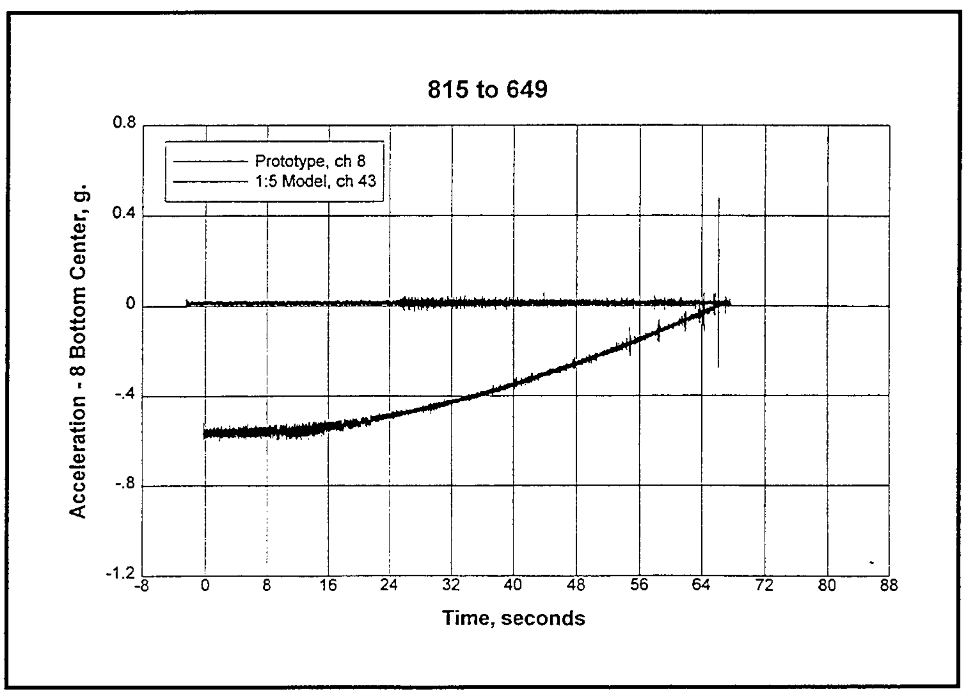

Figure B84. Effects of strain-gauge accelerometer 8 on the prototype response (drifted) for 2-GG (EL) up condition

Appendix C Time-Domain Reaction and Pressure Plots— Prototype Steel vs 1:5 Model

Selected time-domain reaction and pressure responses of prototype steel and 1:5-scale model wickets, for all test configurations (test groups 1 to 7 in Table 5, main text) considered in this study, are compared in this appendix. These plots show the test numbers for which the results are presented. Sensitive axes of the shear transducer were fixed with the gate's local axes such that one axis was normal to the gate surface (vertical) and another was parallel to its longitudinal axis (horizontal). Thus, a positive horizontal force results due to the pulling of the gate away from the sill, and a positive vertical reaction resists the downward motion of the gate. A comparison of right and left reaction indicates that the reaction forces for both hinges are asymmetrically distributed and their directions are reversed as the gate is raised from the down to up position. This type of reverse loading at the bottom hinges may exhibit fatigue distress due to long-term loading. An observation of the test results indicates that the peak response is attained right at or about the moment when the downstream air bubble (vacuum) beneath the gate pops up. The same phenomenon was observed during the 1:5-scale tests which showed that a three-gate gap (lone condition) is the critical configuration irrespective of head difference in the pool condition. This critical position for the 3GG(L) case was at about 16 to 24 deg.

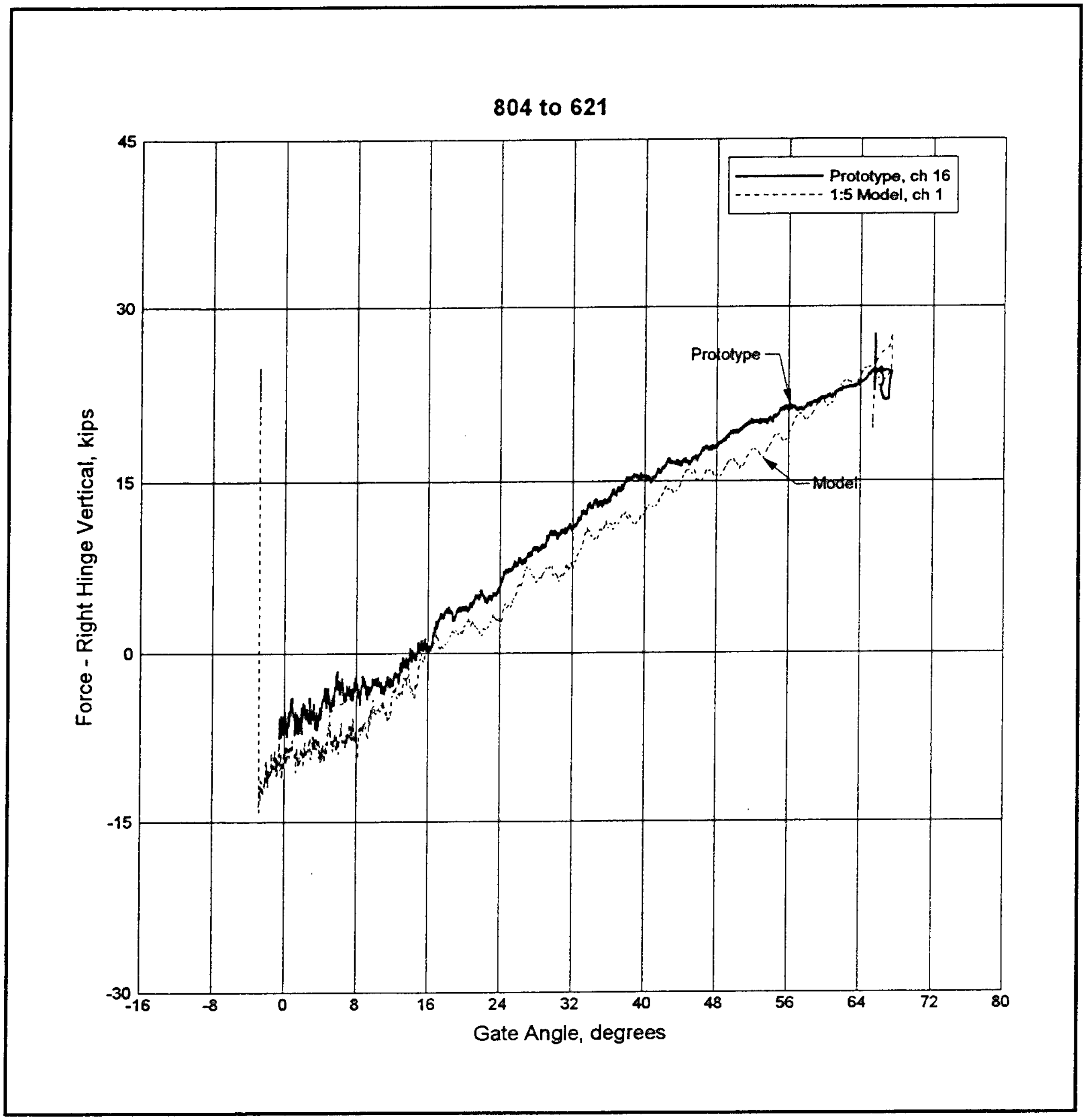

Figure C1. Right hinge vertical force vs gate position for 1GG up condition

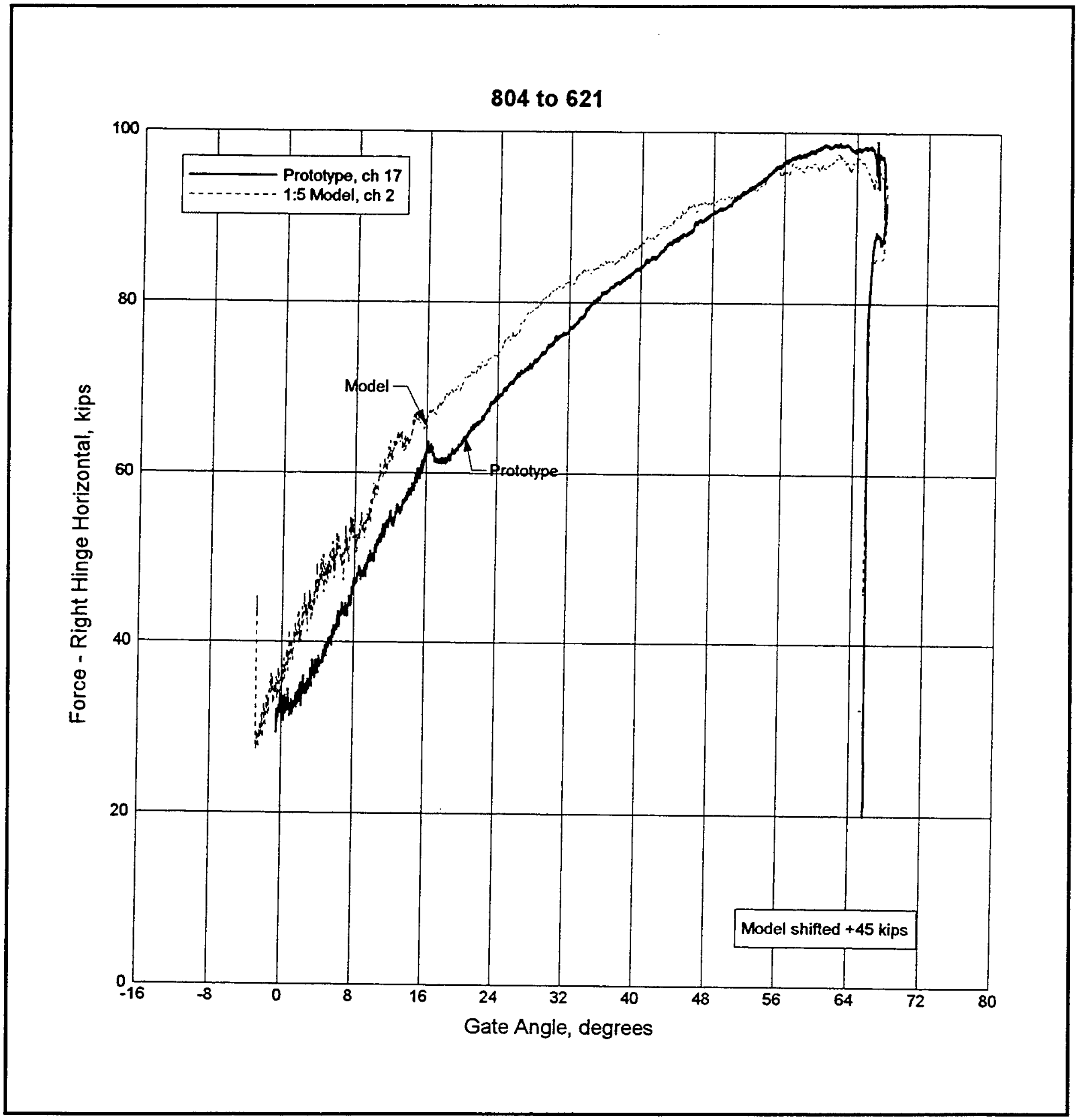

Figure C2. Right hinge horizontal force vs gate position for 1GG up condition

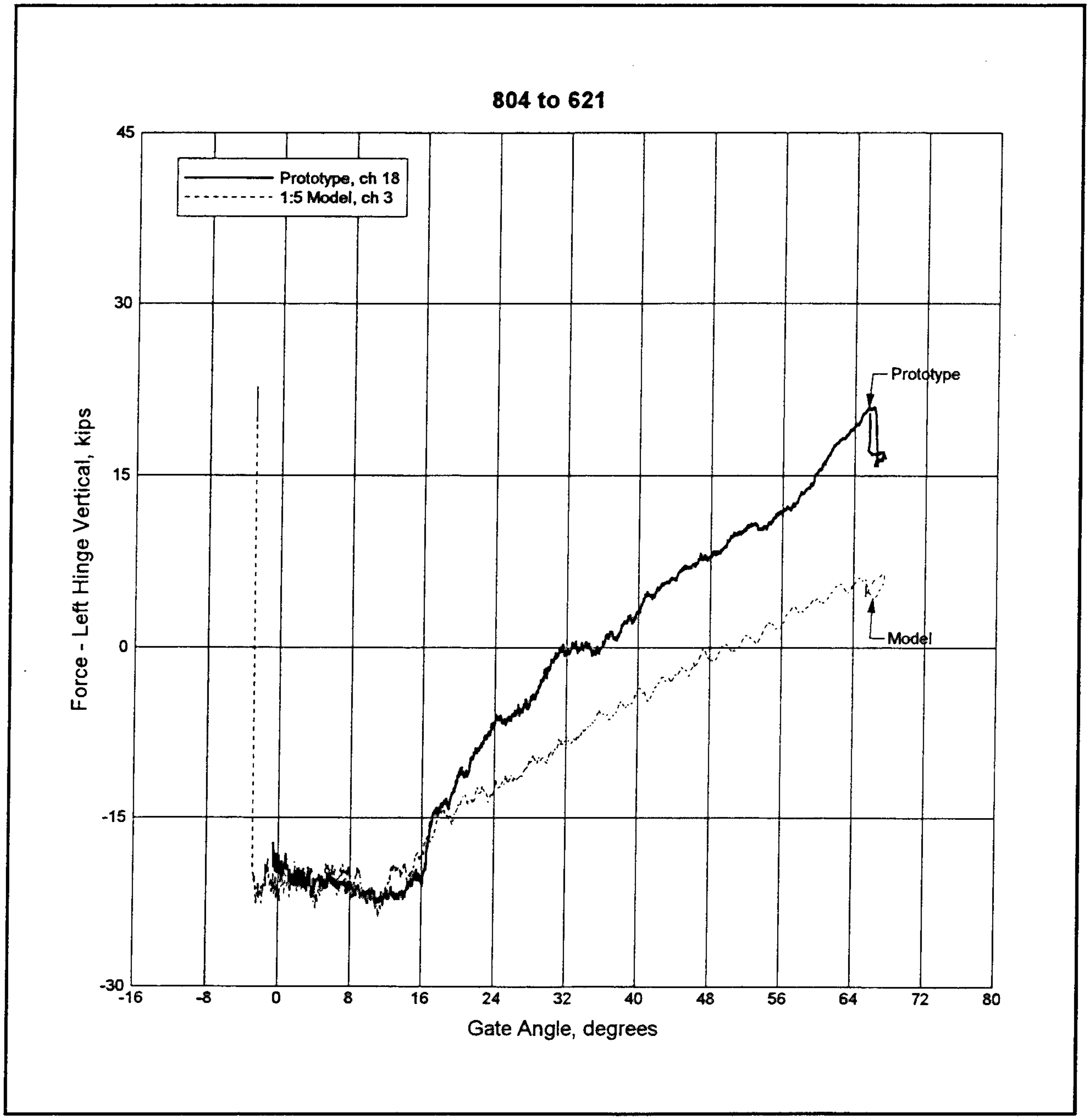

Figure C3. Left hinge vertical force vs gate position for 1-GG up condition

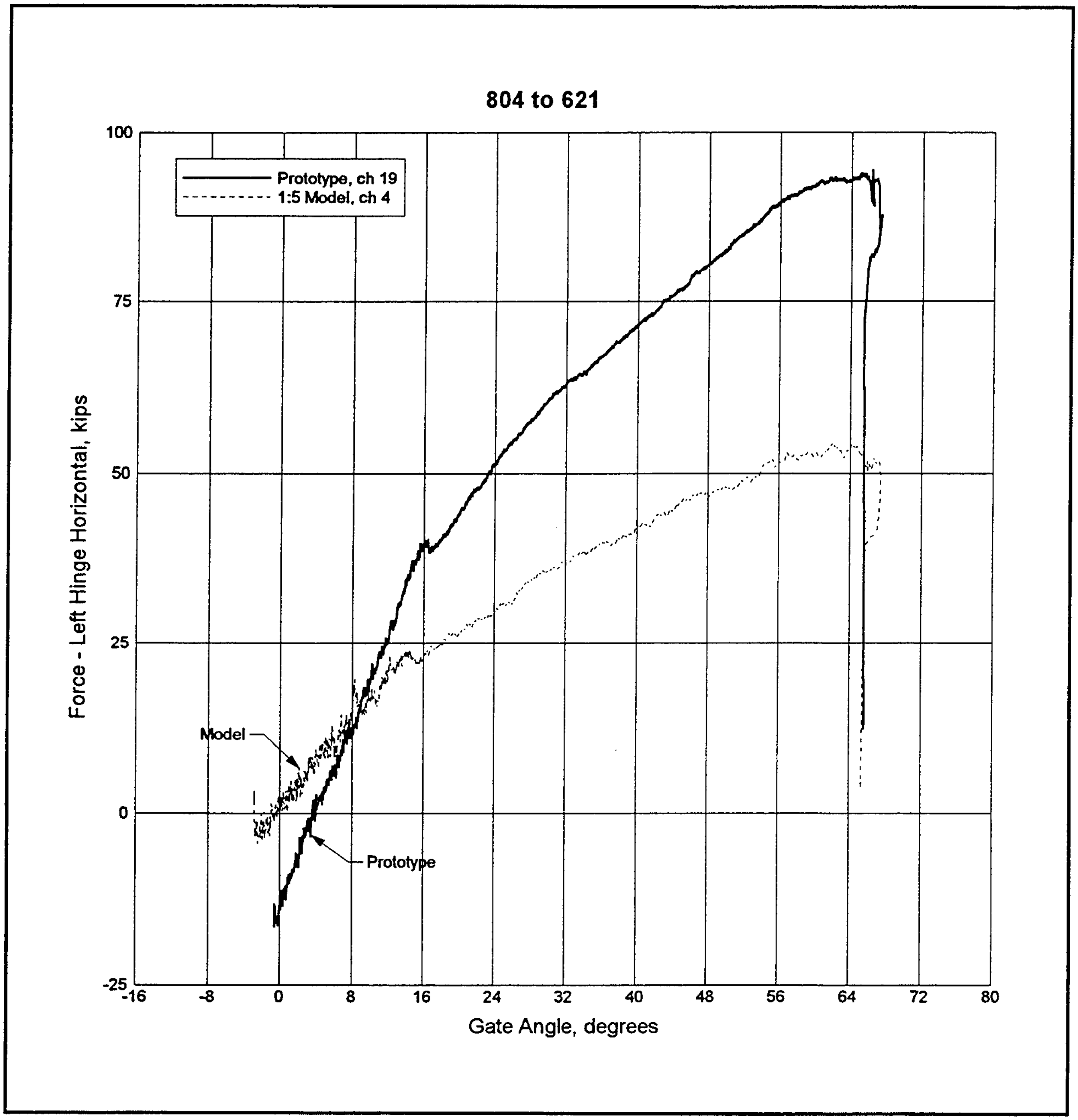

Figure C4. Left hinge horizontal force vs gate position for 1-GG up condition

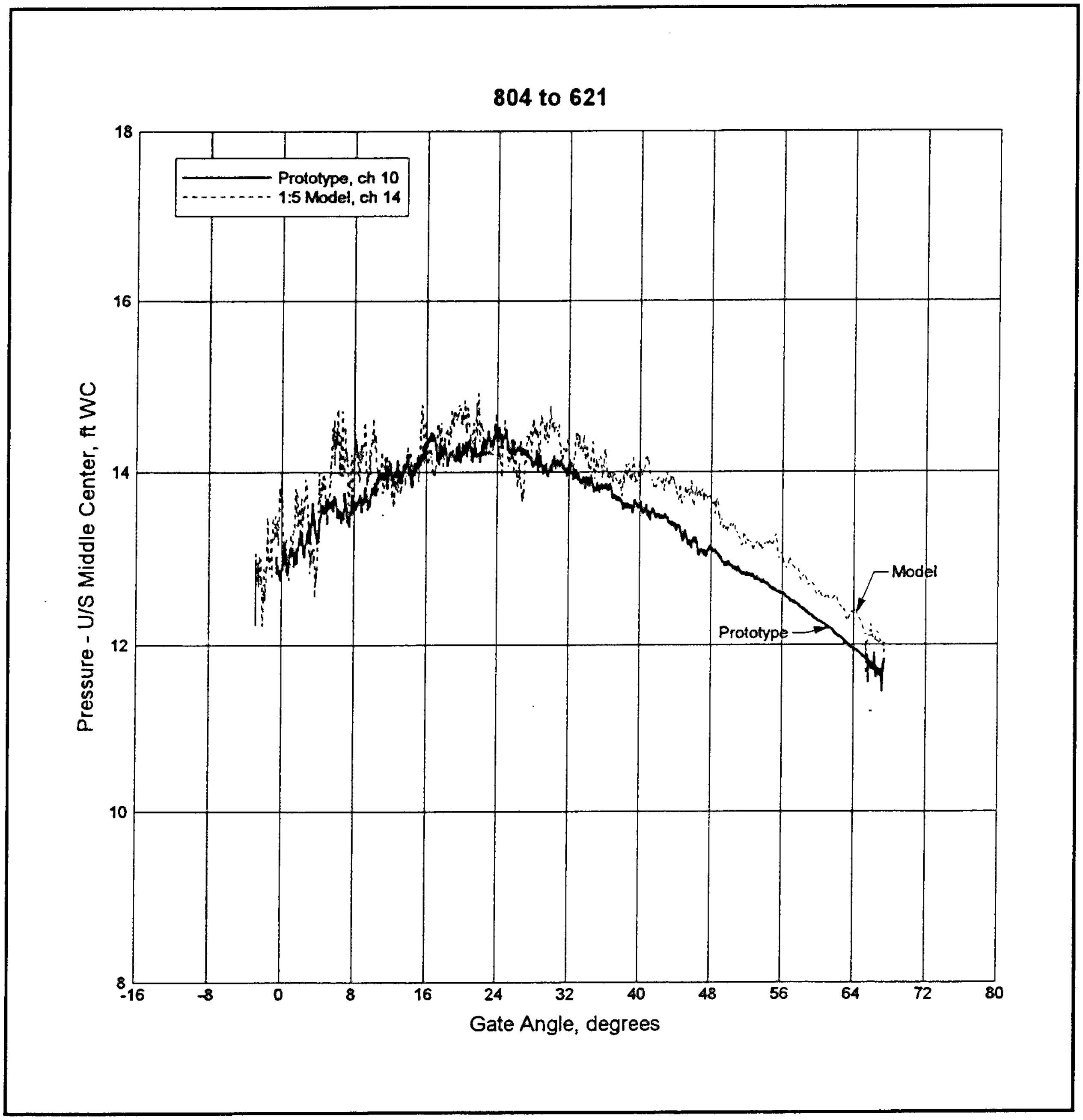

Figure C5. Upstream middle center pressure vs gate position for 1-GG up condition

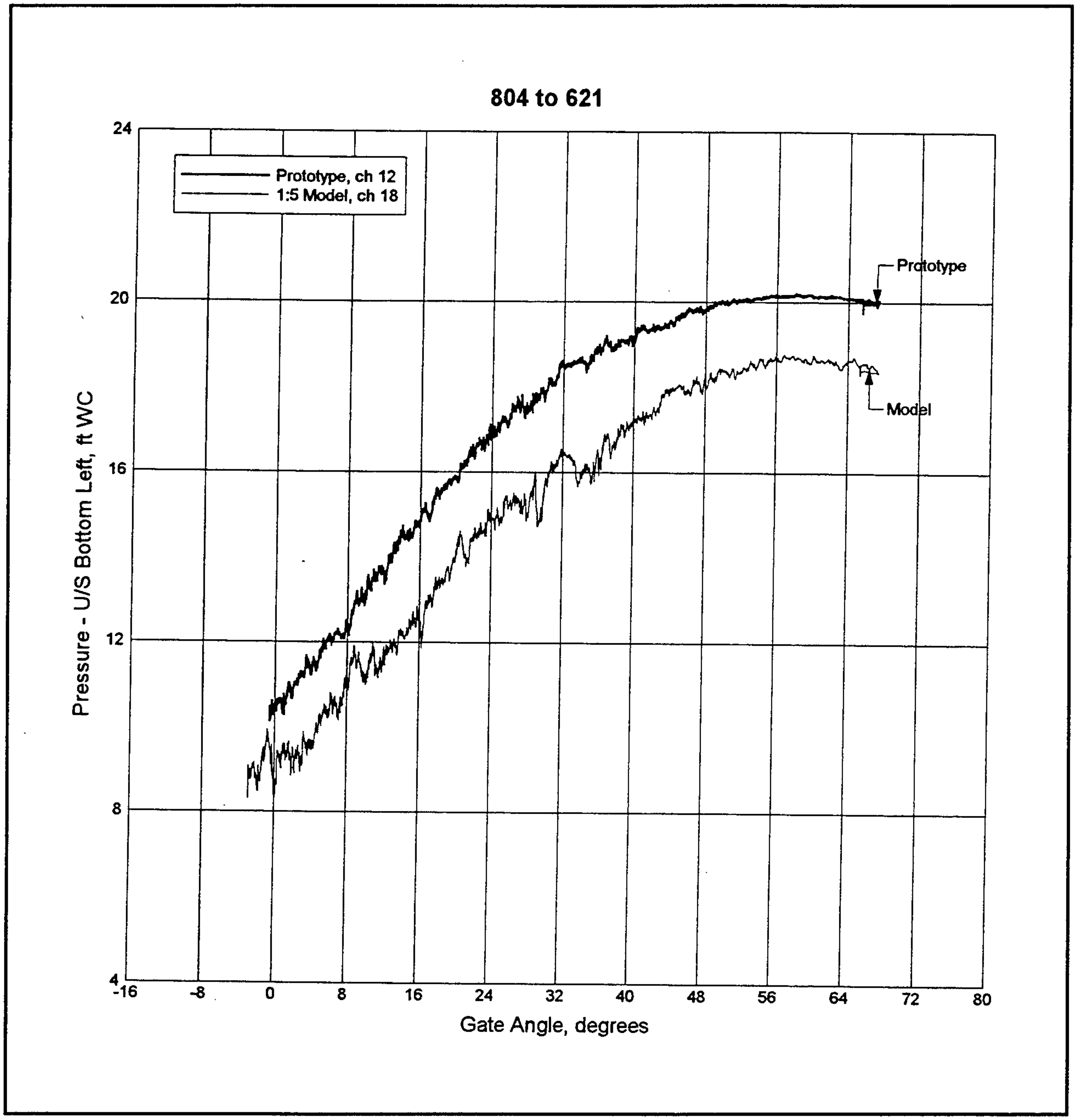

Figure C6. Upstream bottom left pressure vs gate position for 1-GG up condition

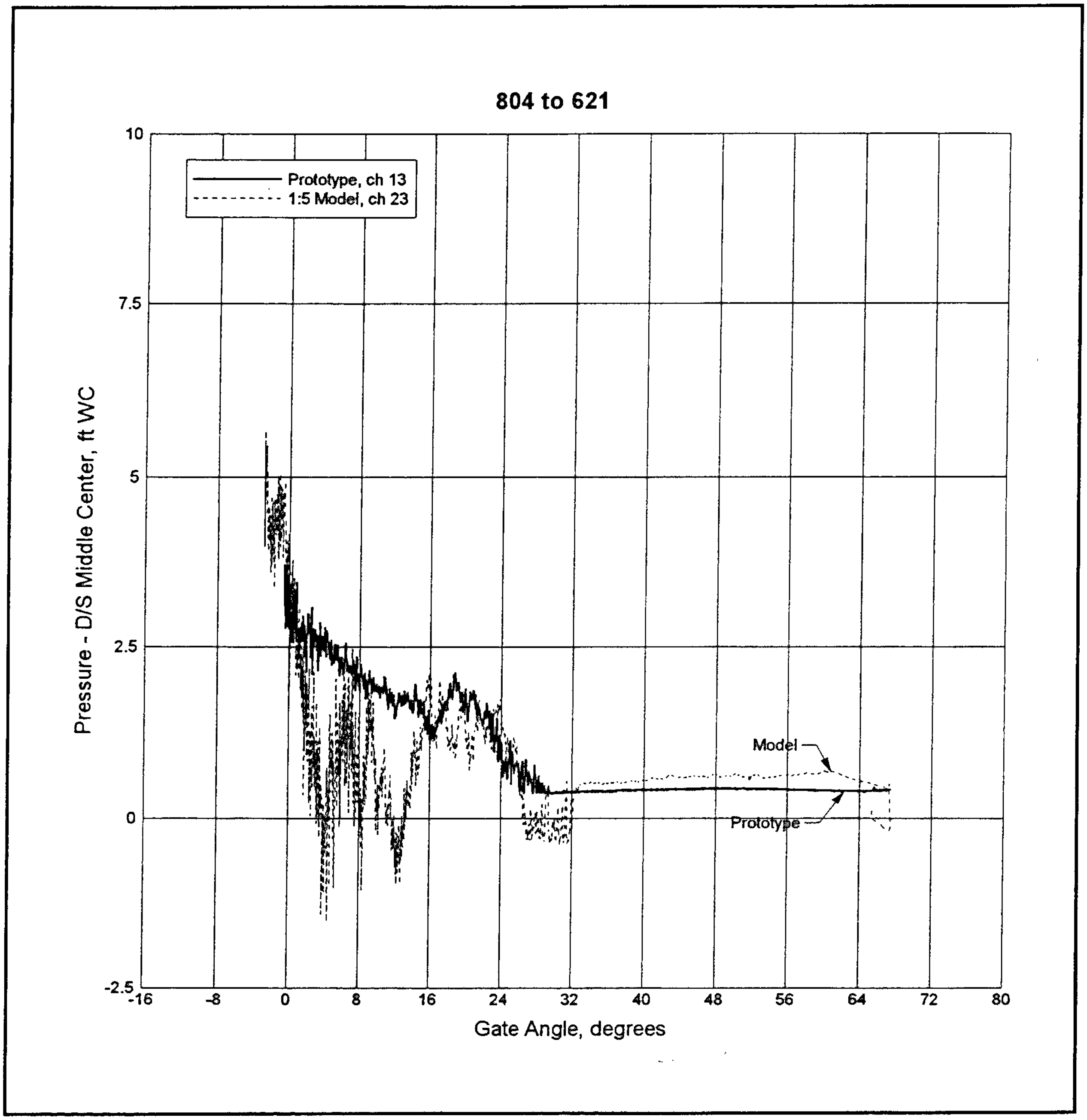

Figure C7. Downstream middle center pressure vs gate position for 1-GG up condition

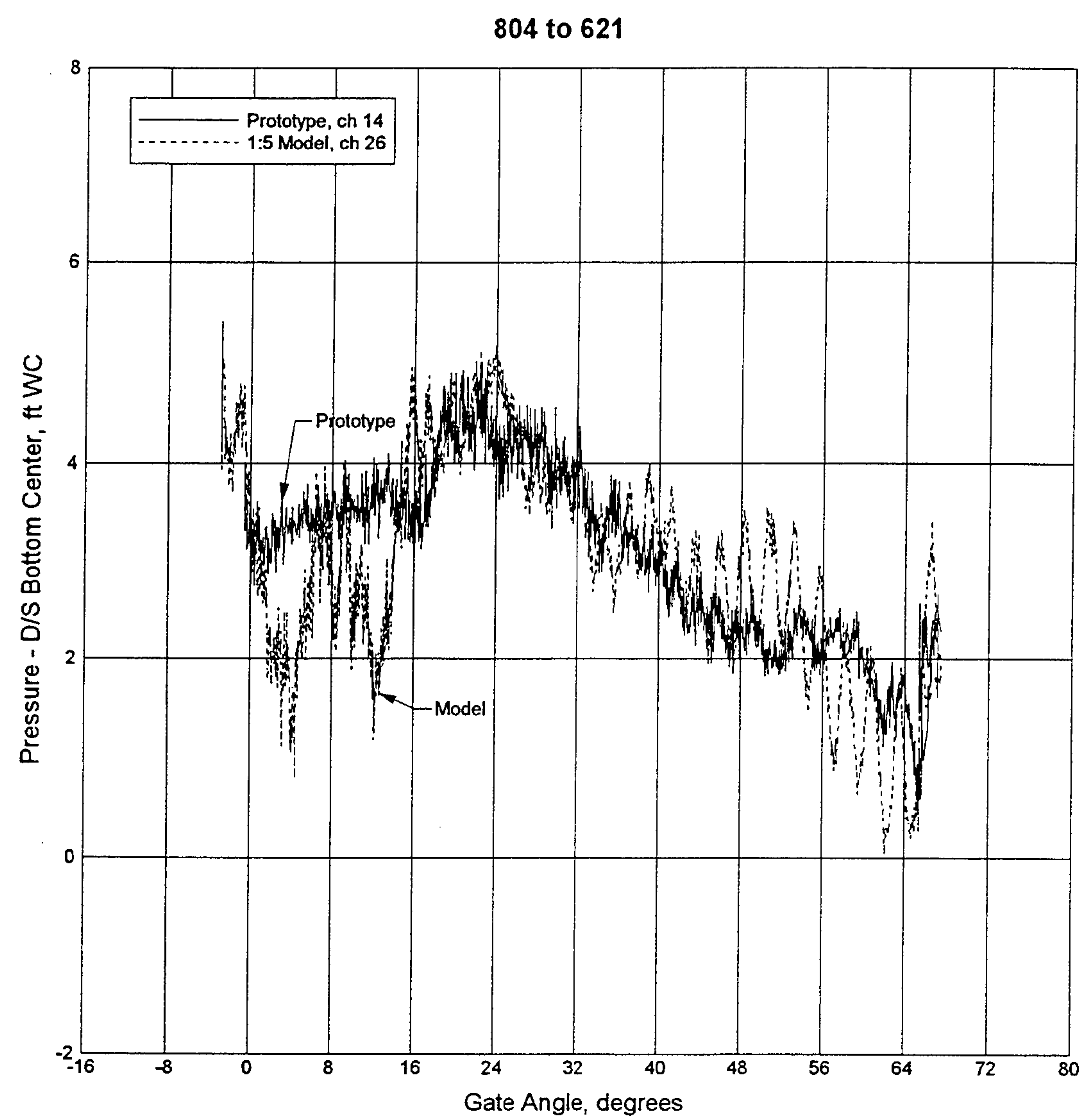

Figure C8. Downstream bottom center pressure vs gate position for 1-GG up condition

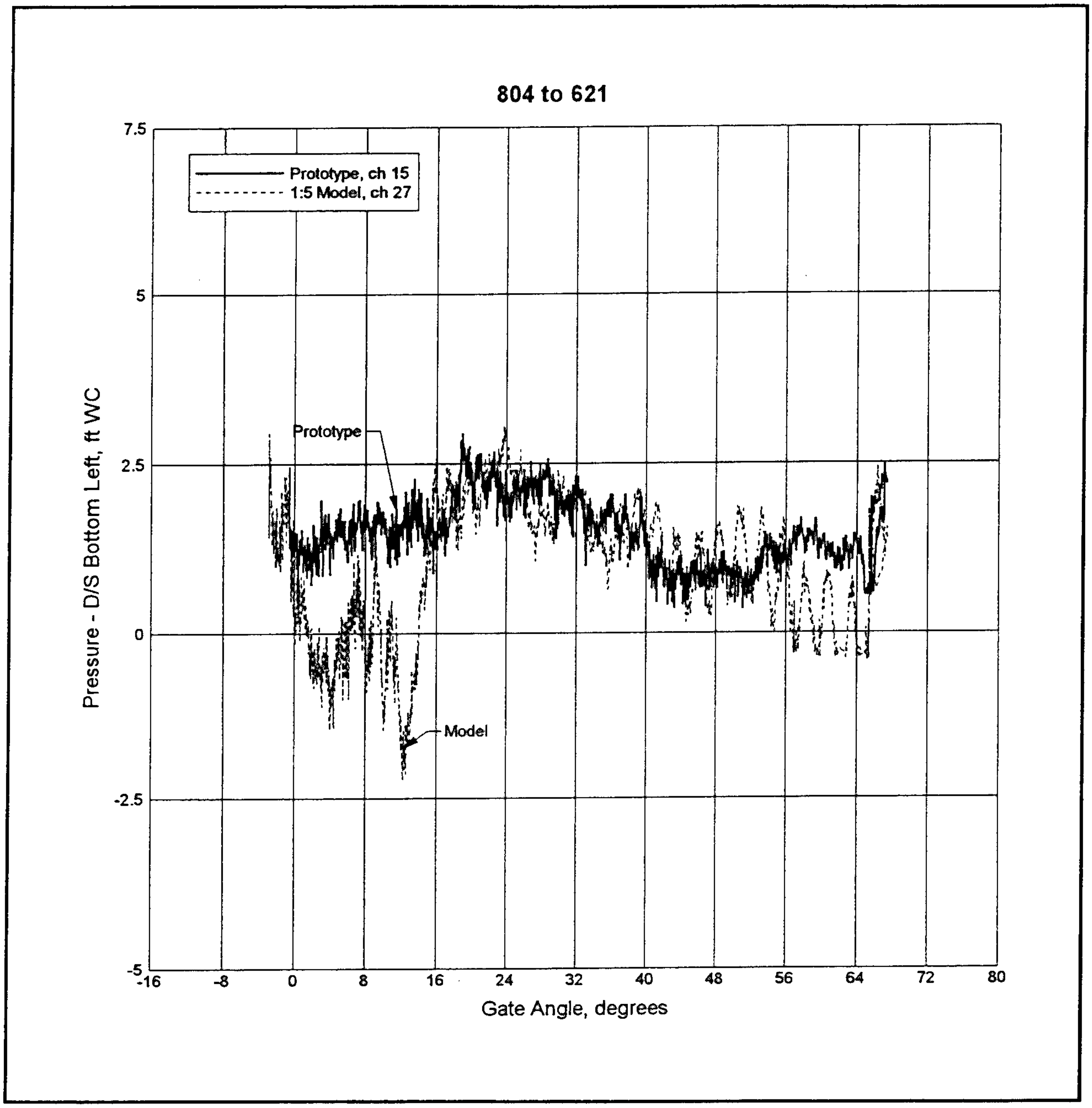

Figure C9. Downstream bottom left pressure vs gate position for 1-GG up condition

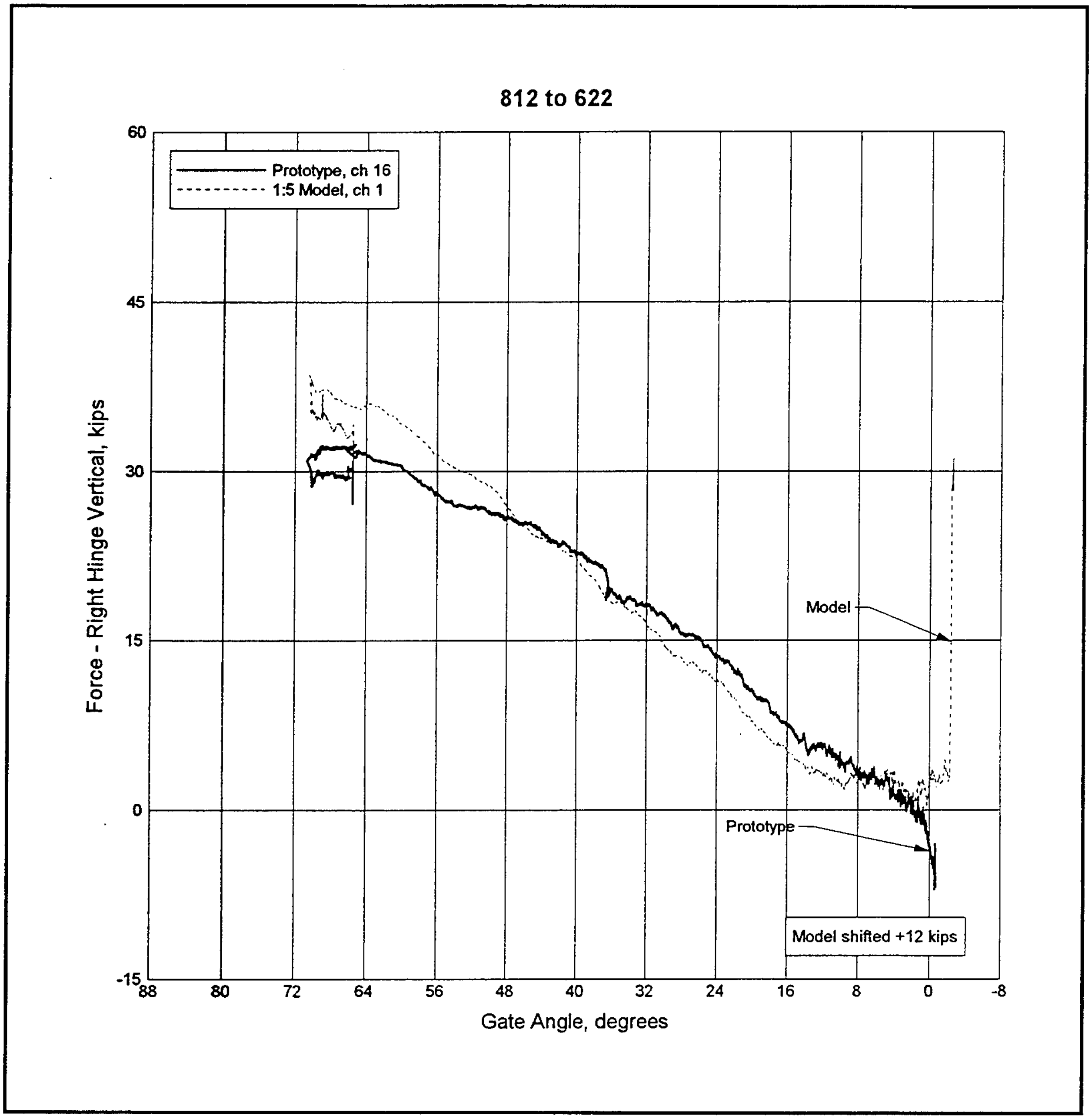

Figure C10. Right hinge vertical force vs gate position for 1-GG down condition

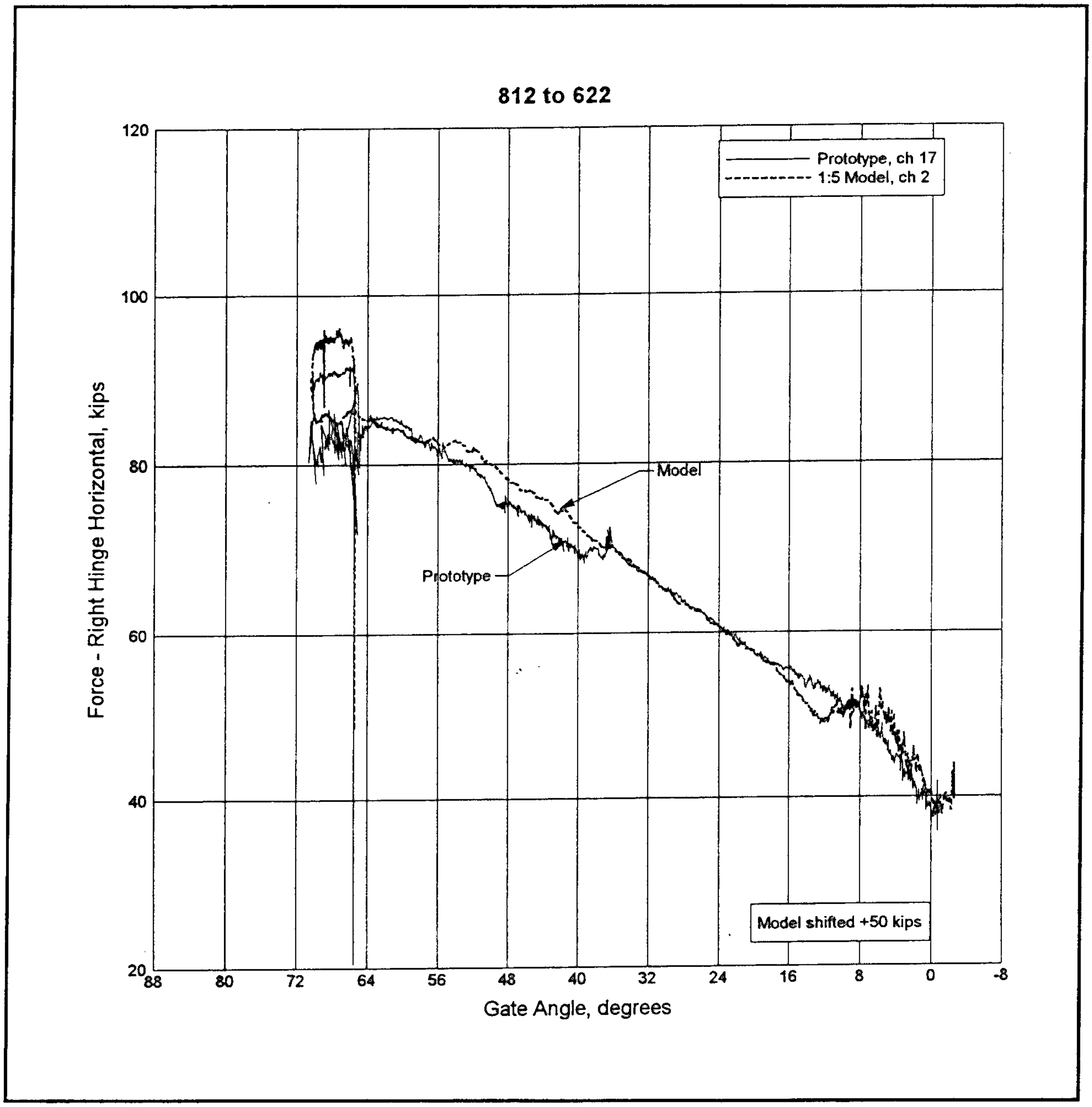

Figure C11. Right hinge horizontal force vs gate position for 1-GG down condition

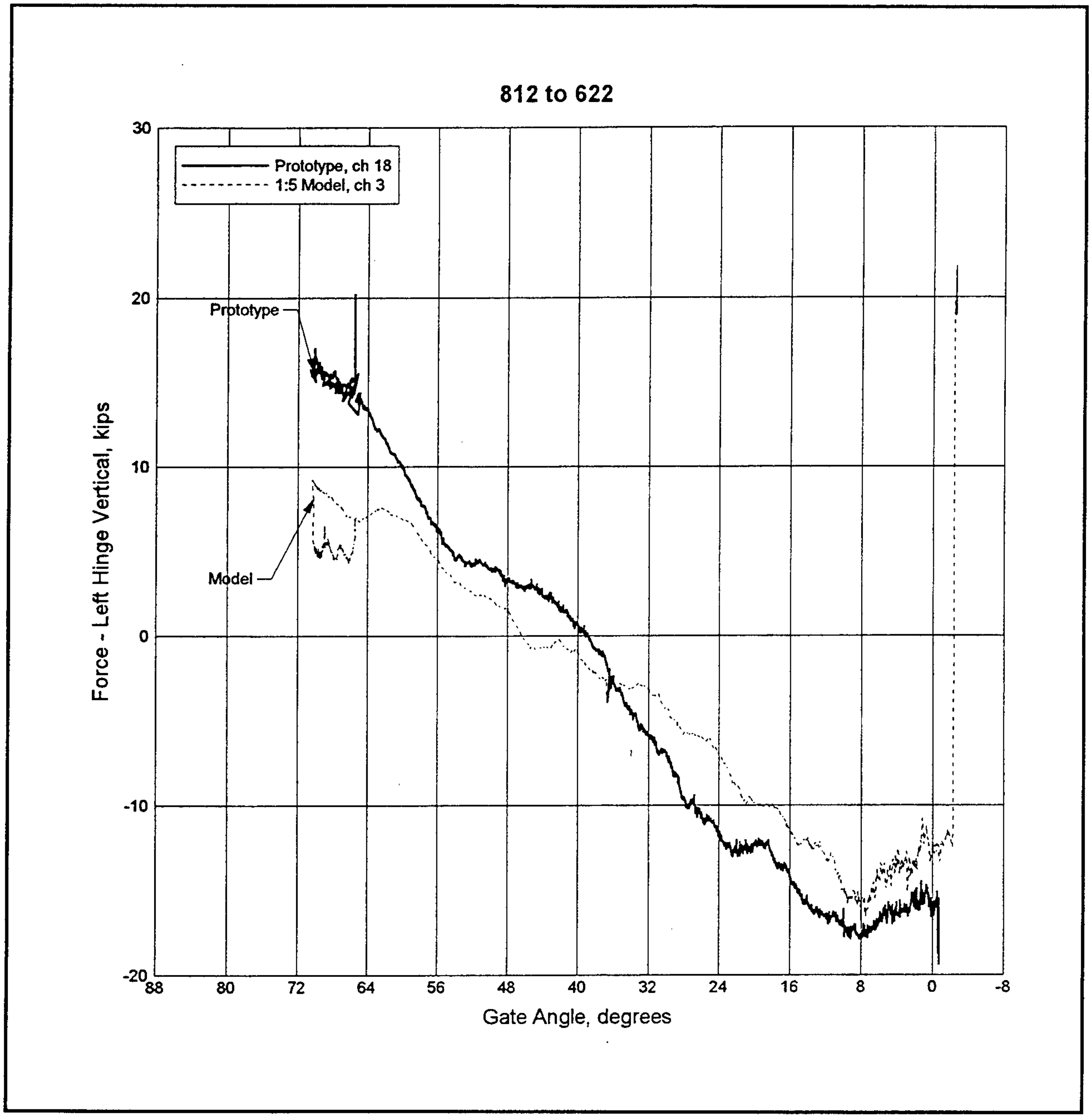

Figure C12. Left hinge vertical force vs gate position for 1-GG down condition

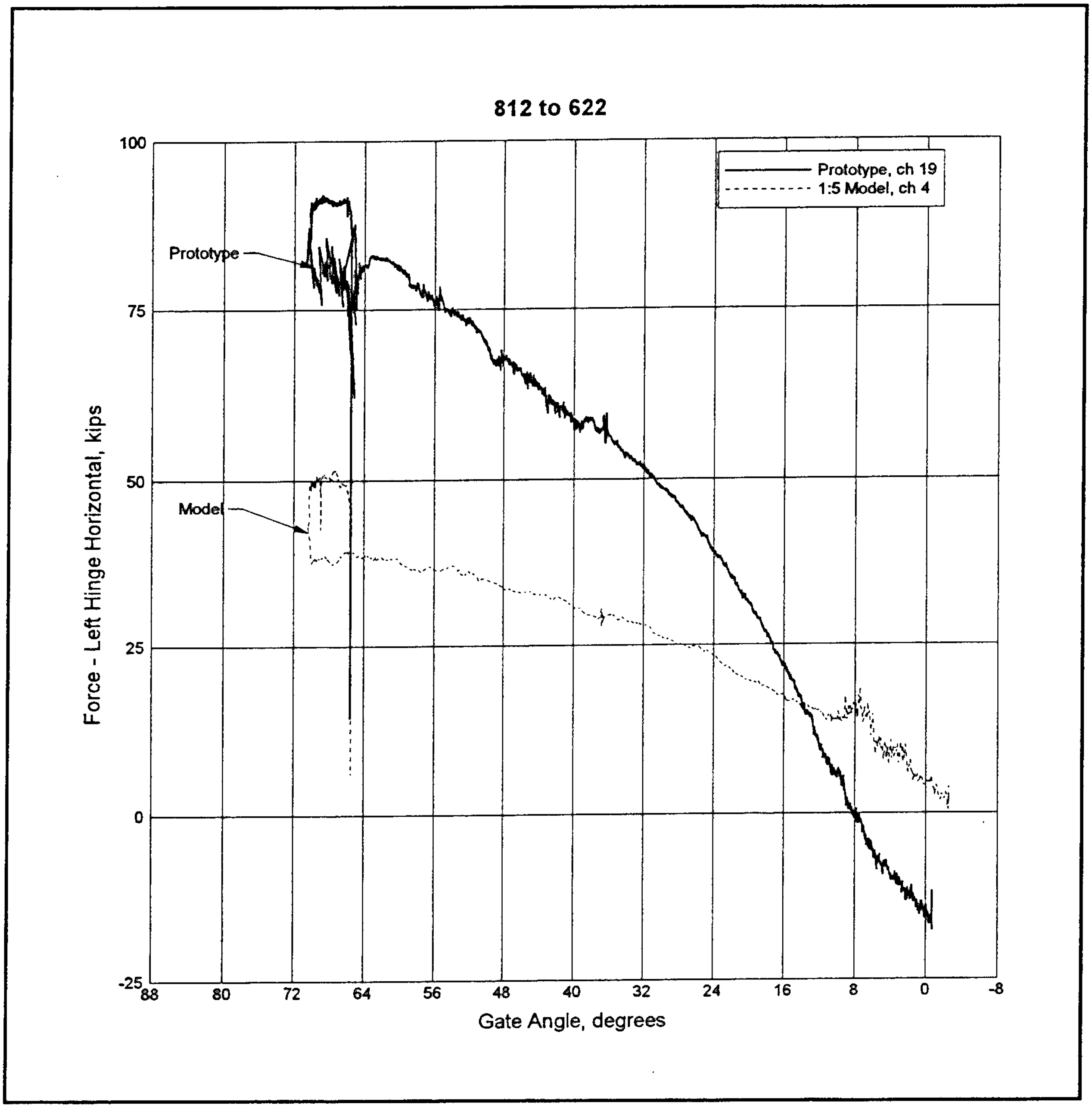

Figure C13. Left hinge horizontal force vs gate position for 1-GG down condition

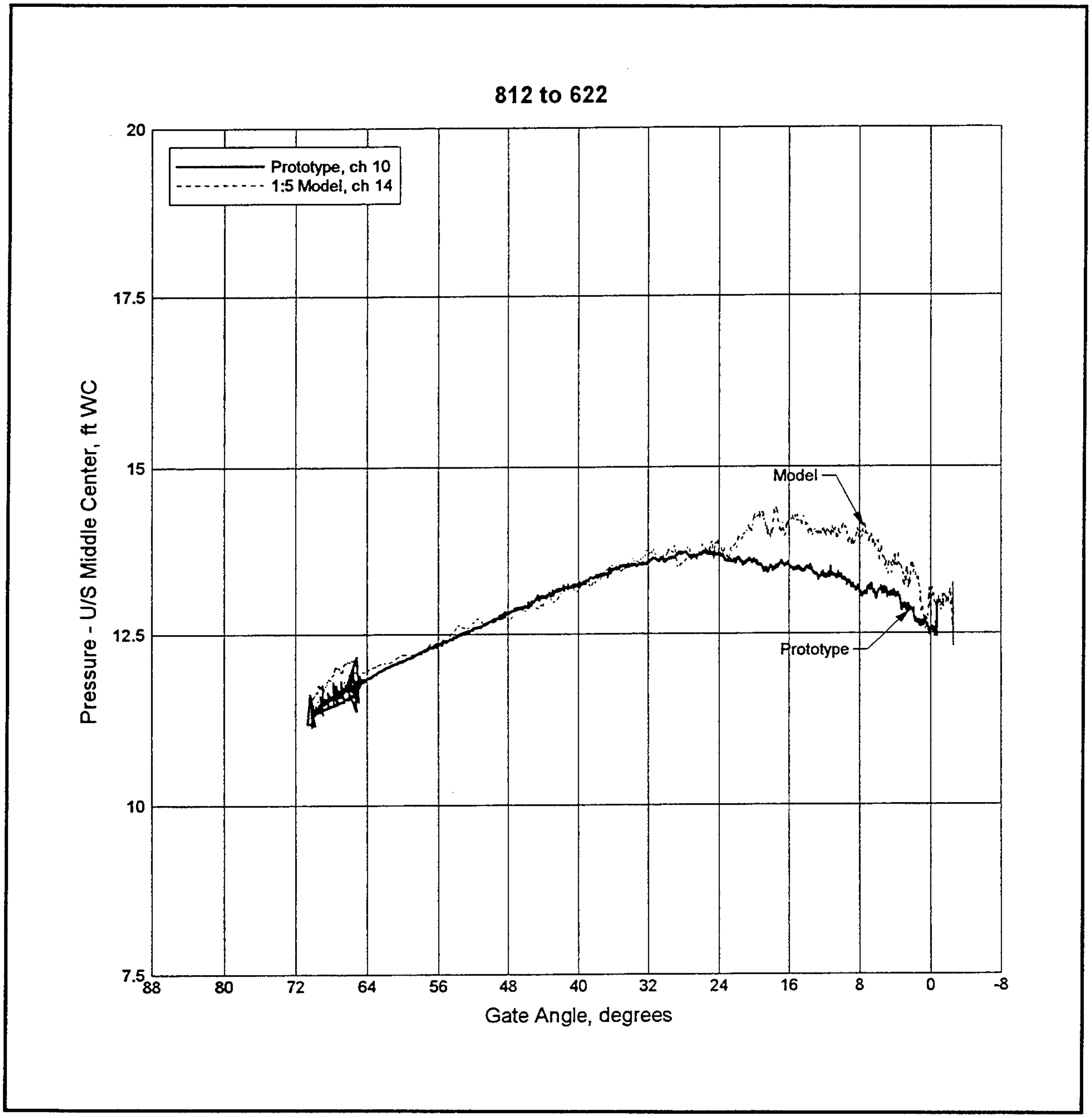

Figure C14. Upstream middle center pressure vs gate position for 1-GG down condition

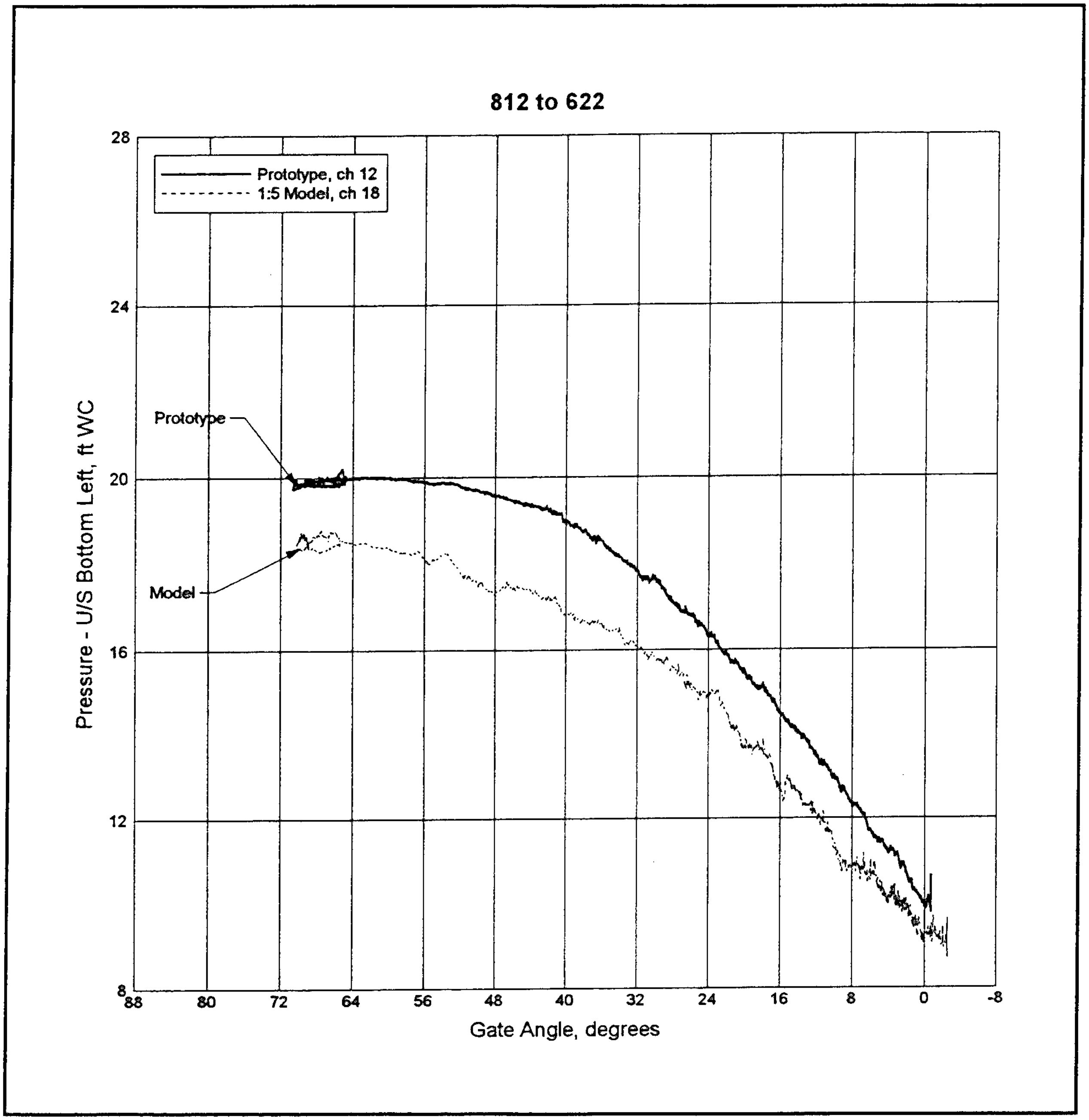

Figure C15. Upstream bottom left pressure vs gate position for 1-GG down condition

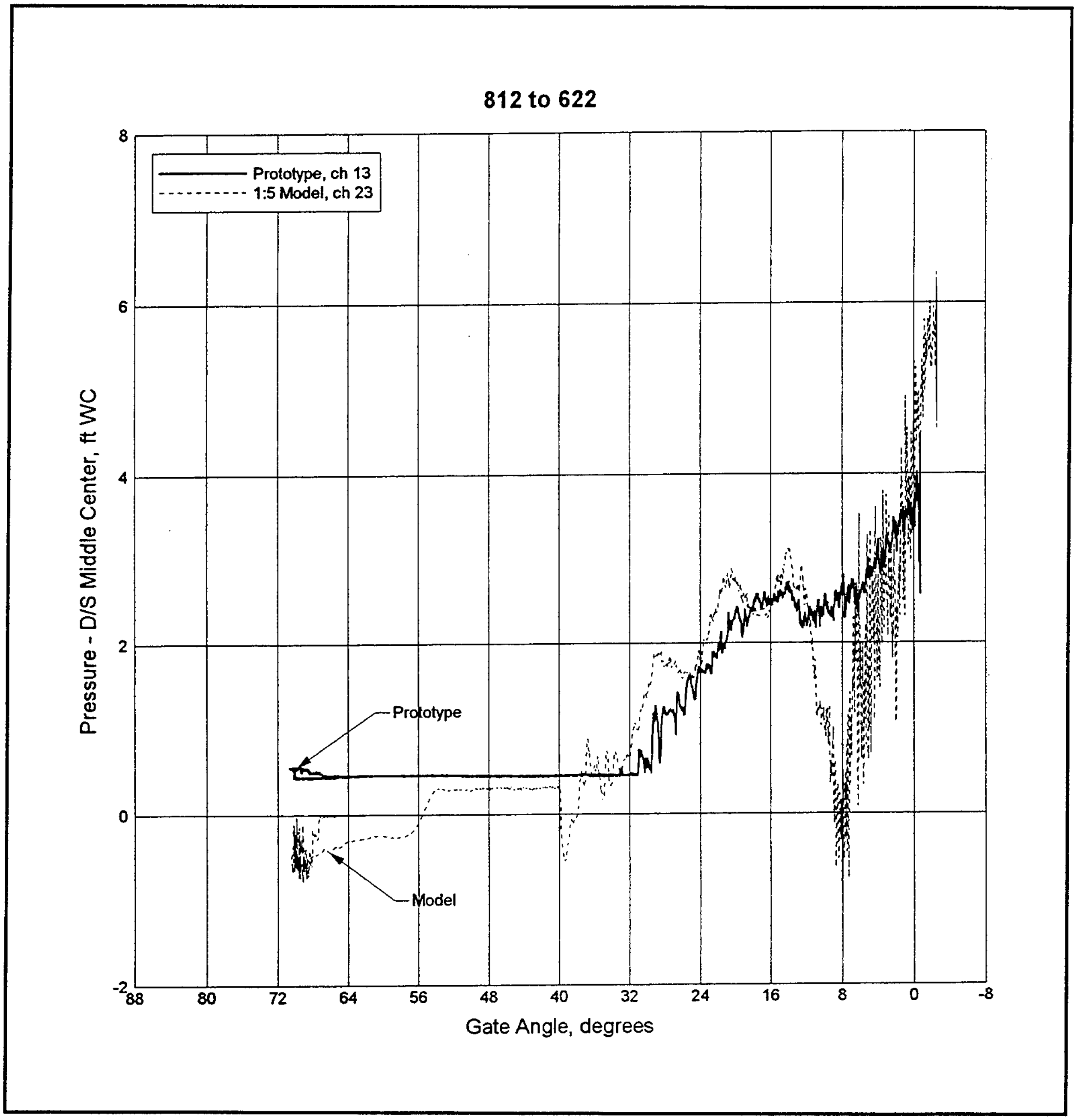

Figure C16. Downstream middle center pressure vs gate position for 1-GG down condition

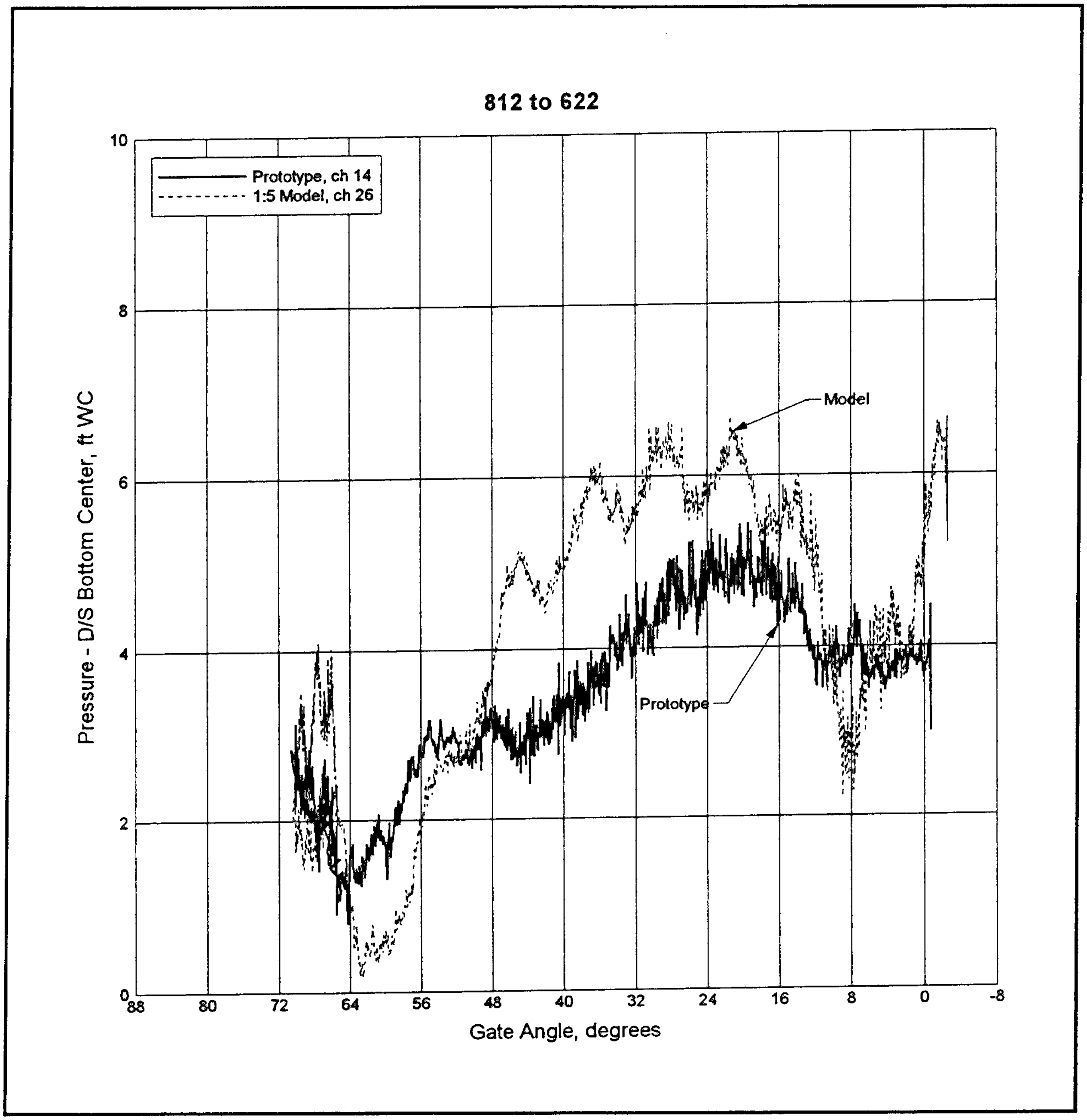

Figure C17. Downstream bottom center pressure vs gate position for 1-GG down condition

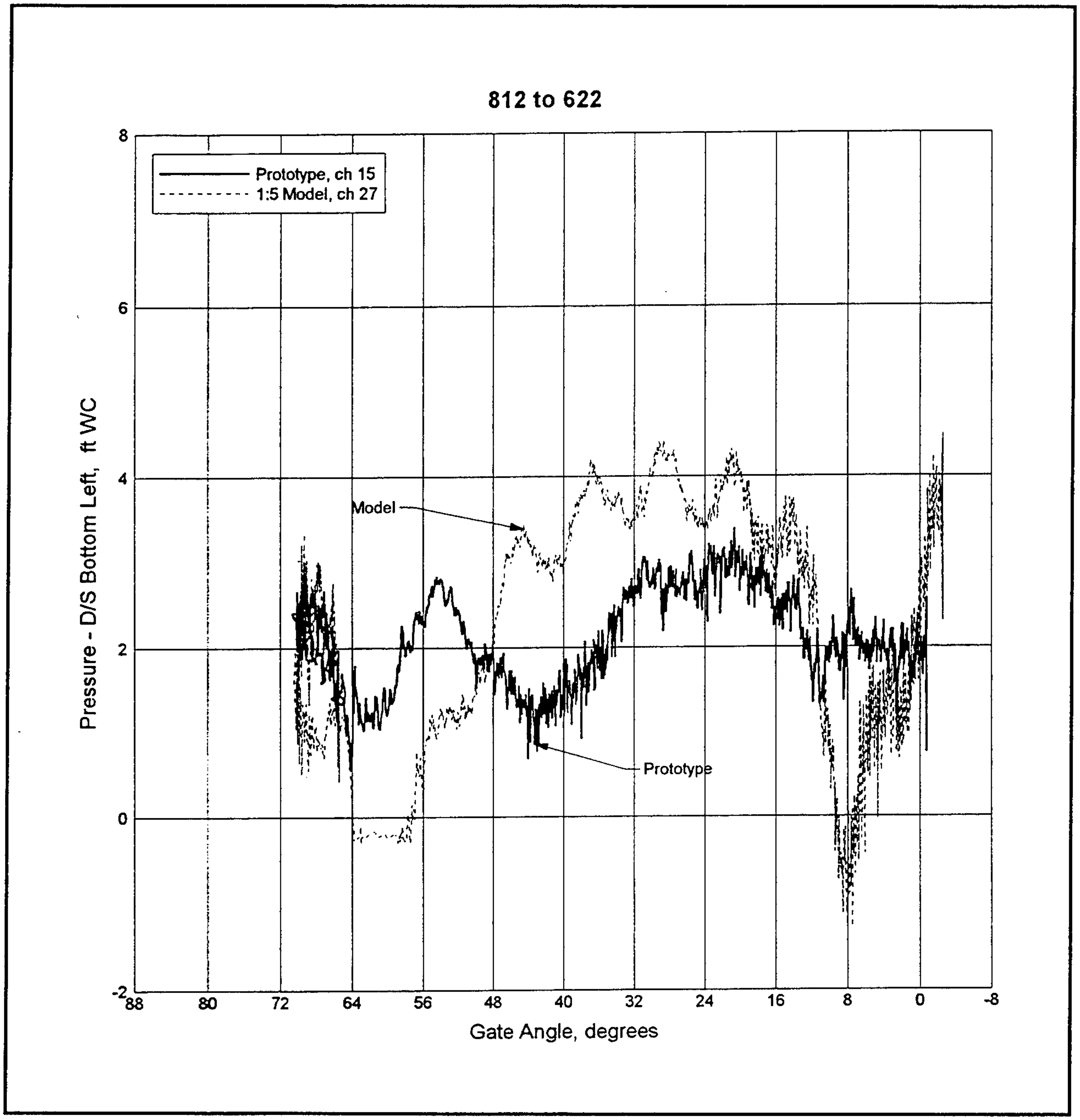

Figure C18. Downstream bottom left pressure vs gate position for 1-GG down condition

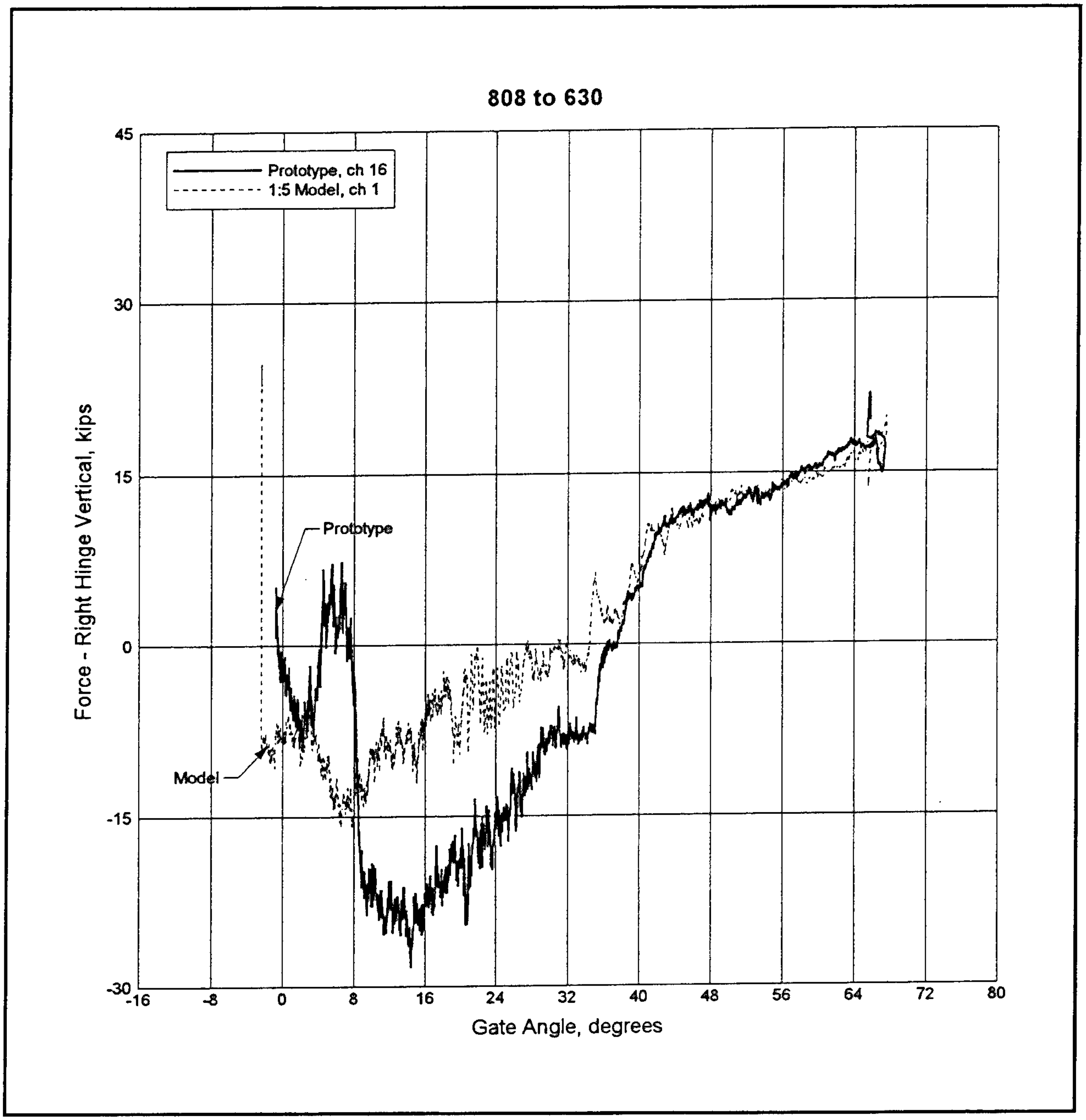

Figure C19. Right hinge vertical force vs gate position for 3-GG up condition

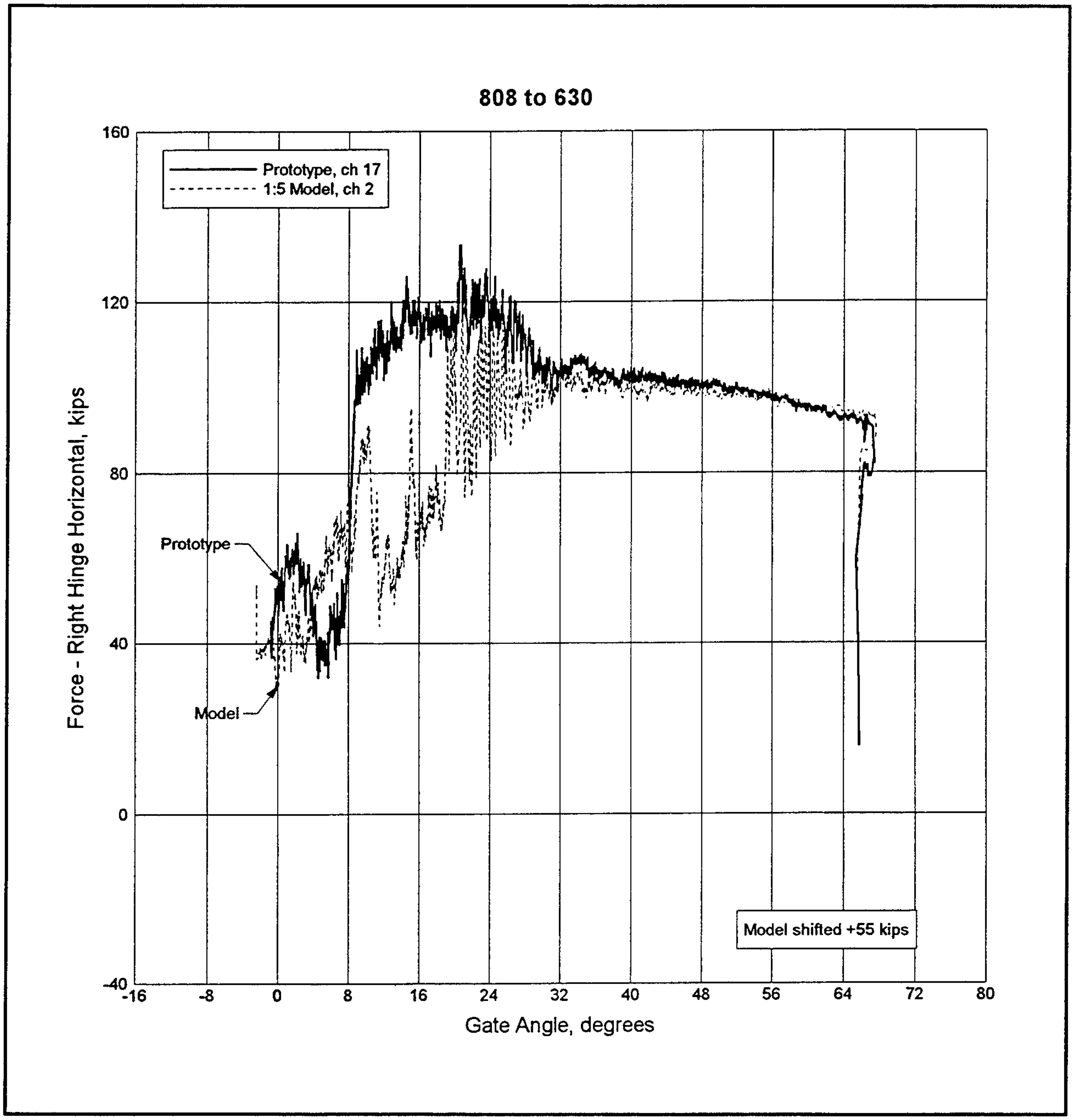

Figure C20. Right hinge horizontal force vs gate position for 3-GG up condition

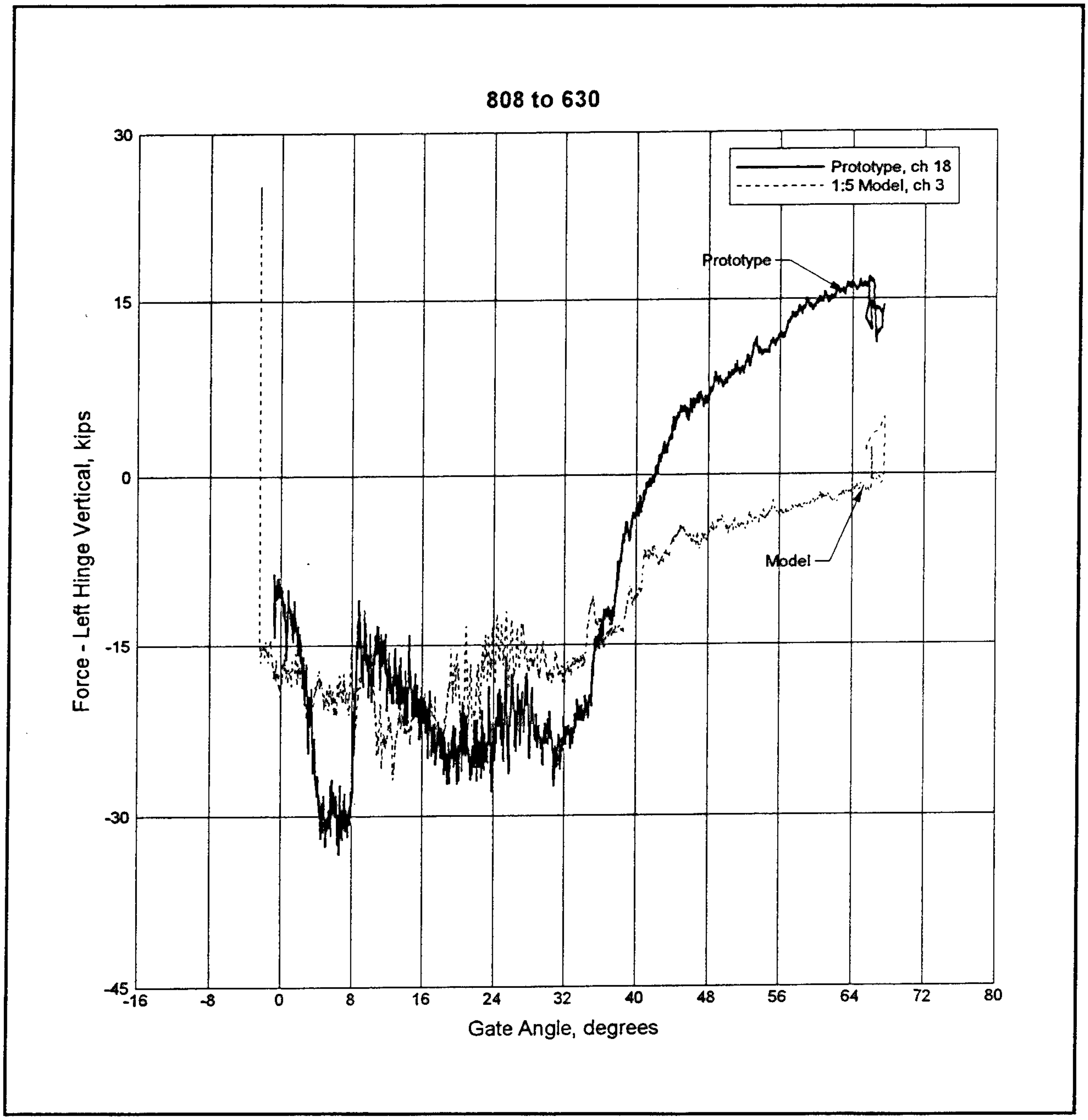

Figure C21. Left hinge vertical force vs gate position for 3-GG up condition

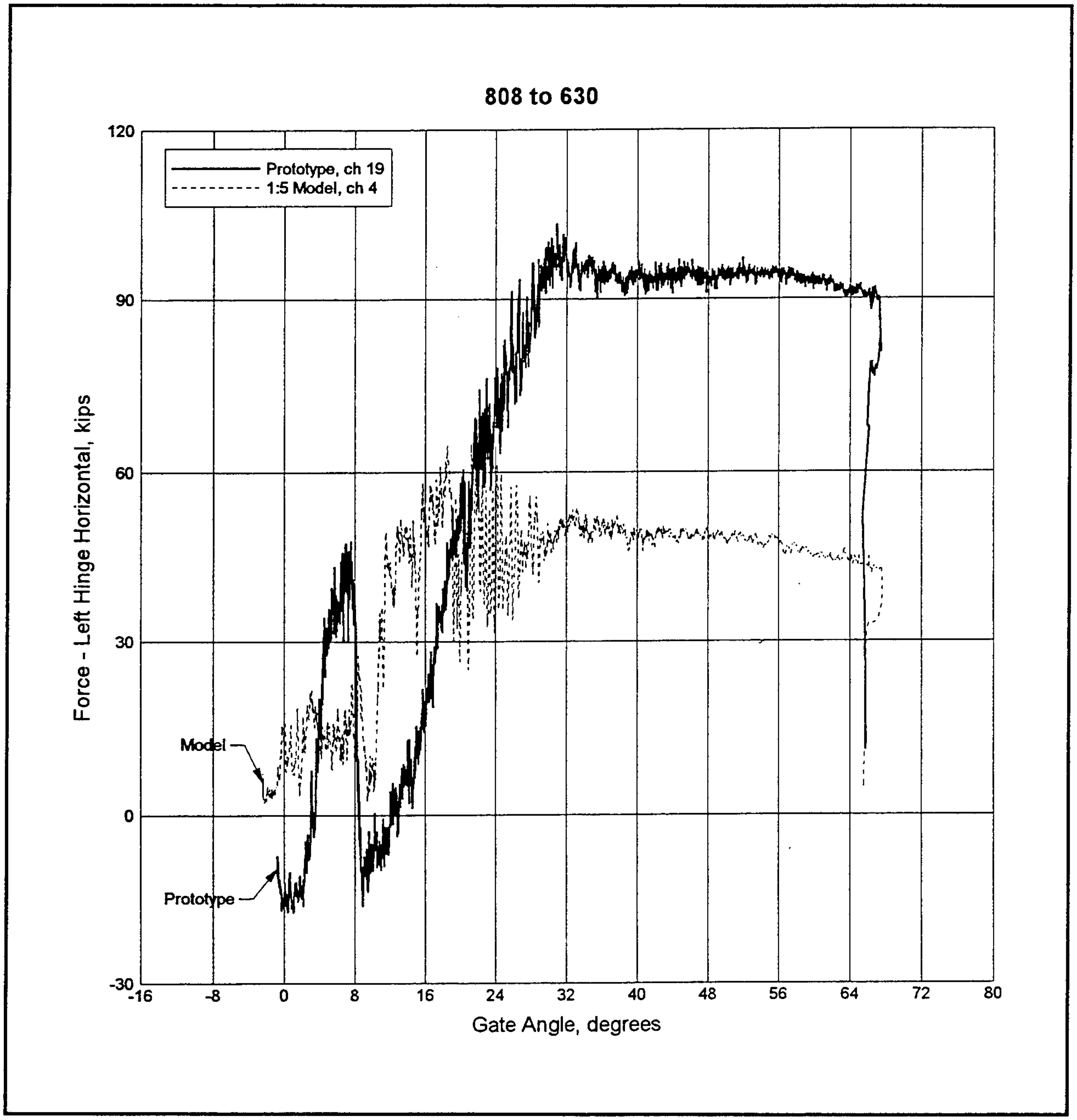

Figure C22. Left hinge horizontal force vs gate position for 3-GG up condition

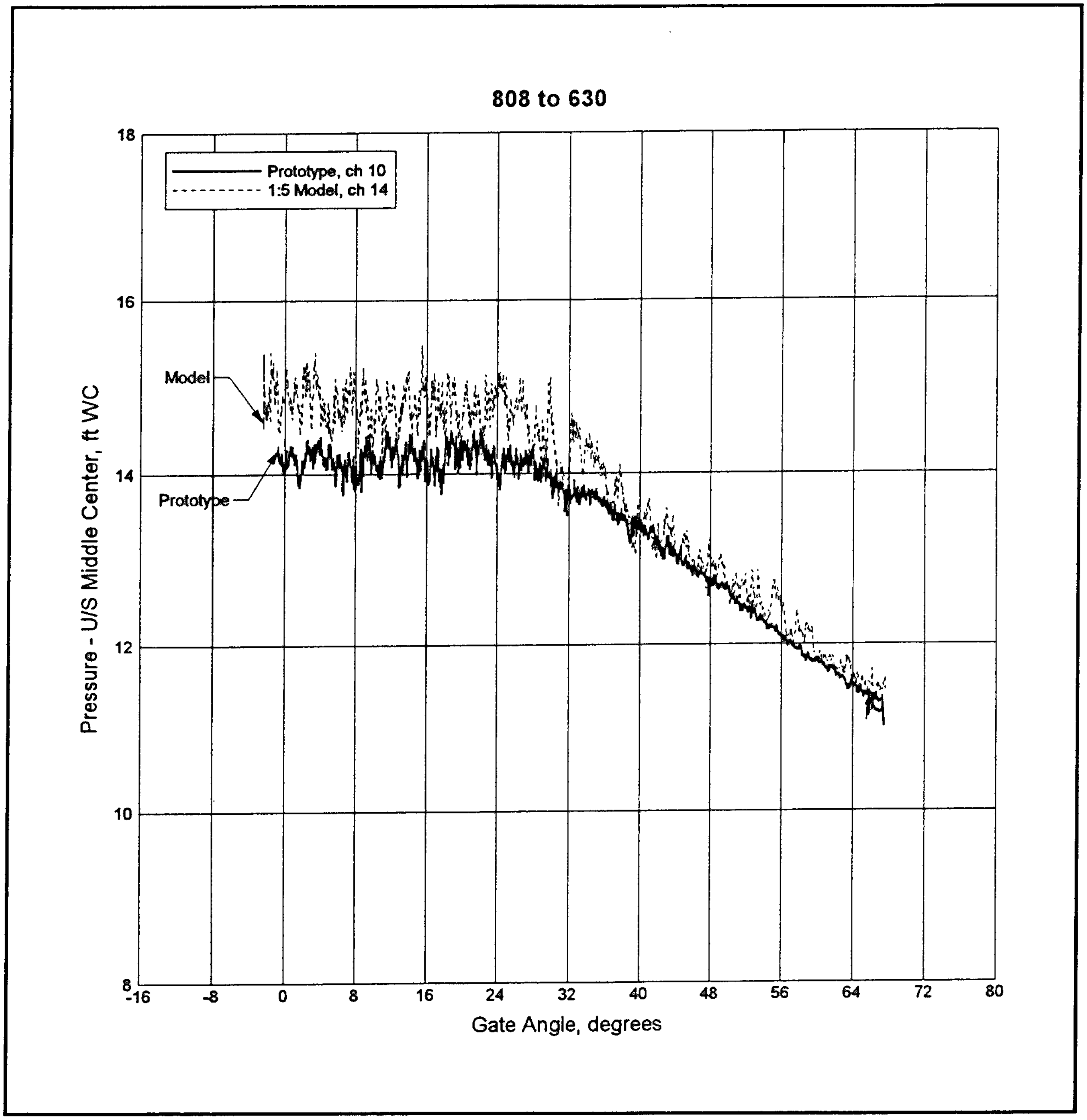

Figure C23. Upstream middle center pressure vs gate position for 3-GG up condition

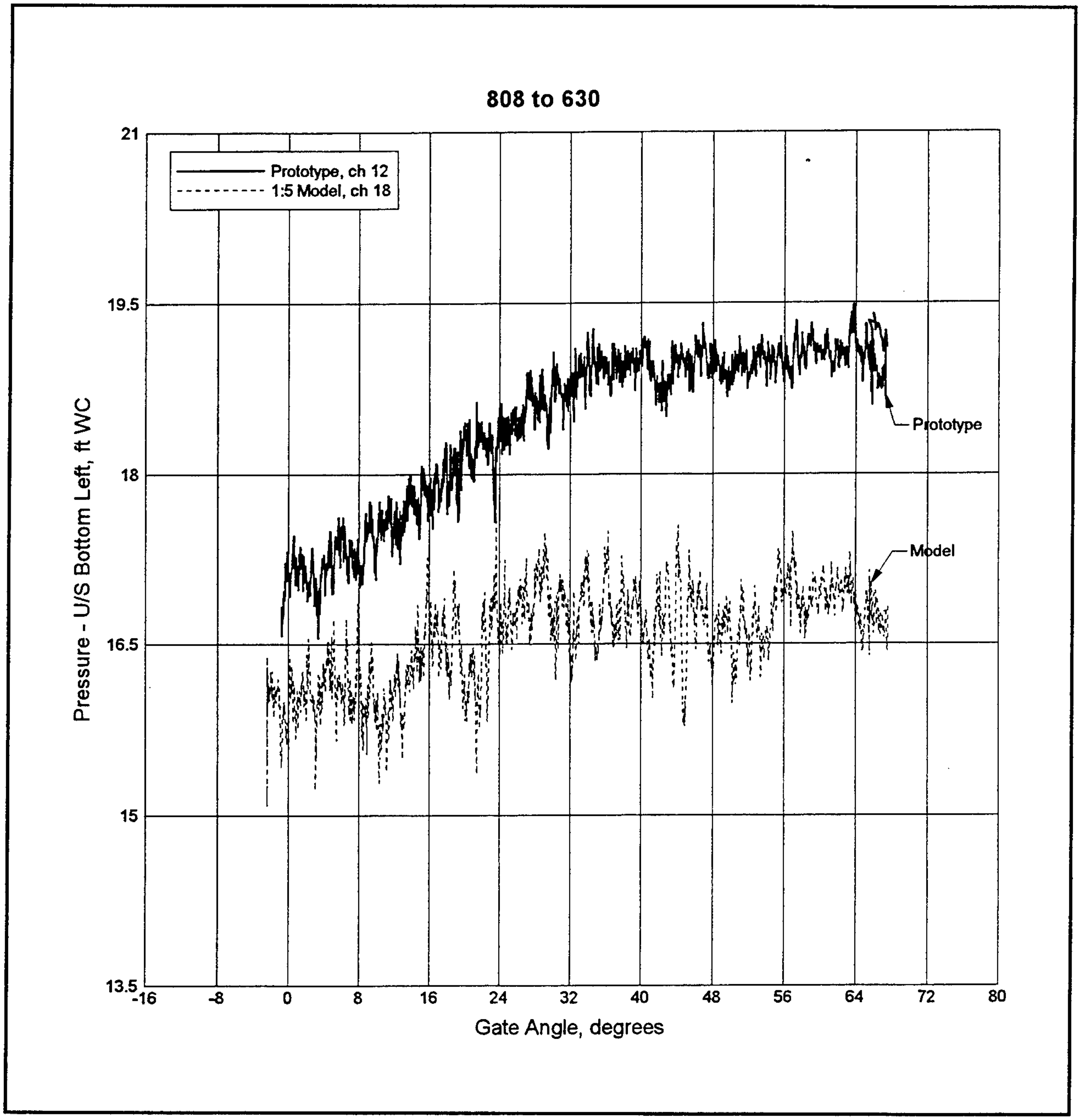

Figure C24. Upstream bottom left pressure vs gate position for 3-GG up condition

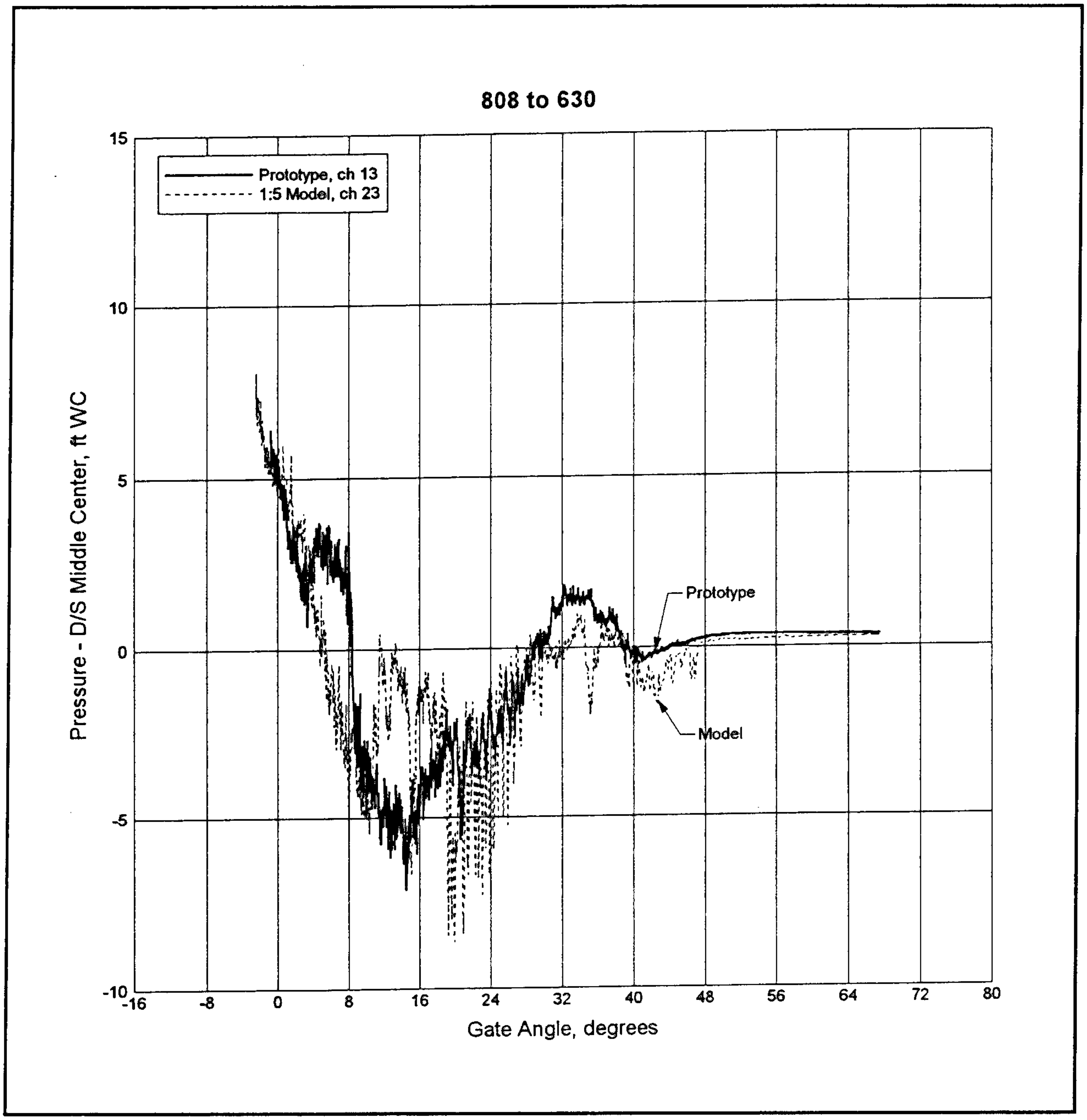

Figure C25. Downstream middle center pressure vs gate position for 3-GG up condition

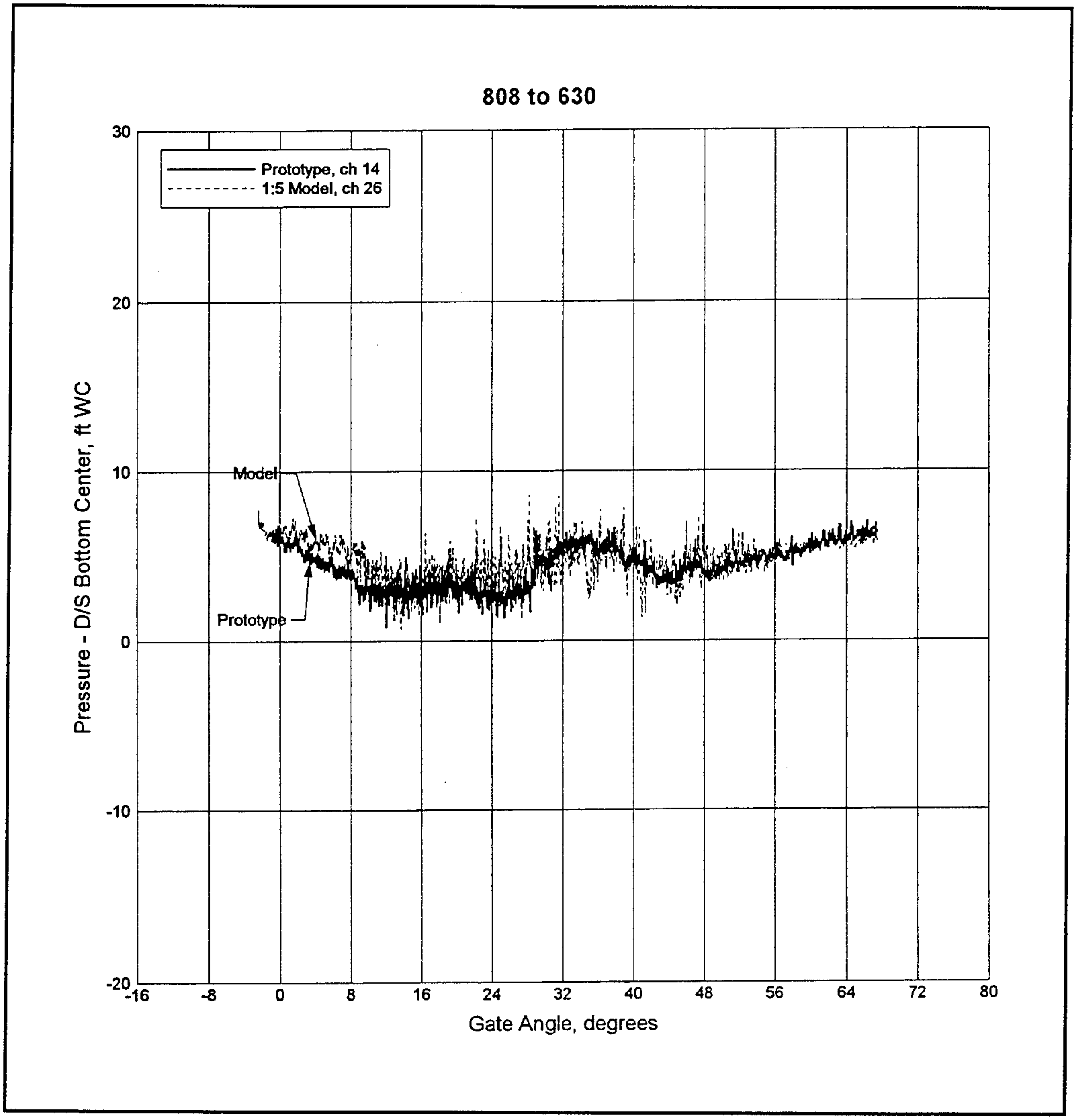

Figure C26. Downstream bottom center pressure vs gate position for 3-GG up condition

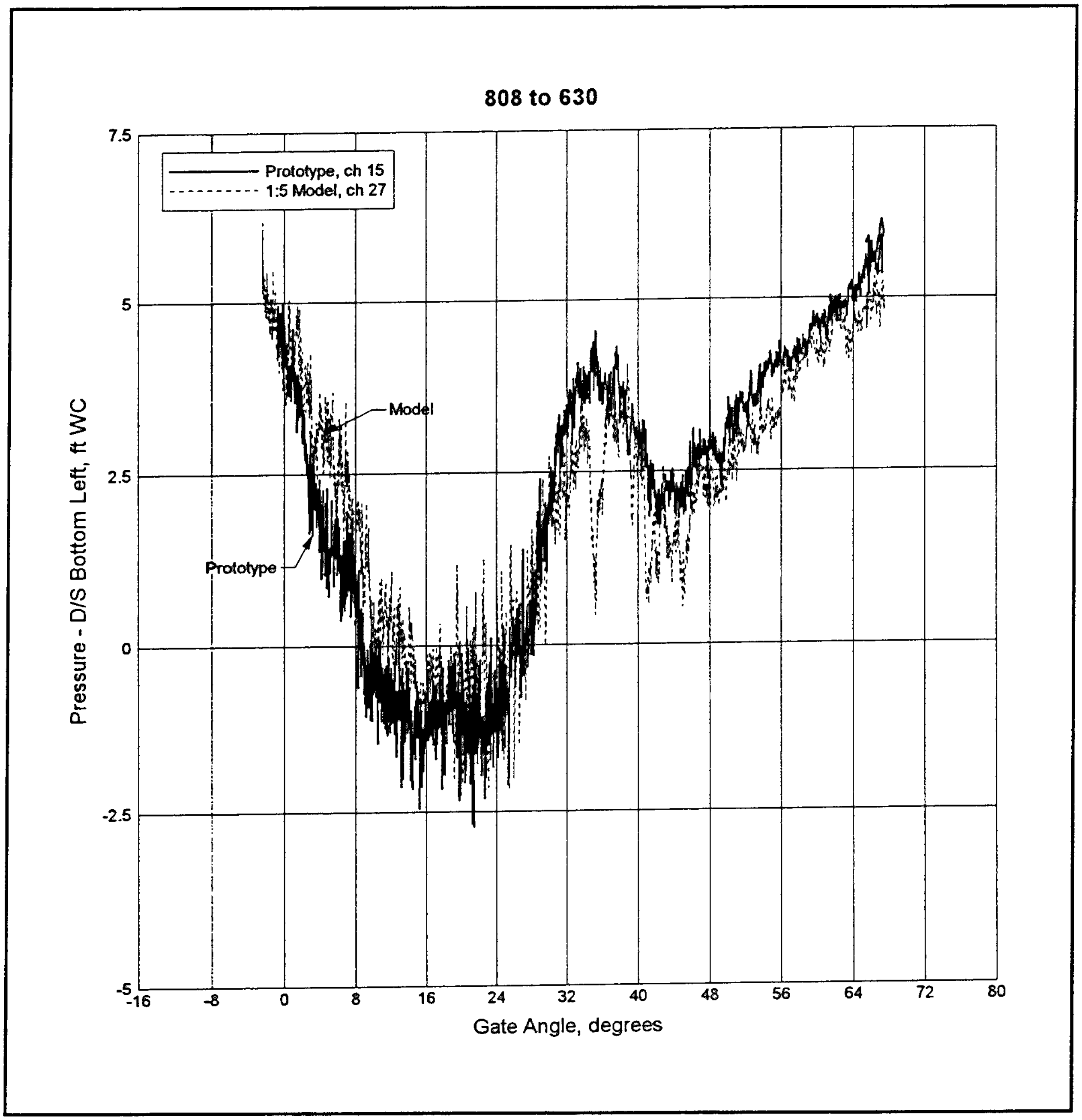

Figure C27. Downstream bottom left pressure vs gate position for 3-GG up condition

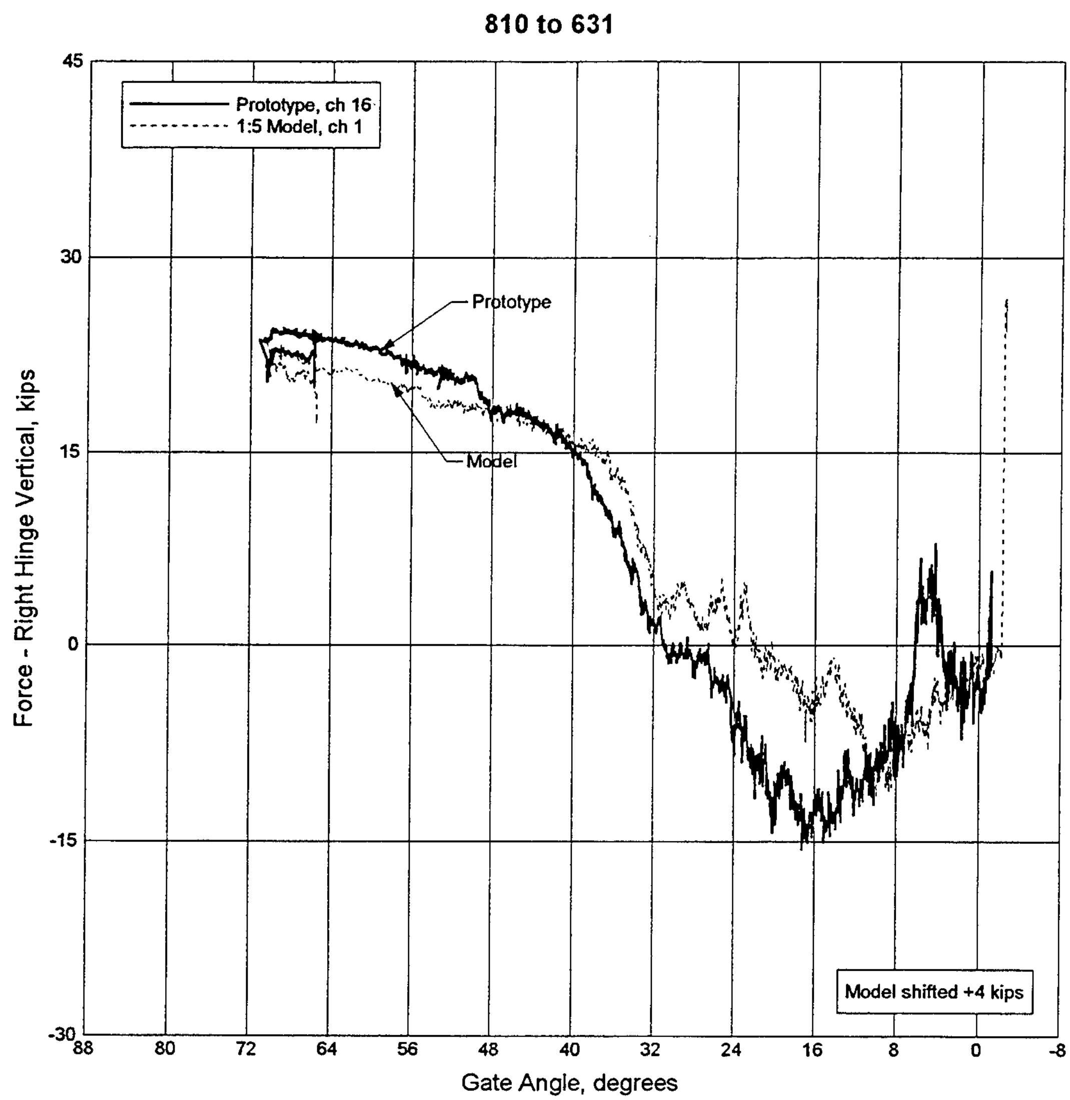

Figure C28. Right hinge vertical force vs gate position for 3-GG down condition

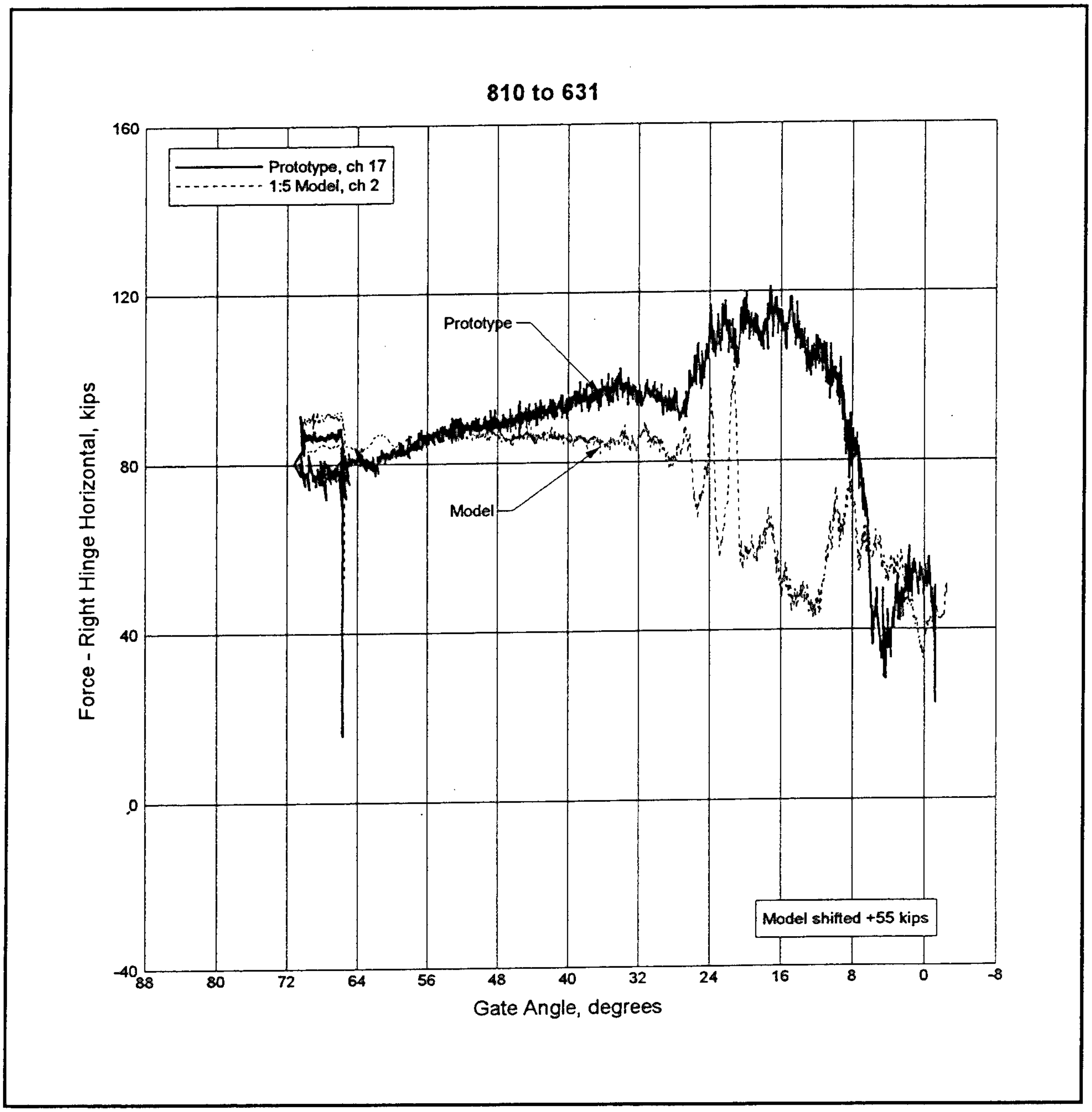

Figure C29. Right hinge horizontal force vs gate position for 3-GG down condition

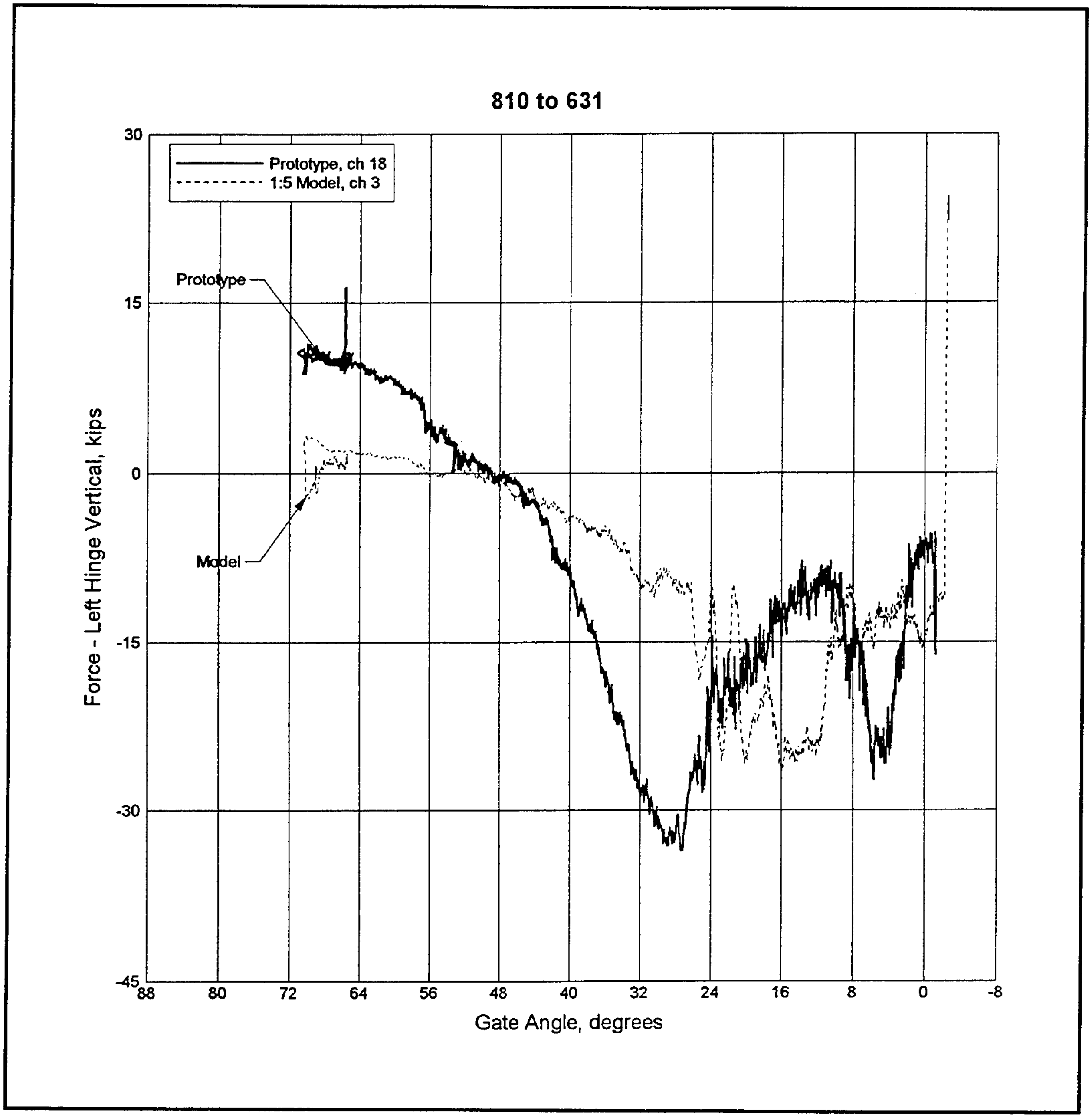

Figure C30. Left hinge vertical force vs gate position for 3-GG down condition

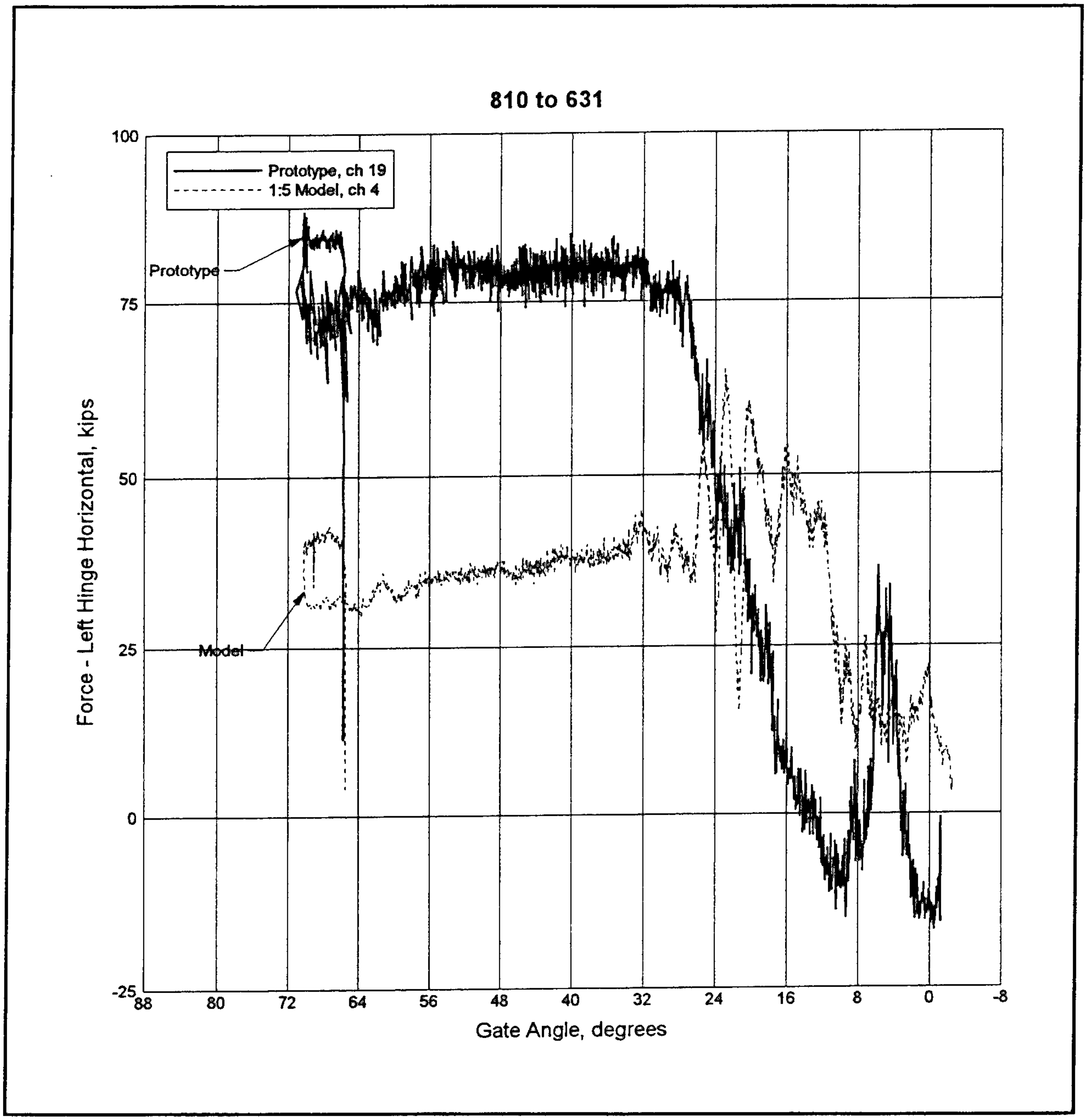

Figure C31. Left hinge horizontal force vs gate position for 3-GG down condition

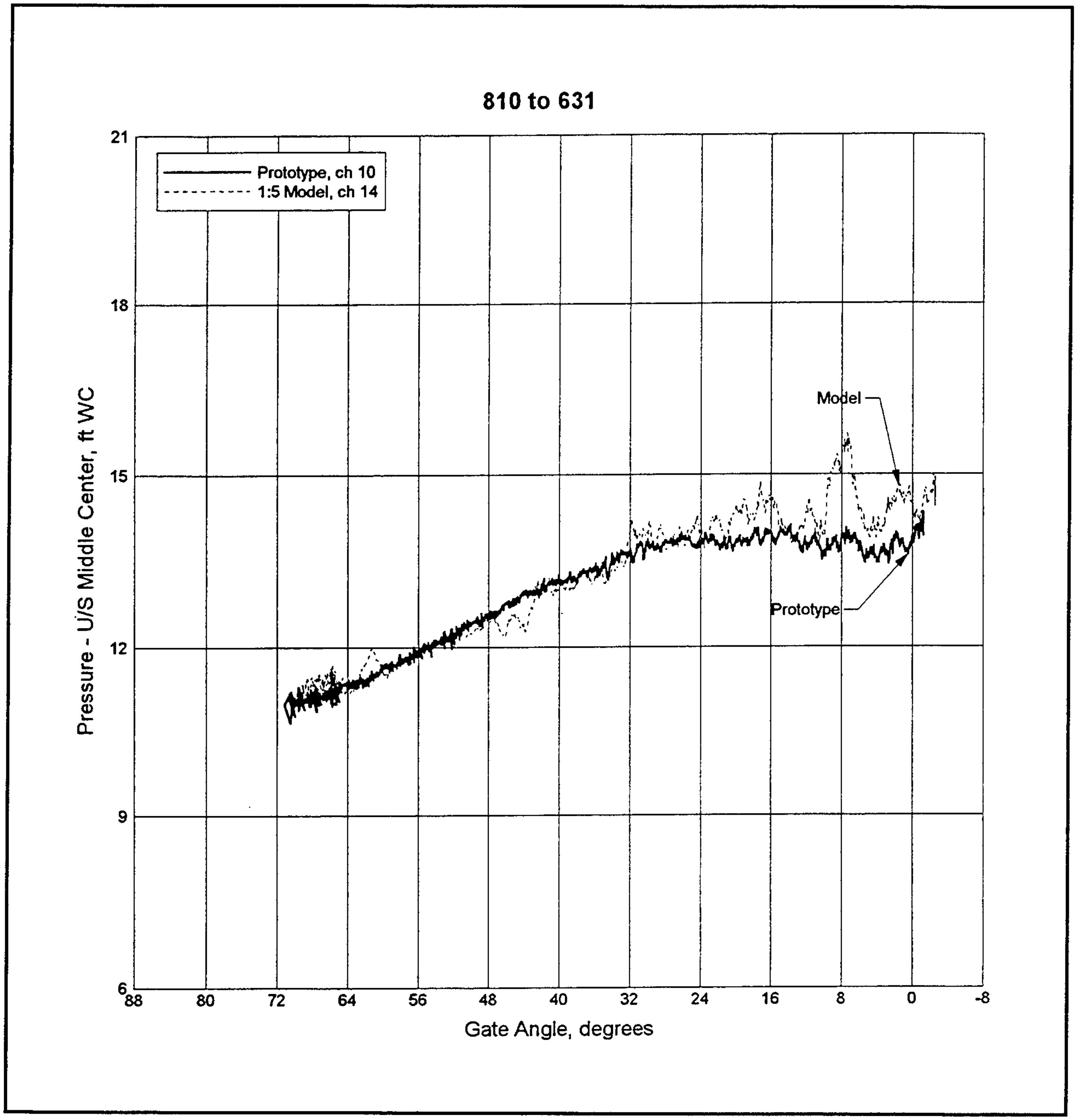

Figure C32. Upstream middle center pressure vs gate position for 3-GG down condition

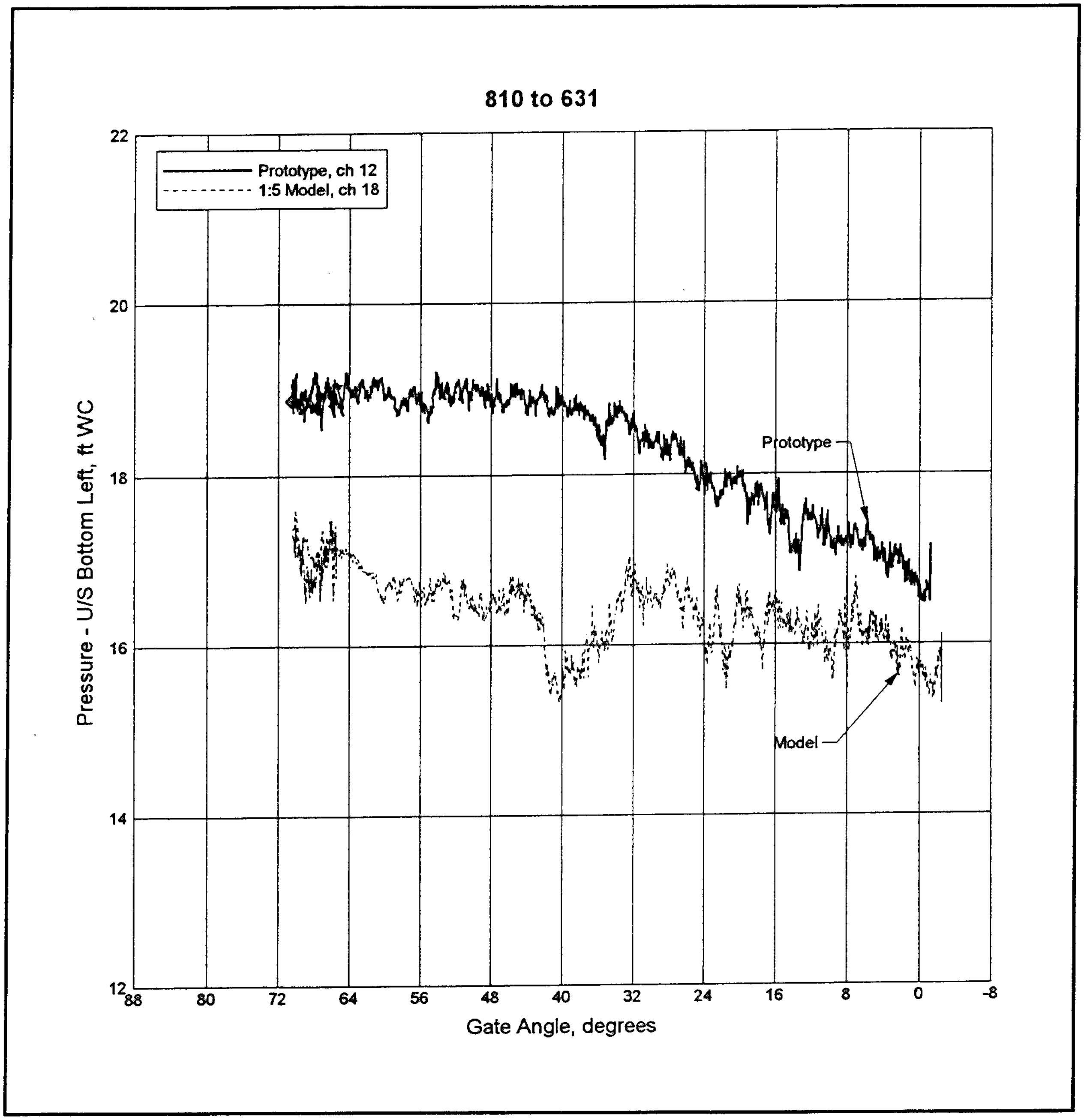

Figure C33. Upstream bottom left pressure vs gate position for 3-GG down condition

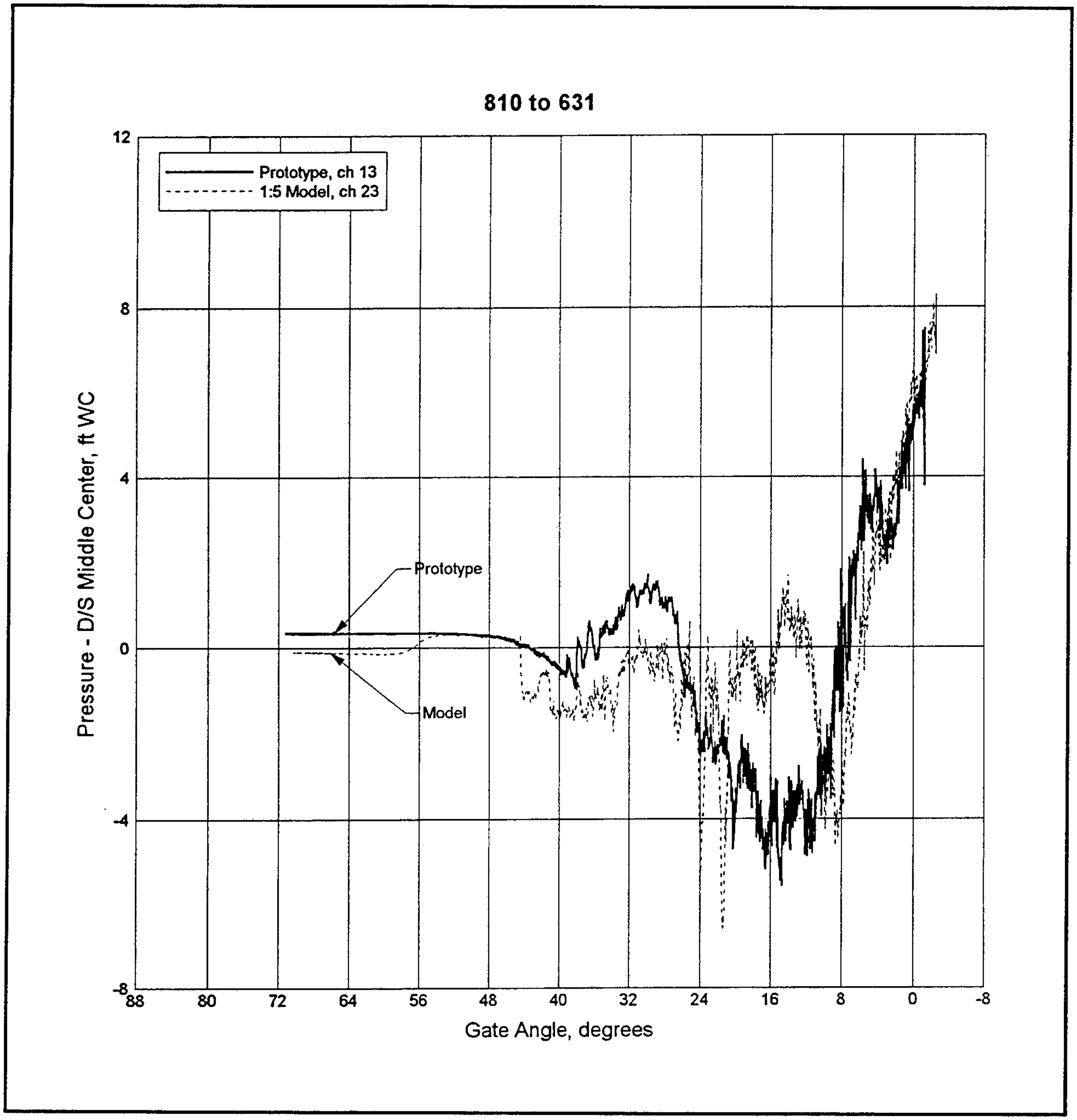

Figure C34. Downstream middle center pressure vs gate position for 3-GG down condition

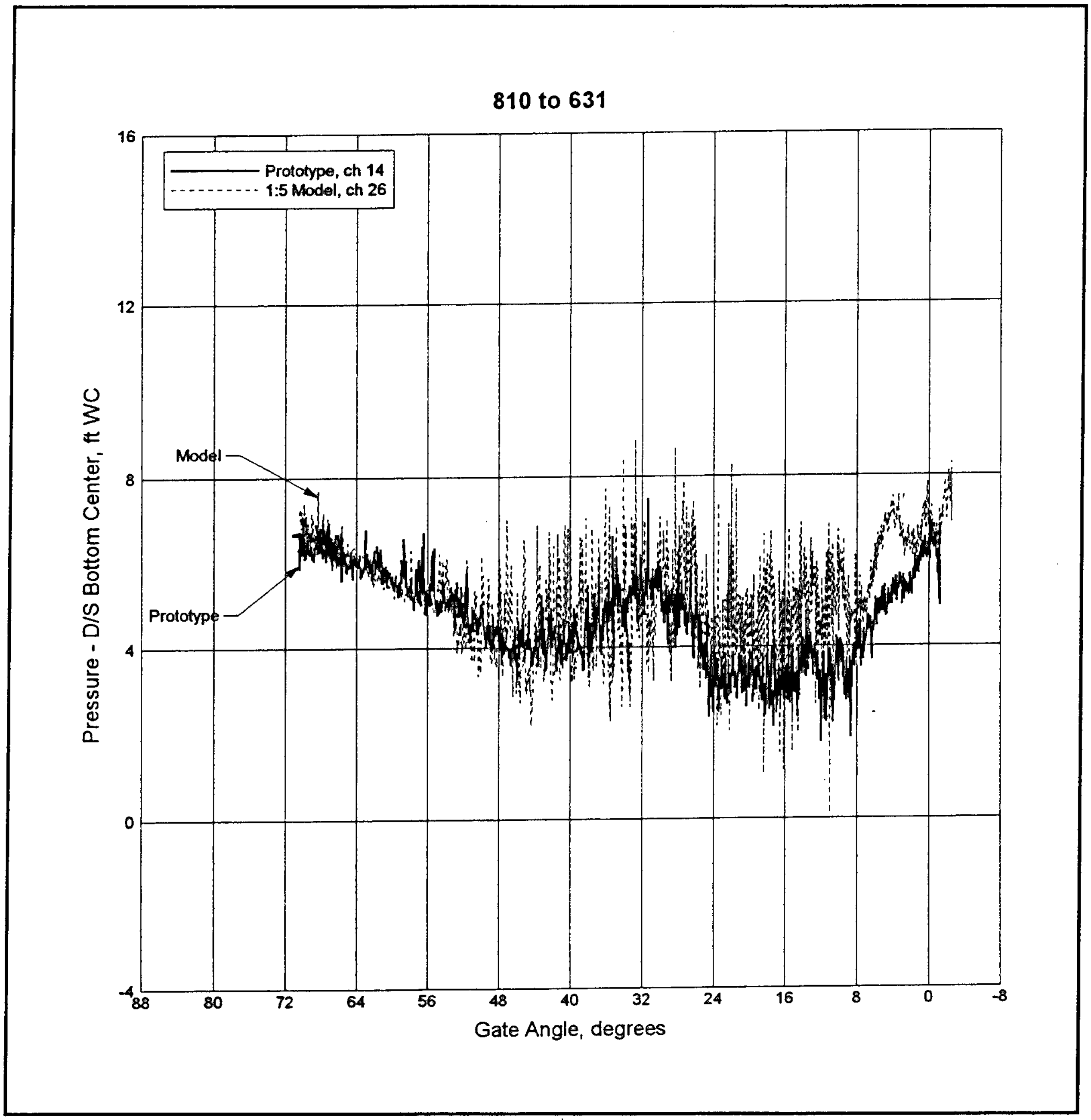

Figure C35. Downstream bottom center pressure vs gate position for 3-GG down condition

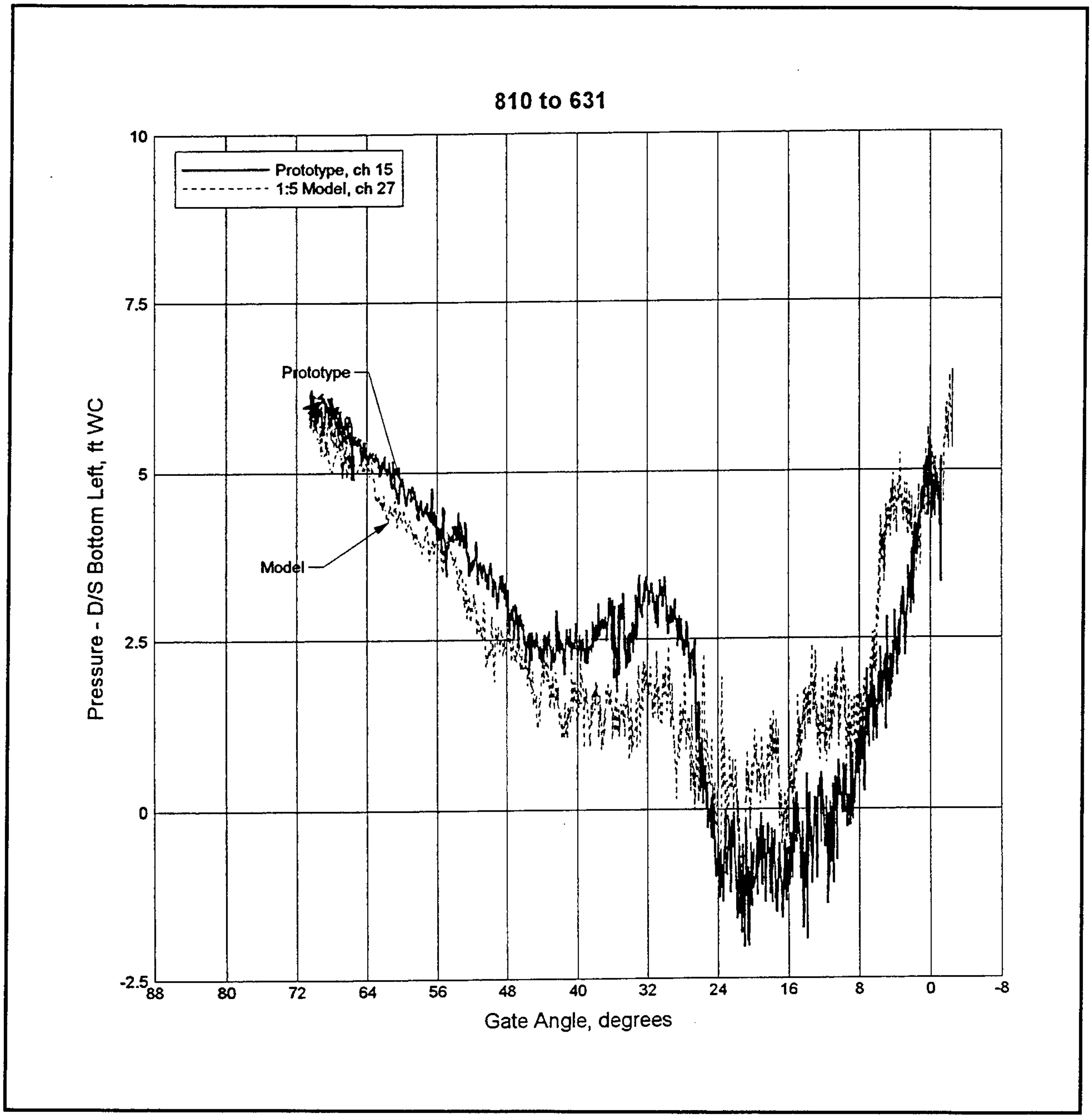

Figure C36. Downstream bottom left pressure vs gate position for 3-GG down condition

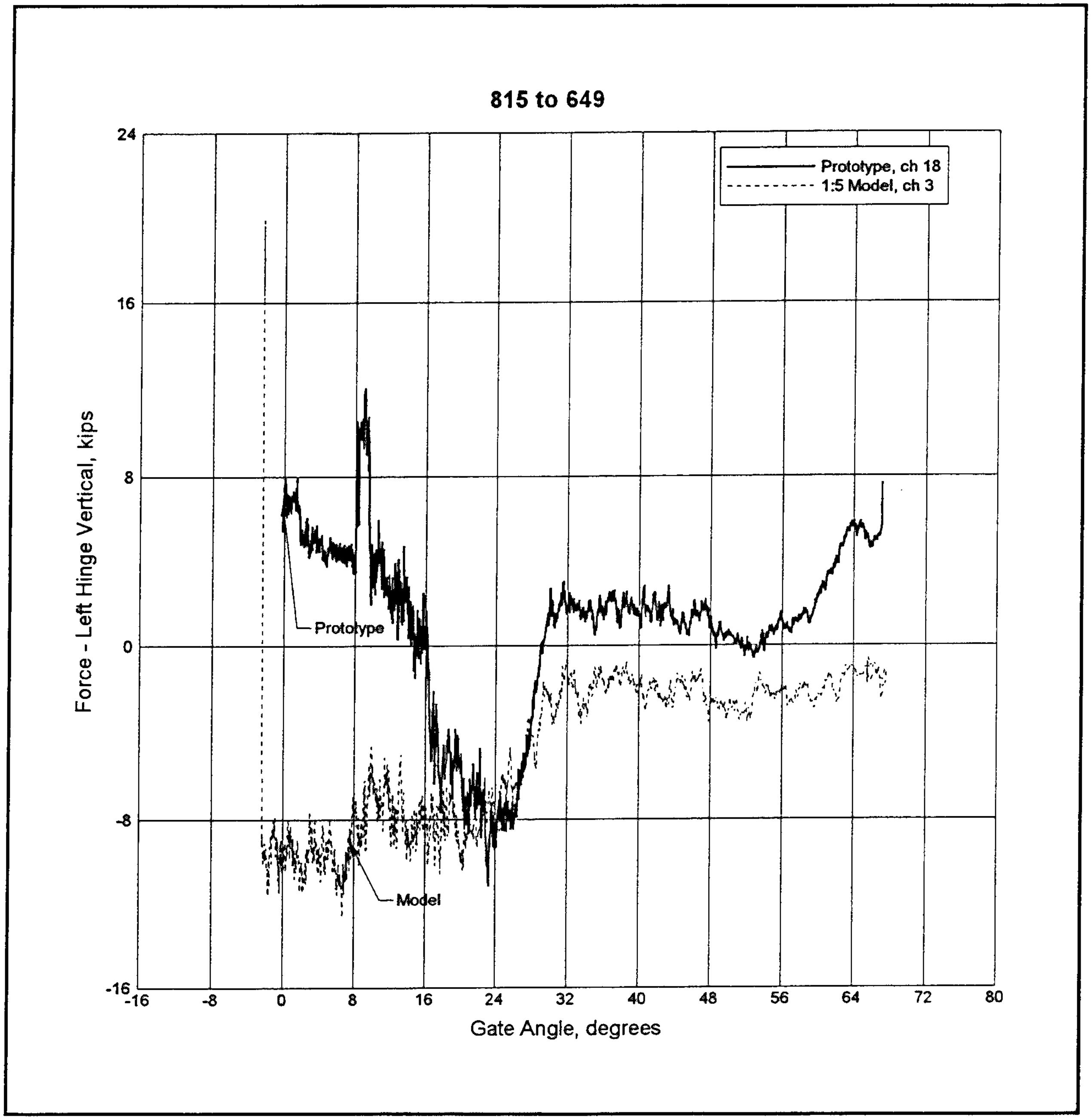

Figure C37. Left hinge vertical force vs gate position for 2-GG (EL) up condition

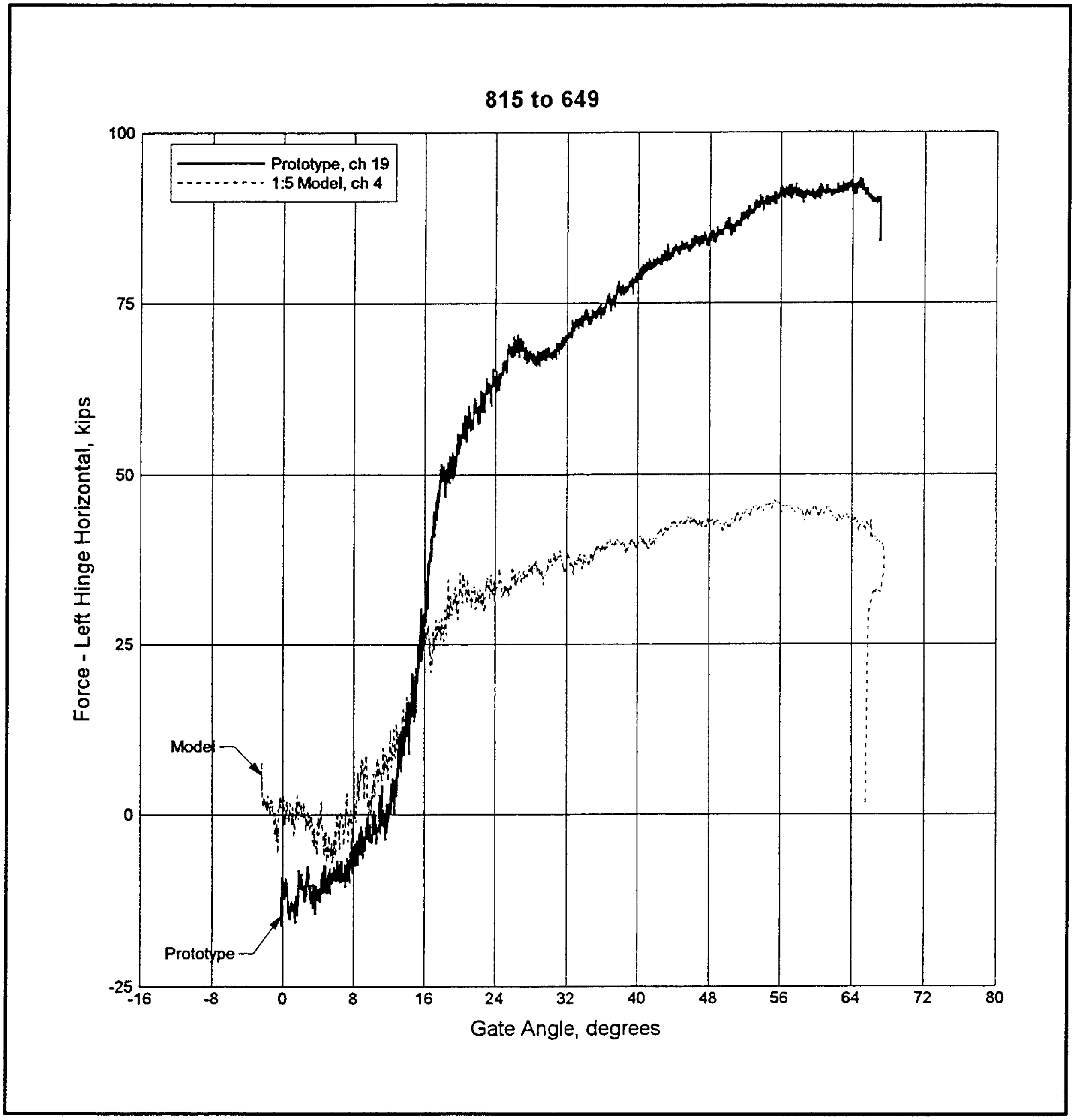

Figure C38. Left hinge horizontal force vs gate position for 2-GG (EL) up condition

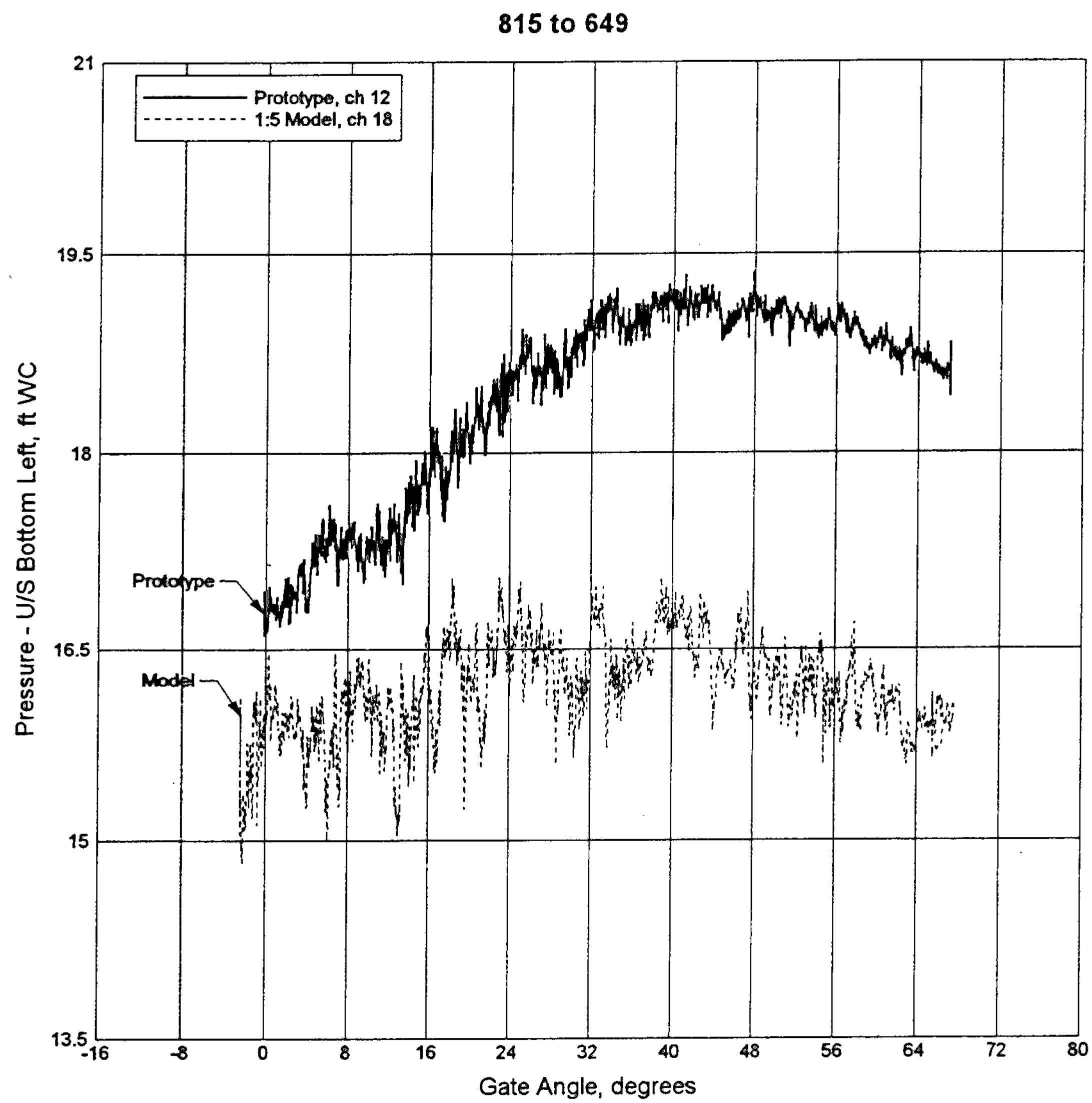

Figure C39. Upstream bottom left pressure vs gate position for 2-GG (EL) up condition

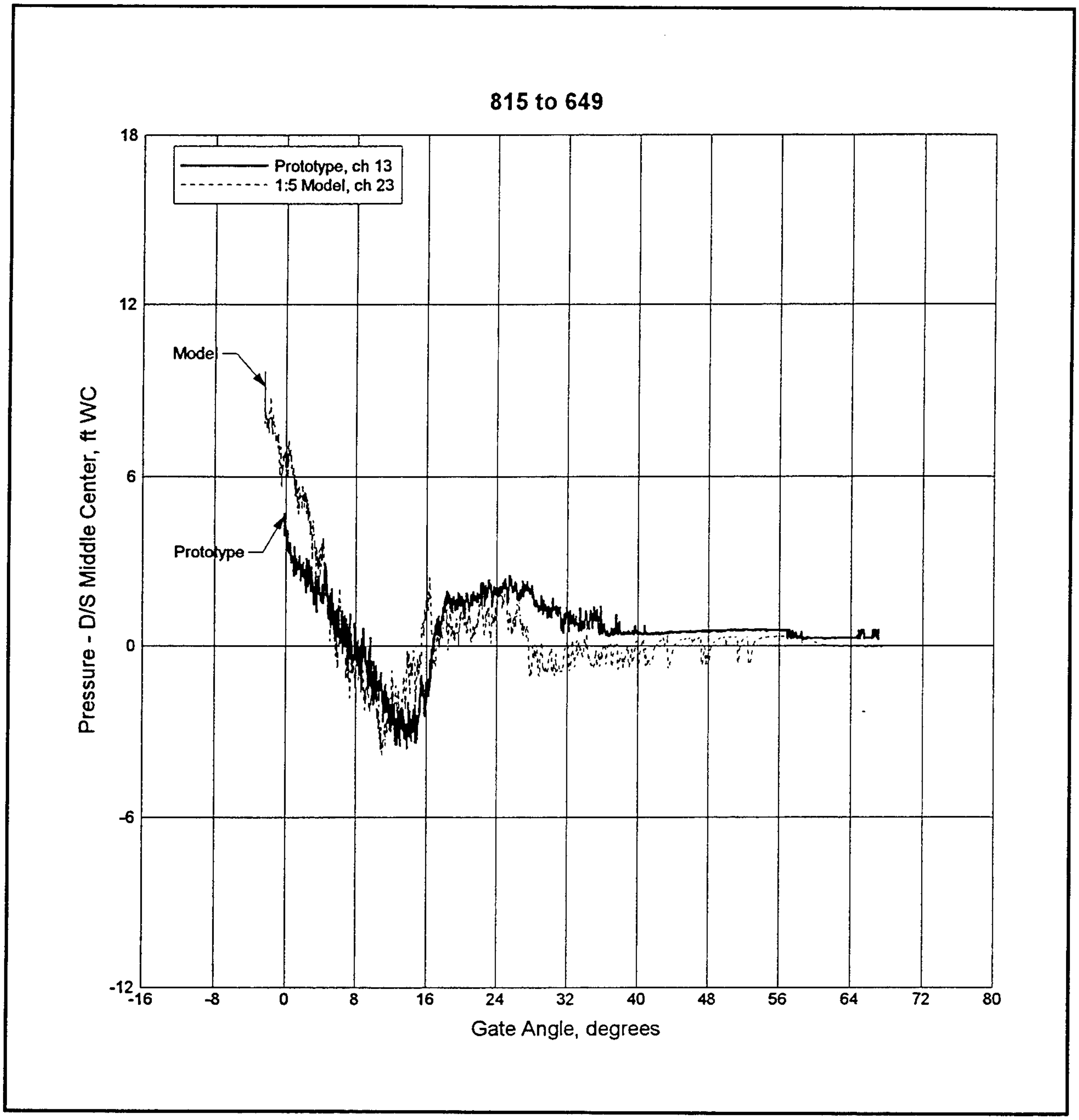

Figure C40. Downstream middle center pressure vs gate position for 2-GG (EL) up condition

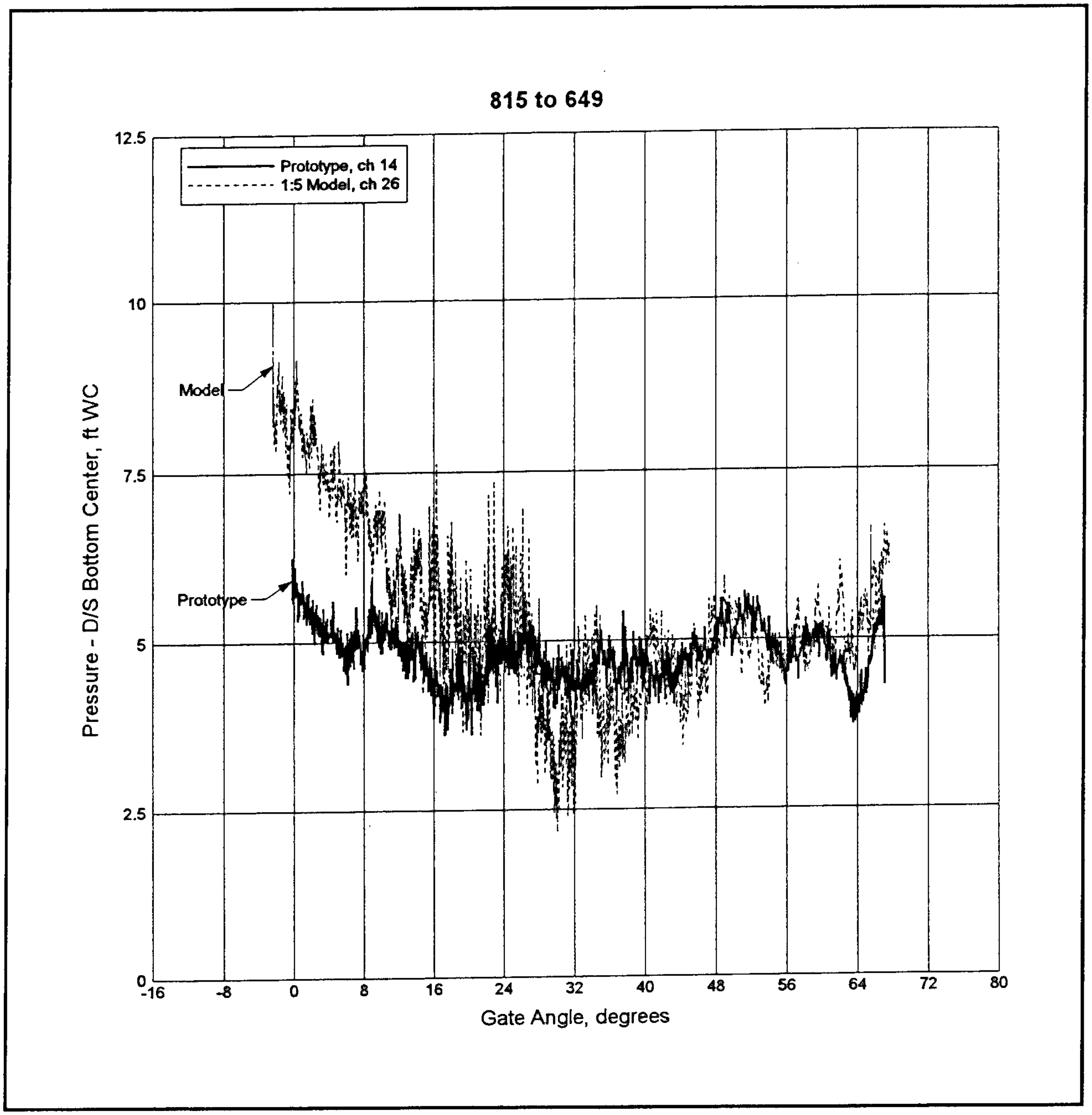

Figure C41. Downstream bottom center pressure vs gate position for 2-GG (EL) up condition

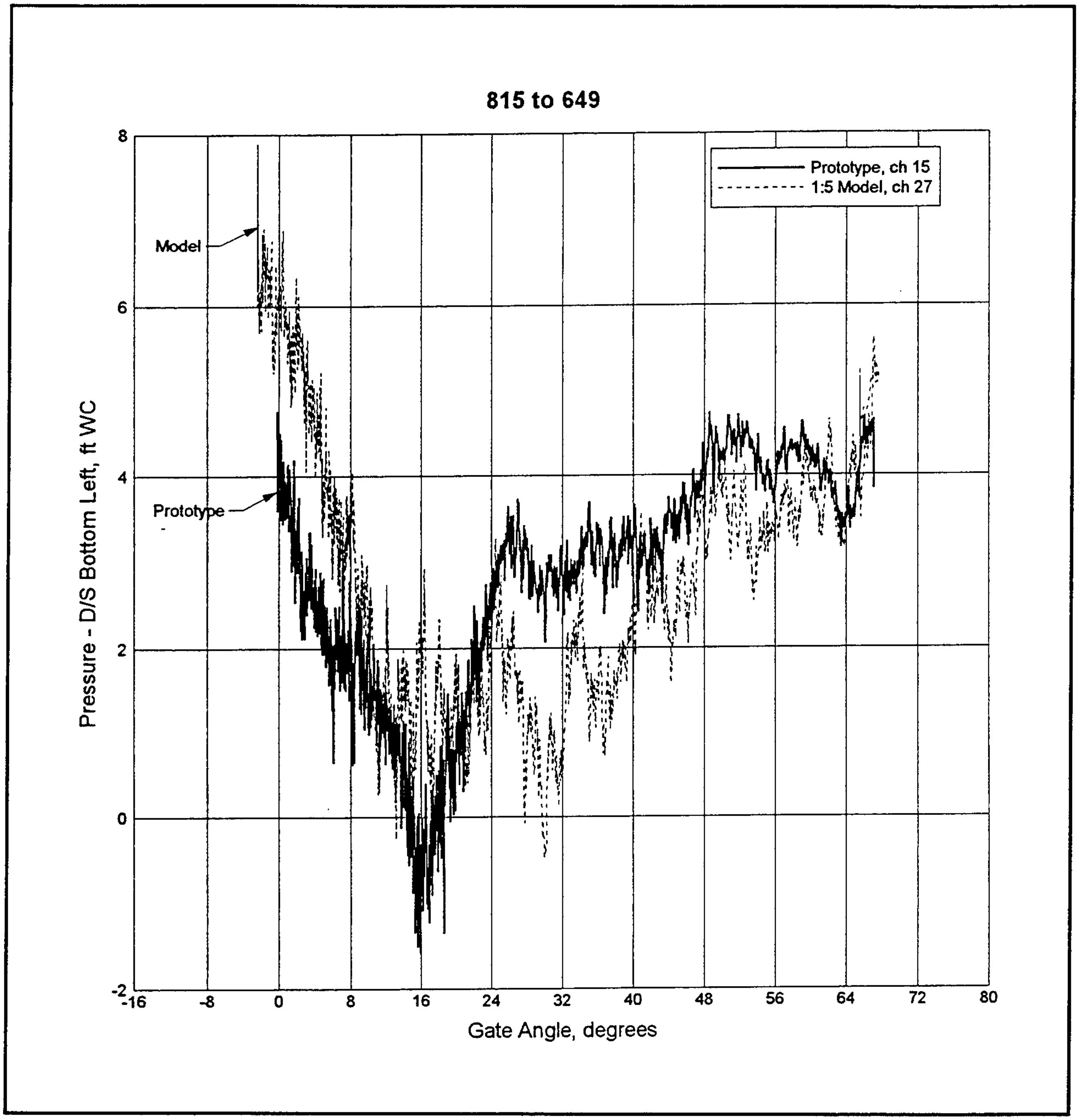

Figure C42. Downstream bottom left pressure vs gate position for 2-GG (EL) up condition

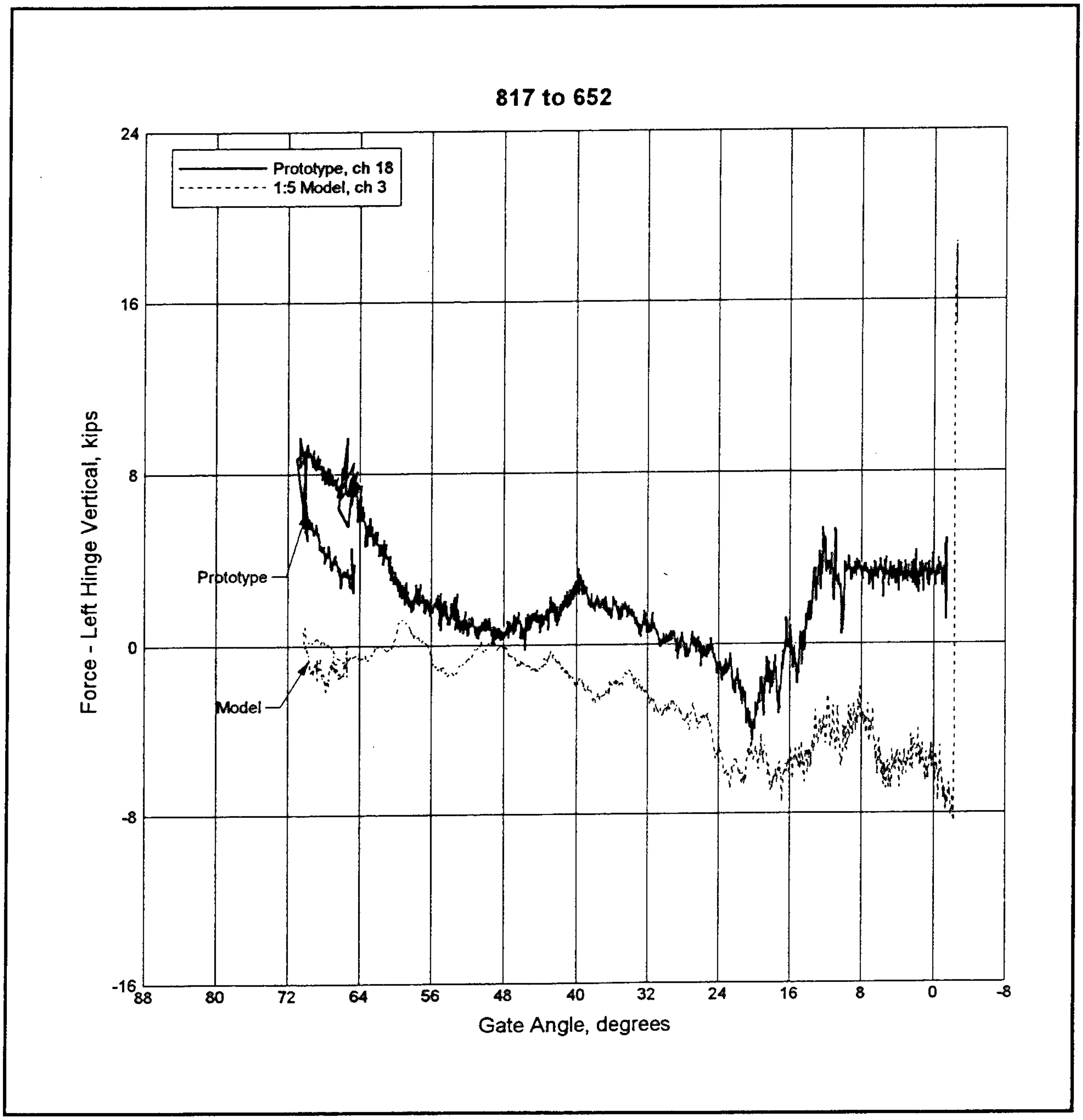

Figure C43. Left hinge vertical force vs gate position for 2-GG (EL) down condition

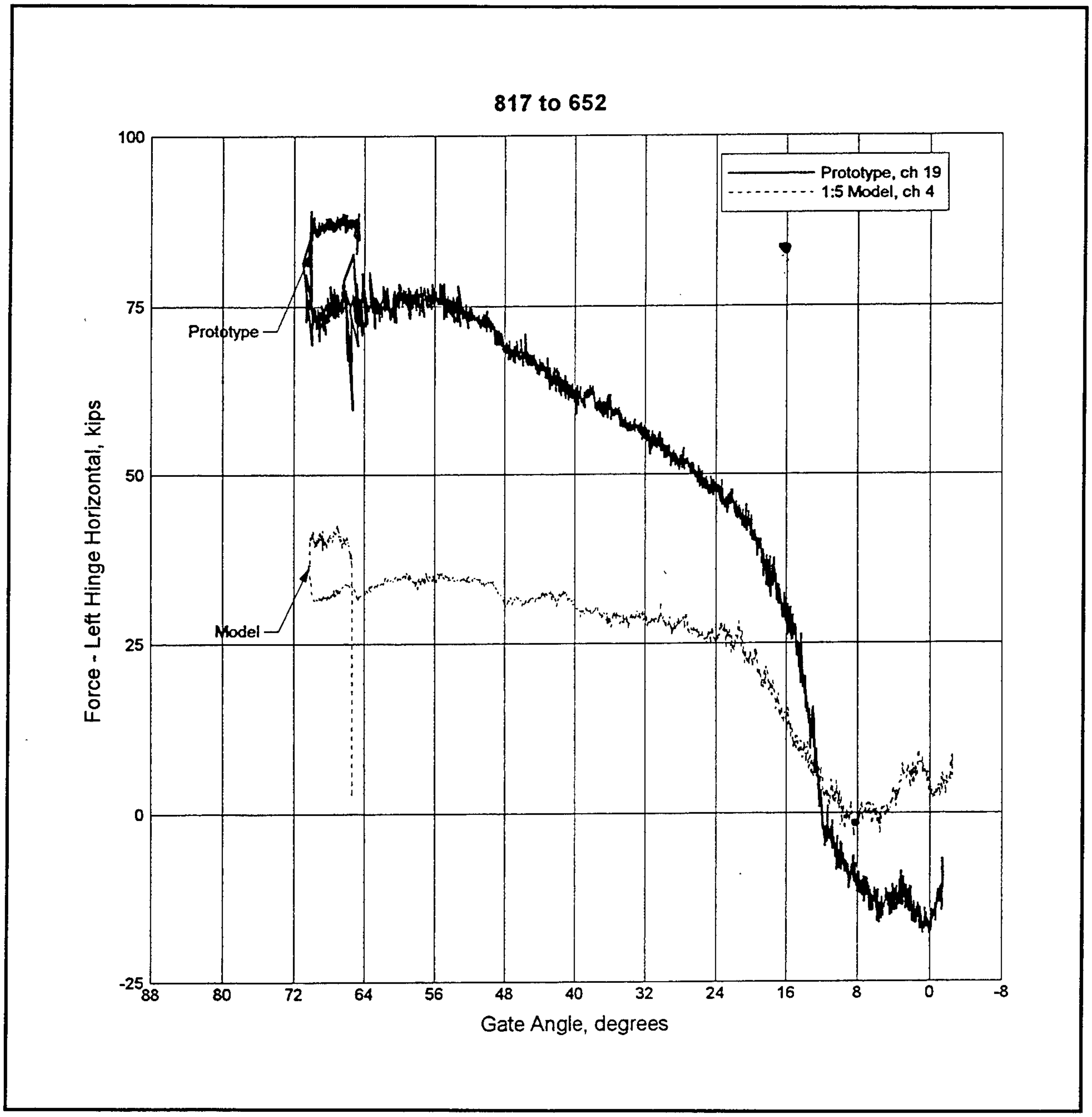

Figure C44. Left hinge horizontal force vs gate position for 2-GG (EL) down condition

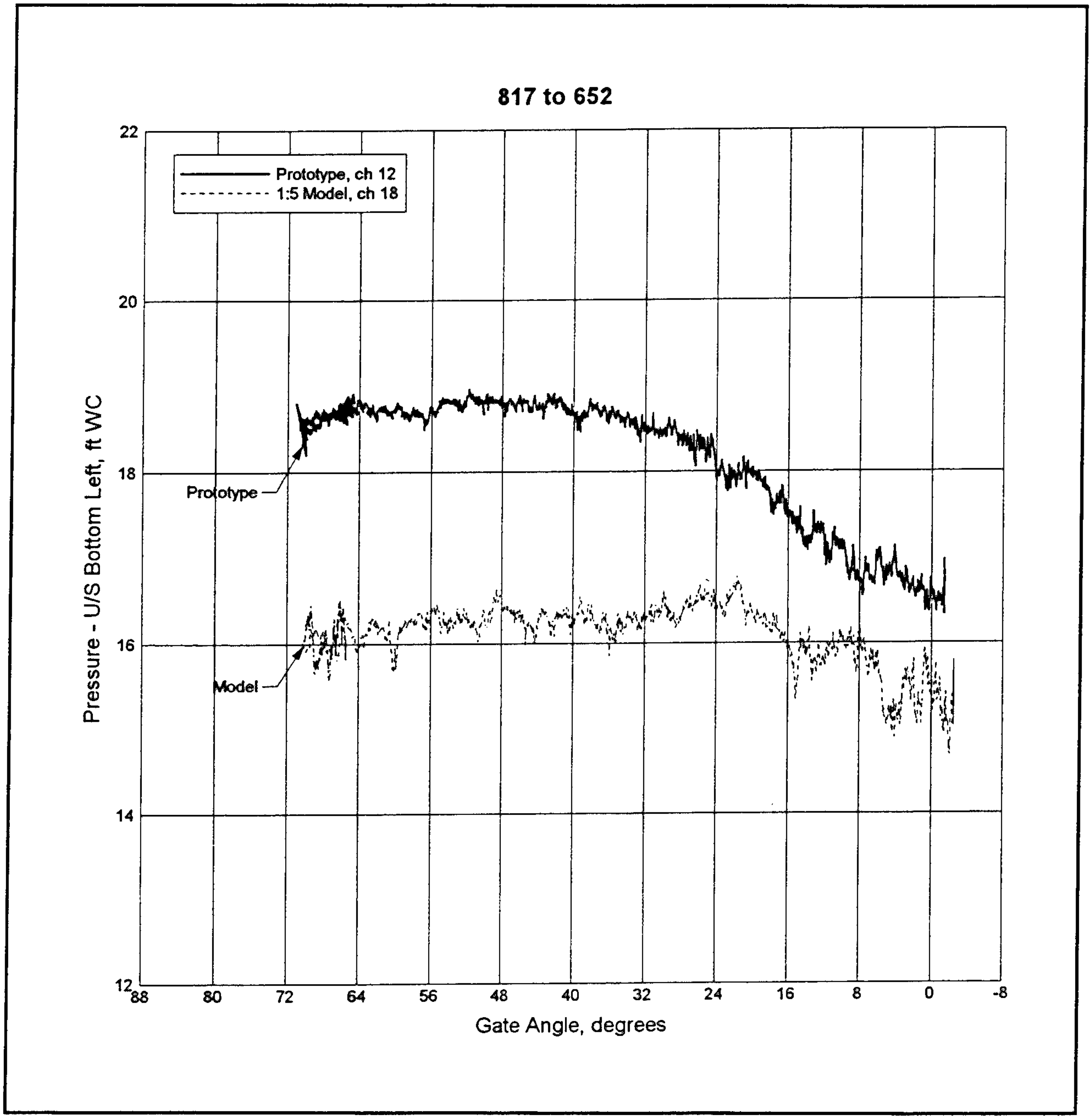

Figure C45. Upstream bottom left pressure vs gate position for 2-GG (EL) down condition

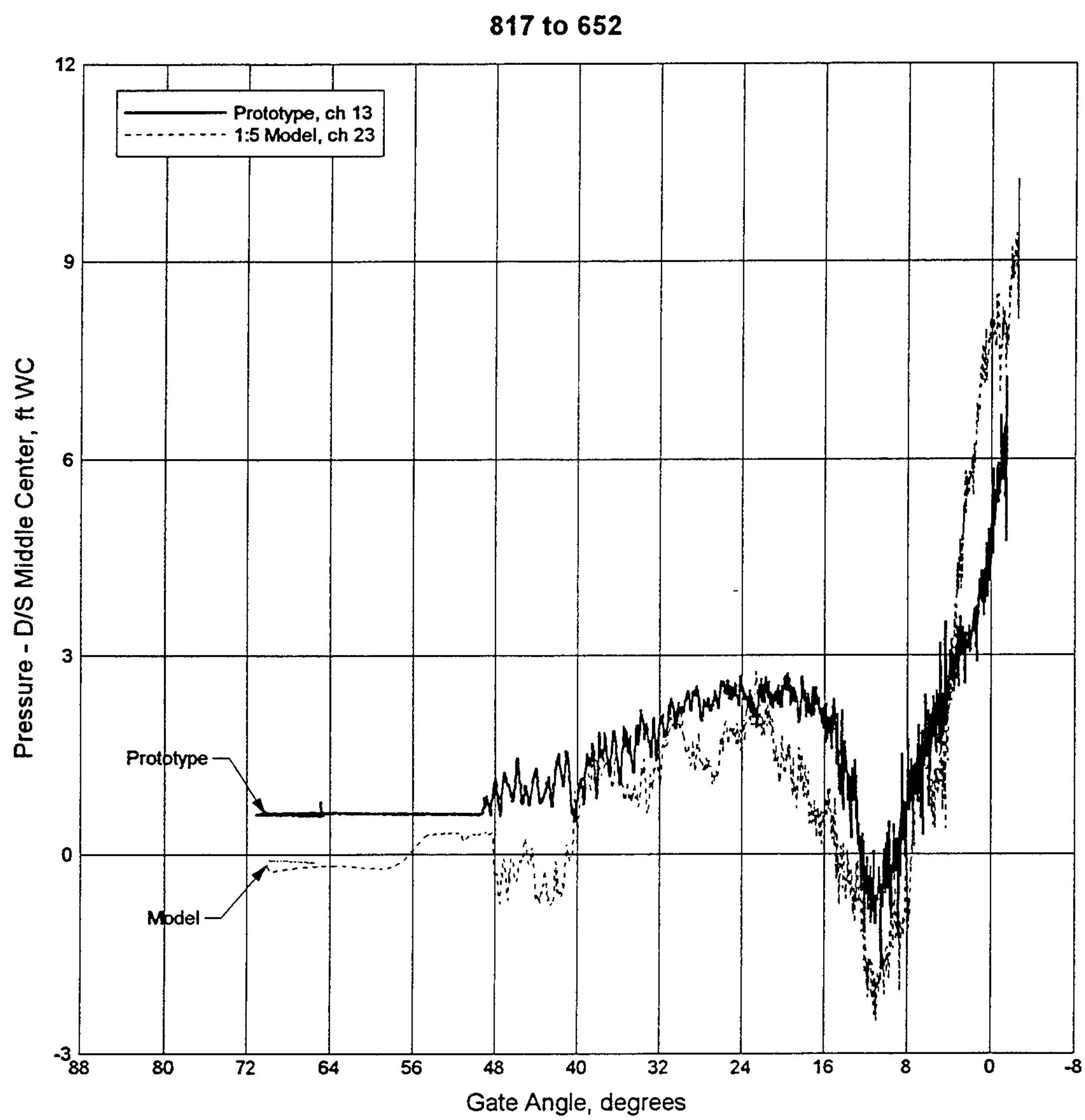

Figure C46. Downstream middle center pressure vs gate position for 2-GG (EL) down condition

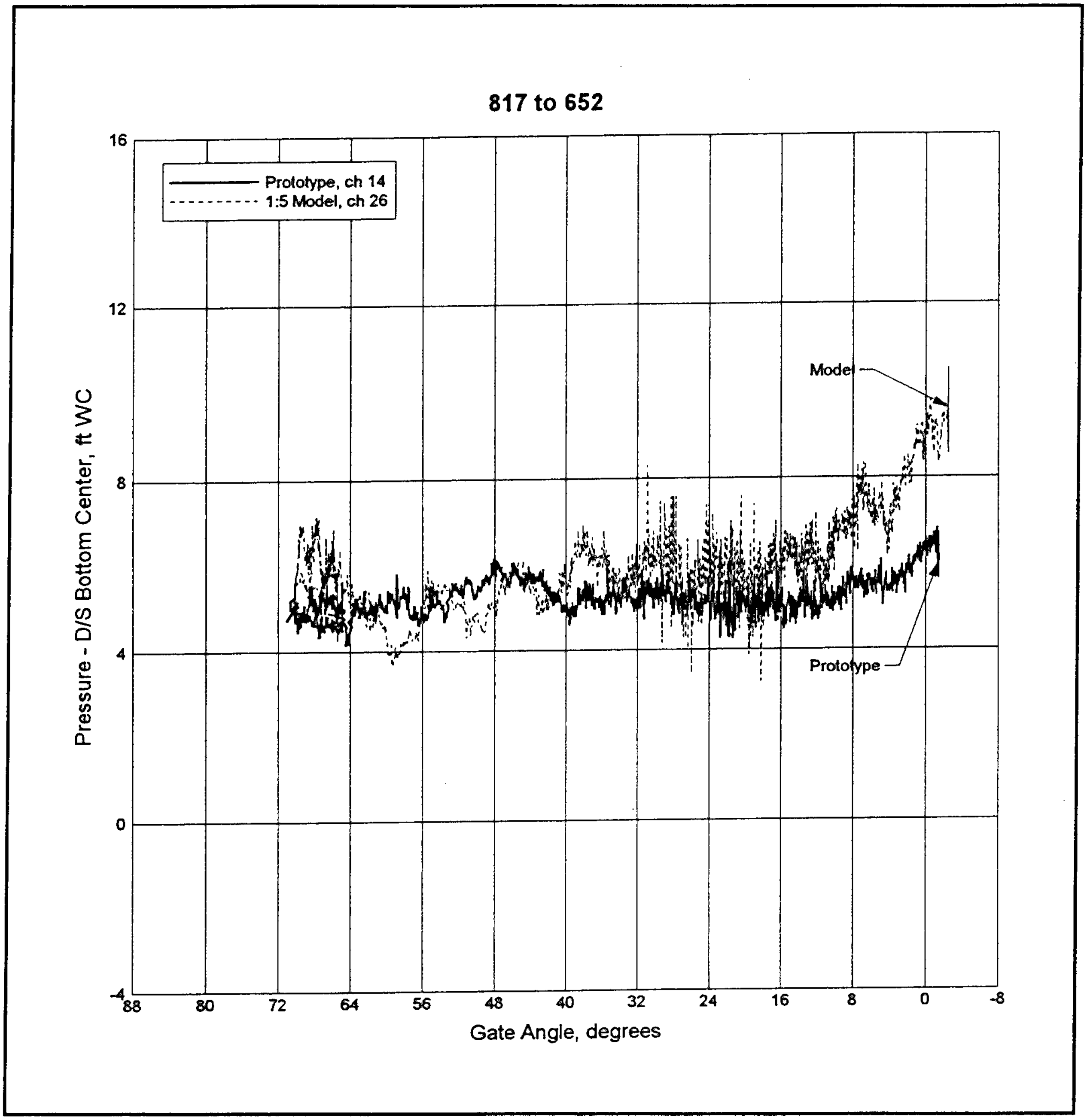

Figure C47. Downstream bottom center pressure vs gate position for 2-GG (EL) down condition

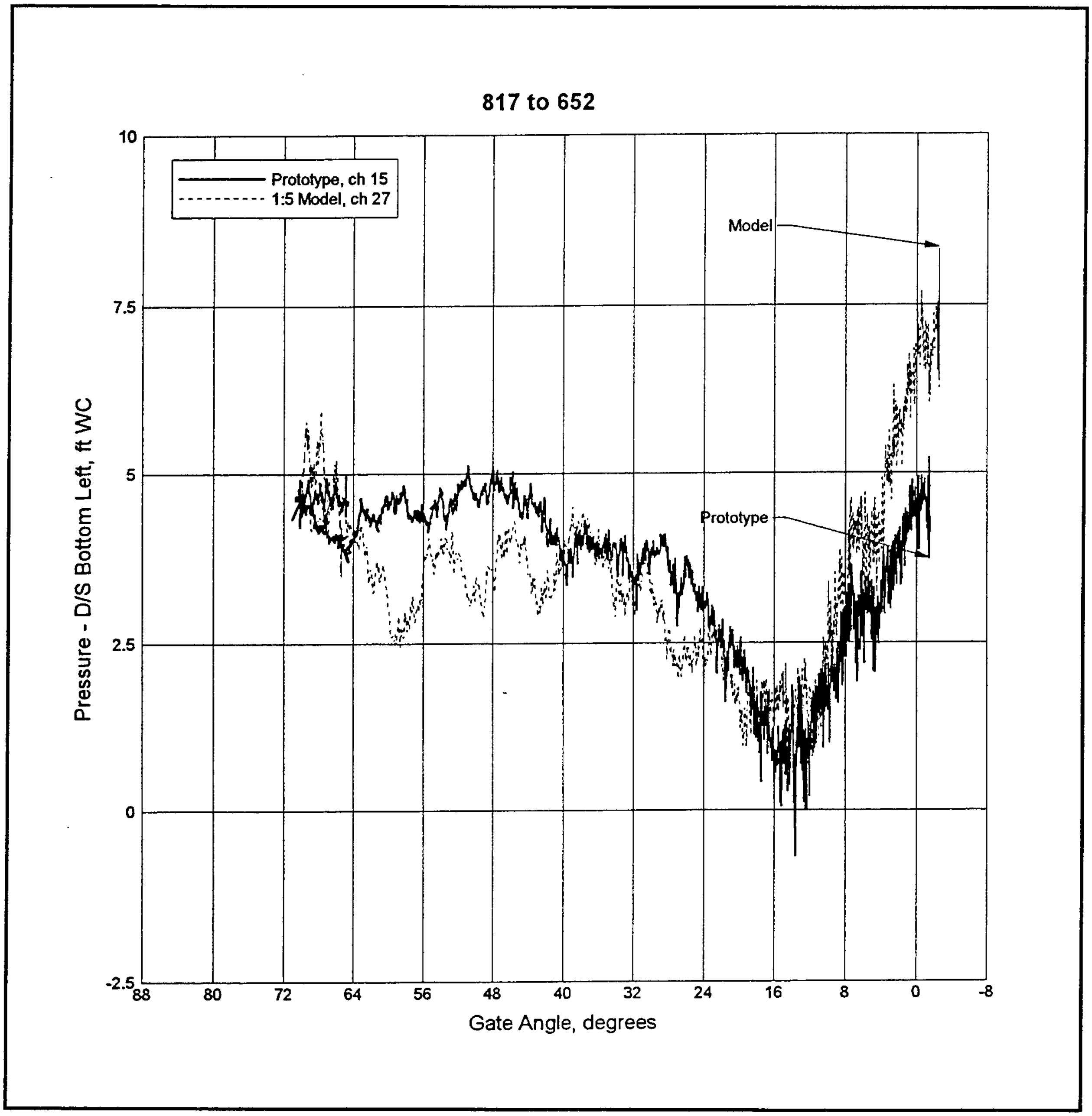

Figure C48. Downstream bottom left pressure vs gate position for 2-GG (EL) down condition

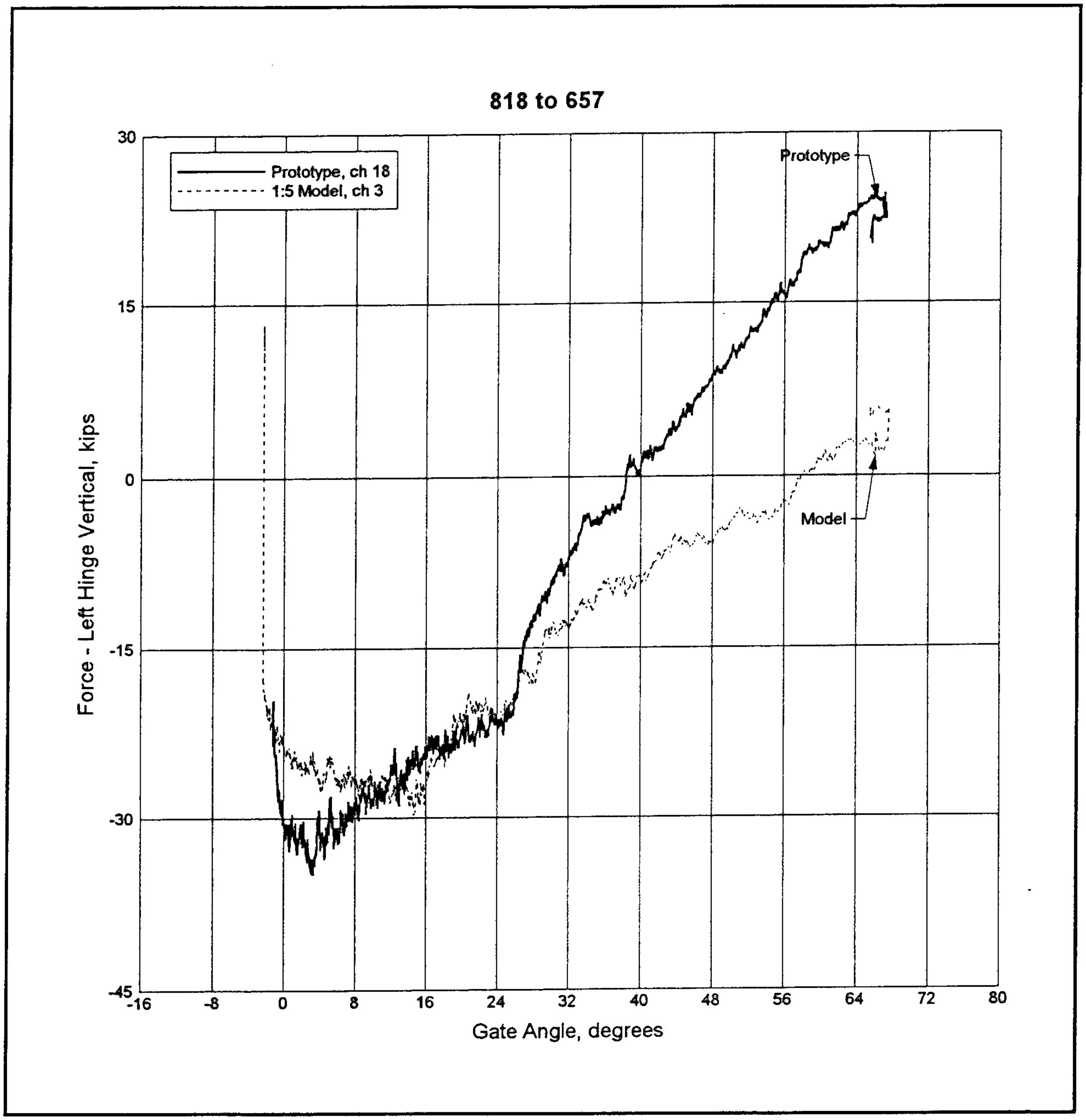

Figure C49. Left hinge vertical force vs gate position for 2-GG (ER) up condition

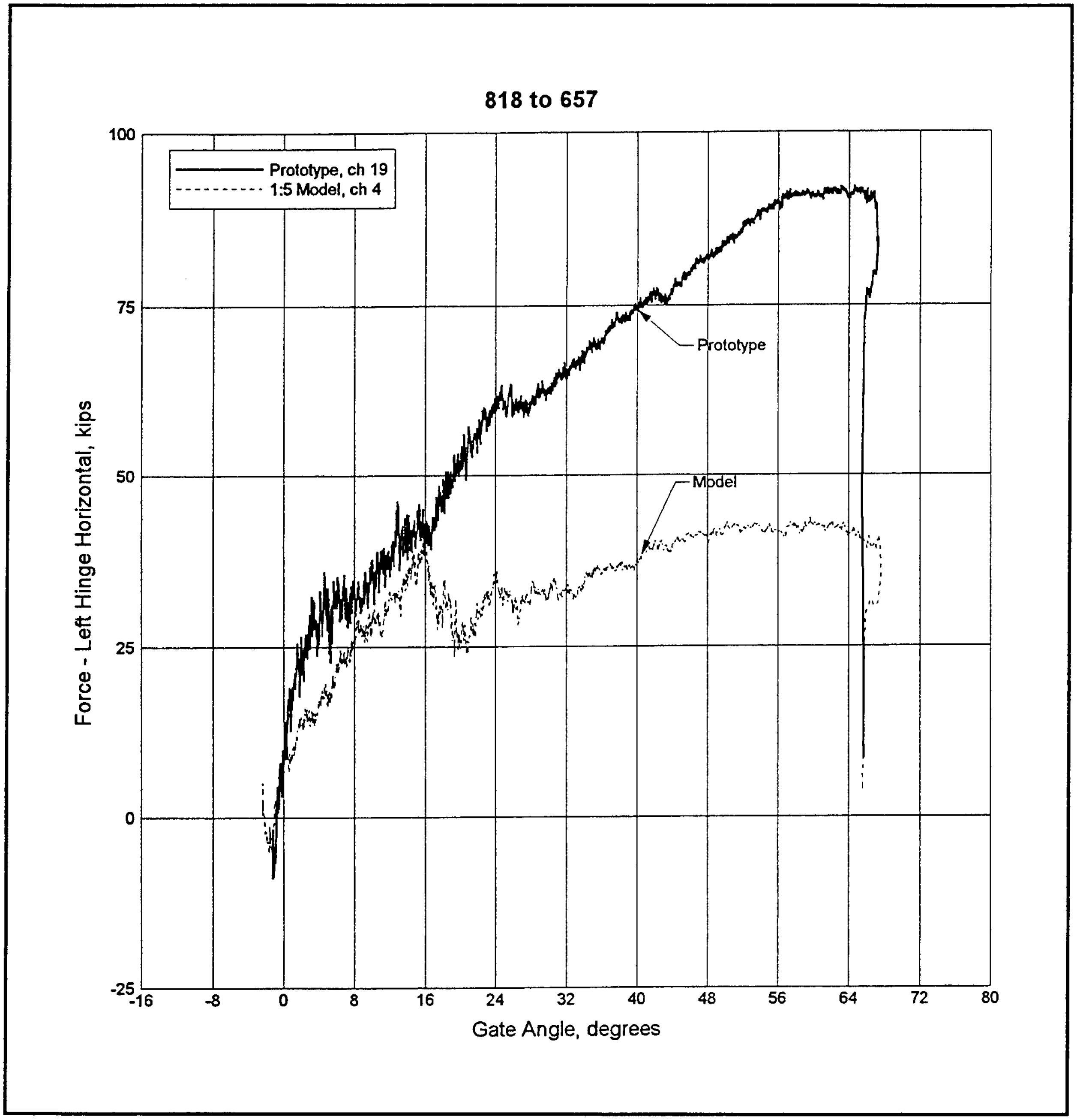

Figure C50. Left hinge horizontal force vs gate position for 2-GG (ER) up condition

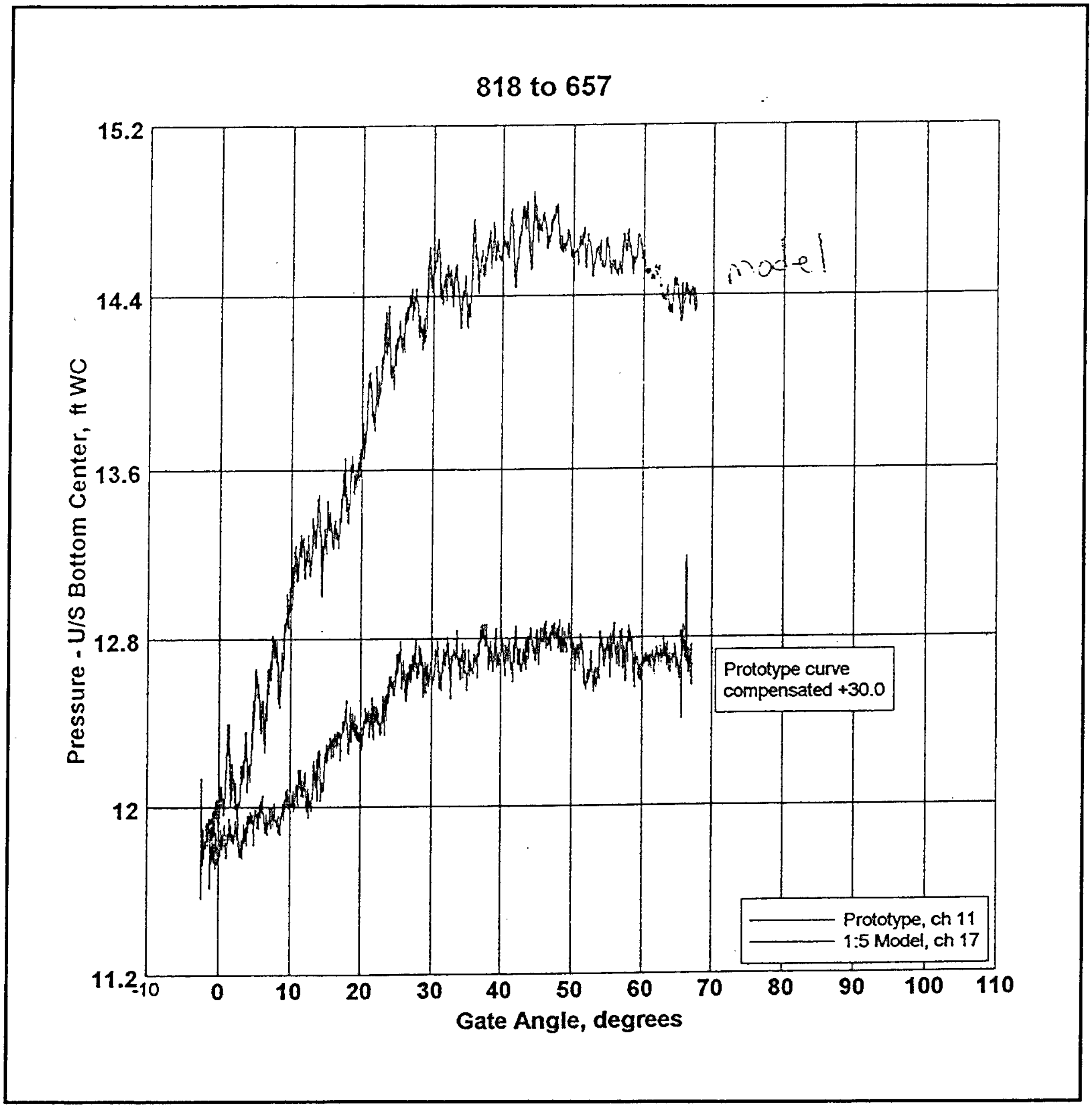

Figure C51. Upstream bottom center pressure vs gate position for 2-GG (ER) up condition

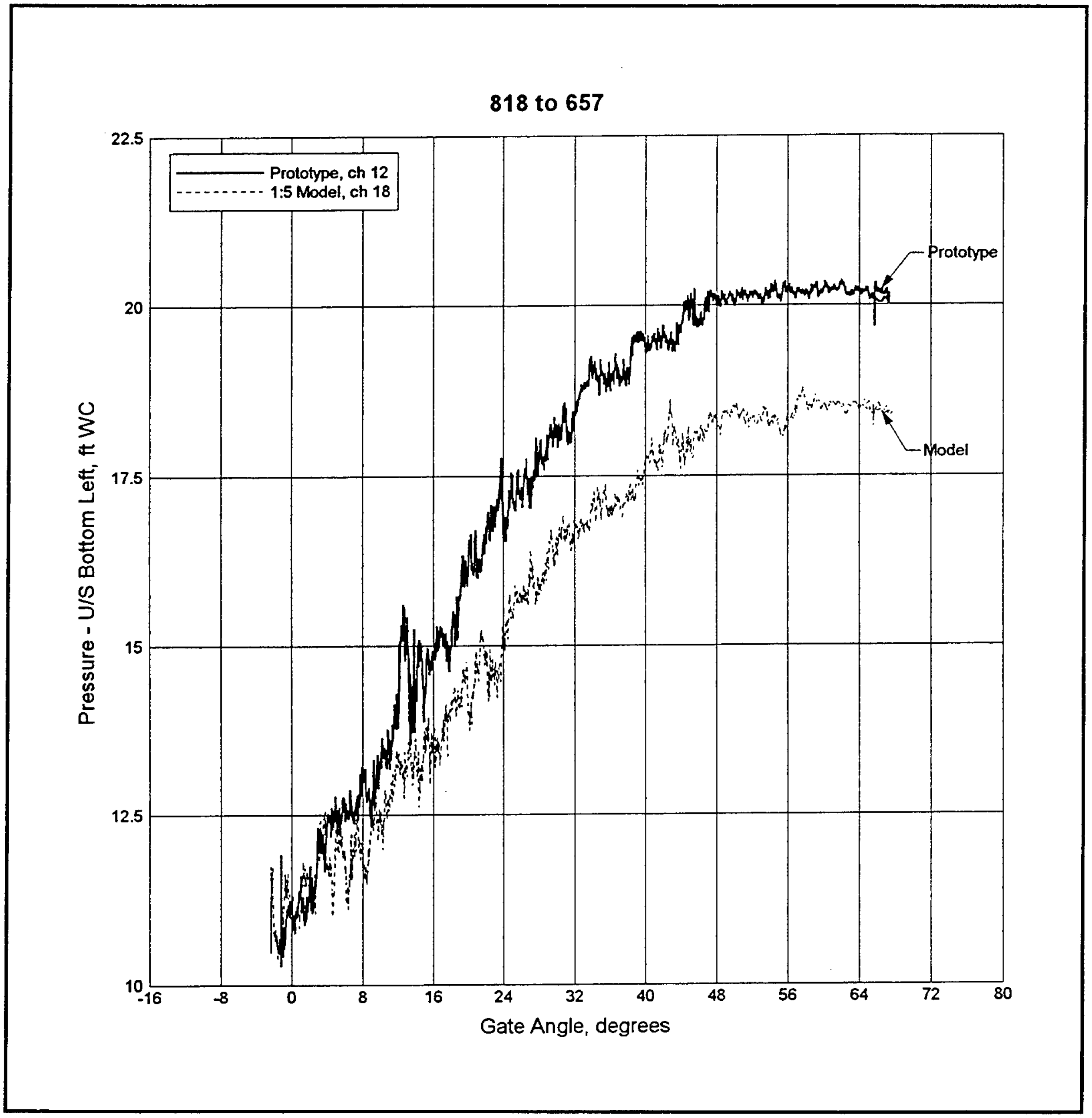

Figure C52. Upstream bottom left pressure vs gate position for 2-GG (ER) up condition

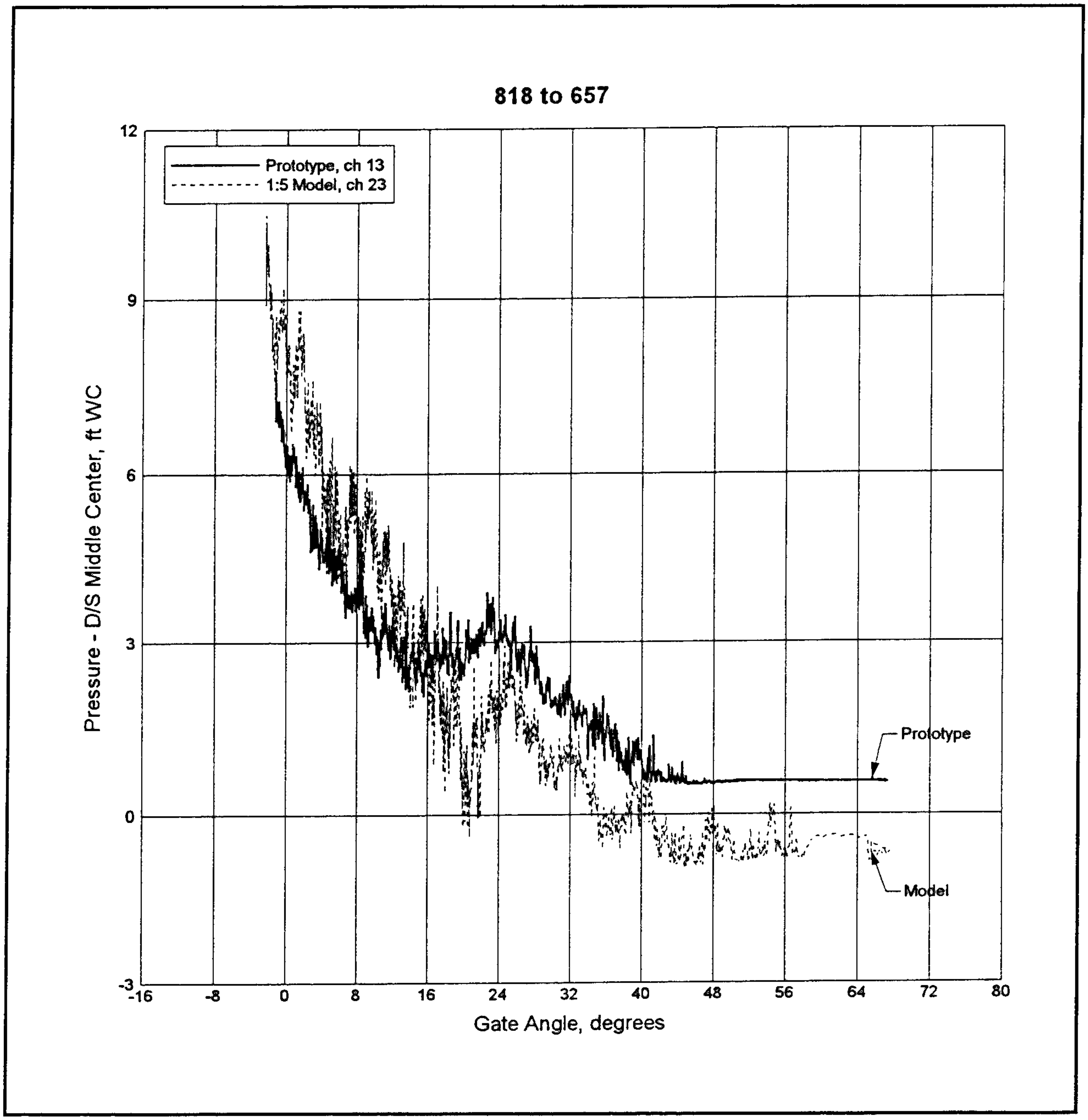

Figure C53. Downstream middle center pressure vs gate position for 2-GG (ER) up condition

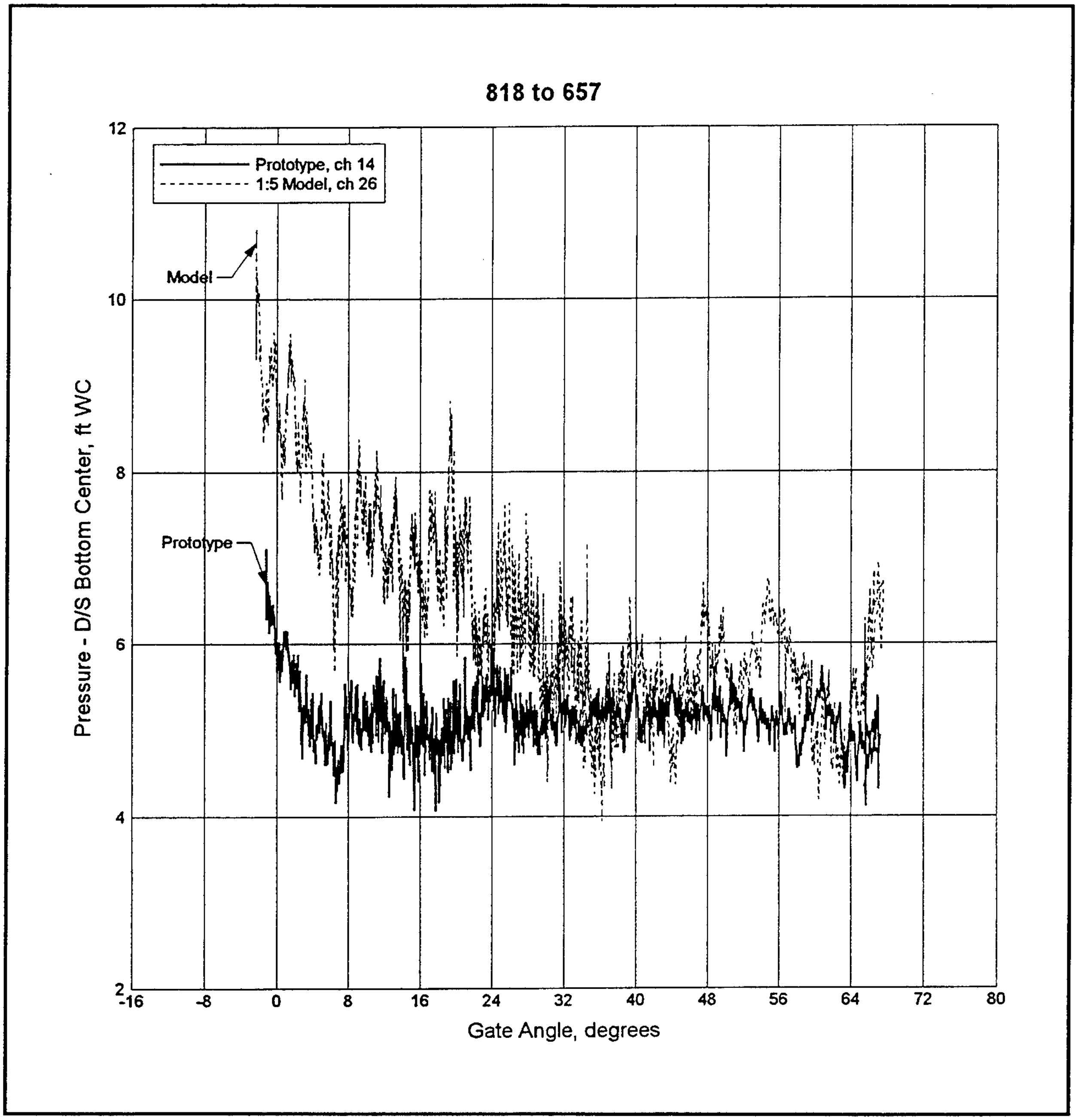

Figure C54. Downstream bottom center pressure vs gate position for 2-GG (ER) up condition

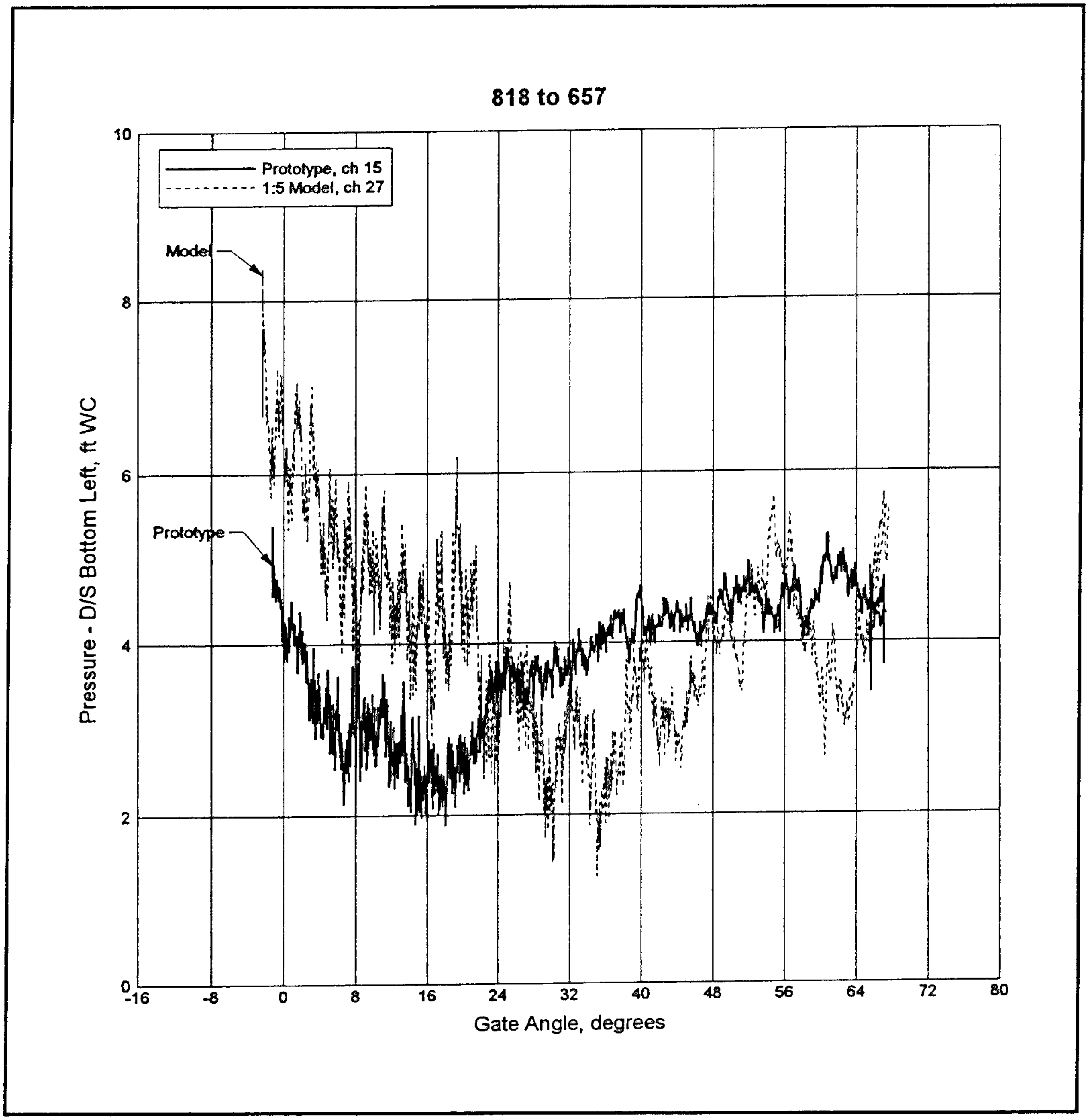

Figure C55. Downstream bottom left pressure vs gate position for 2-GG (ER) up condition

Appendix D Time-Domain Pressure and Acceleration Plots— Prototype Composite vs 1:5 Model

Selected time-domain pressure and acceleration history of the prototype composite and 1:5-scale model wickets for seven different flow configurations (test groups 8 to 14 in Table 5, main text) are compared in this appendix. Each plot shows the test numbers for which the results are presented. Note that the composite gate acceleration always displays a higher fluctuation than the model. Unlike the steel gate geometry, the composite gate had a box-type transverse section (see Figure 10, main text). The composite gate was designed such that it is compatible and interchangeable in any of the five gate stations in the prototype facility. Thus, the supporting devices were independent of the wicket types. A detailed discussion of the design guidelines for the composite gate is presented elsewhere (Chowdhury et al. 1997).

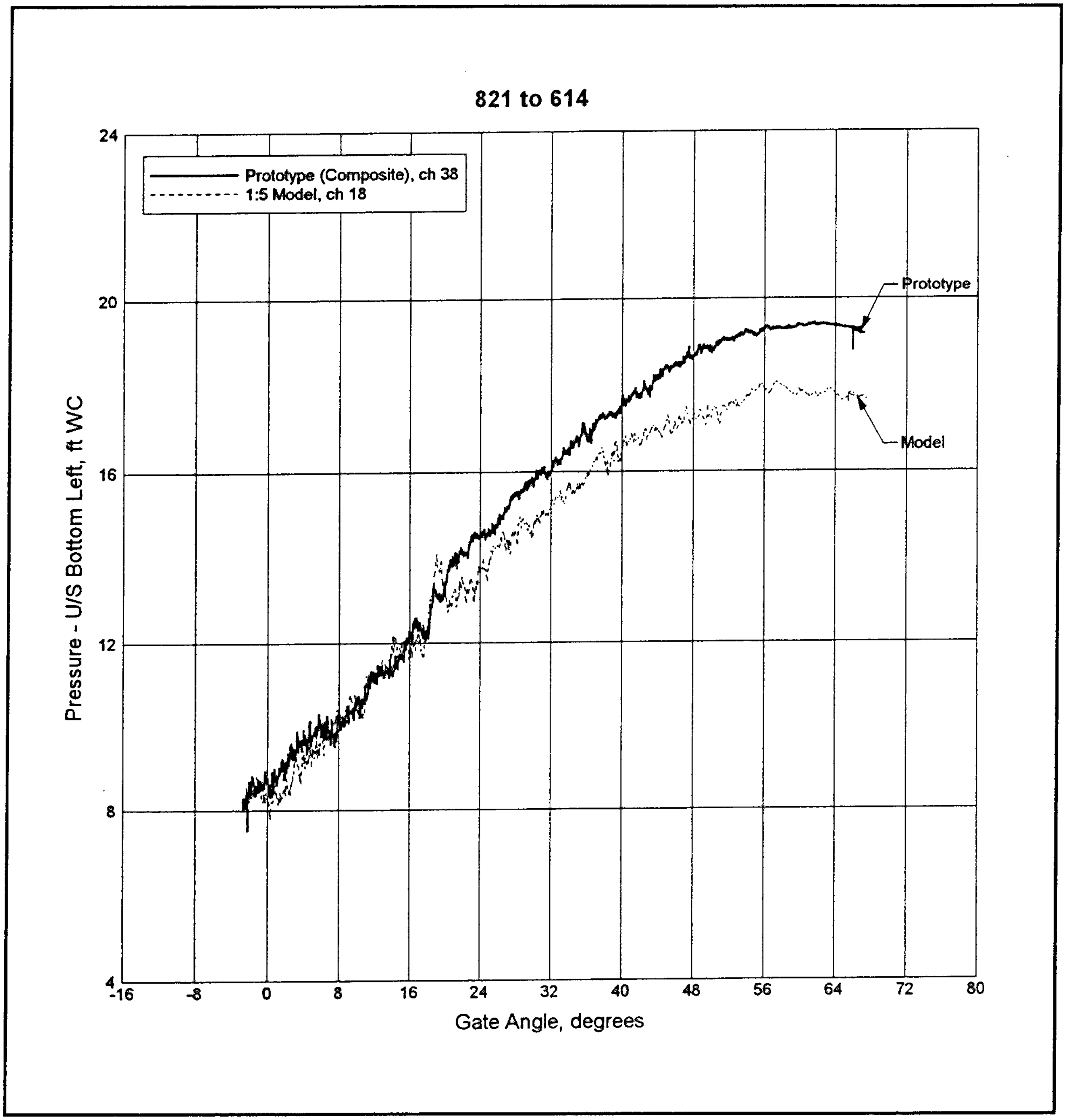

Figure D1. Upstream bottom left pressure variation for 1-GG up condition

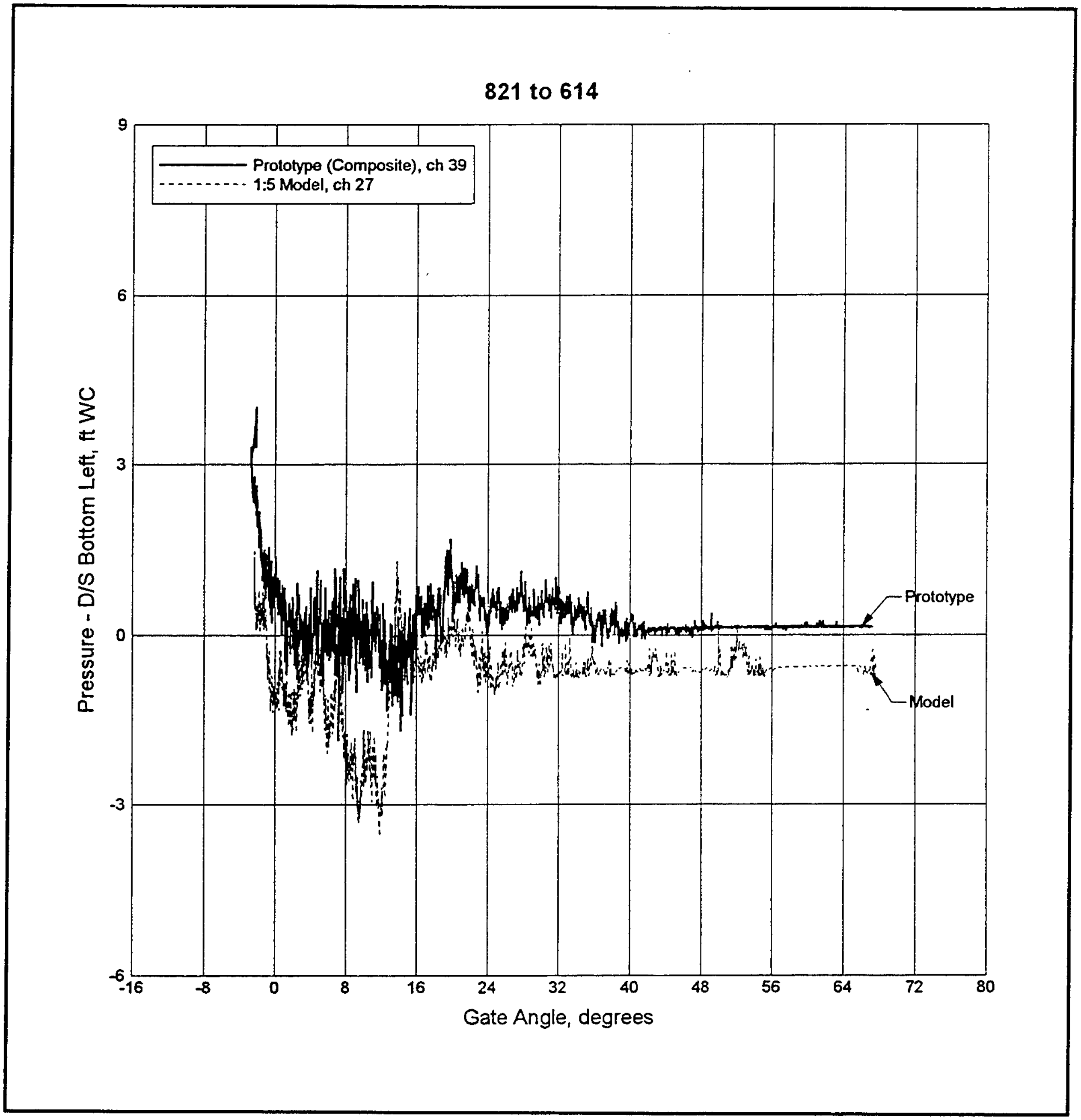

Figure D2. Downstream bottom left pressure variation for 1-GG up condition

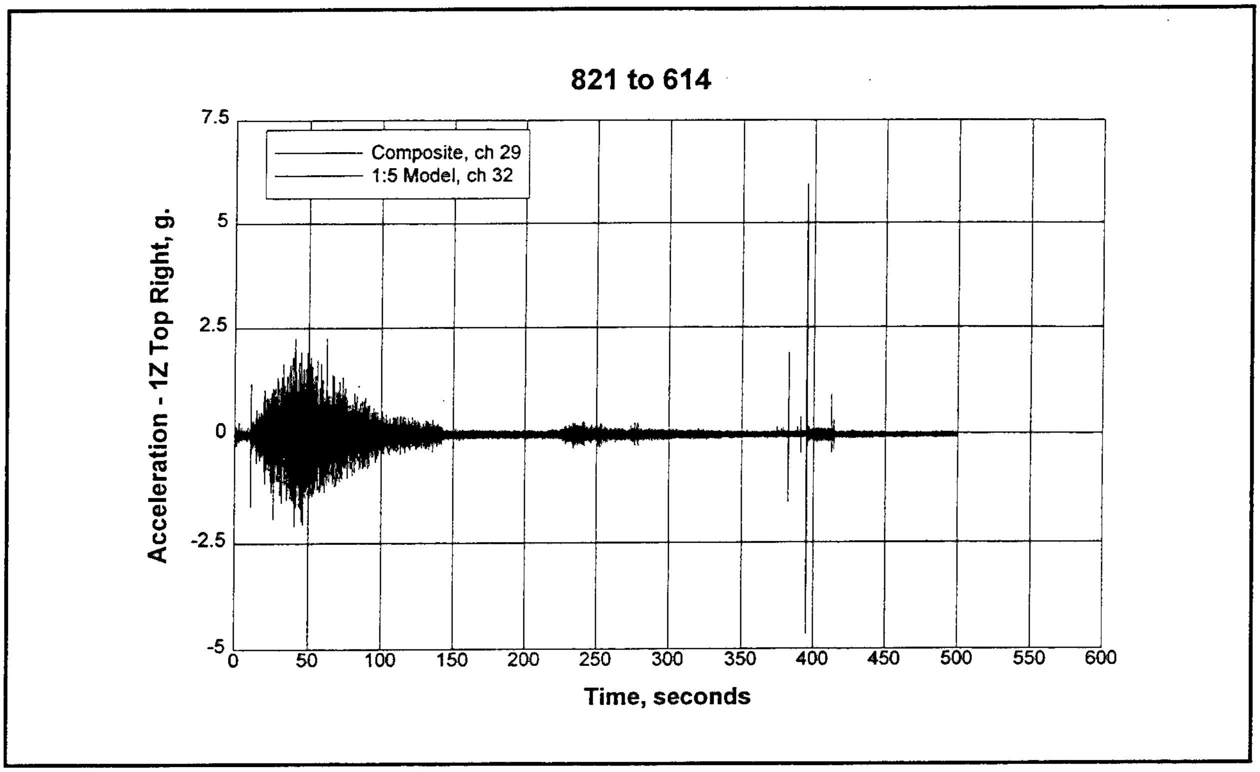

Figure D3. 1Z top right acceleration response of composite and model wickets for 1-GG up condition

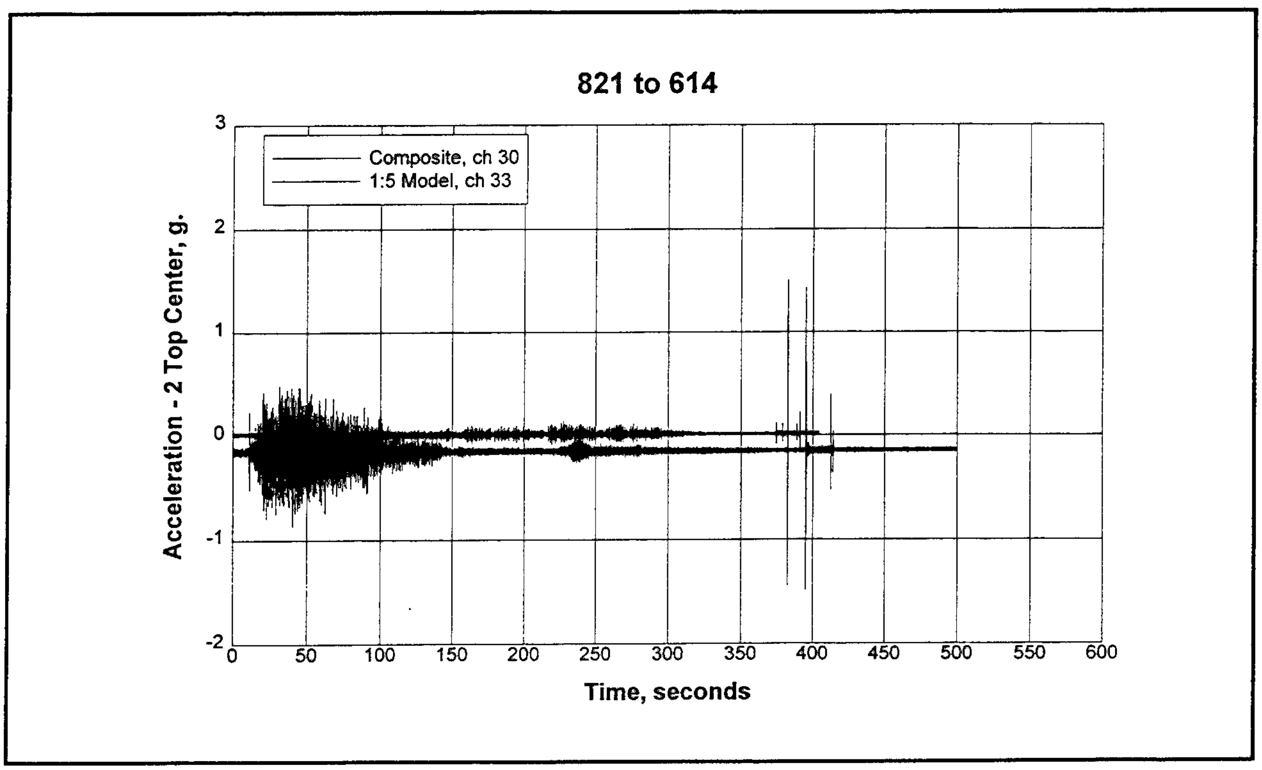

Figure D4. 2 top center acceleration response of composite and model wickets for 1-GG up condition

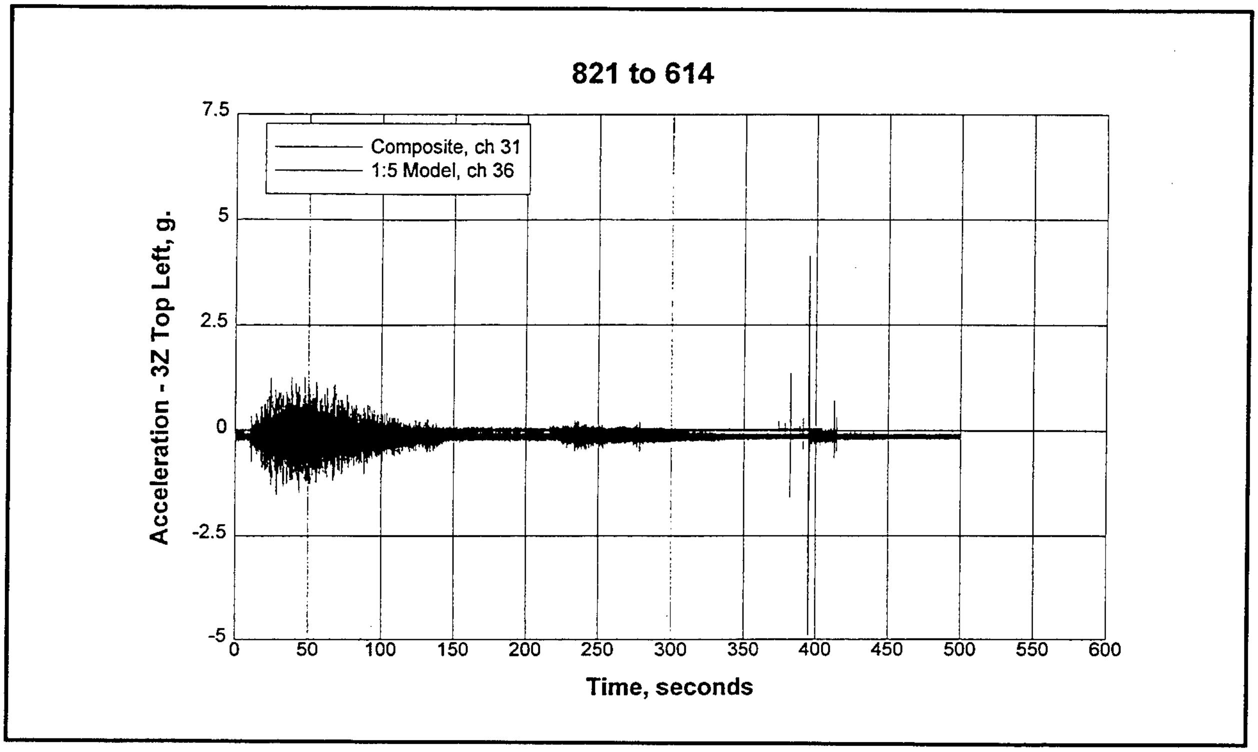

Figure D5. 3Z top left acceleration response of composite and model wickets for 1-GG up condition

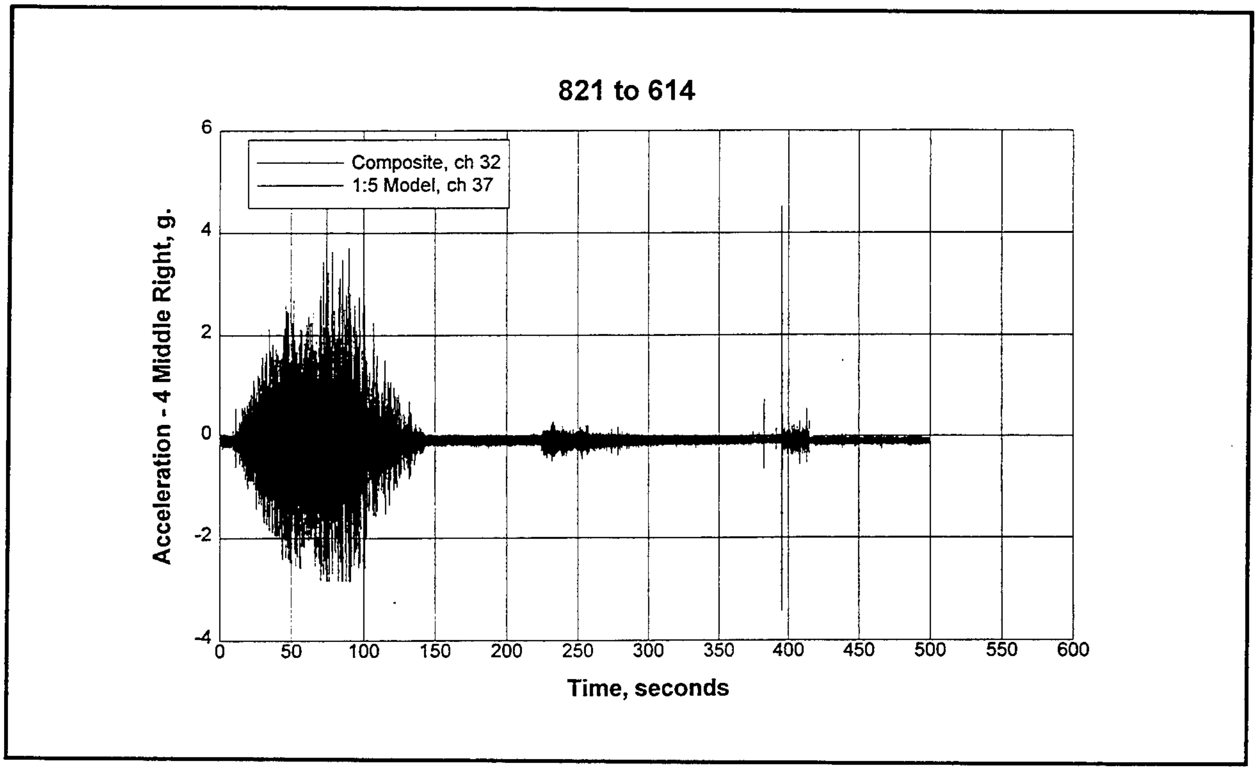

Figure D6. 4 middle right acceleration response of composite and model wickets for 1-GG up condition

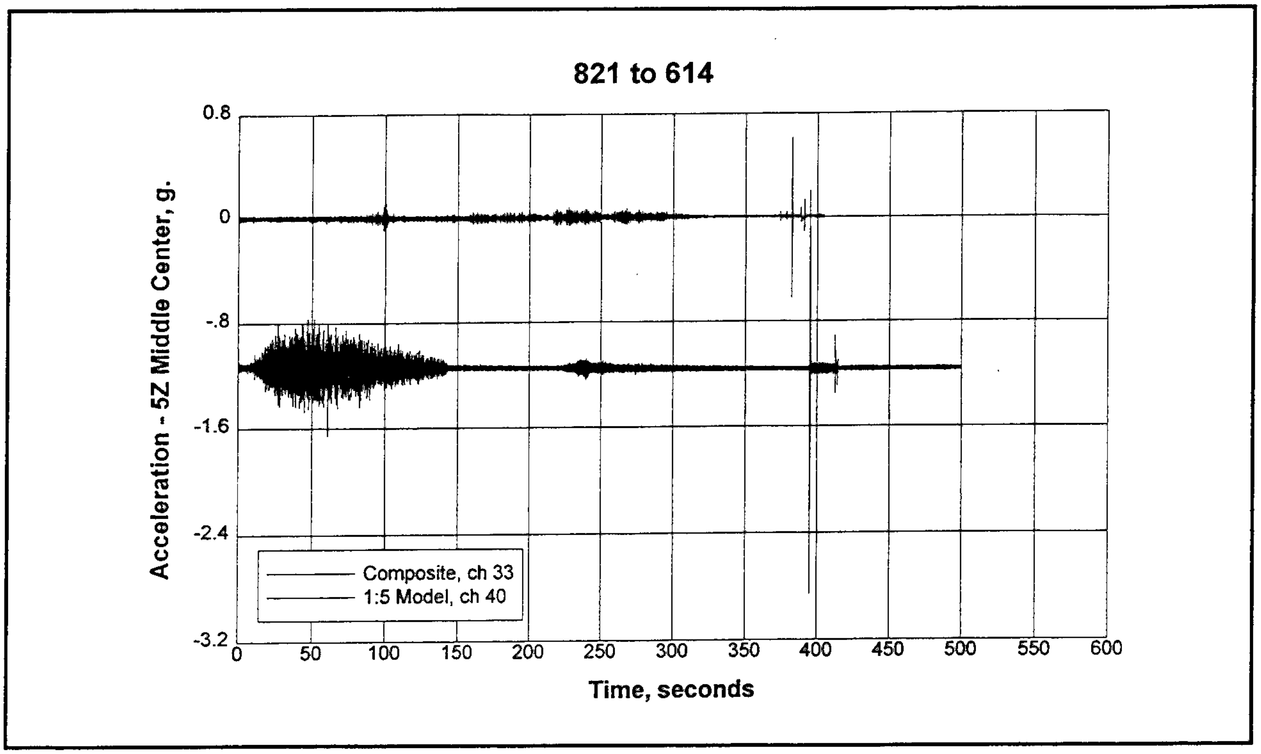

Figure D7. 5Z middle center acceleration response of composite and model wickets for 1-GG up condition

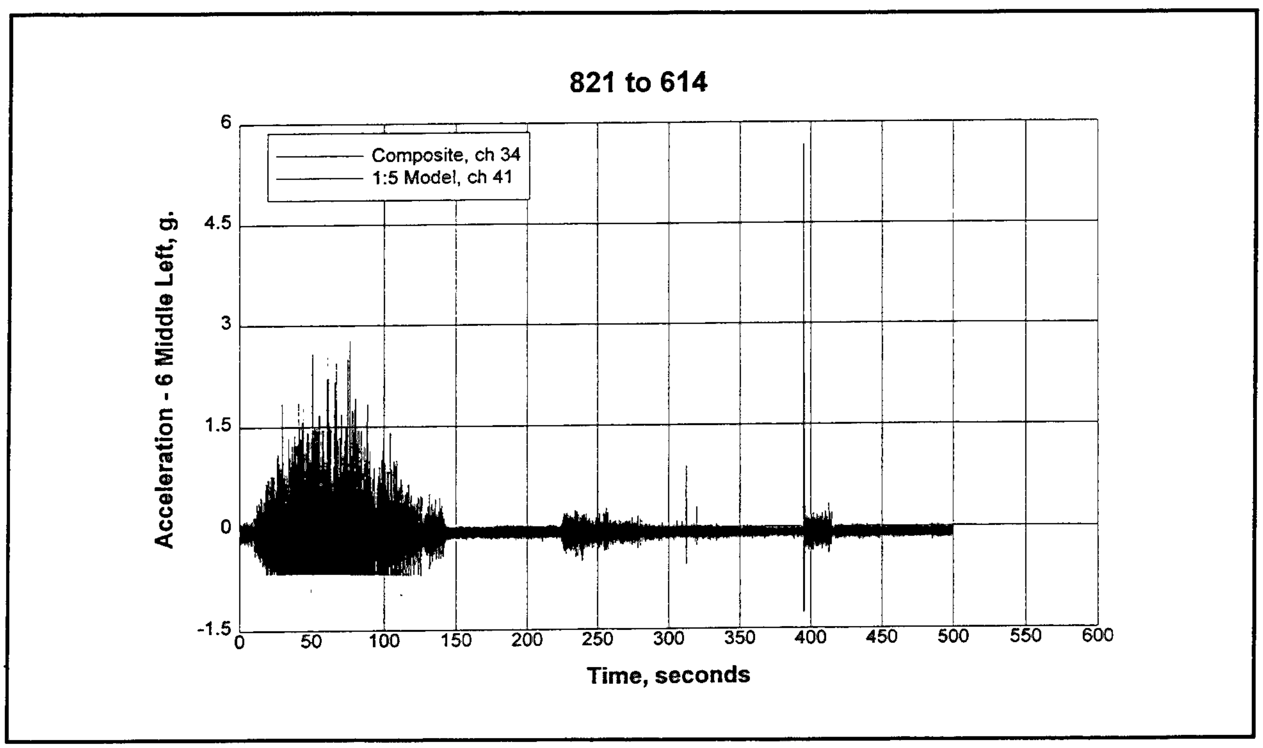

Figure D8. 6 middle left acceleration response of composite and model wickets for 1-GG up condition

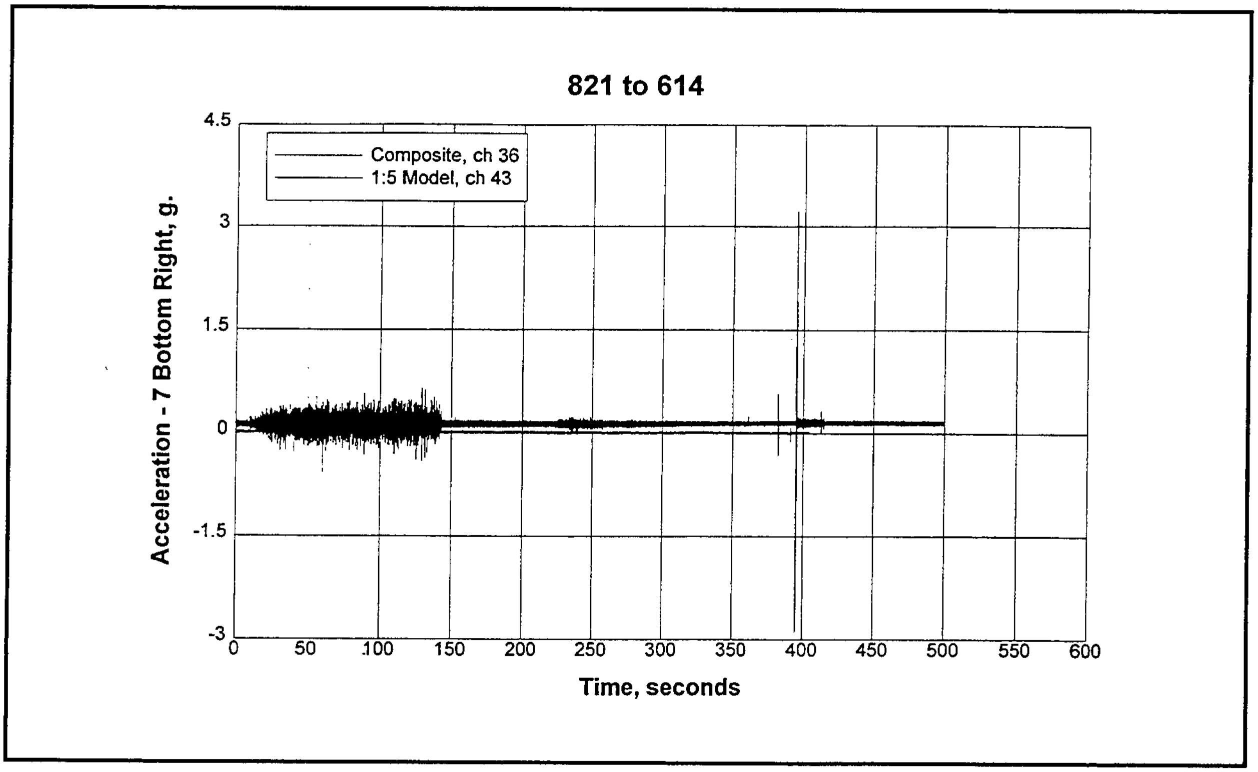

Figure D9. 7 bottom right acceleration response of composite and model wickets for 1-GG up condition

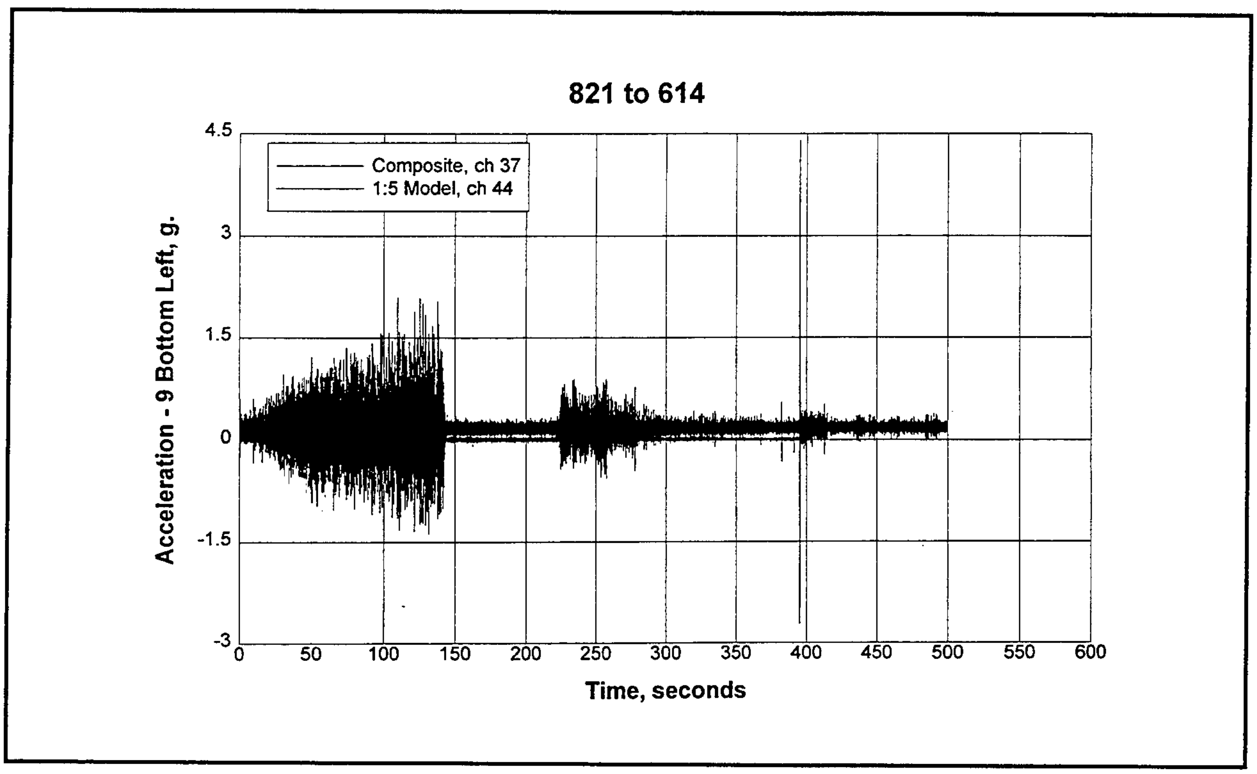

Figure D10. 9 bottom left acceleration response of composite and model wickets for 1-GG up condition

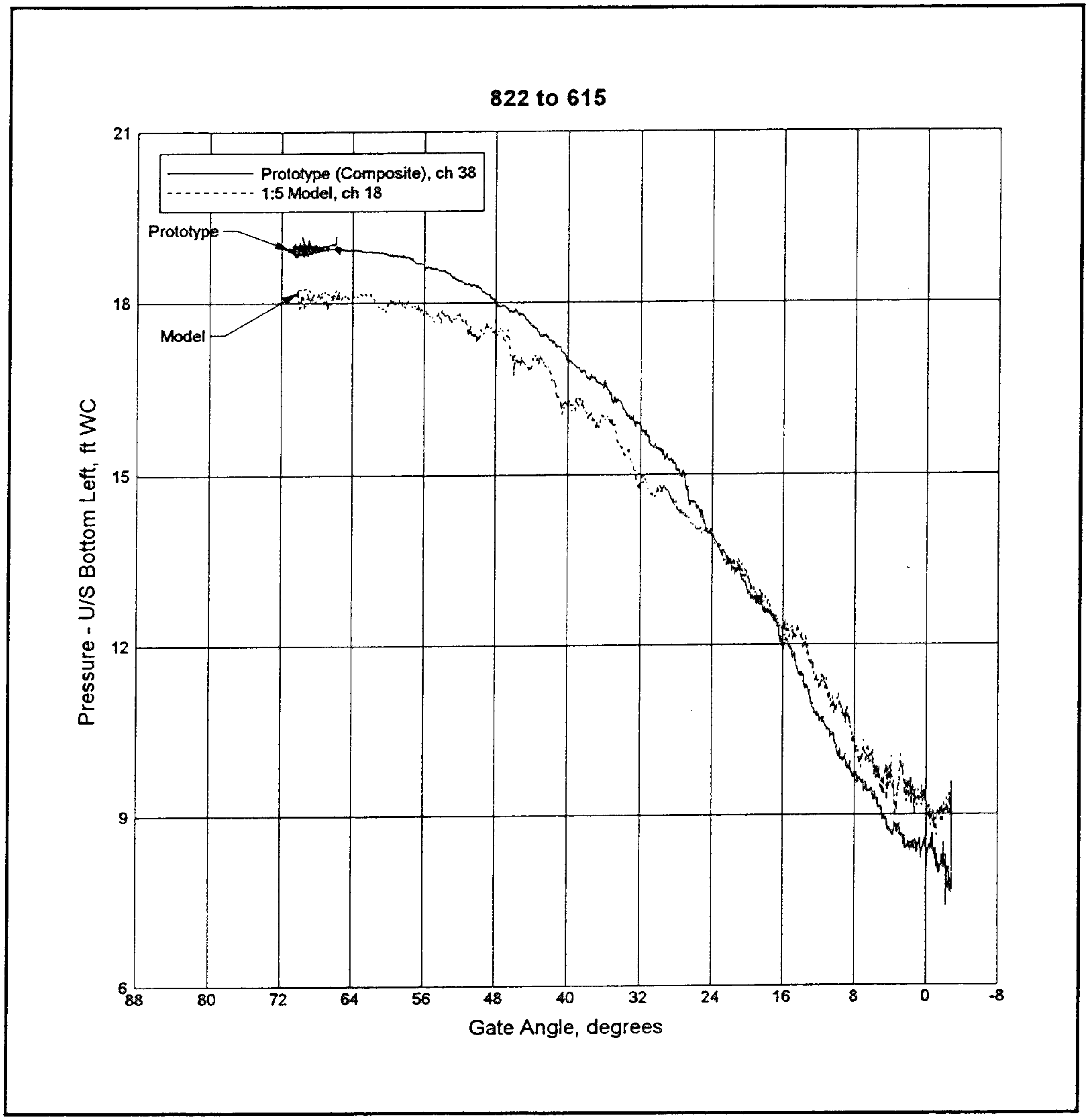

Figure D11. Upstream bottom left pressure variation for 1-GG down condition

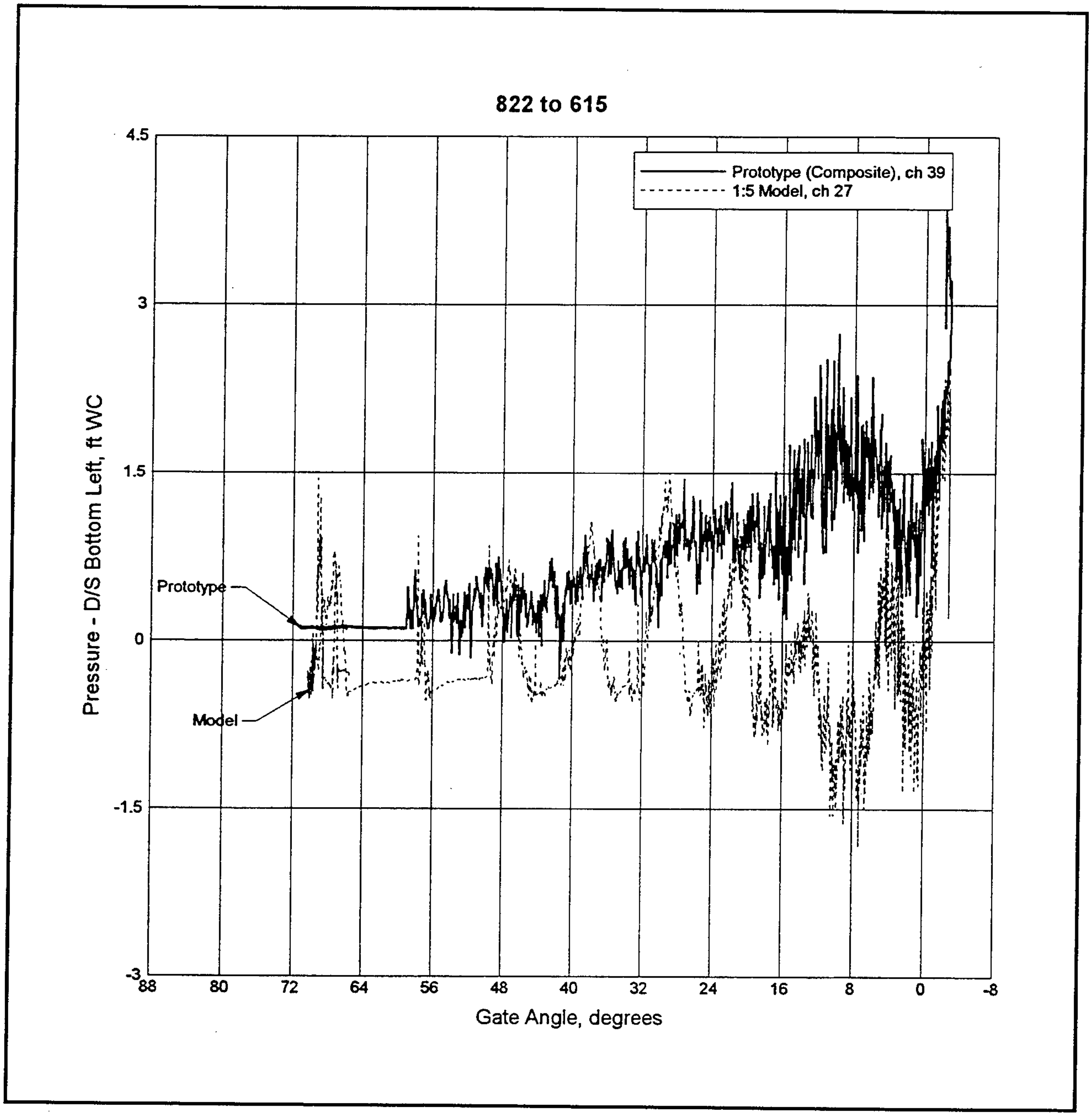

Figure D12. Downstream bottom left pressure variation for 1-GG down condition

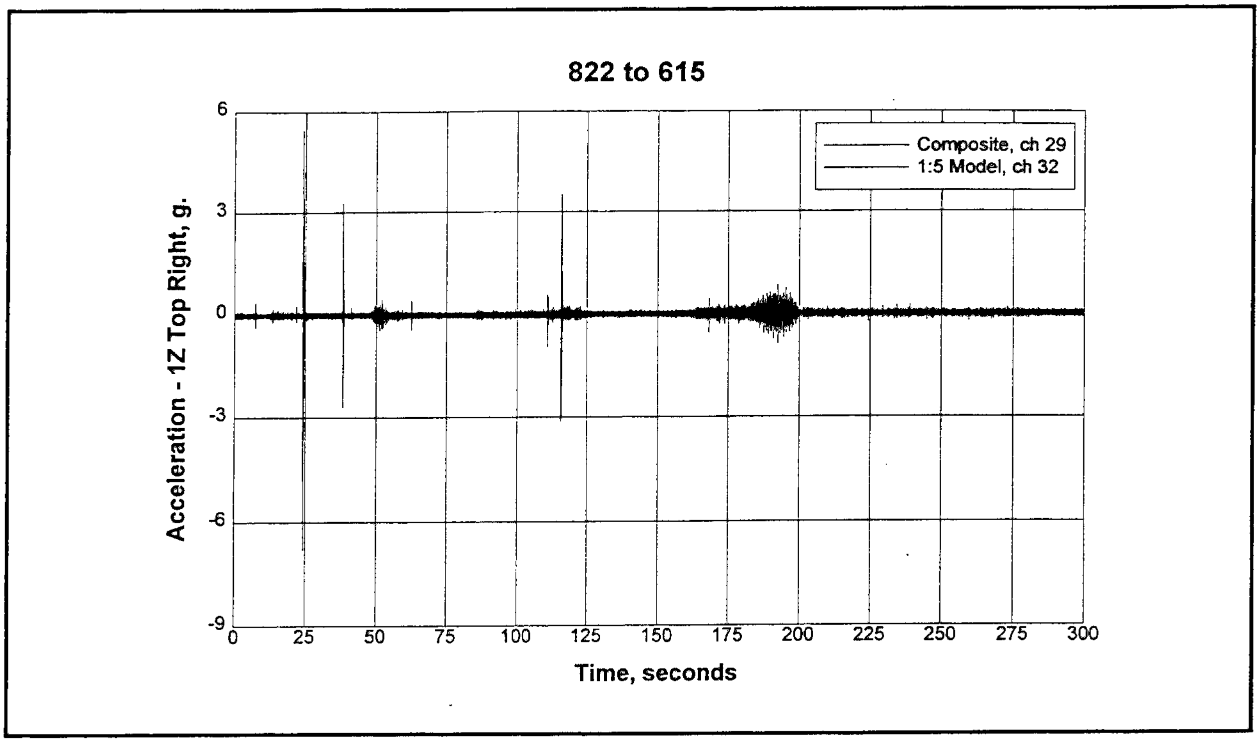

Figure D13. 1Z top right acceleration response of composite and model wickets for 1-GG down condition

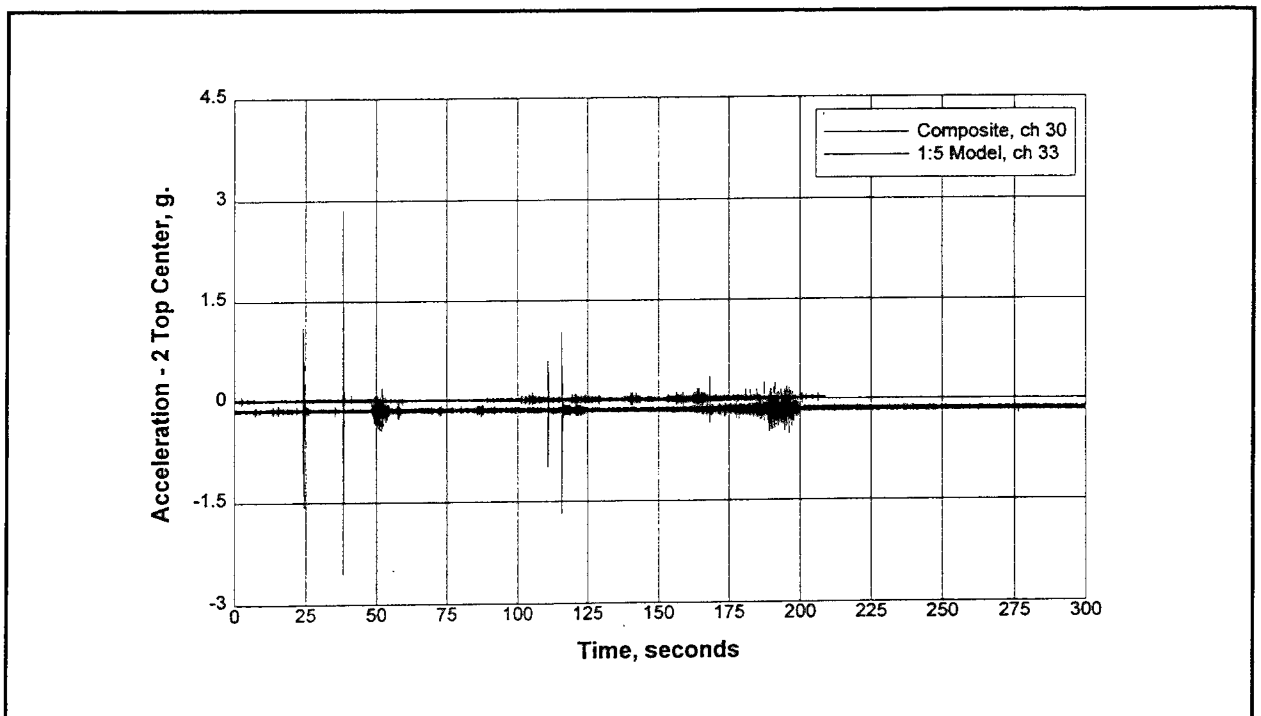

Figure D14. 2 top center acceleration response of composite and model wickets for 1-GG down condition

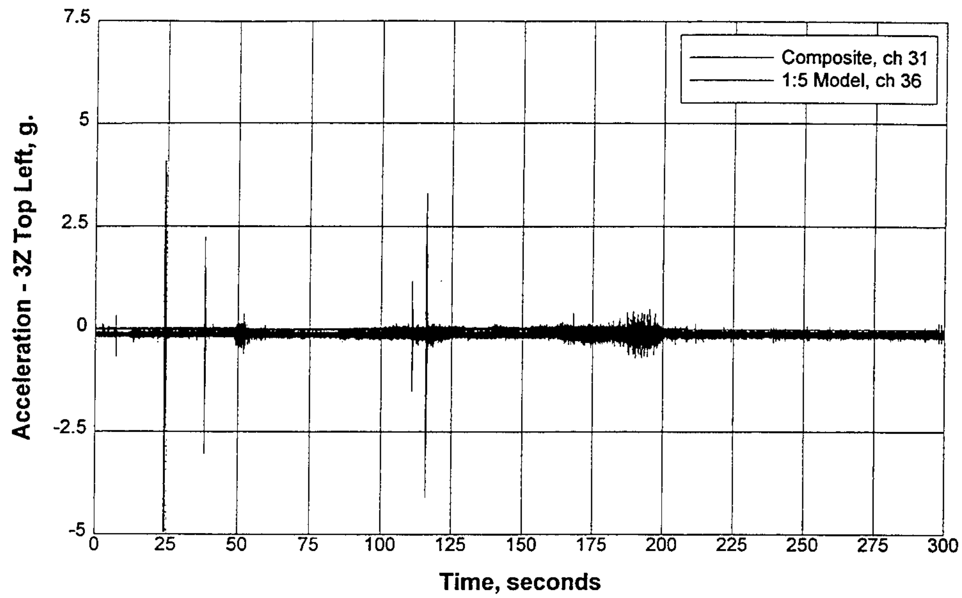

Figure D15. 3Z top left acceleration response of composite and model wickets for 1-GG down condition

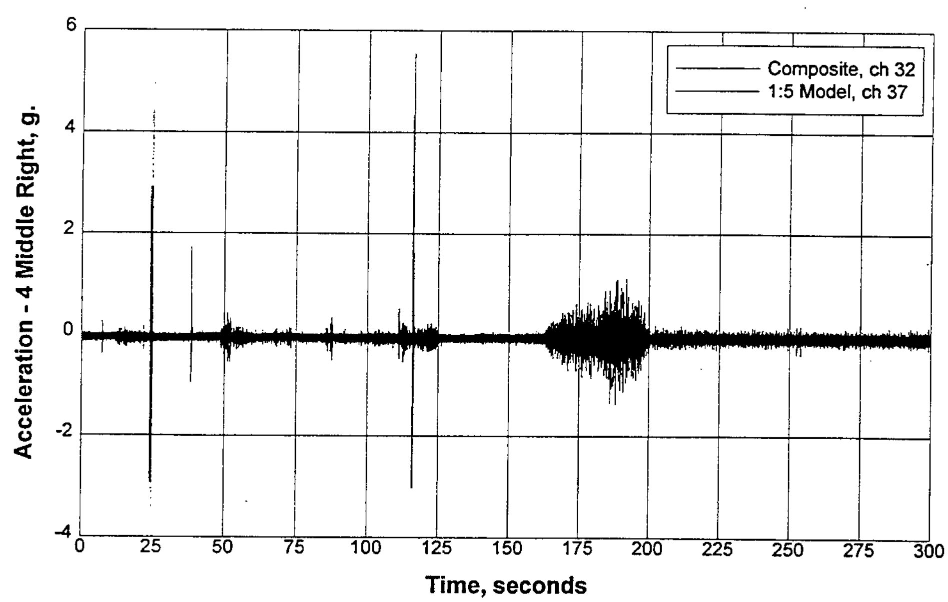

Figure D16. 4 middle right acceleration response of composite and model wickets for 1-GG down condition

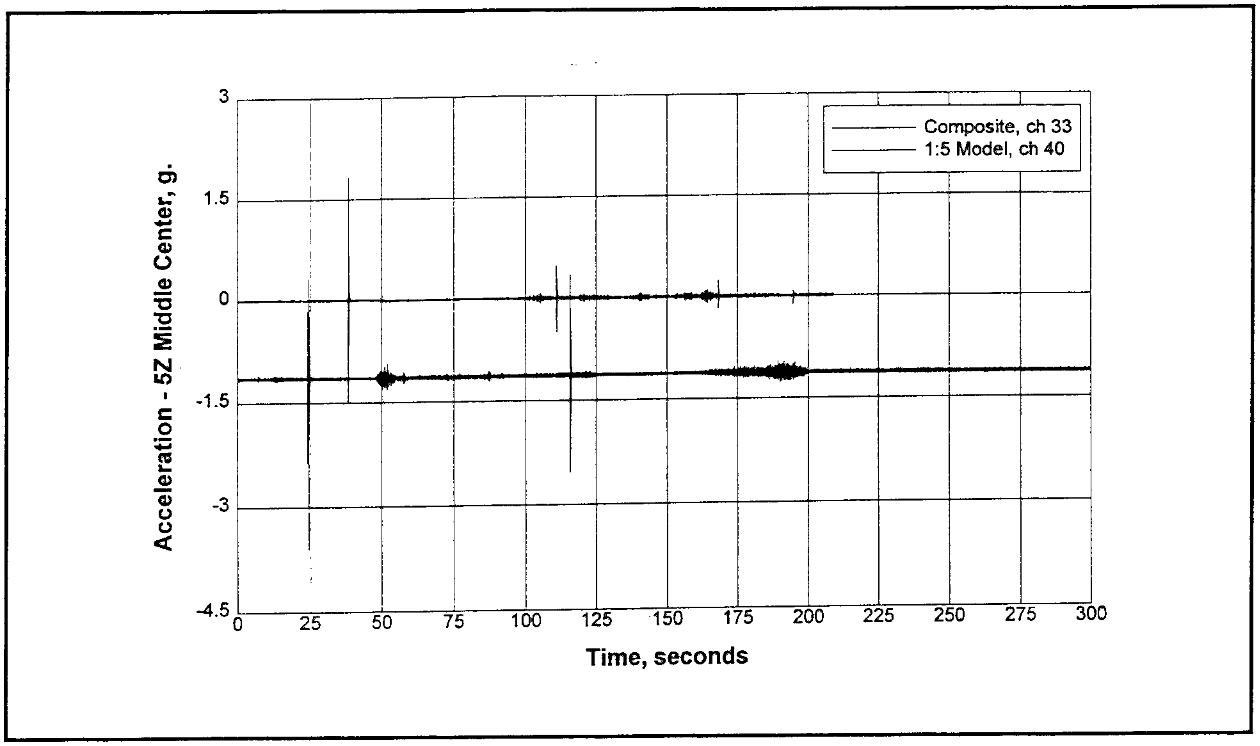

Figure D17. 5Z middle center acceleration response of composite and model wickets for 1-GG down condition

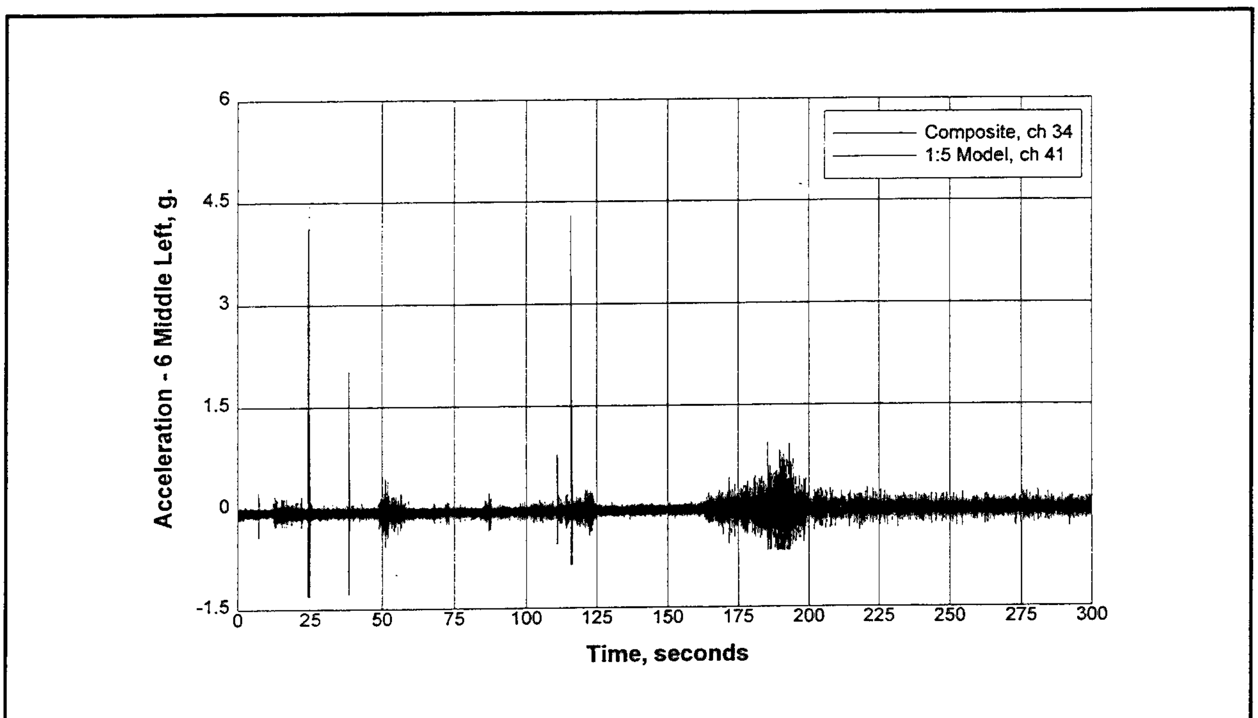

Figure D18. 6 middle left acceleration response of composite and model wickets for 1-GG down condition

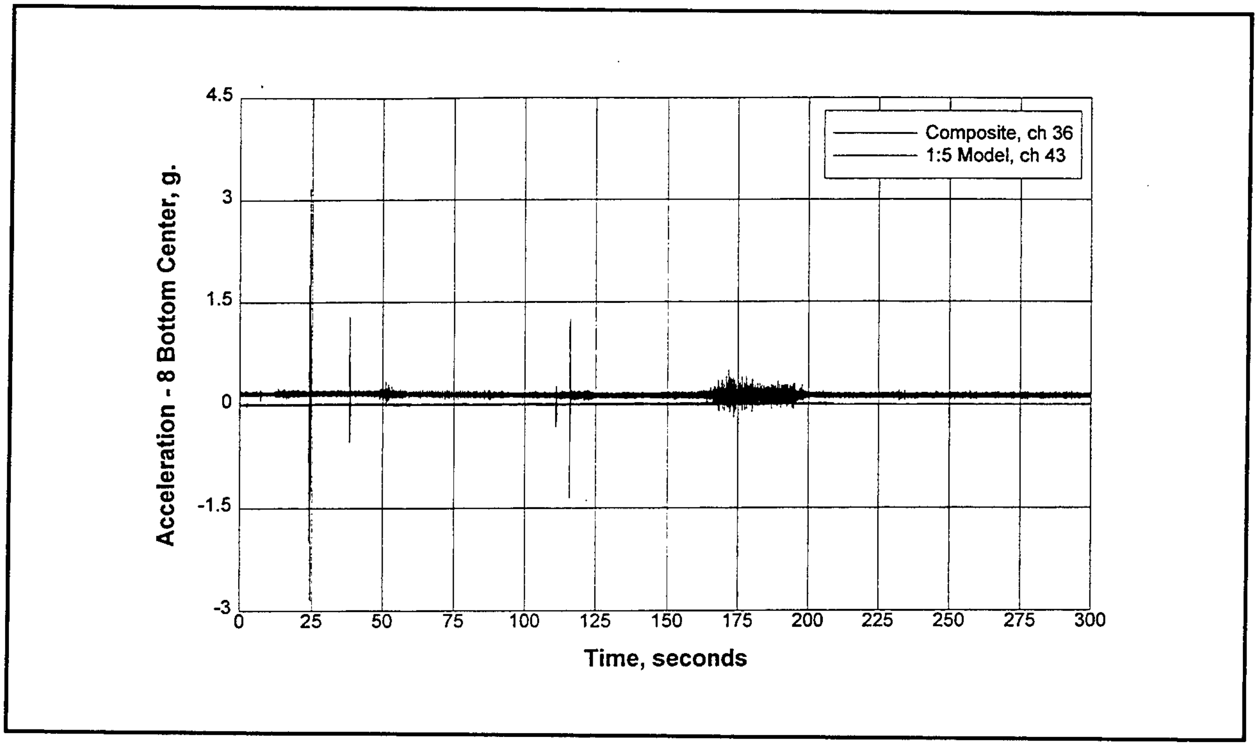

Figure D19. 8 bottom center acceleration response of composite and model wickets for 1-GG down condition

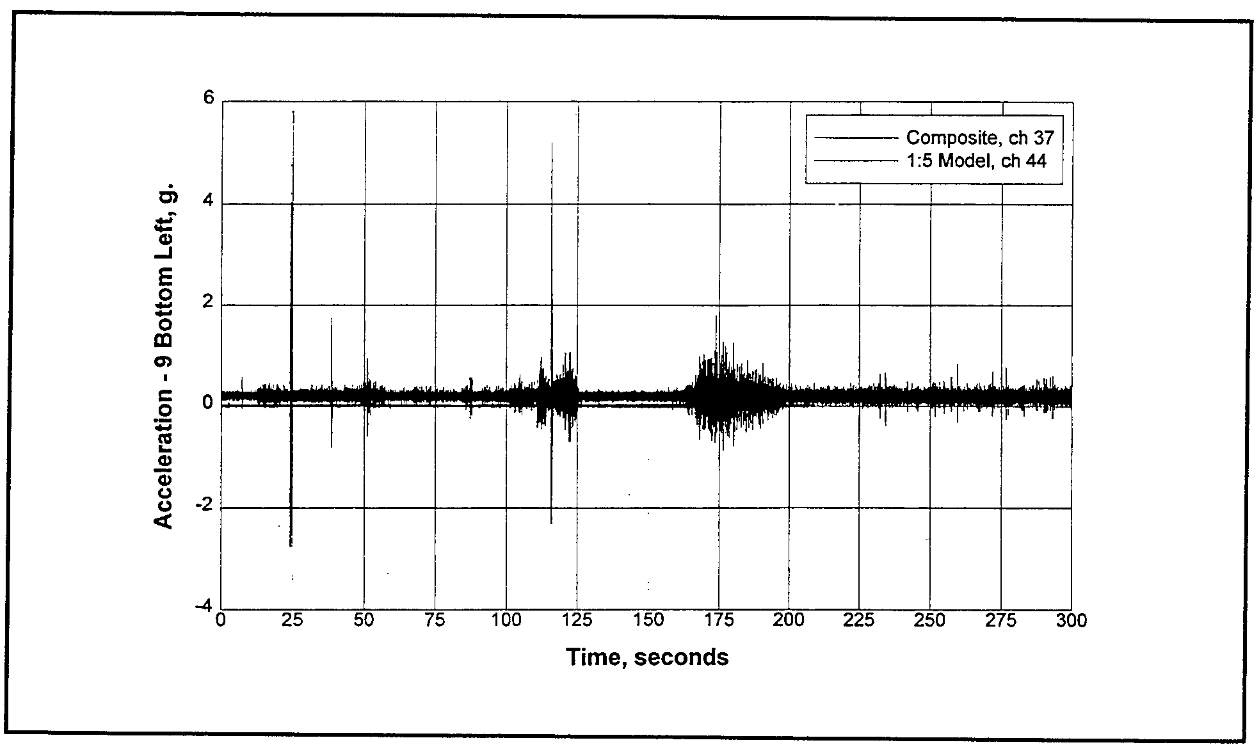

Figure D20. 9 bottom left acceleration response of composite and model wickets for 1-GG down condition

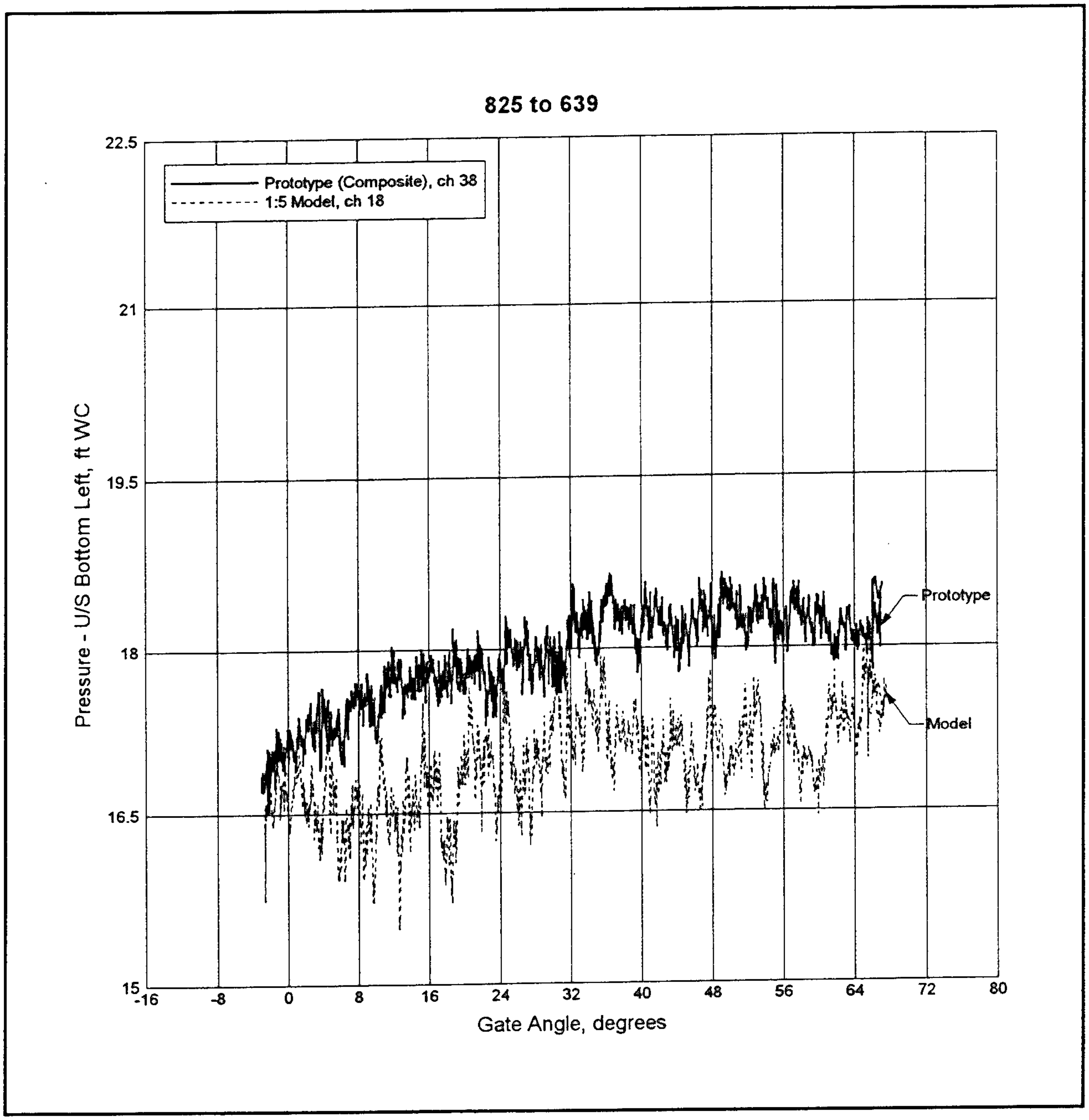

Figure D21. Upstream bottom left pressure variation for 3-GG (L) up condition

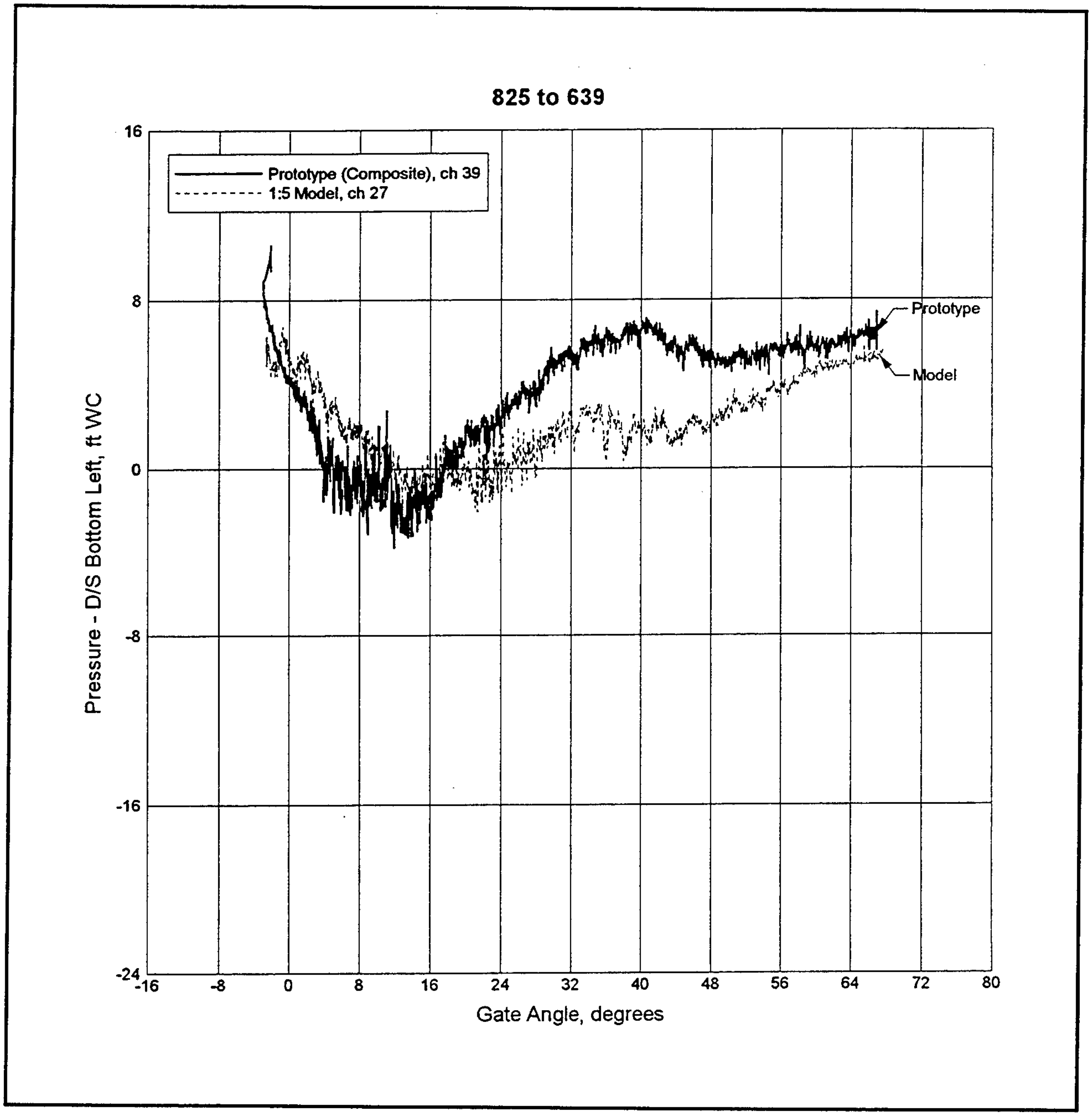

Figure D22. Downstream bottom left pressure variation for 3-GG (L) up condition

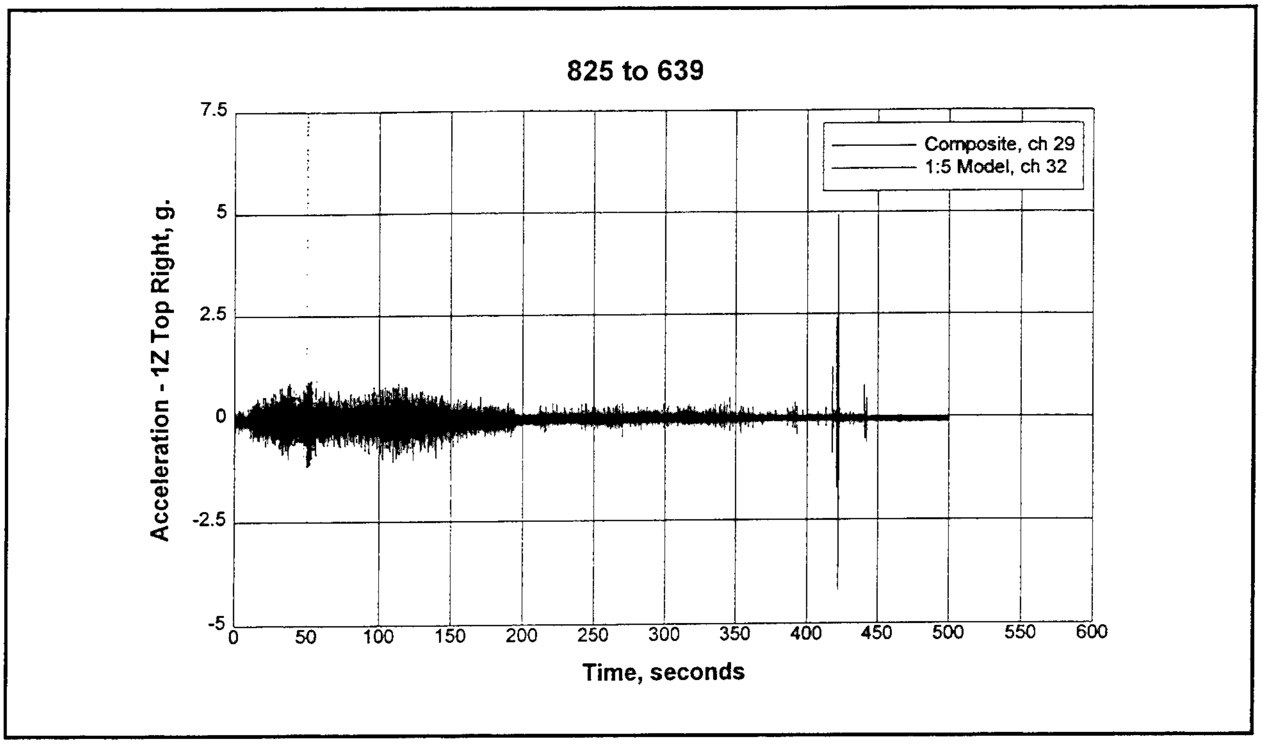

Figure D23. 1Z top right acceleration response of composite and model wickets for 3-GG (L) up condition

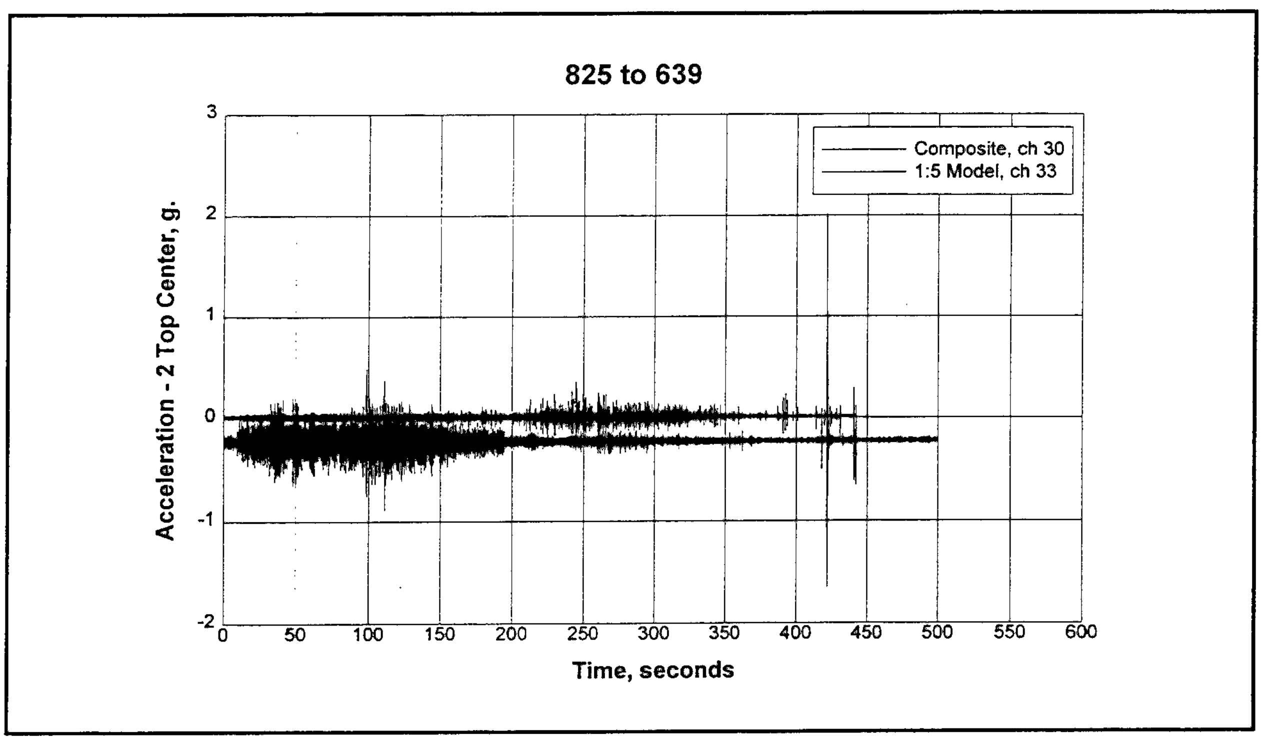

Figure D24. 2 top center acceleration response of composite and model wickets for 3-GG (L) up condition

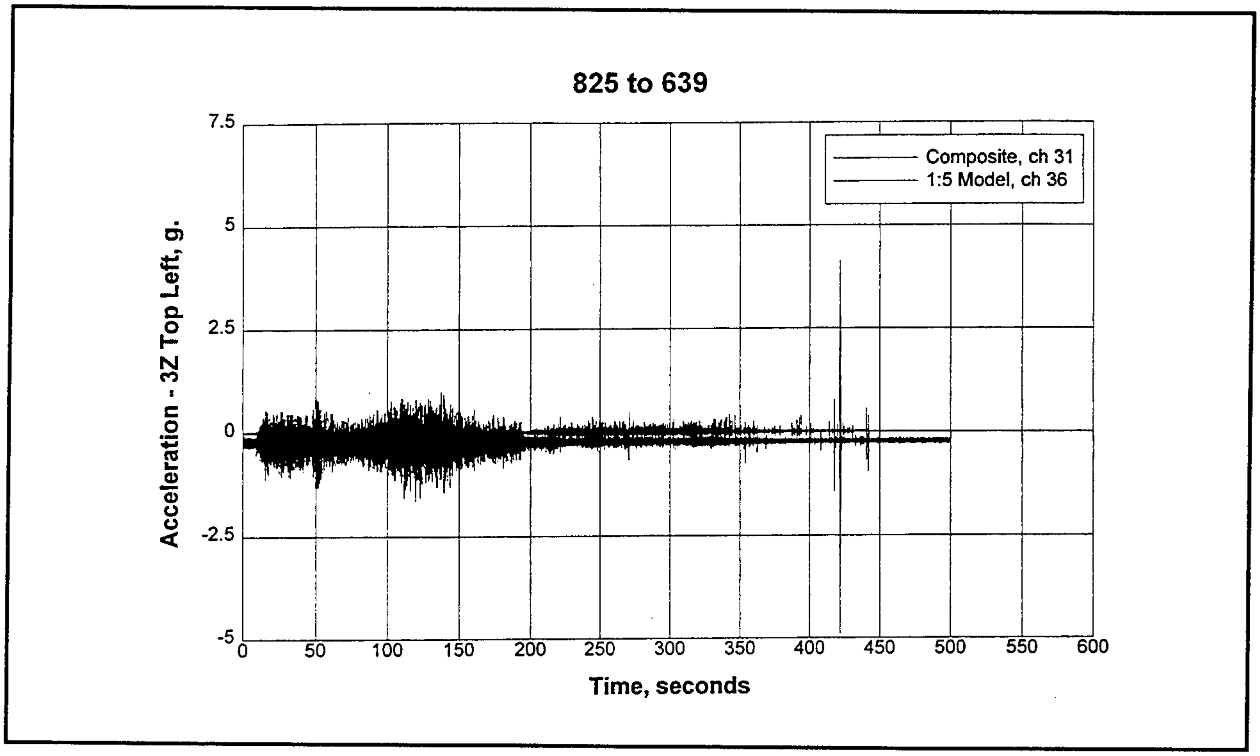

Figure D25. 3Z top left acceleration response of composite and model wickets for 3-GG (L) up condition

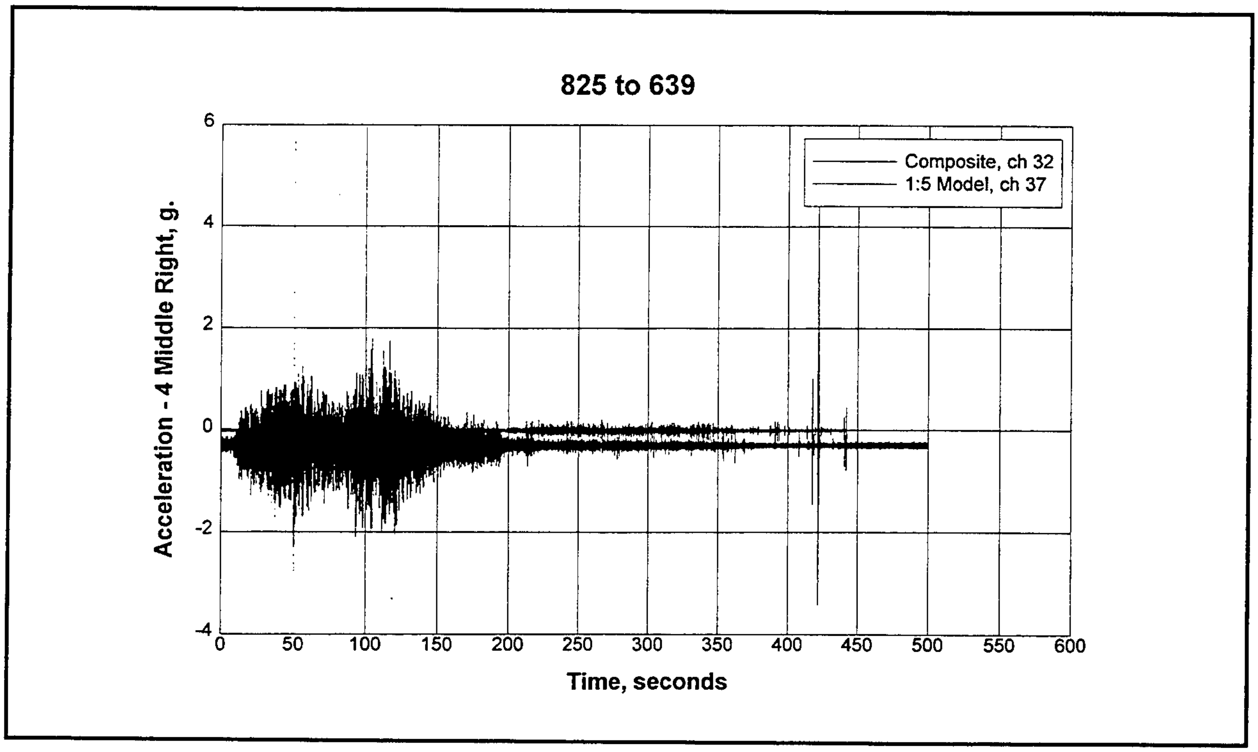

Figure D26. 4 middle right acceleration response of composite and model wickets for 3-GG (L) up condition

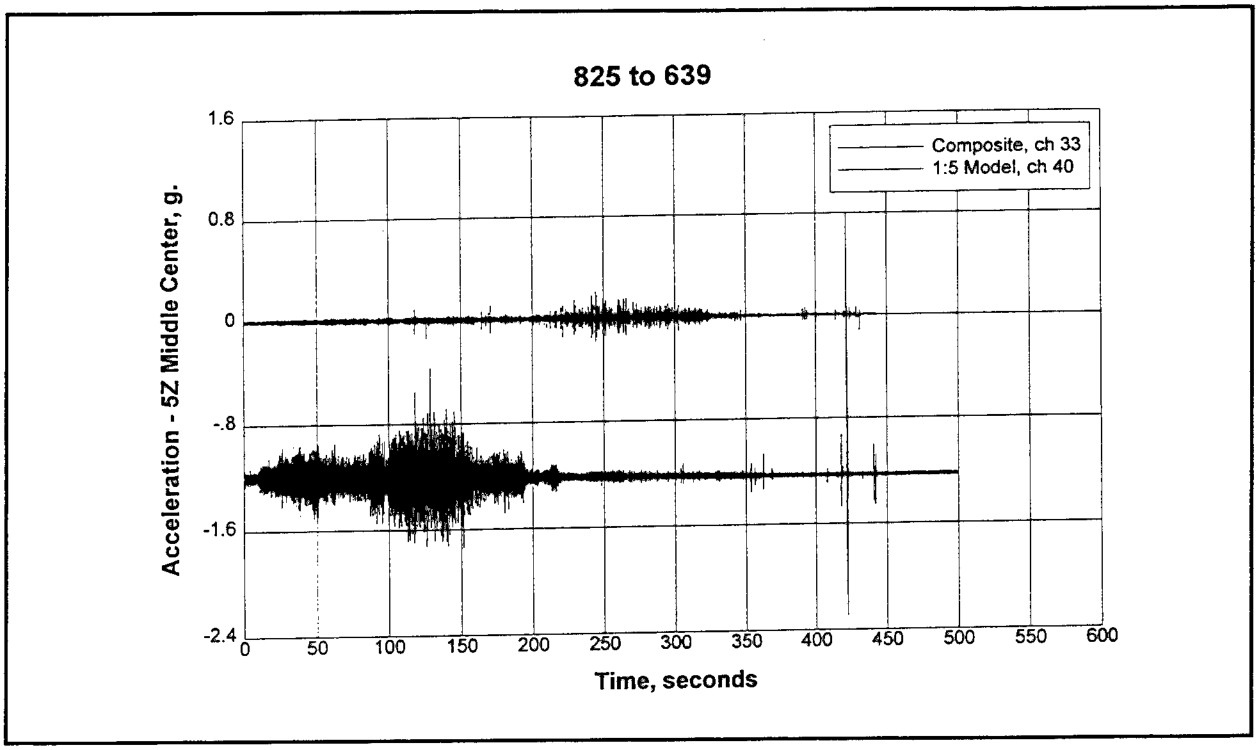

Figure D27. 5Z middle center acceleration response of composite and model wickets for 3-GG (L) up condition

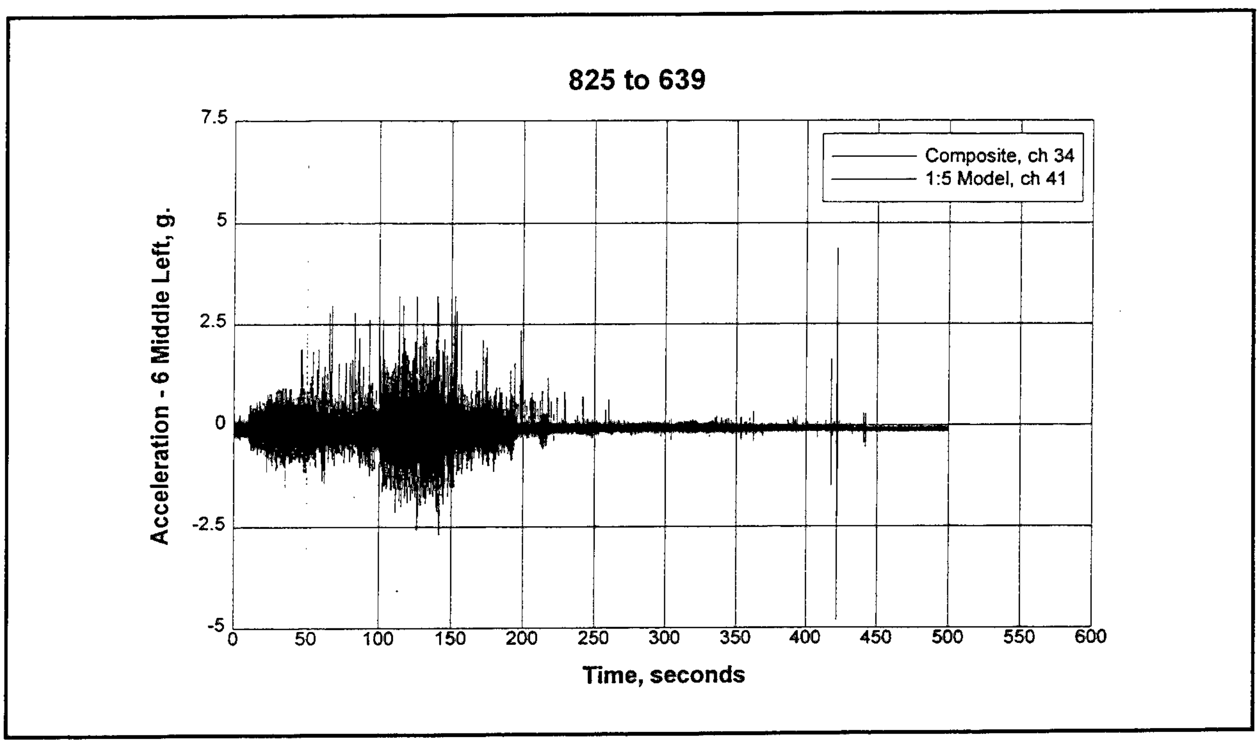

Figure D28. 6 middle left acceleration response of composite and model wickets for 3-GG (L) up condition

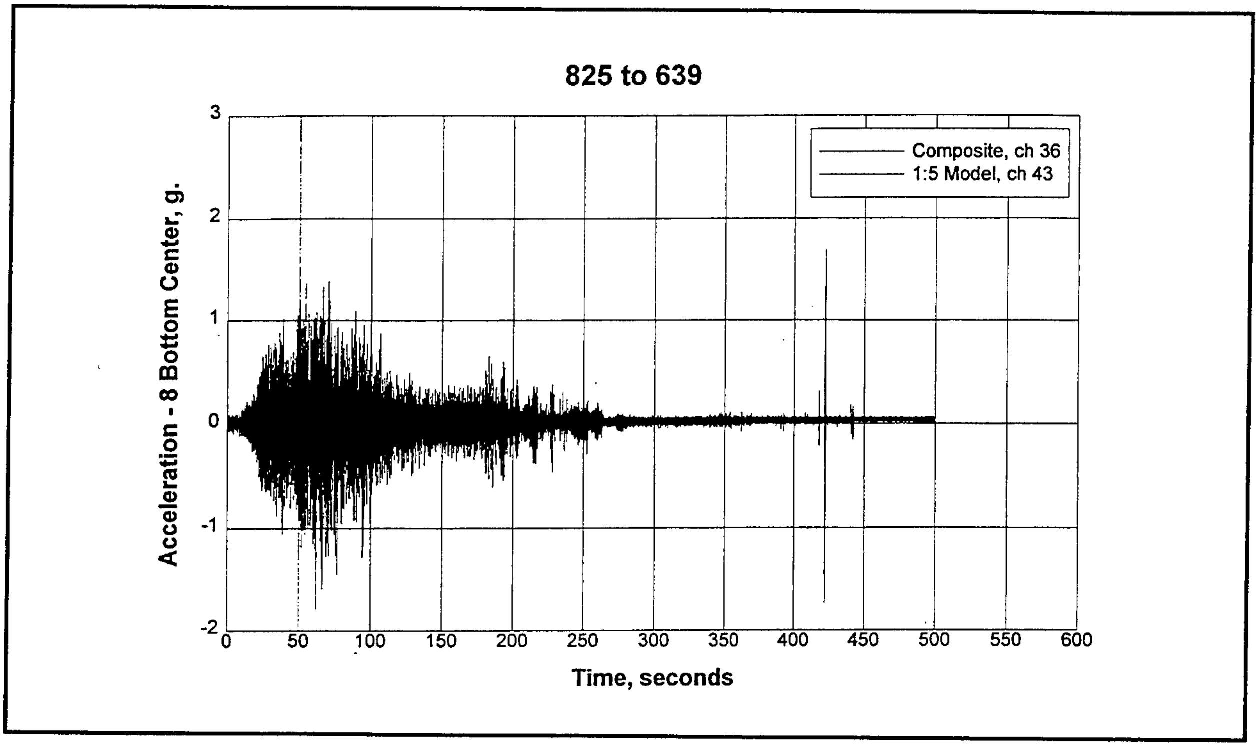

Figure D29. 8 bottom center acceleration response of composite and model wickets for 3-GG (L) up condition

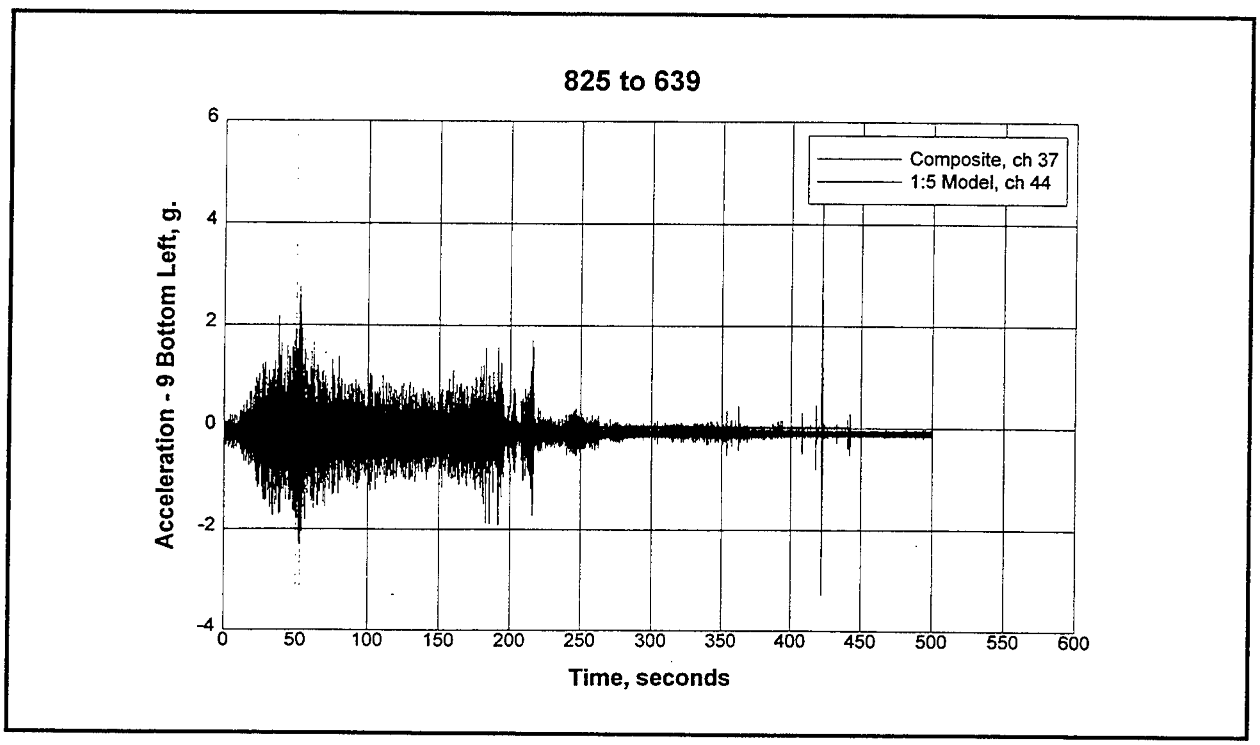

Figure D30. 9 bottom left acceleration response of composite and model wickets for 3-GG (L) up condition

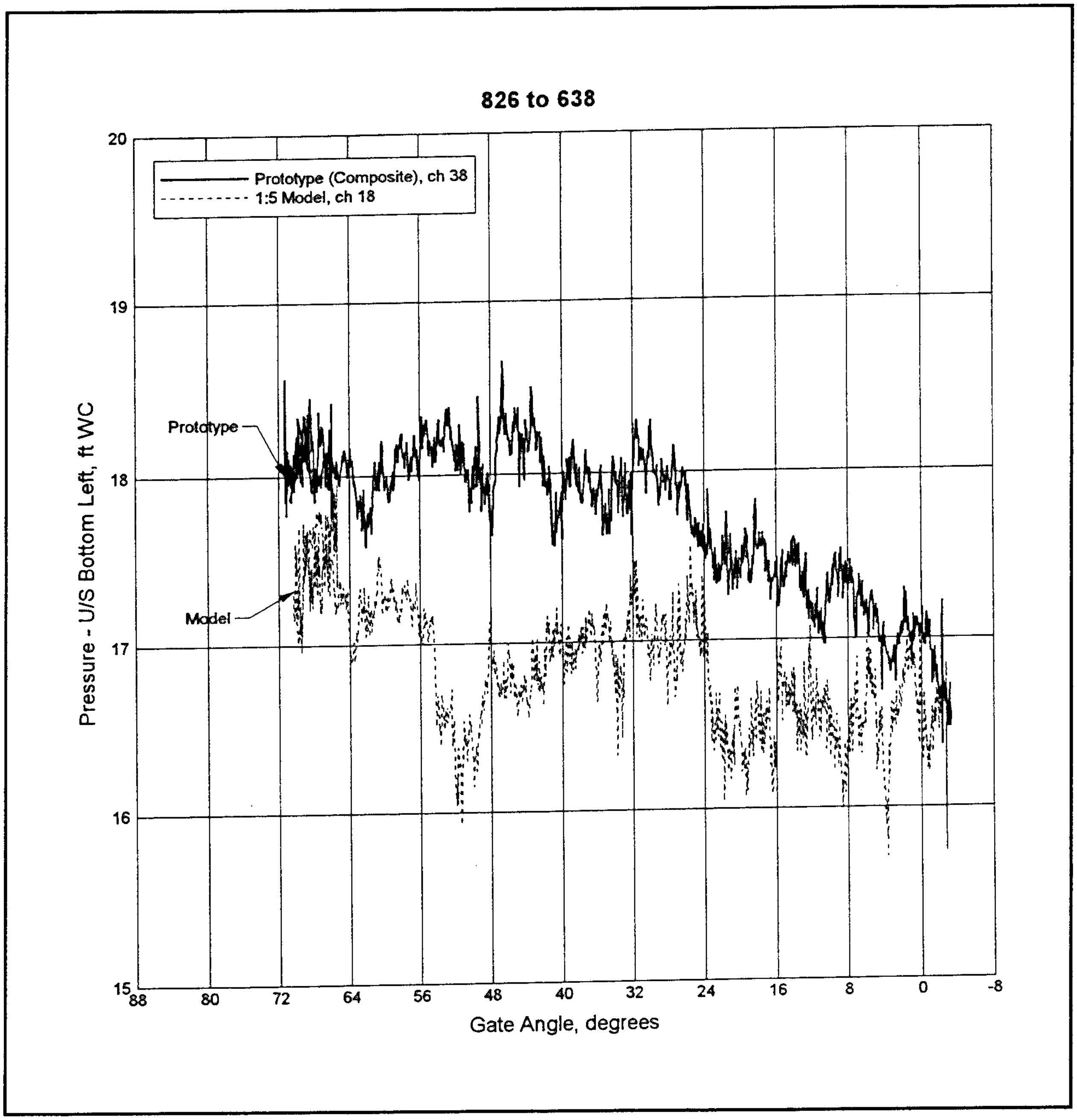

Figure D31. Upstream bottom left pressure variation for 3-GG (L) down condition

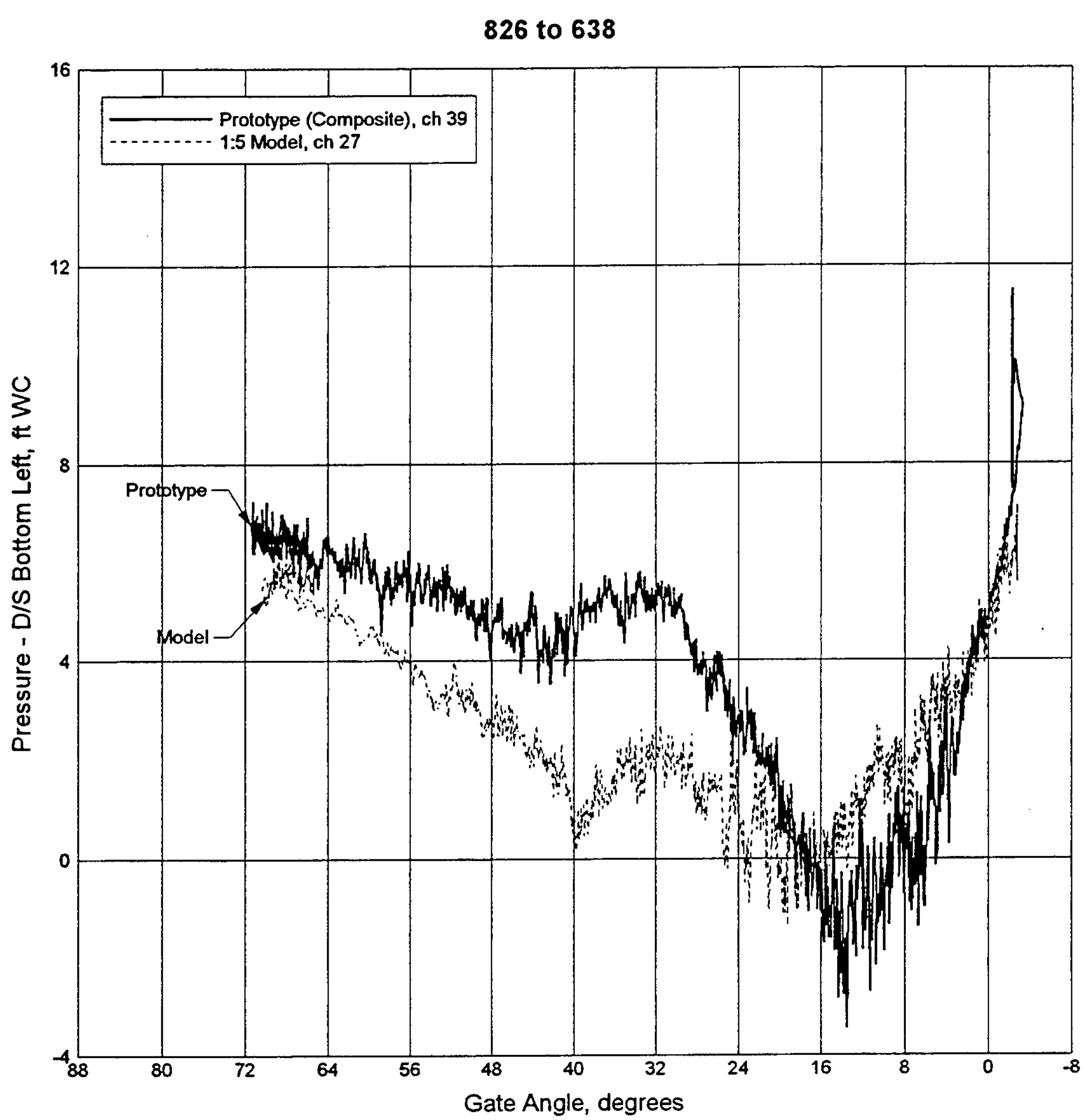

Figure D32. Downstream bottom left pressure variation for 3-GG (L) down condition

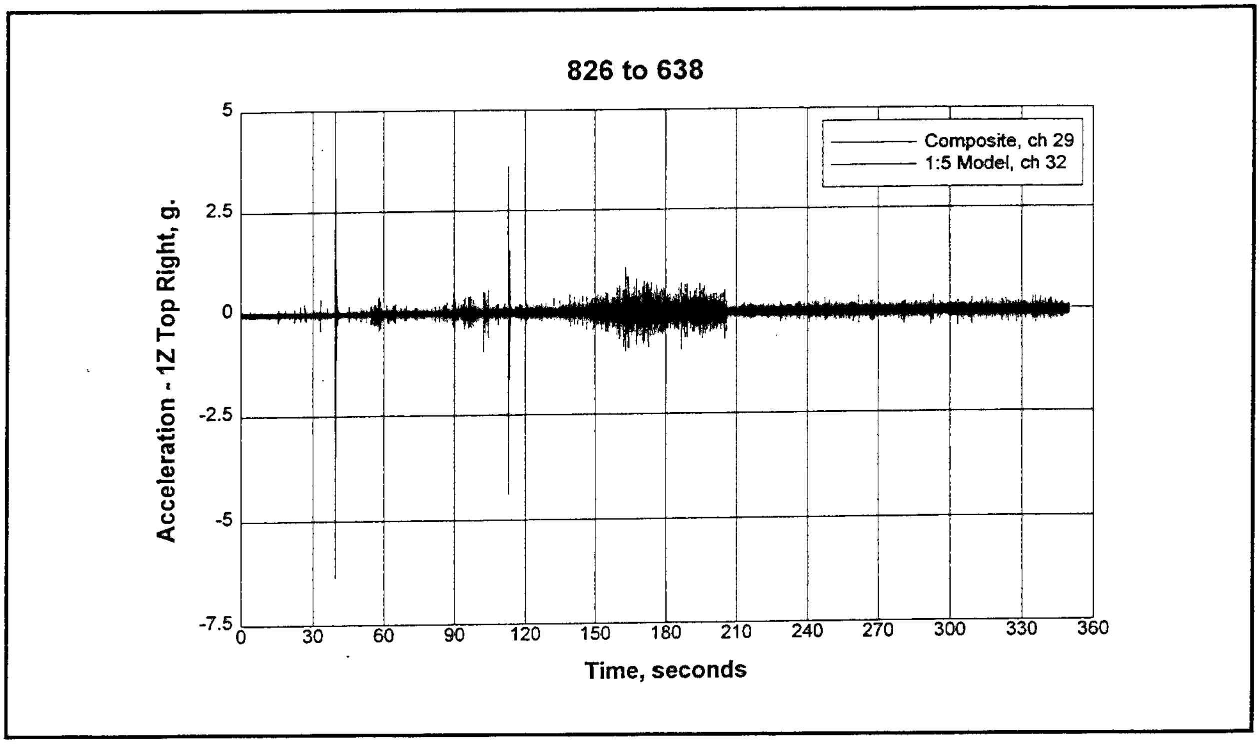

Figure D33. 1Z top right acceleration response of composite and model wickets for 3-GG (L) down condition

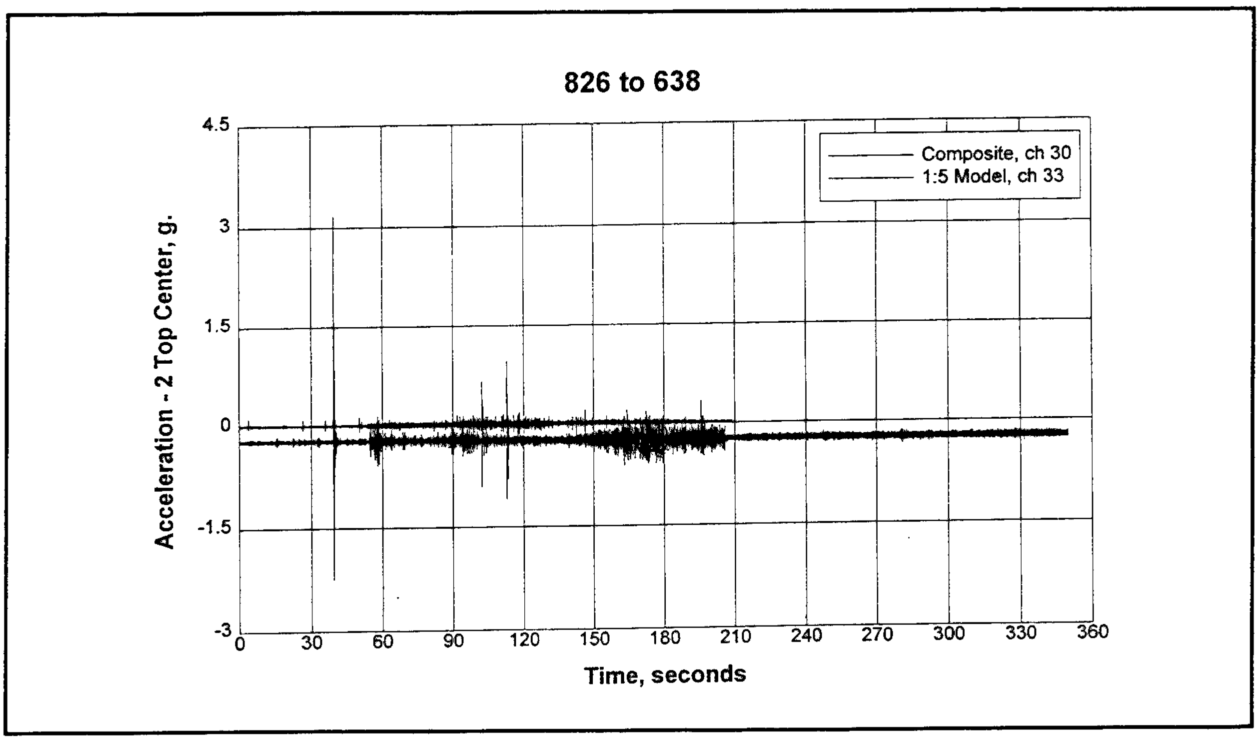

Figure D34. 2 top center acceleration response of composite and model wickets for 3-GG (L) down condition

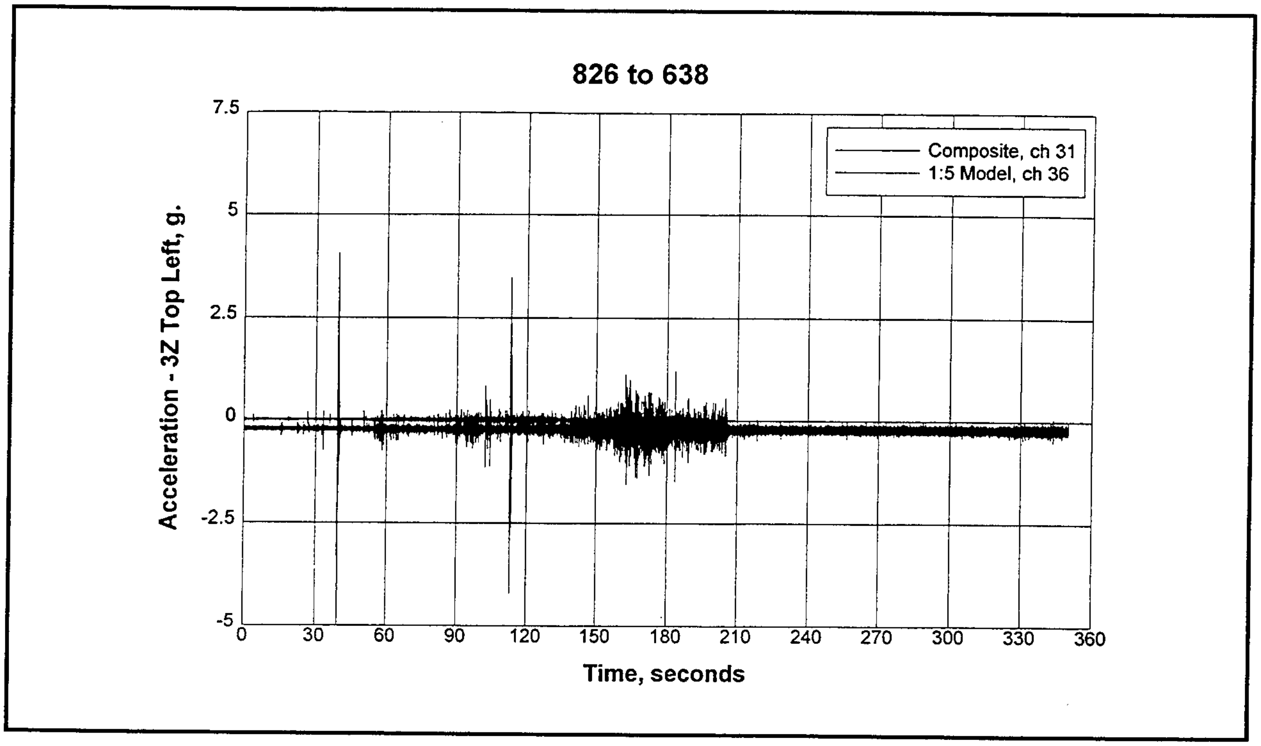

Figure D35. 3Z top left acceleration response of composite and model wickets for 3-GG (L) down condition

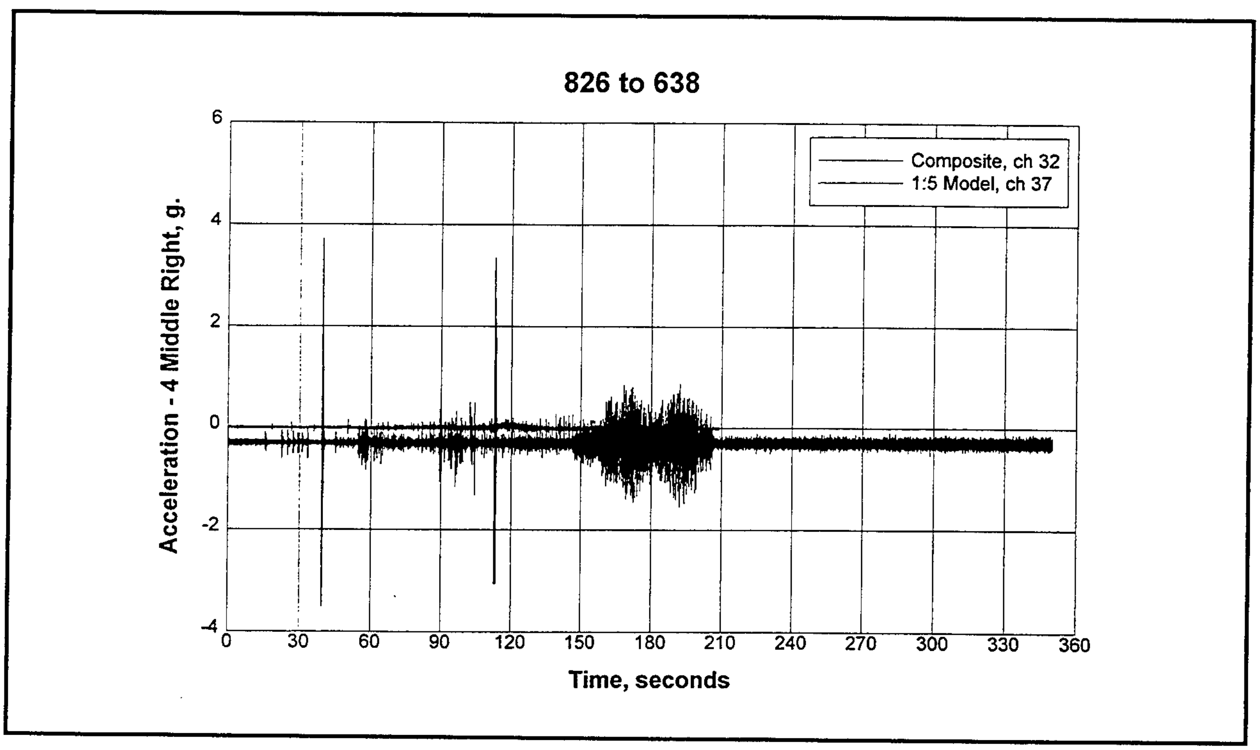

Figure D36. 4 middle right acceleration response of composite and model wickets for 3-GG (L) down condition

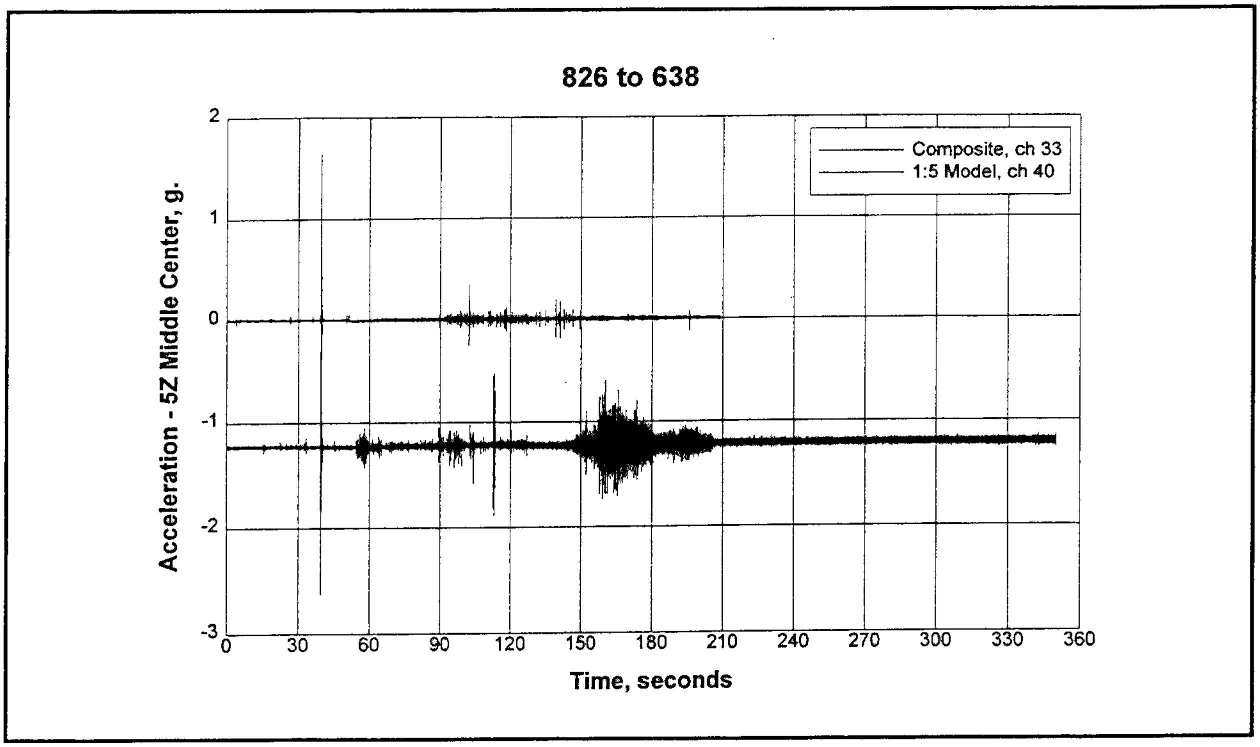

Figure D37. 5Z middle center acceleration response of composite and model wickets for 3-GG (L) down condition

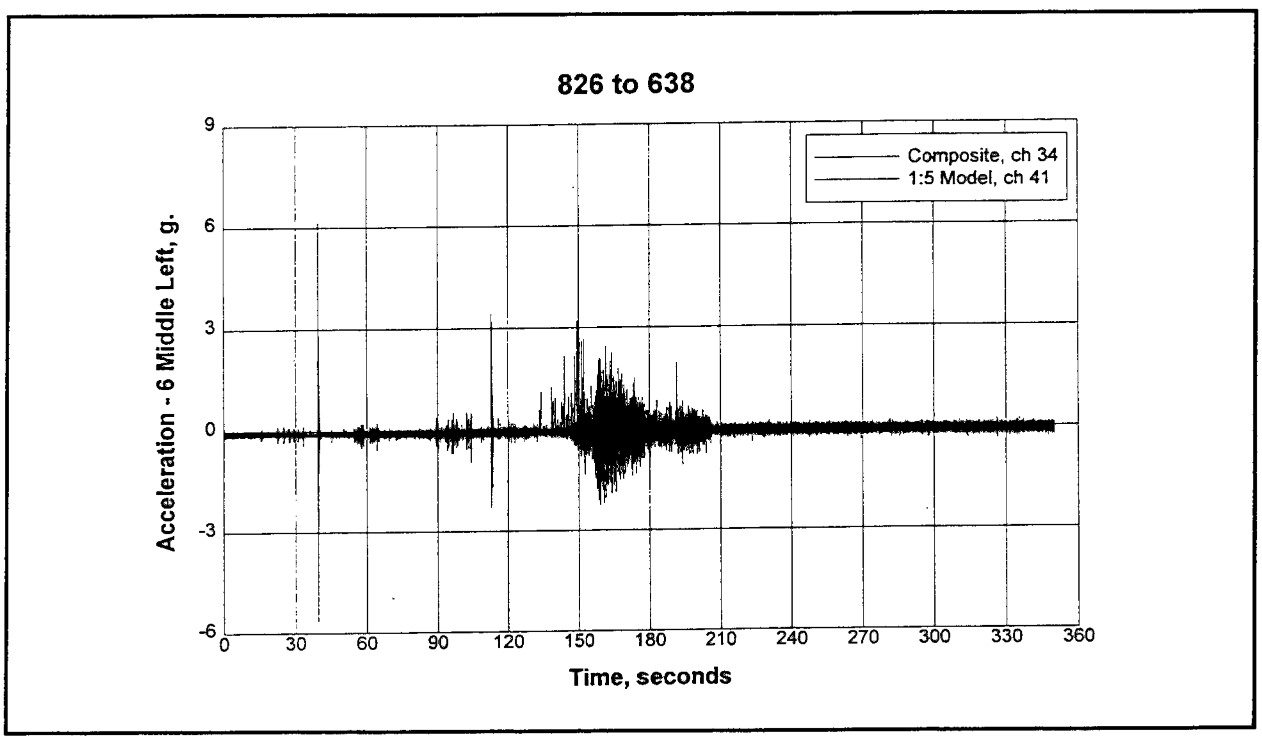

Figure D38. 6 middle left acceleration response of composite and model wickets for 3-GG (L) down condition

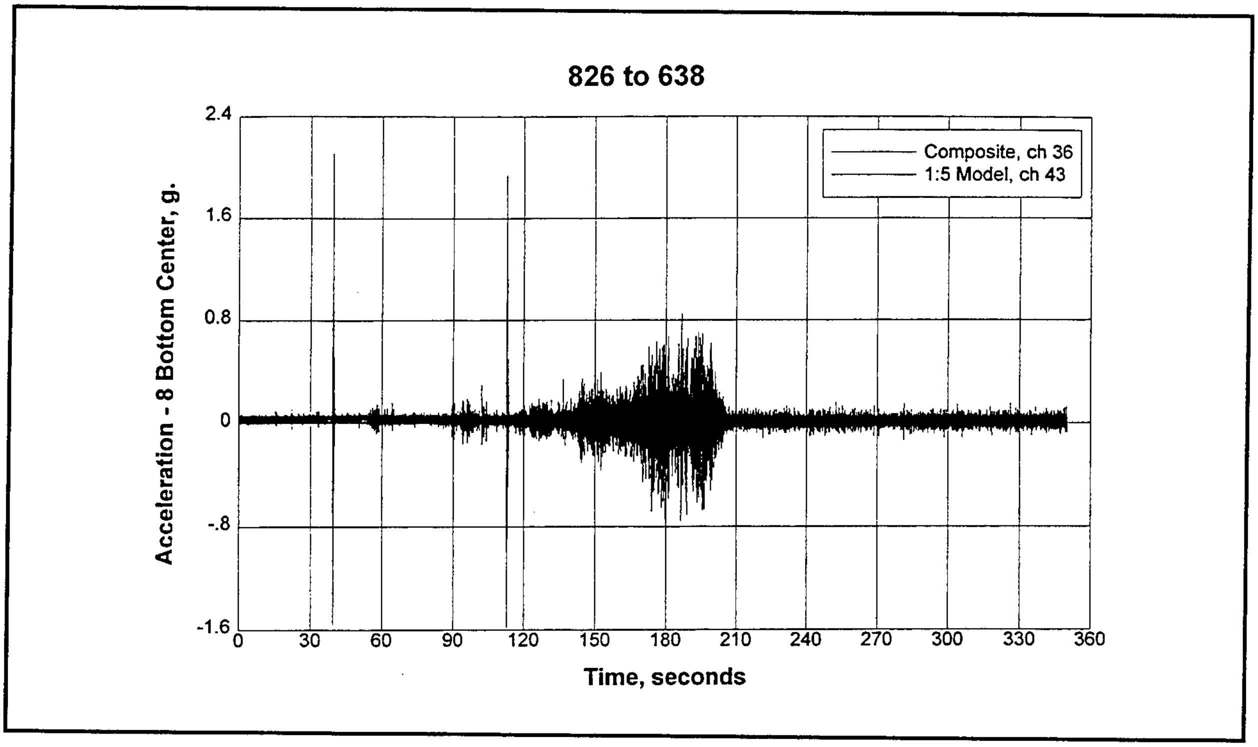

Figure D39. 8 bottom center acceleration response of composite and model wickets for 3-GG (L) down condition

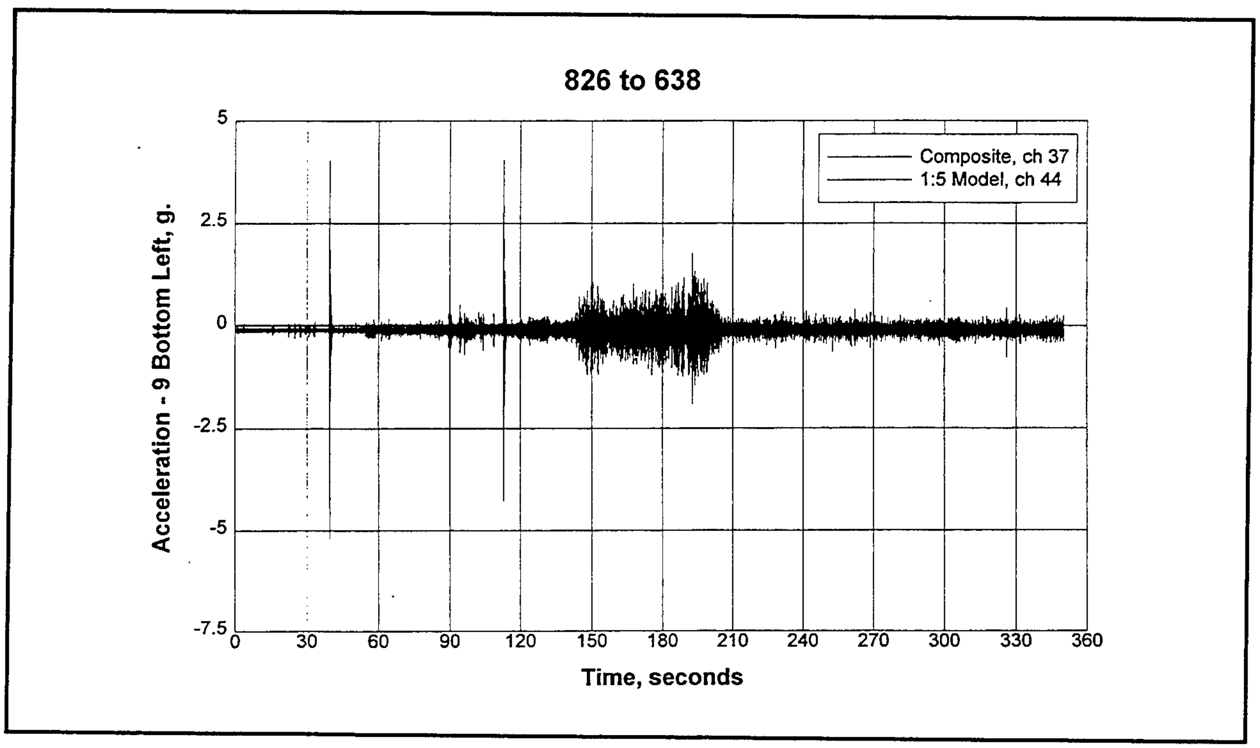

Figure D40. 9 bottom left acceleration response of composite and model wickets for 3-GG (L) down condition

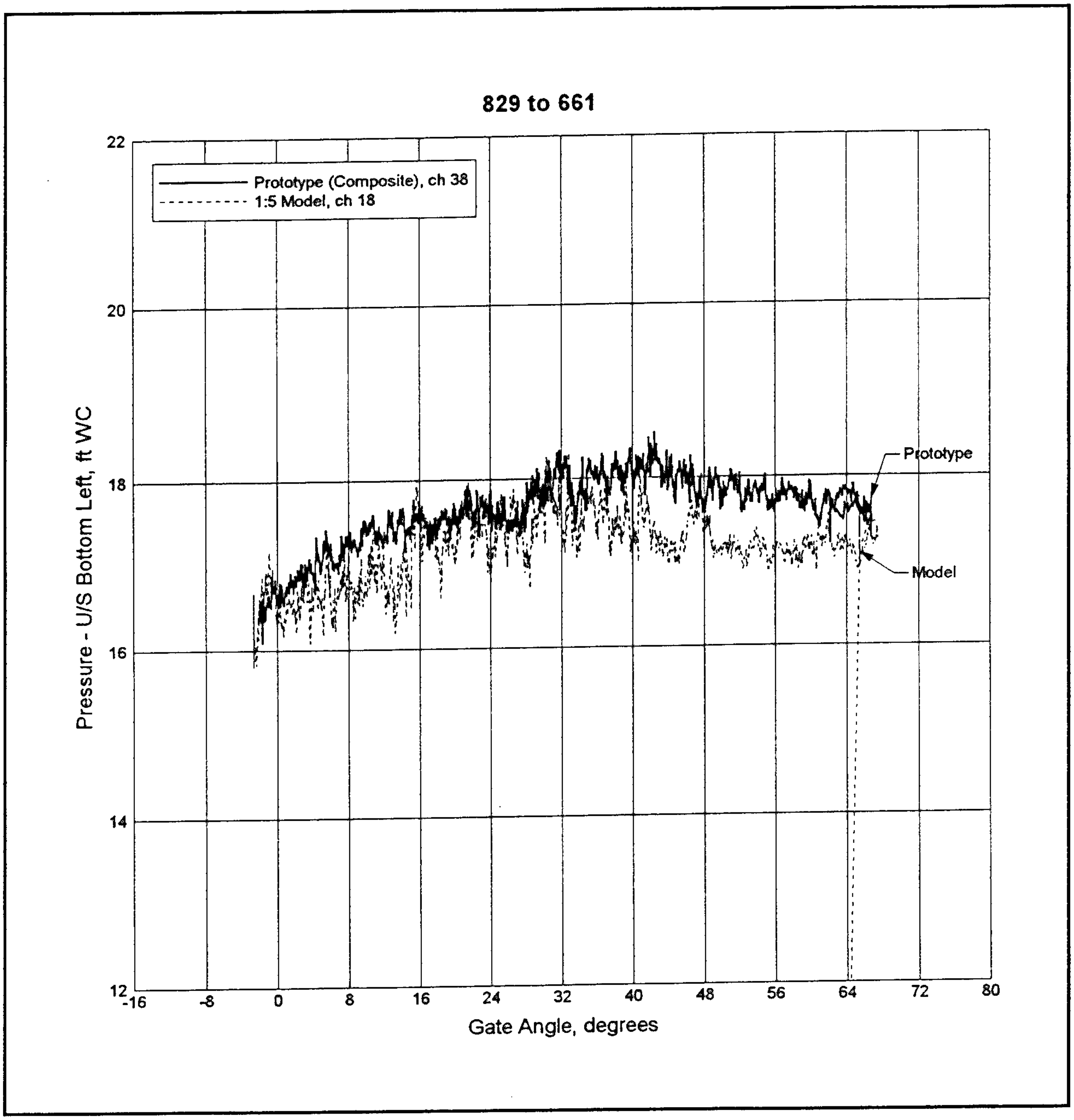

Figure D41. Upstream bottom left pressure variation for 2-GG (ER) up condition

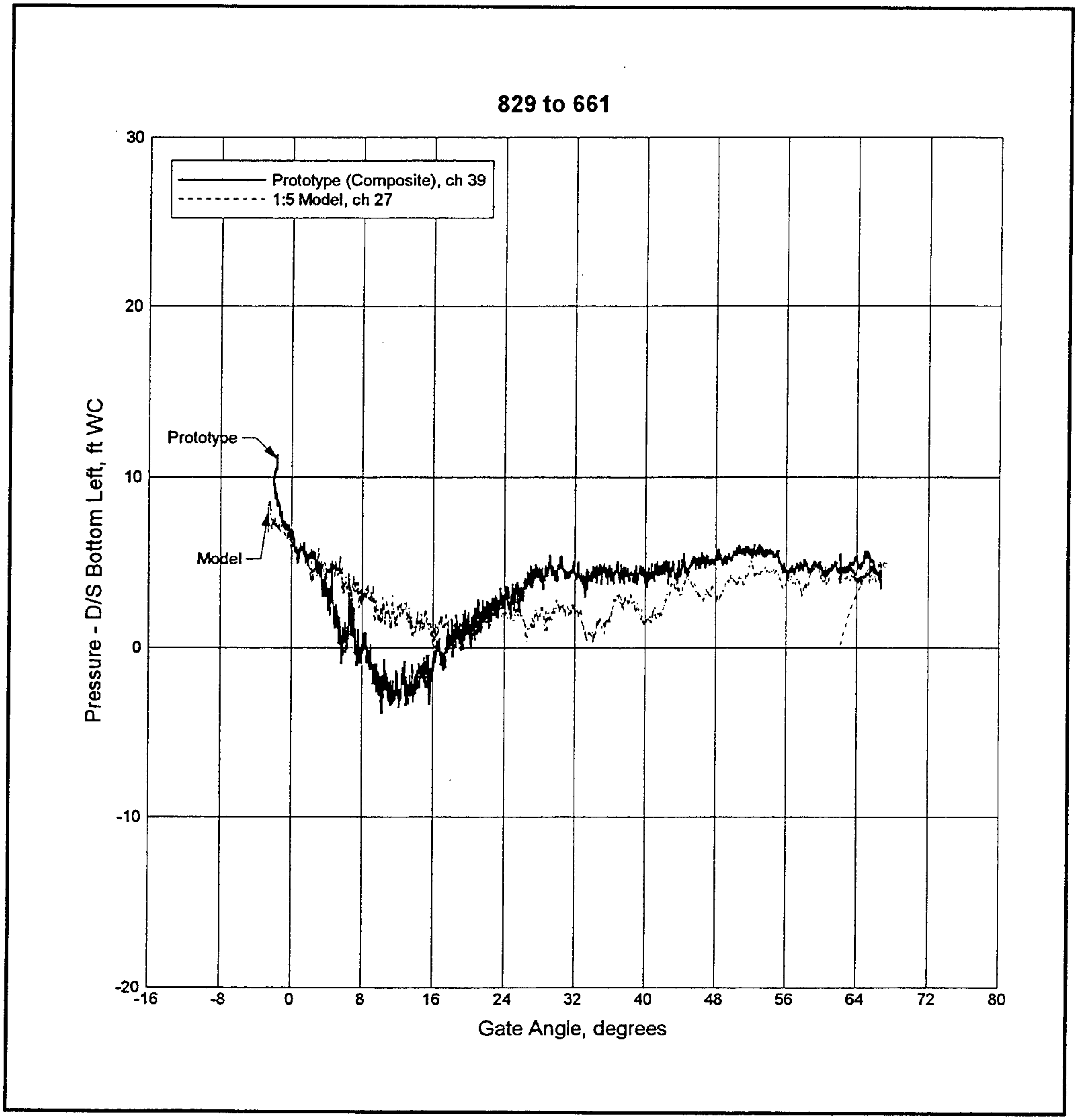

Figure D42. Downstream bottom left pressure variation for 2-GG (ER) up condition

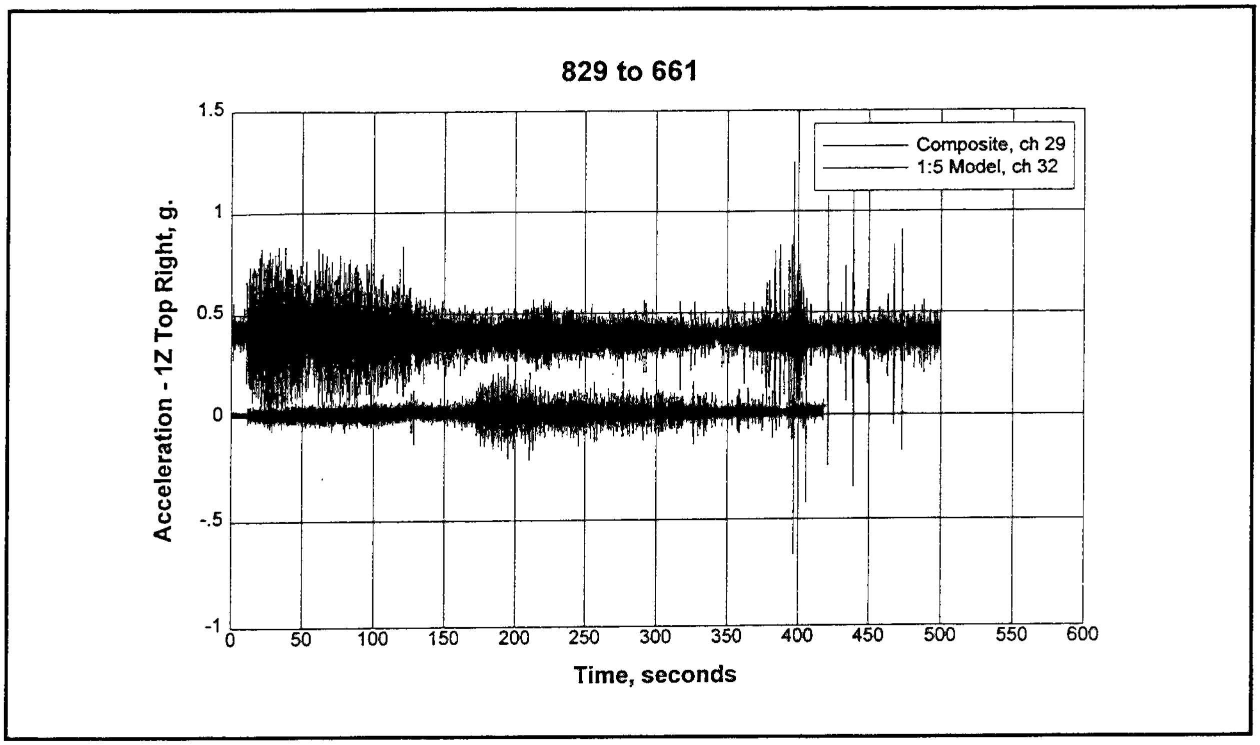

Figure D43. 1Z top right acceleration response of composite and model wickets for 2-GG (ER) up condition

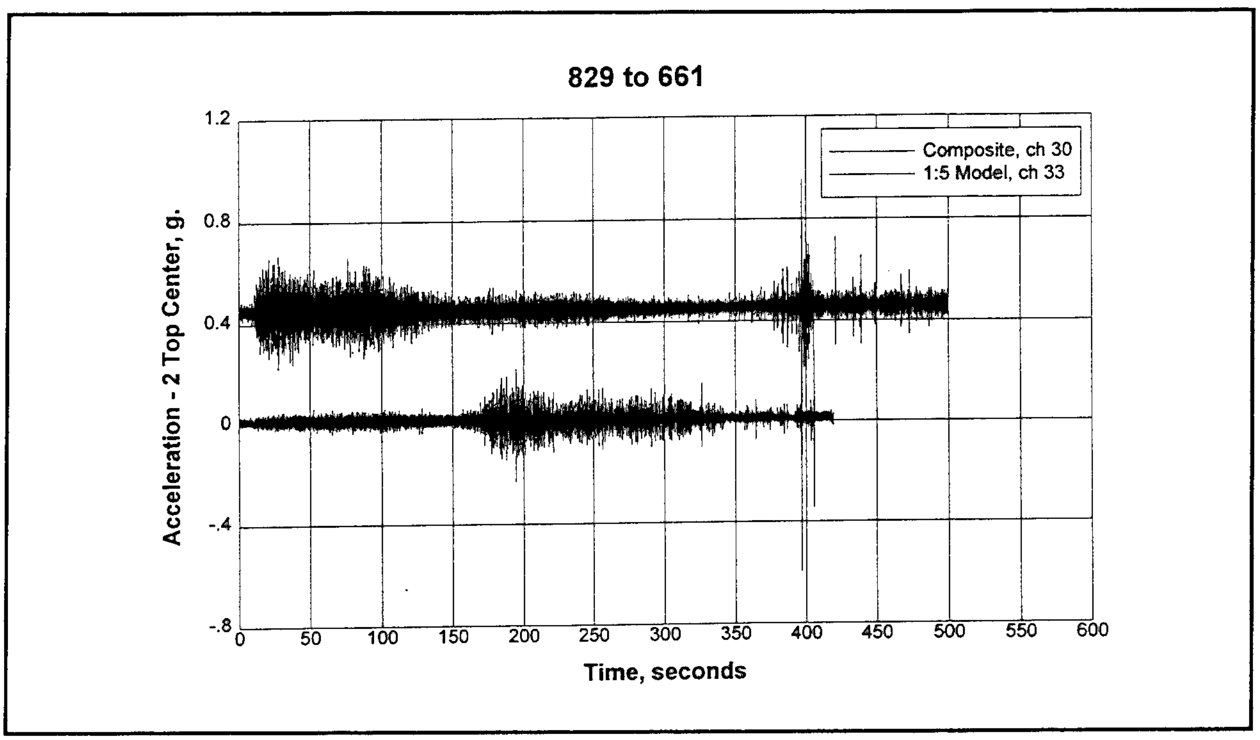

Figure D44. 2 top center acceleration response of composite and model wickets for 2-GG (ER) up condition

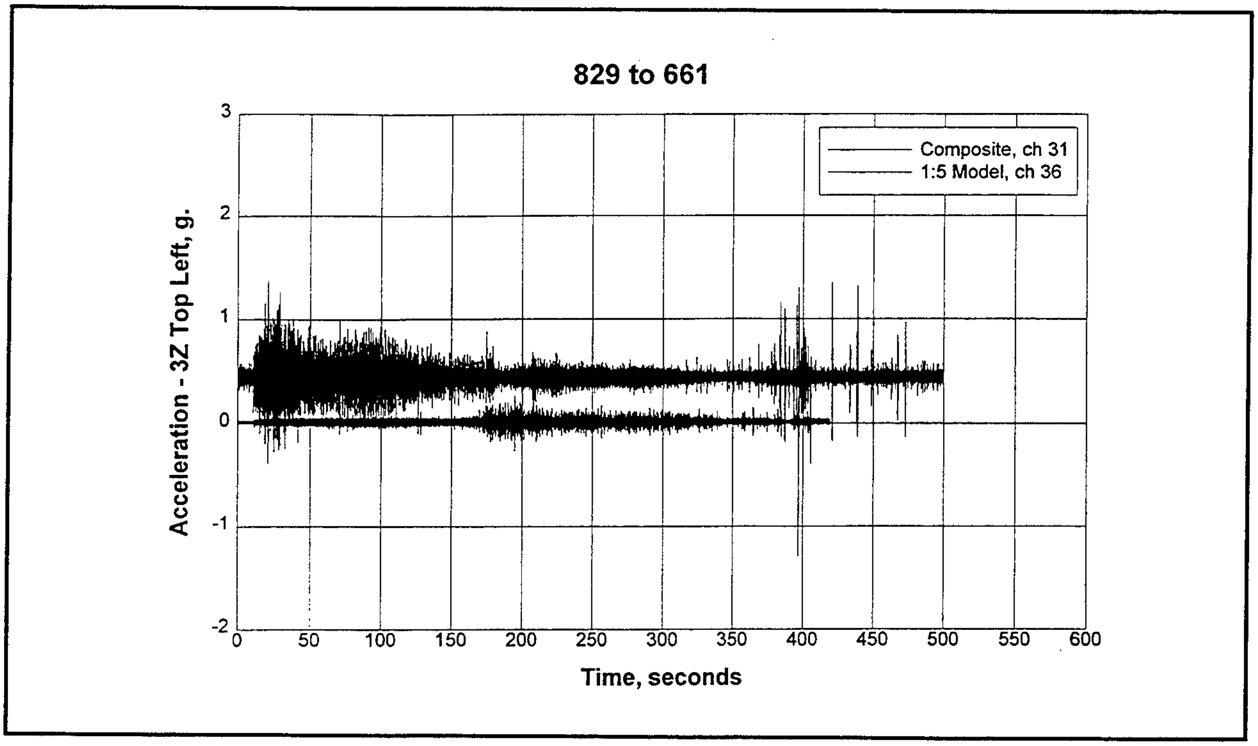

Figure D45. 3Z top left acceleration response of composite and model wickets for 2-GG (ER) up condition

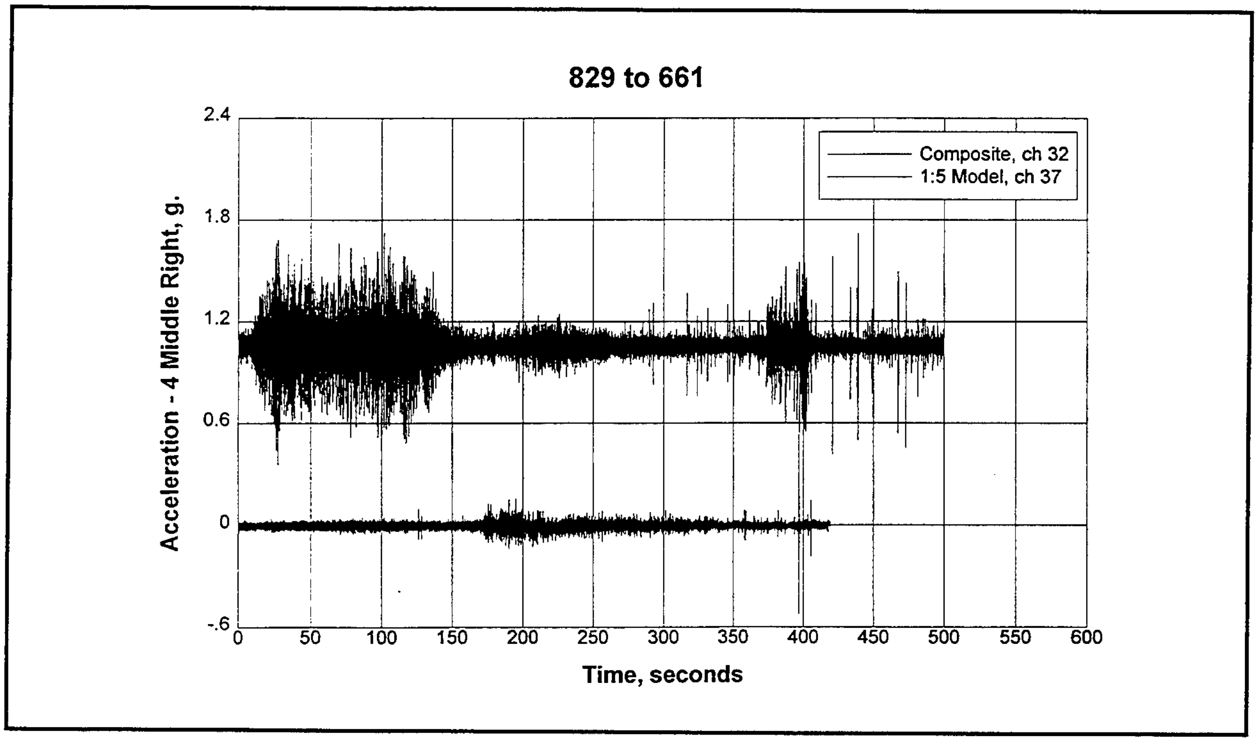

Figure D46. 4 middle right acceleration response of composite and model wickets for 2-GG (ER) up condition

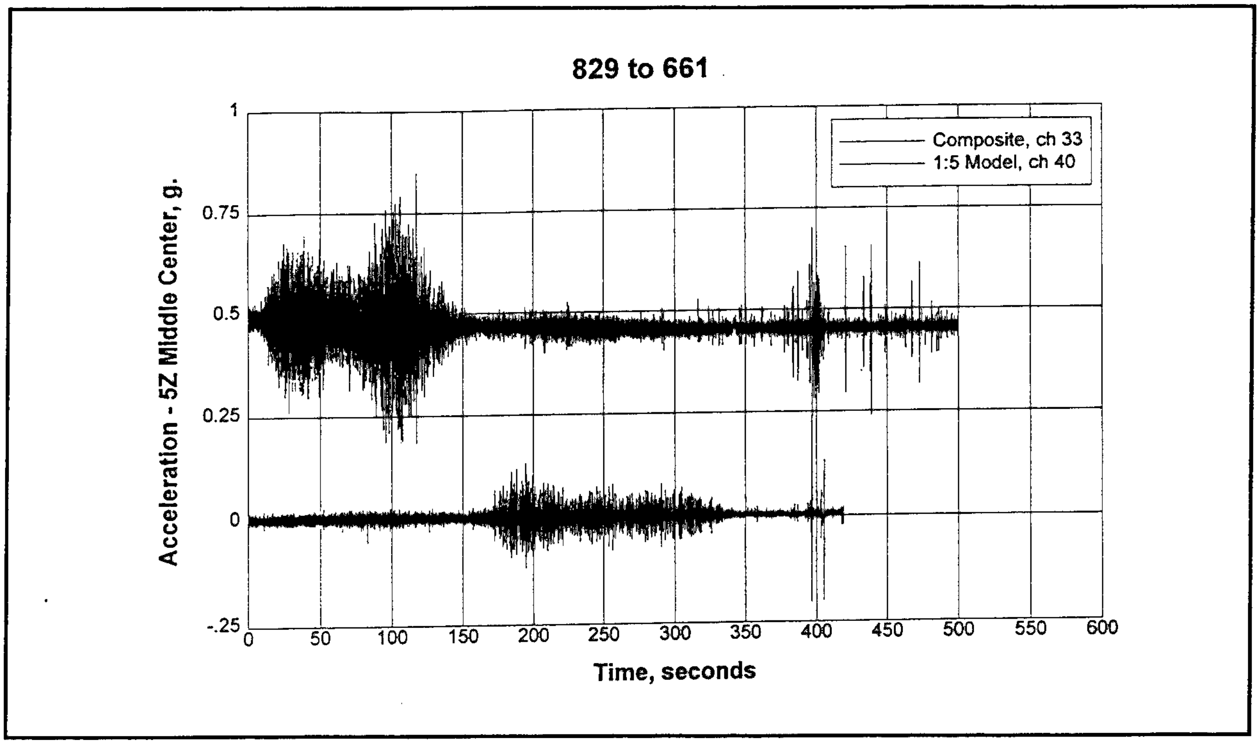

Figure D47. 5Z middle center acceleration response of composite and model wickets for 2-GG (ER) up condition

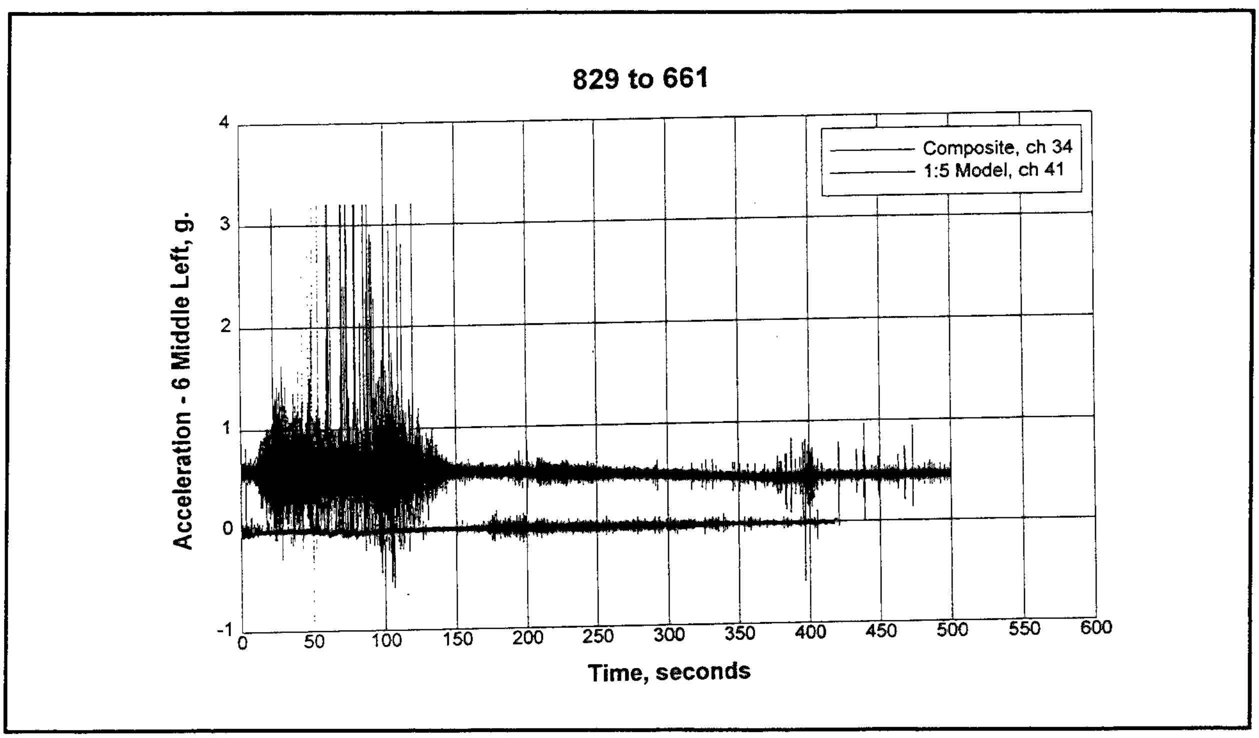

Figure D48. 6 middle left acceleration response of composite and model wickets for 2-GG (ER) up condition

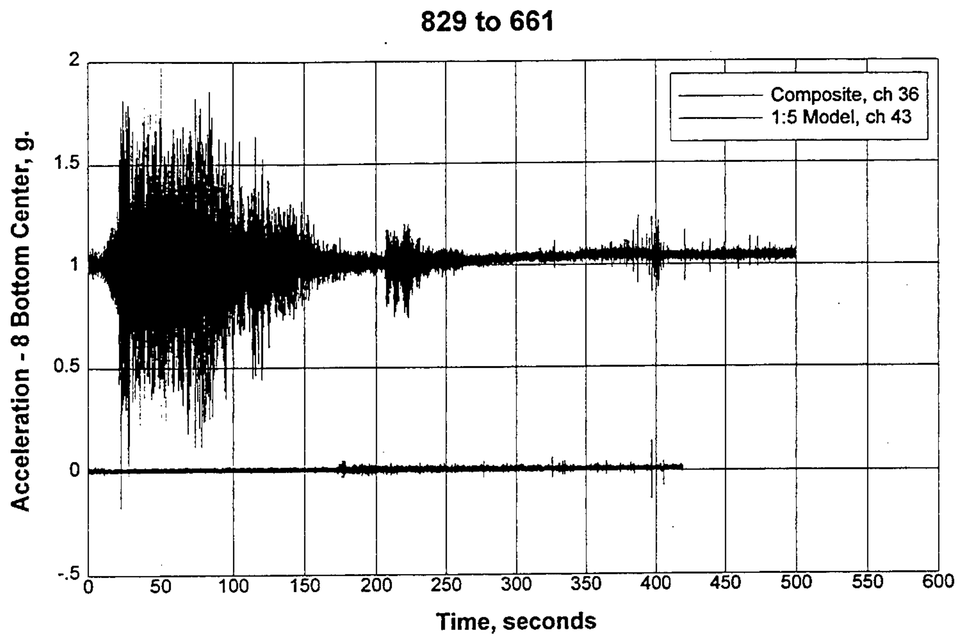

Figure D49. 8 bottom center acceleration response of composite and model wickets for 2-GG (ER) up condition

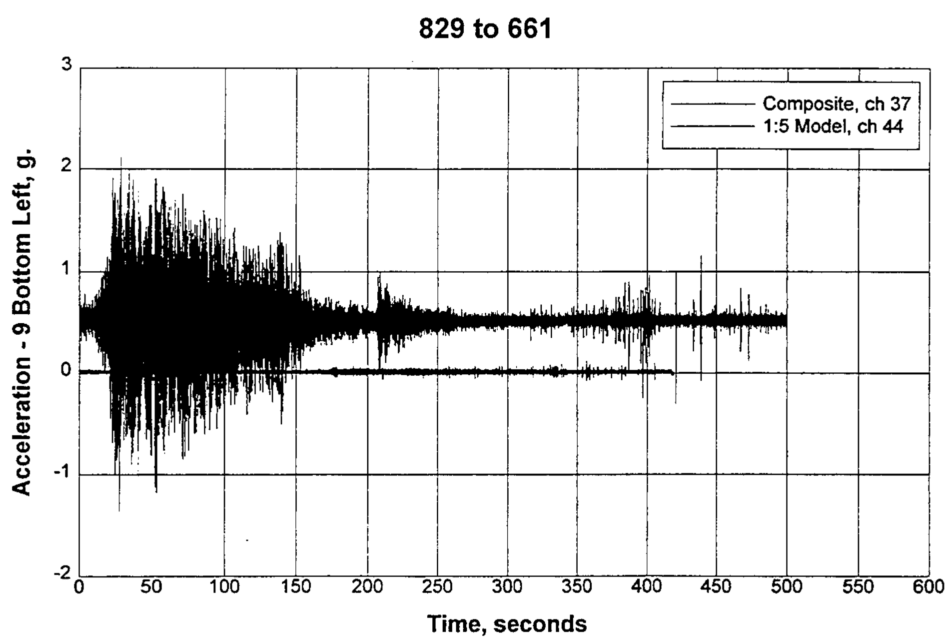

Figure D50. 9 bottom left acceleration response of composite and model wickets for 2-GG (ER) up condition

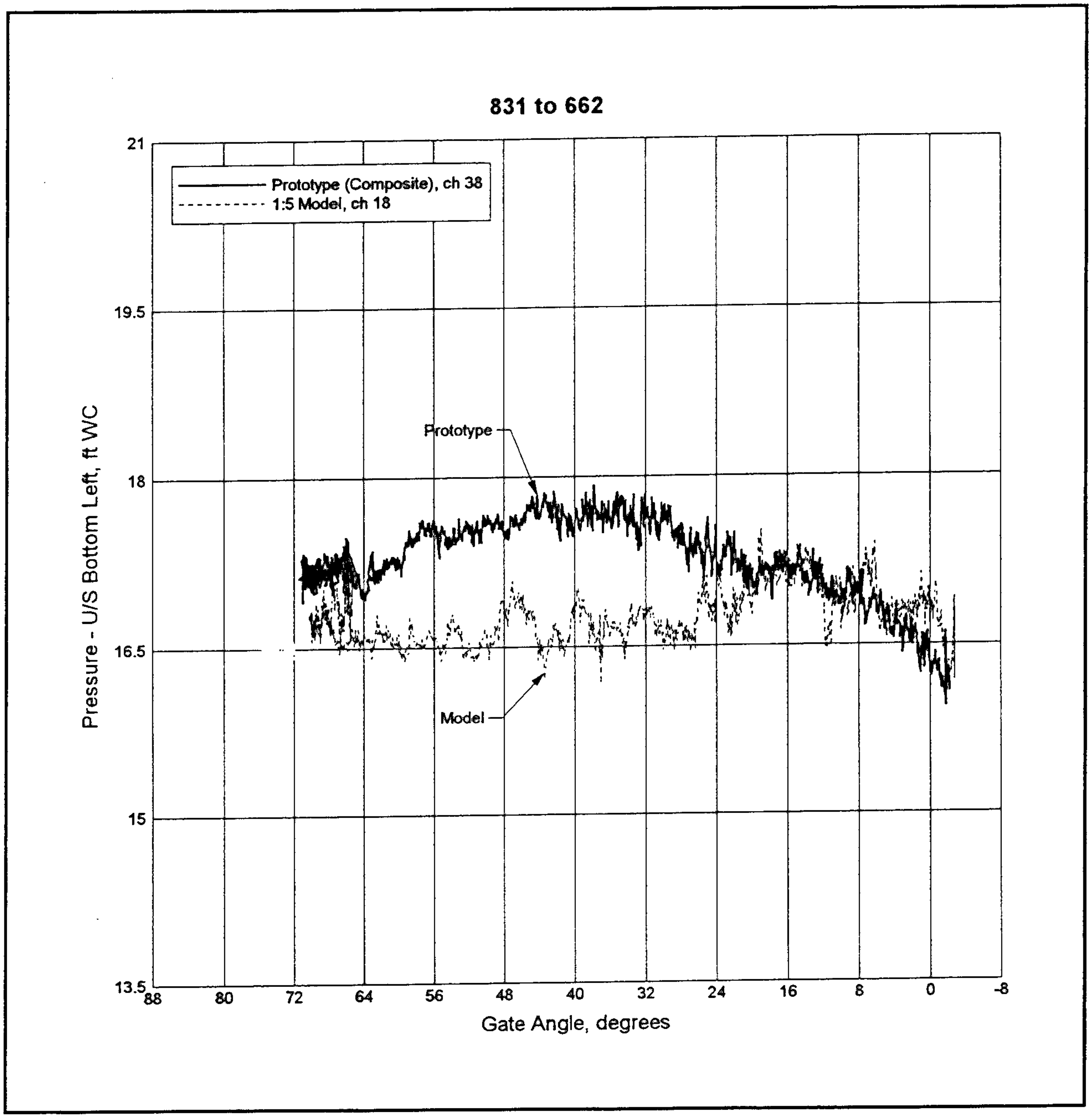

Figure D51. Upstream bottom left pressure variation for 2-GG (ER) down condition

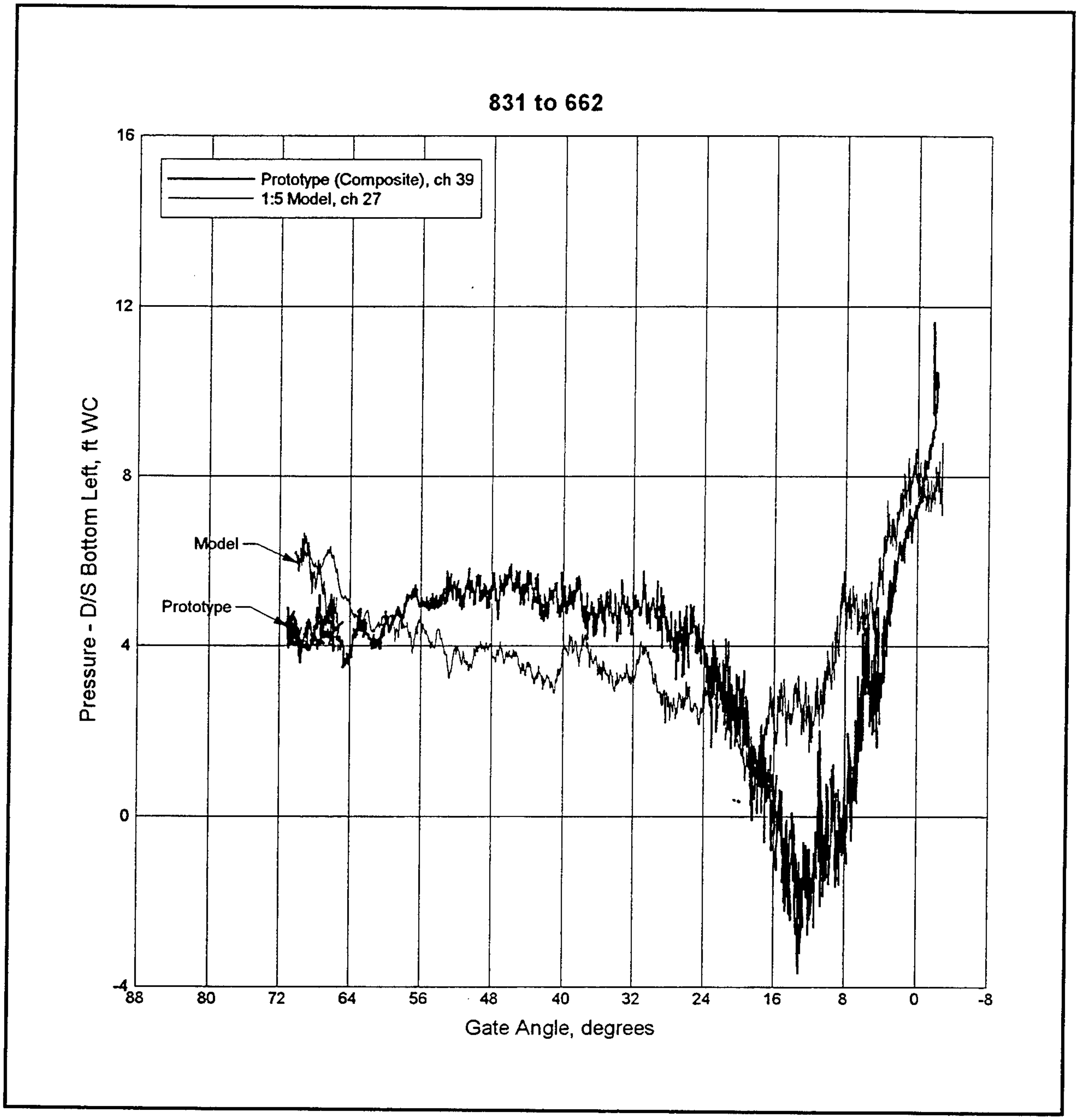

Figure D52. Downstream bottom left pressure variation for 2-GG (ER) down condition

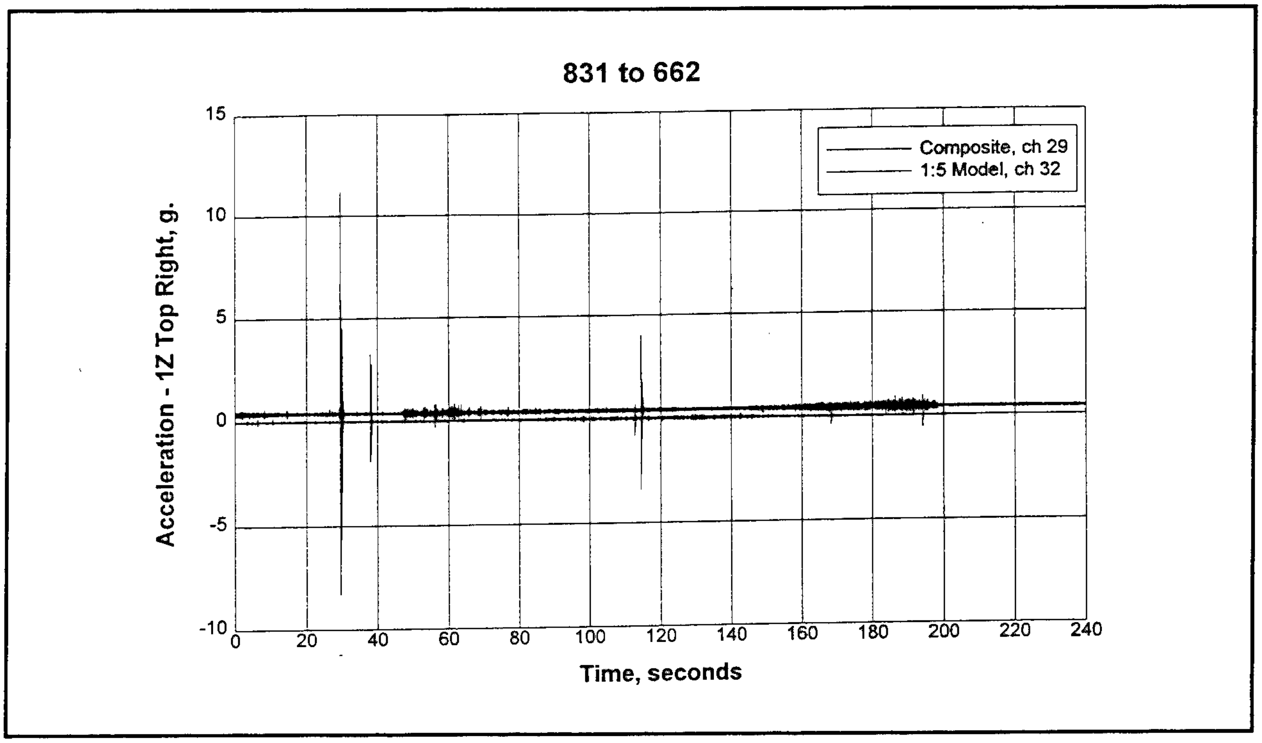

Figure D53. 1Z to right acceleration response of composite and model wickets for 2-GG (ER) down condition

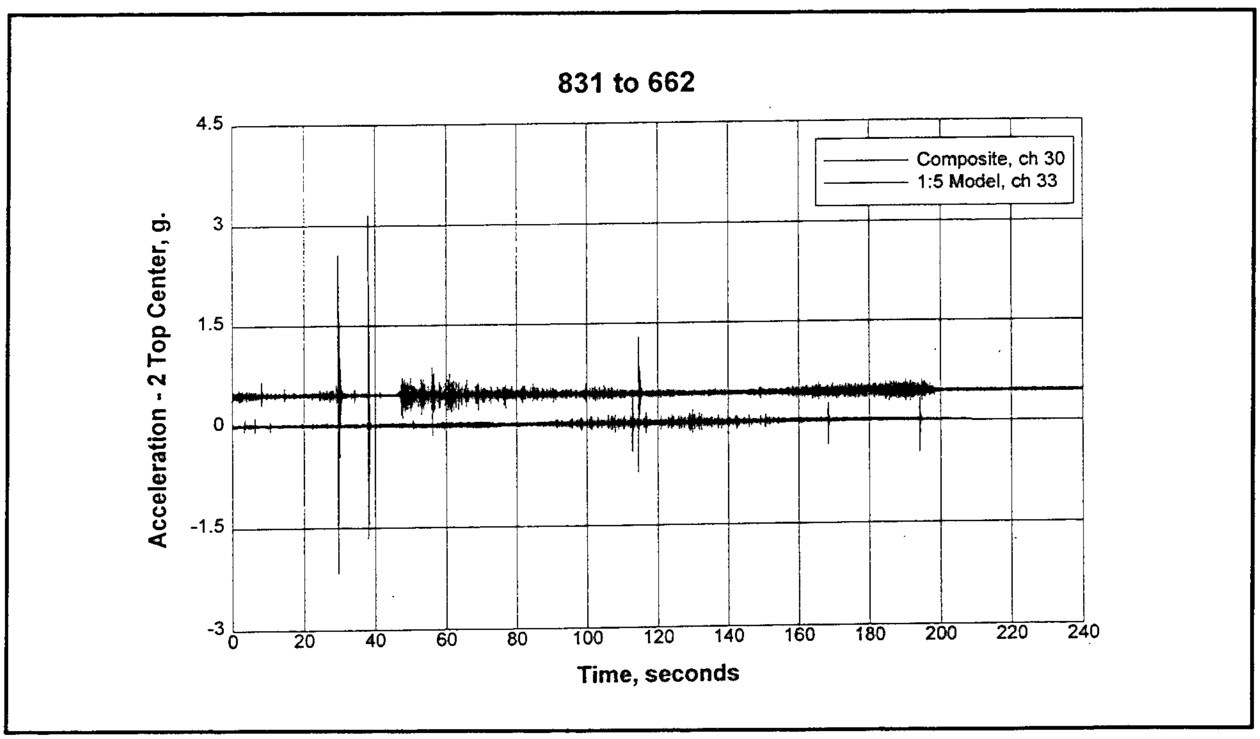

Figure D54. 2 top center acceleration response of composite and model wickets for 2-GG (ER) down condition

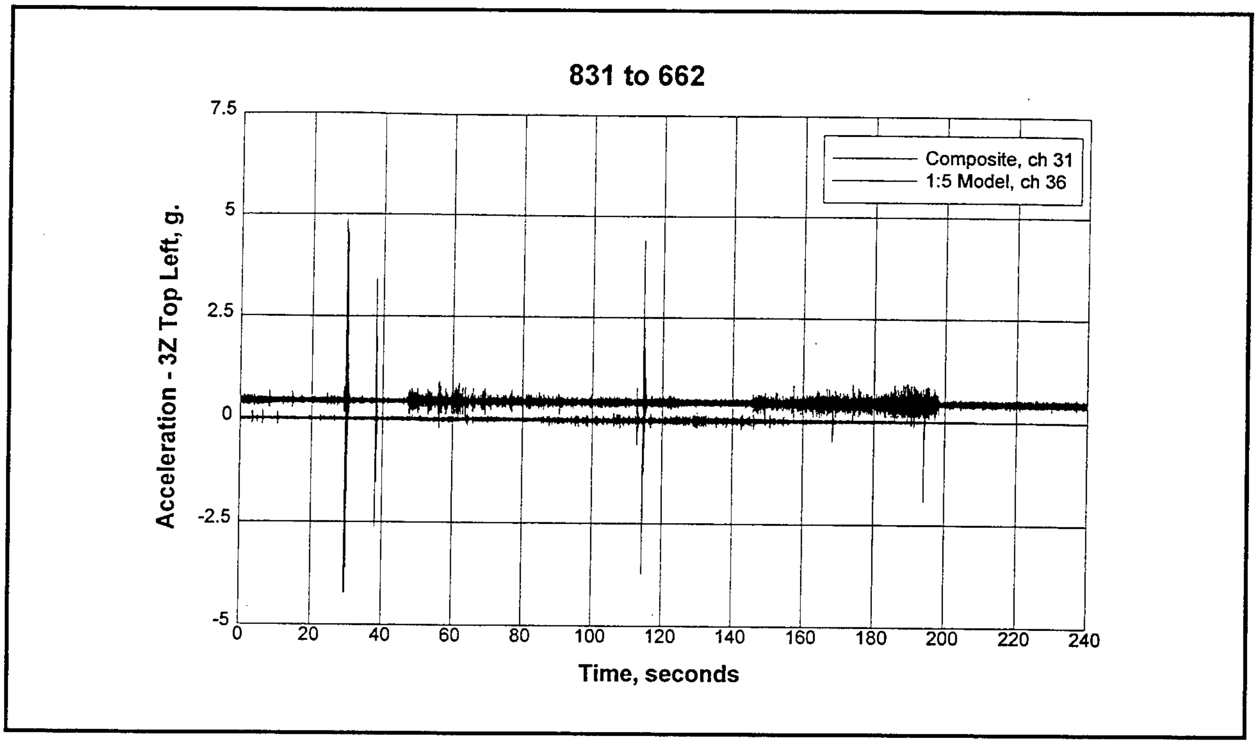

Figure D55. 3Z top left acceleration response of composite and model wickets for 2-GG (ER) down condition

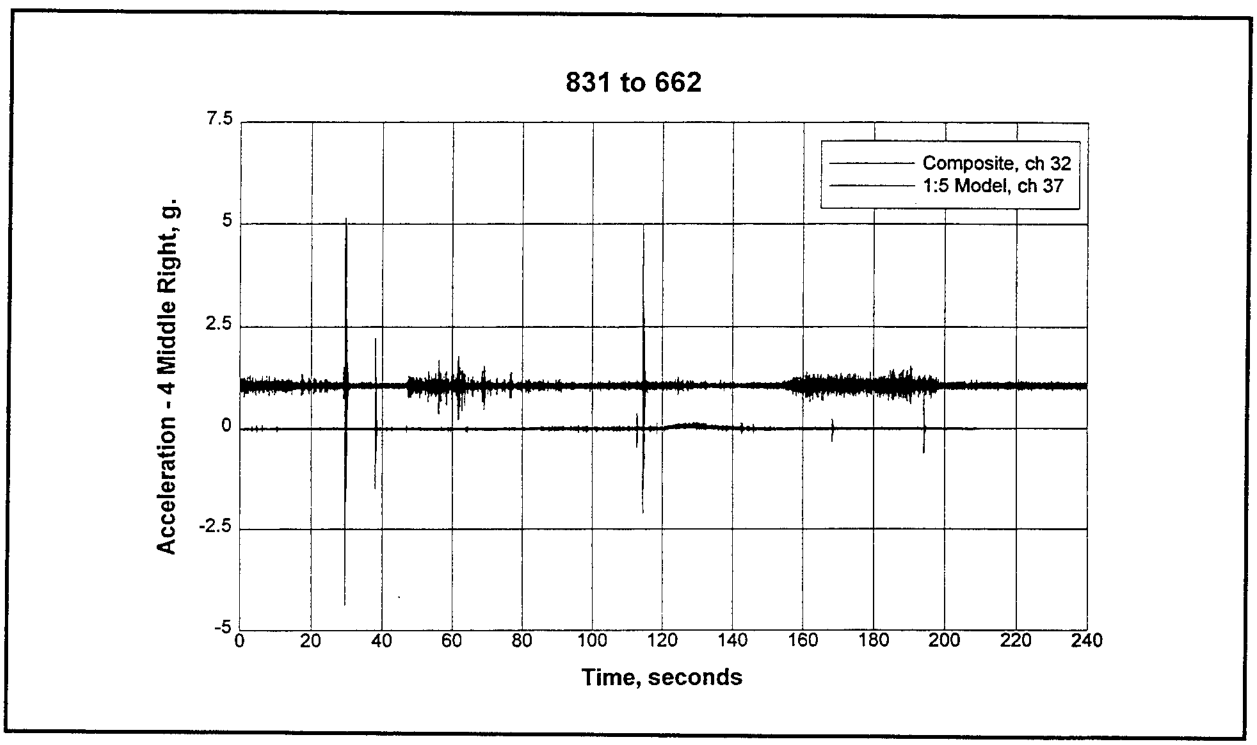

Figure D56. 4 middle right acceleration response of composite and model wickets for 2-GG (ER) down condition

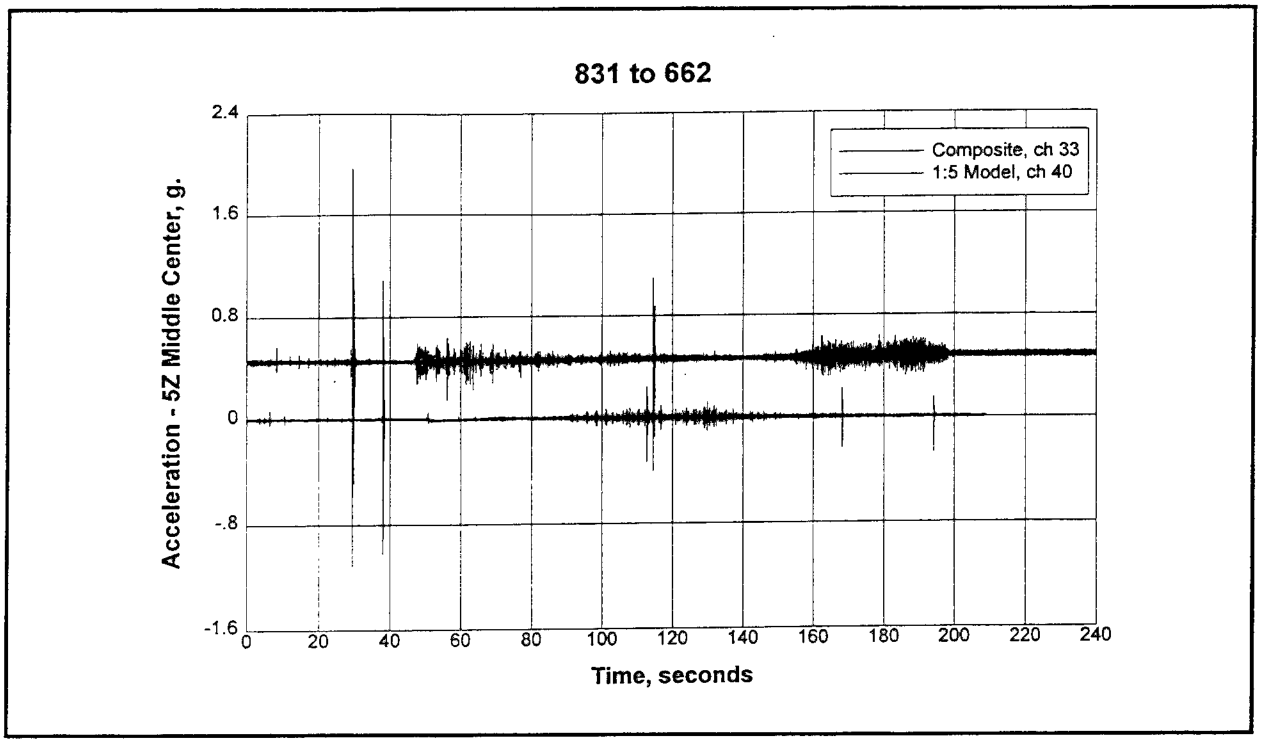

Figure D57. 5Z middle center acceleration response of composite and model wickets for 2-GG (ER) down condition

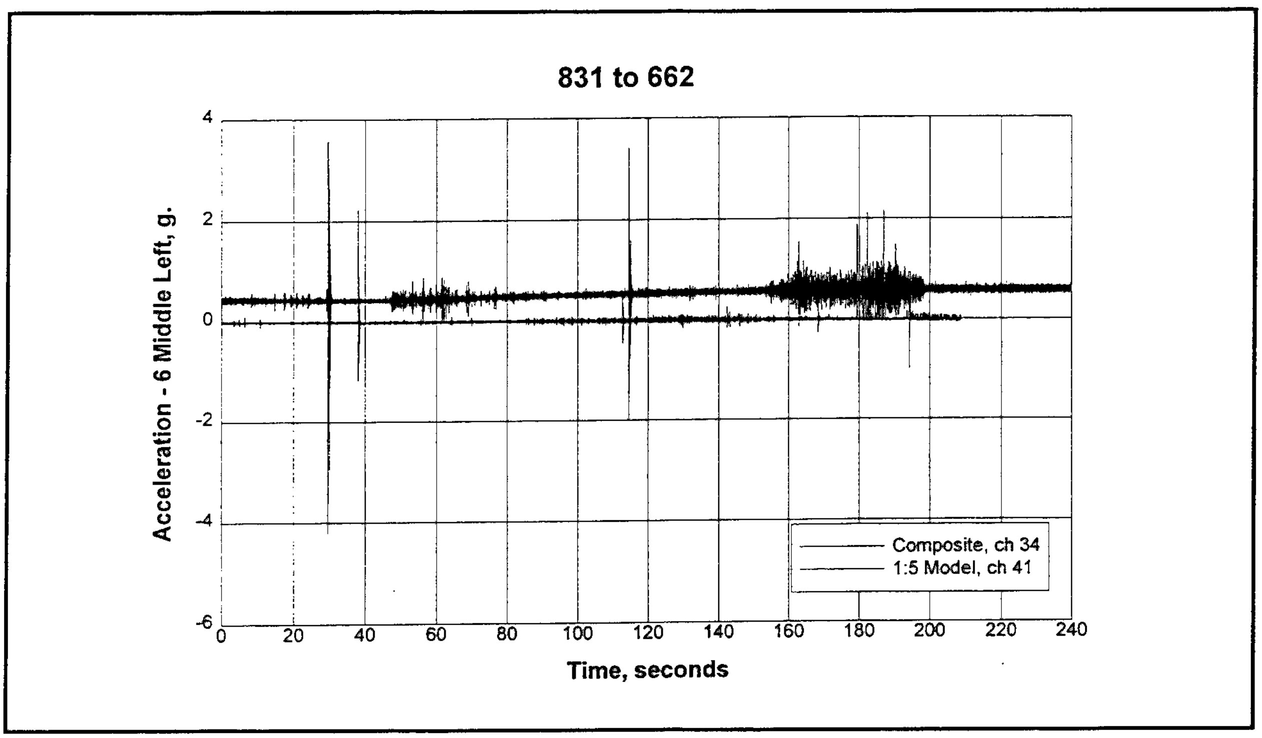

Figure D58. 6 middle left acceleration response of composite and model wickets for 2-GG (ER) down condition

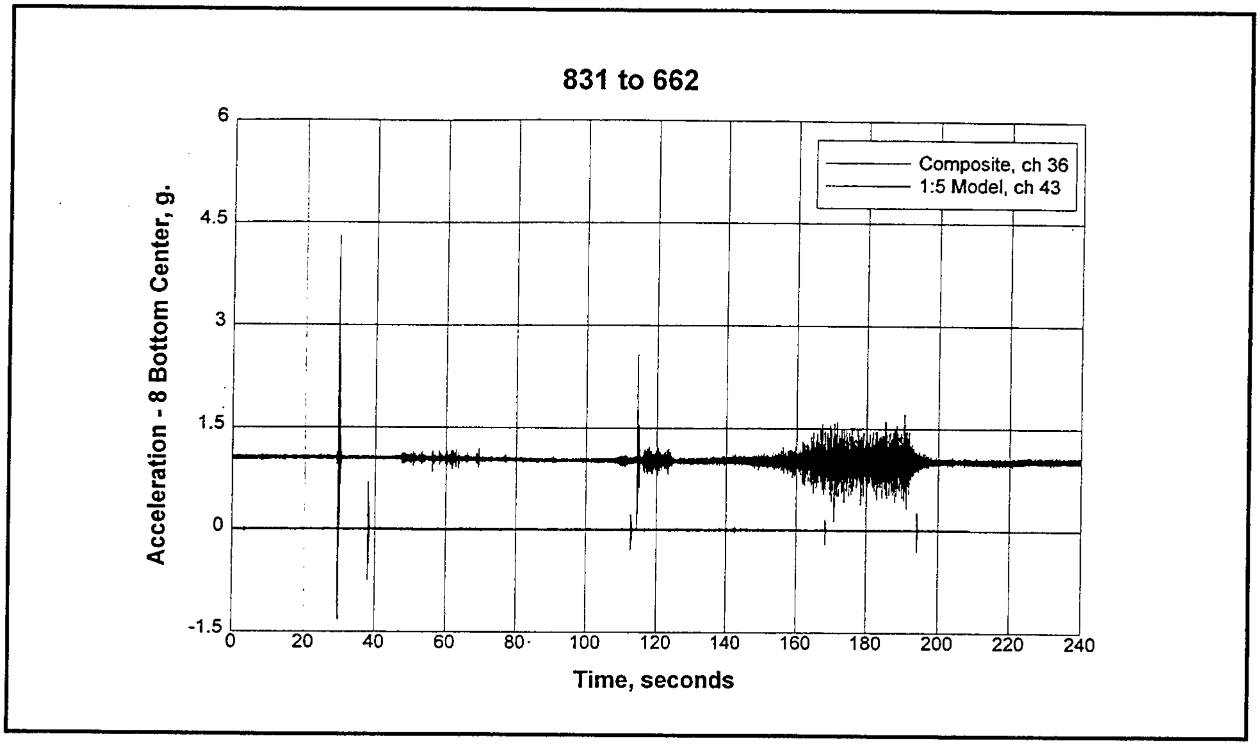

Figure D59. 8 bottom center acceleration response of composite and model wickets for 2-GG (ER) down condition

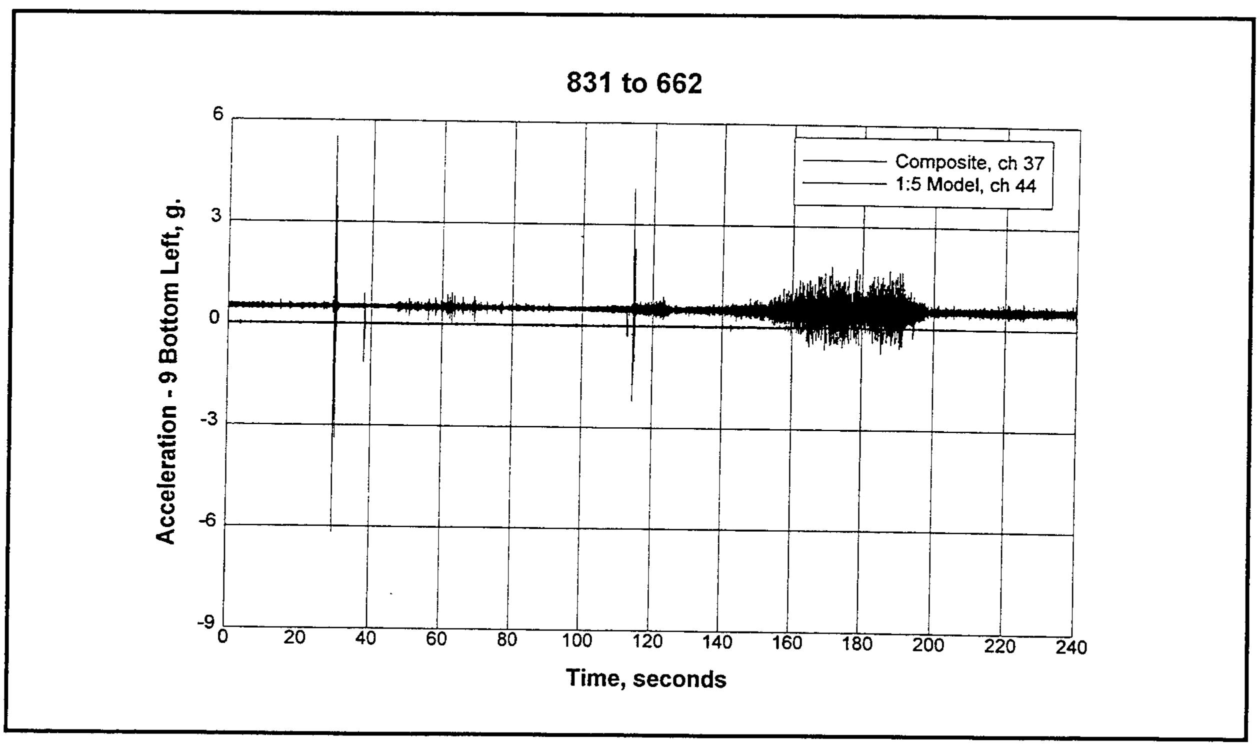

Figure D60. 9 bottom left acceleration response of composite and model wickets for 2-GG (ER) down condition

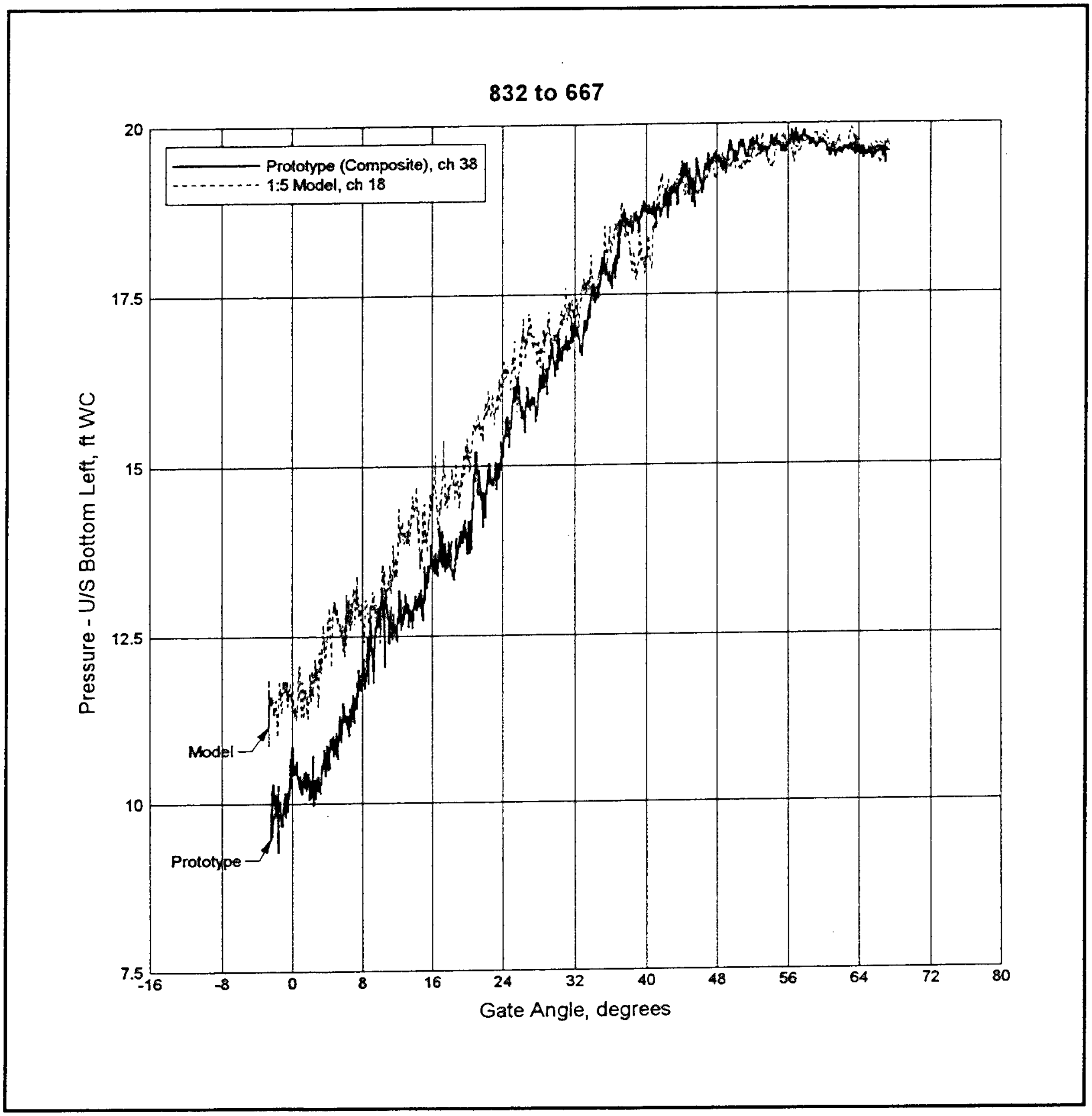

Figure D61. Upstream bottom left pressure variation for 2-GG (EL) up condition

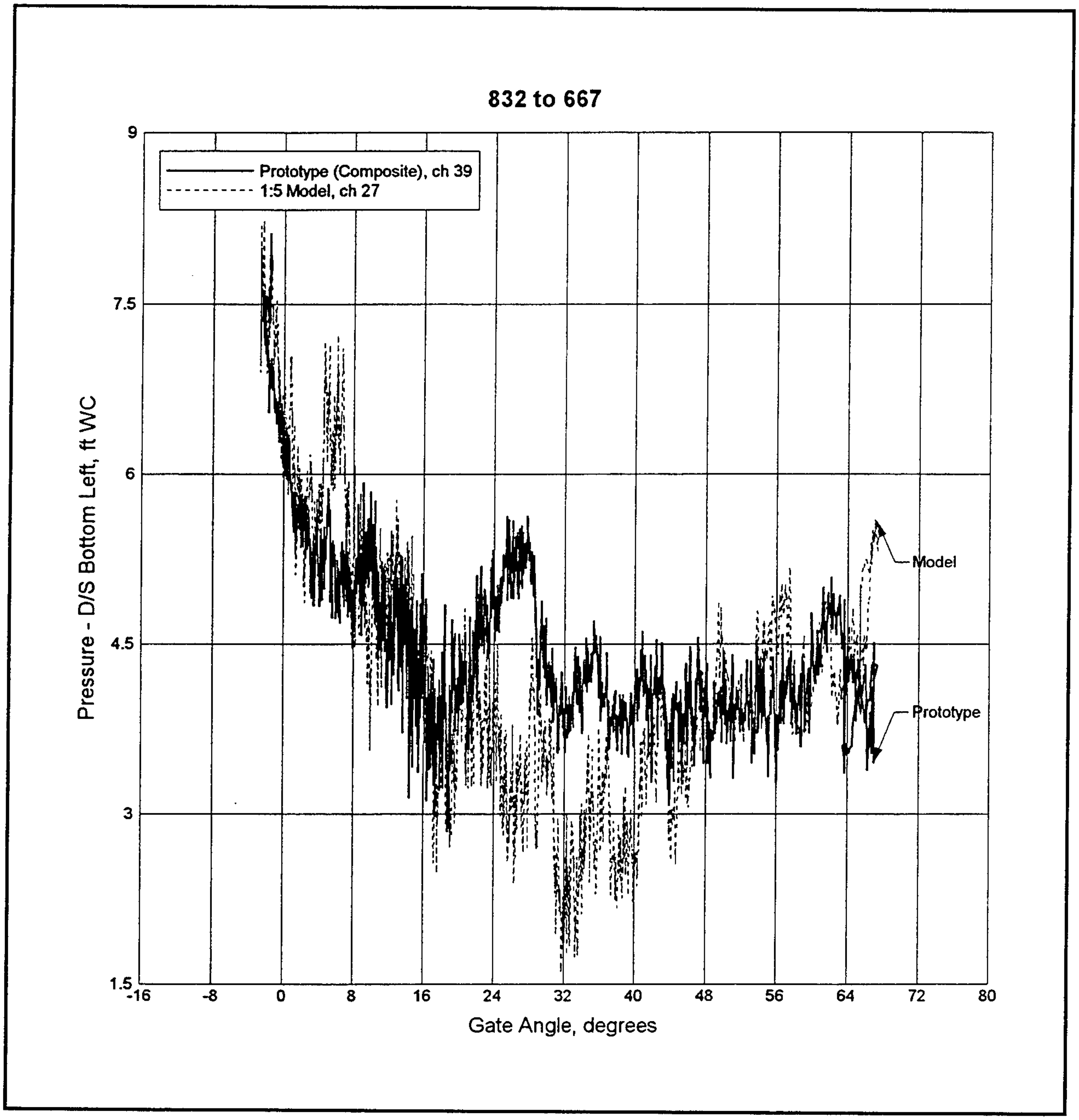

Figure D62. Downstream bottom left pressure variation for 2-GG (EL) up condition

Appendix E
Fixed-Gate Response

In this appendix, the wet gate response for the prop-supported wickets are compared for the prototype and the scale model. During this experiment, all gates were raised and the data were recorded for the fixed gate (see test group 15 in Table 5, main text). No calibration factor was used in the prototype data. As mentioned in the text, the left-hinge vertical sensor was found inactive during the recalibration process. For design purpose, however, one should use the recalibration factor for estimating the design loads for the hinges.

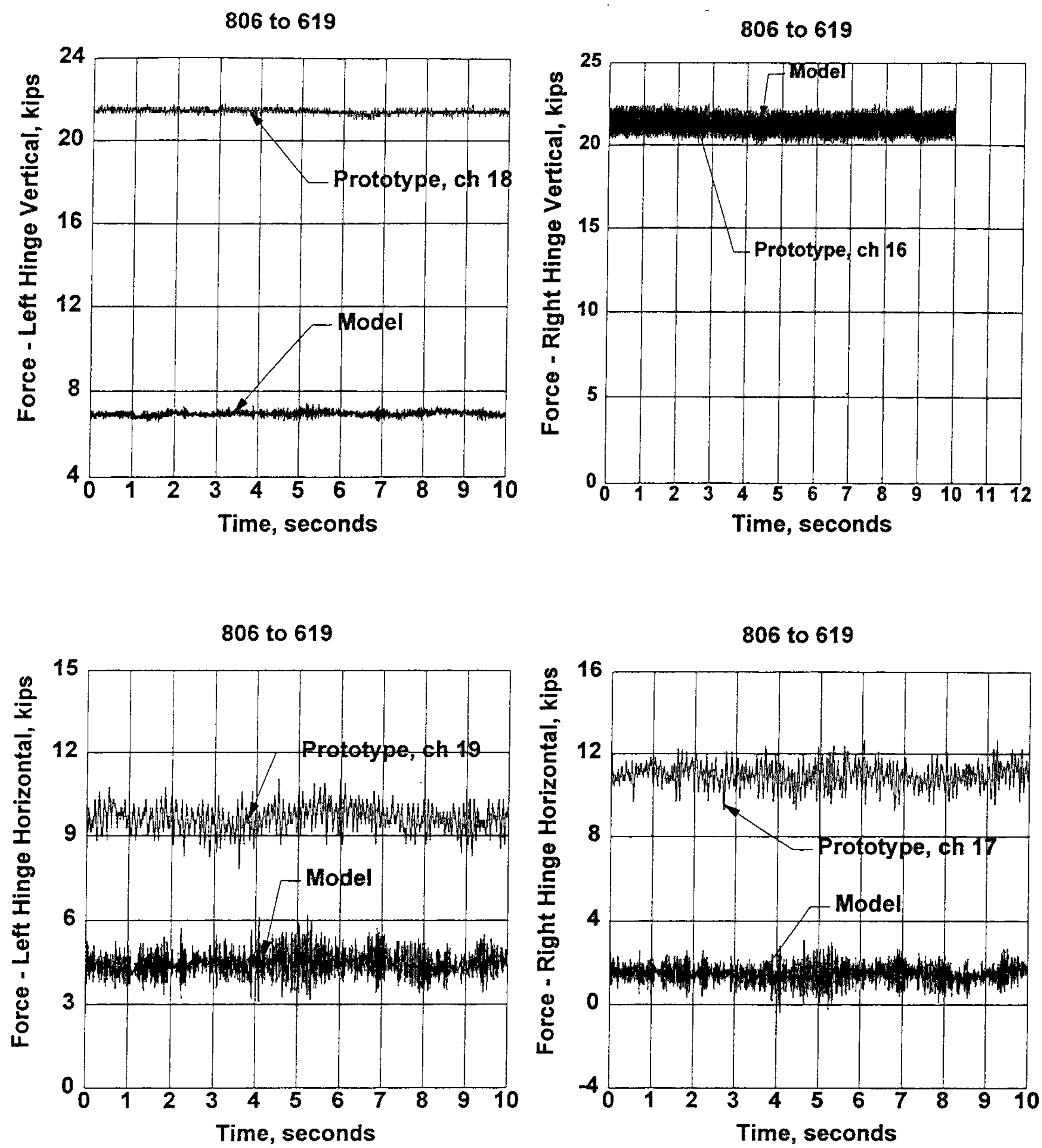

Figure E1. A comparison of hinge reactions for prop-supported model and prototype wickets

Appendix F Prop-Rod Forces

These plots show the responses of the supporting devices for a very small portion of the entire movement of a raising wicket. During a raising cycle, the primary cylinder is extended, thereby rotating the gate through an arc from -3 to 68 deg, then stopped and retracted, and the load from the lifting cylinder was transferred to the prop rod at the 65-deg position where the prop rod locks in the hurter. Figure F1 shows the load transfer mechanisms on the prop rod when the cylinder is relieved from supporting the dry prototype wicket. During the raising cycle, the prop is being pulled along as it comes up the hurter and this dragging force causes the negative load reading in the prop rod sensor. Figure F1 shows the major transient response of the wicket at 65 deg when the prop falls into the notch in the hurter. The flat response of the prop rod continues to prevail for the stopped cylinder at 68 deg. As the cylinder is retracted from stopped position, the wicket load is transferred to the prop rod and the lifting cylinder is relieved from carrying the load of the wicket. Figure F2 shows the trunnion reactions (load carried by the hydraulic cylinder) of the model during the time-span when load is transferred from the cylinder to the prop rod. Figure F3 shows the load-transfer history of the trunnions for different flow configurations as indicated. The trunnion reaction at 65 deg, right before the disengagement of the cylinder, was used to estimate the equivalent prop rod reaction for the wickets.

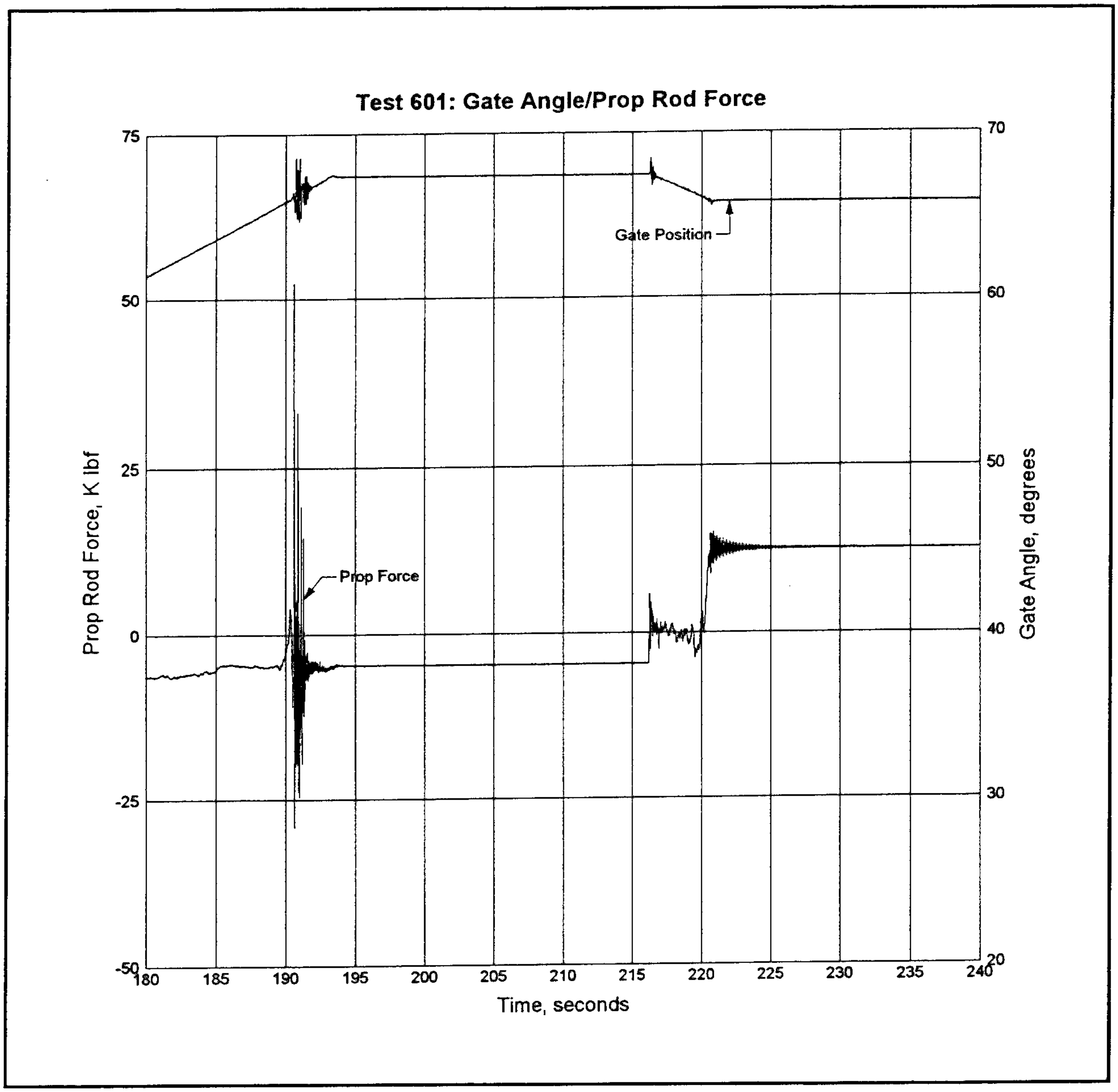

Figure F1. Prop-rod force and gate angle vs time for dry prototype wicket

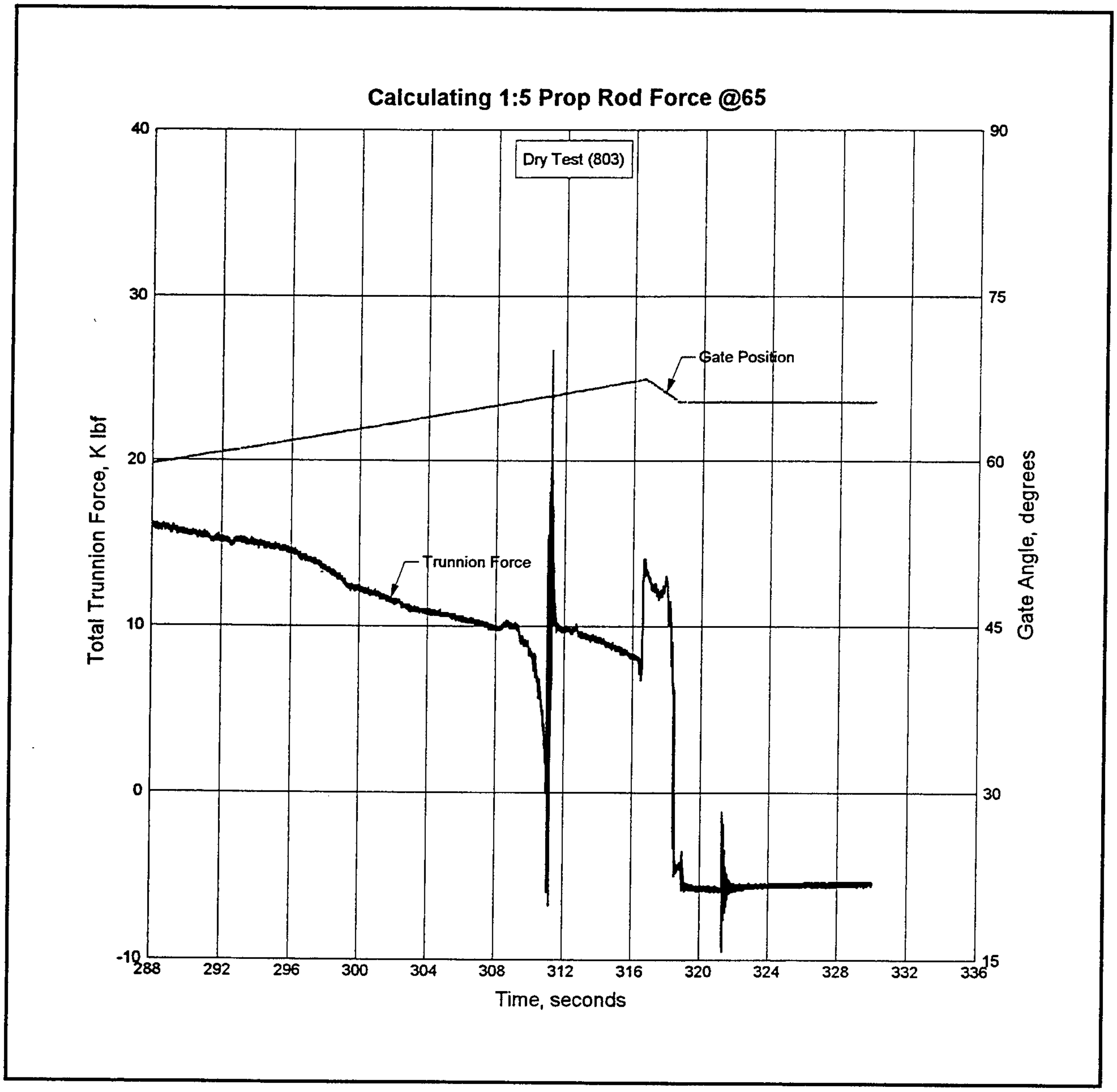

Figure F2. Total trunnion force and gate angle vs time for dry 1:5-scale model

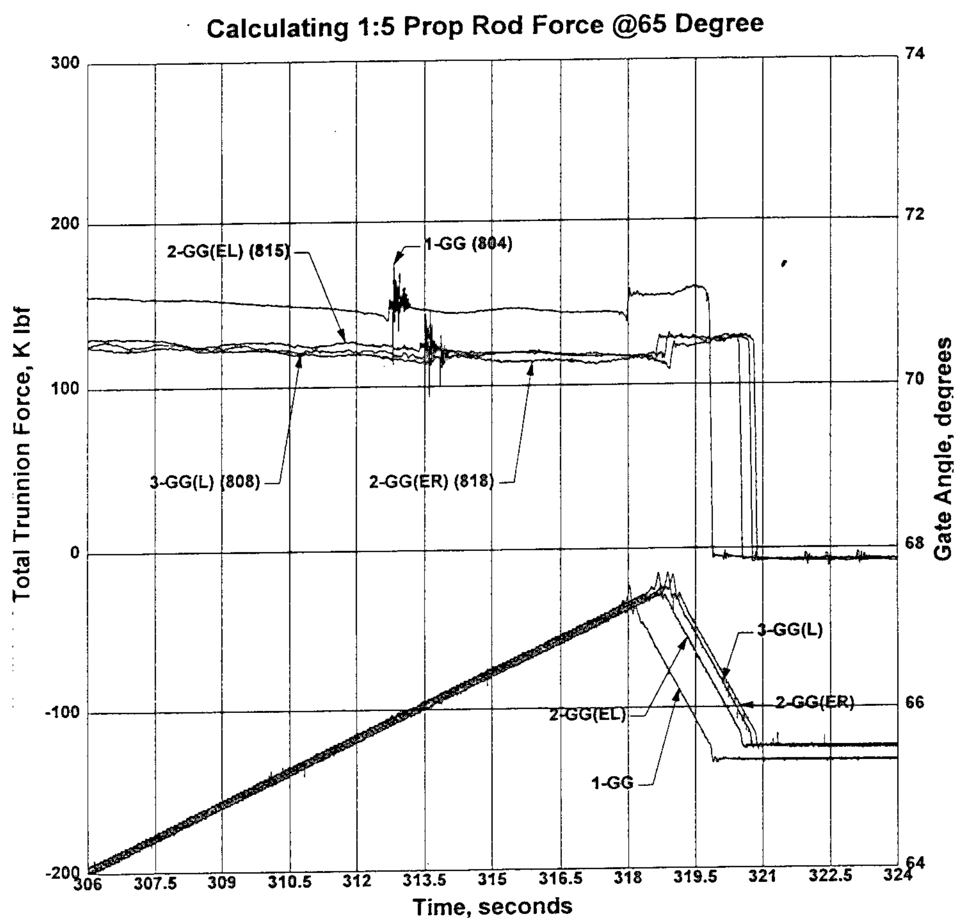

Figure F3. Total trunnion force and gate angle vs time for wet operation of 1:5-scale model

Appendix G
Principal Stress and Strain in the Prototype Steel Gate

Prototype principal stresses, principal strains, and principal planes (for orientation see figure below) for different flow conditions of the steel gate are plotted in this appendix. Strain gauge locations are shown in Figure 12, main text, and all flow conditions shown in Table 5, main text, are used for studying the variation of flow-induced strain of the wicket. Strains are recorded as the gate is raised or lowered according to the condition shown in Table 5, main text. Principal parameters are plotted as a function of gate angle.

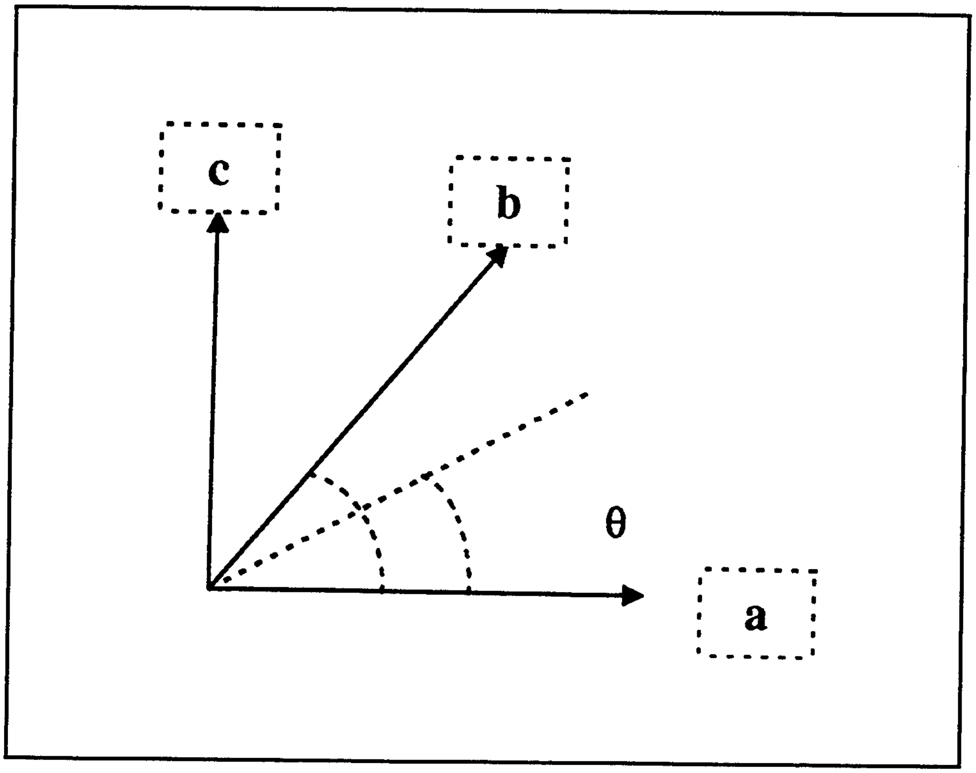

Figure G1. Principal plane orientation from known axis

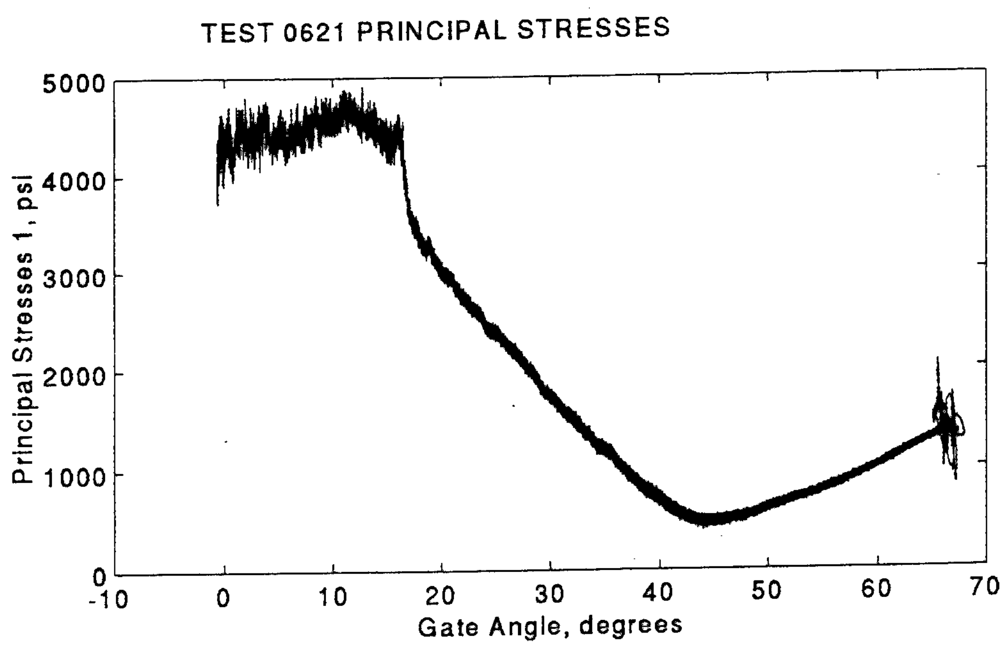

Figure G2. Prototype principal stress 1 vs gate angle for 1-GG up condition

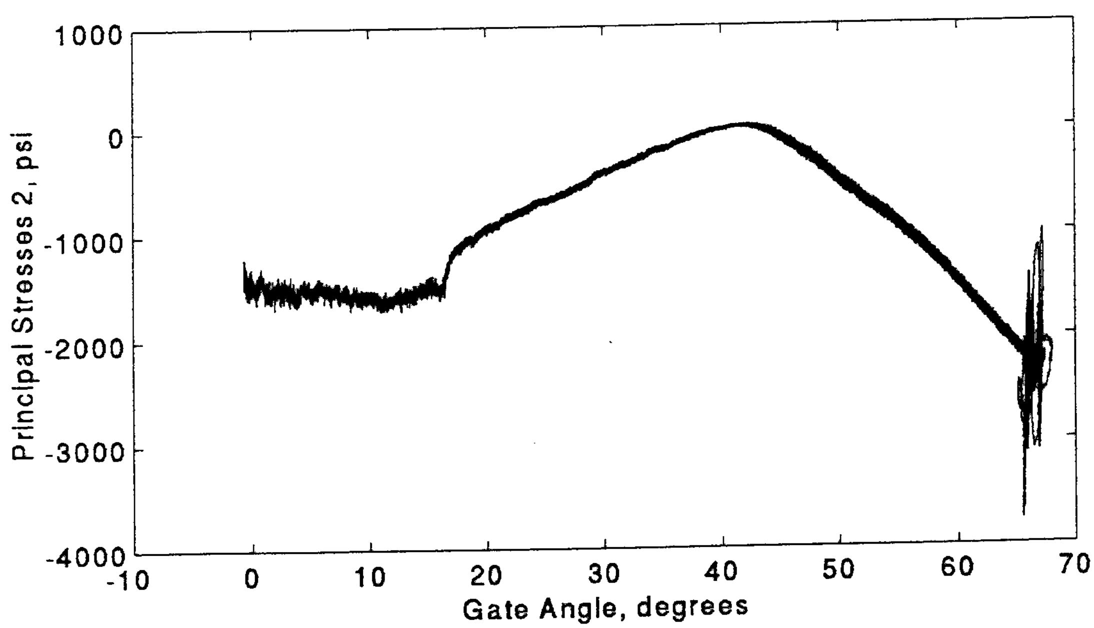

Figure G3. Prototype principal stress 2 vs gate angle for 1-GG up condition

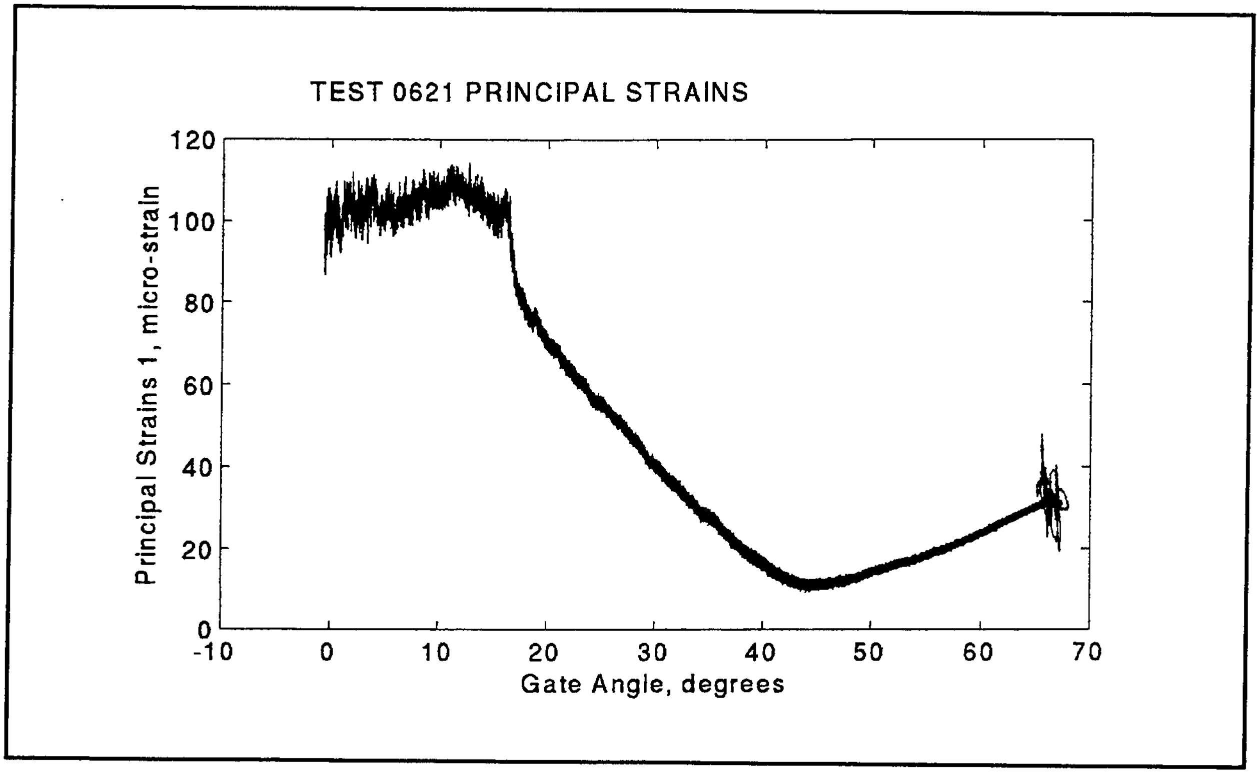

Figure G4. Prototype principal strain 1 vs gate angle for 1-GG up condition

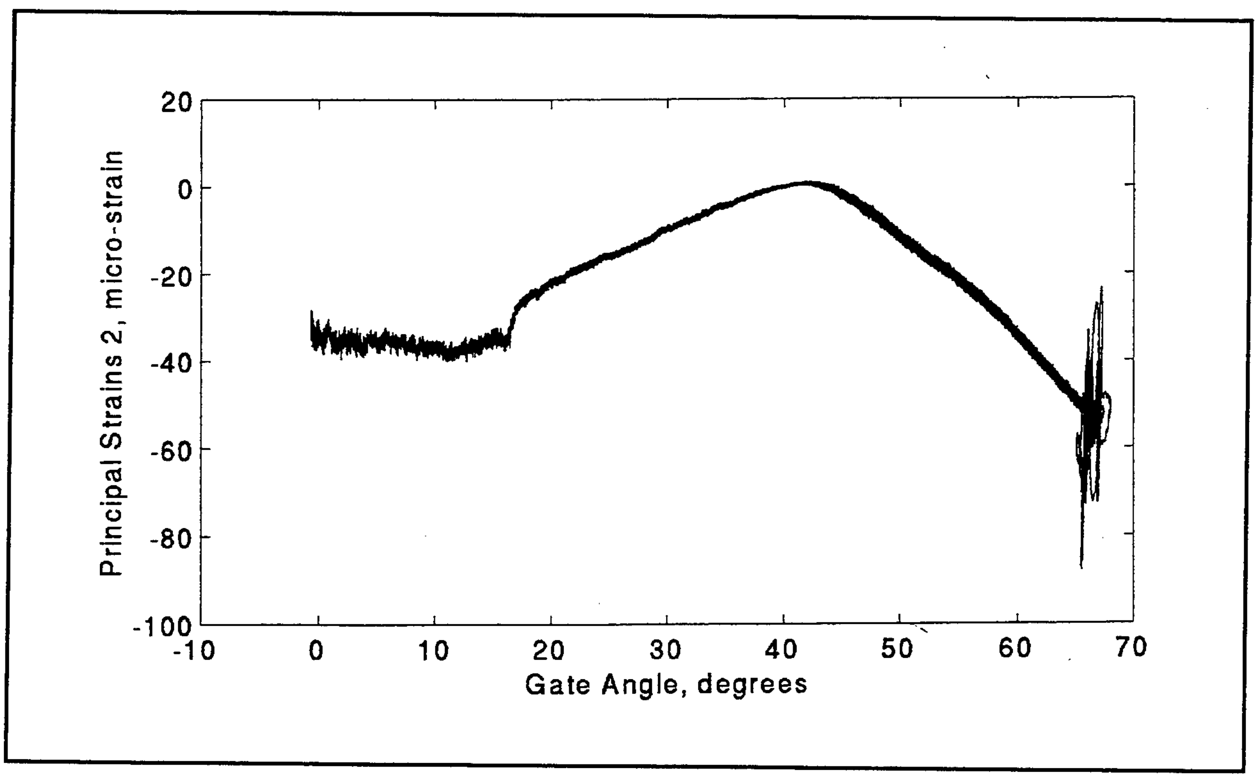

Figure G5. Prototype principal strain 2 vs gate angle for 1-GG up condition

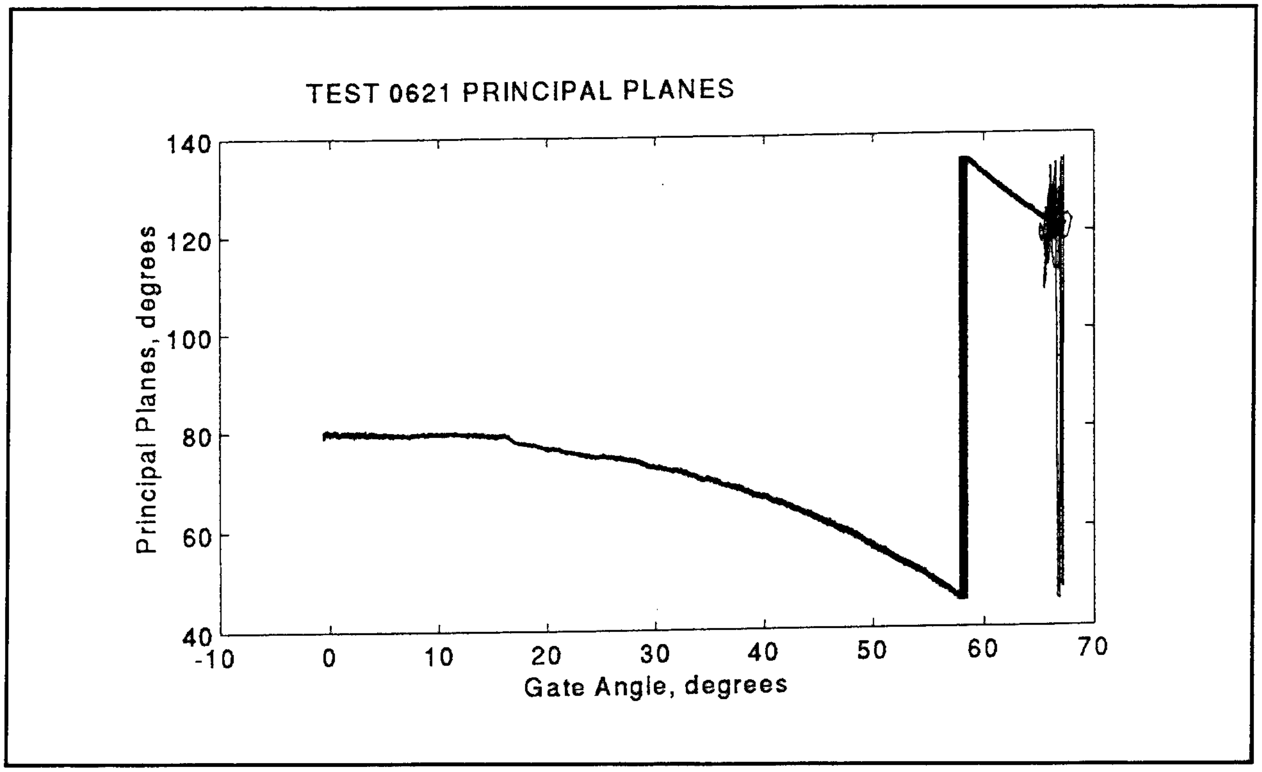

Figure G6. Prototype principal planes vs gate angle for 1-GG up condition

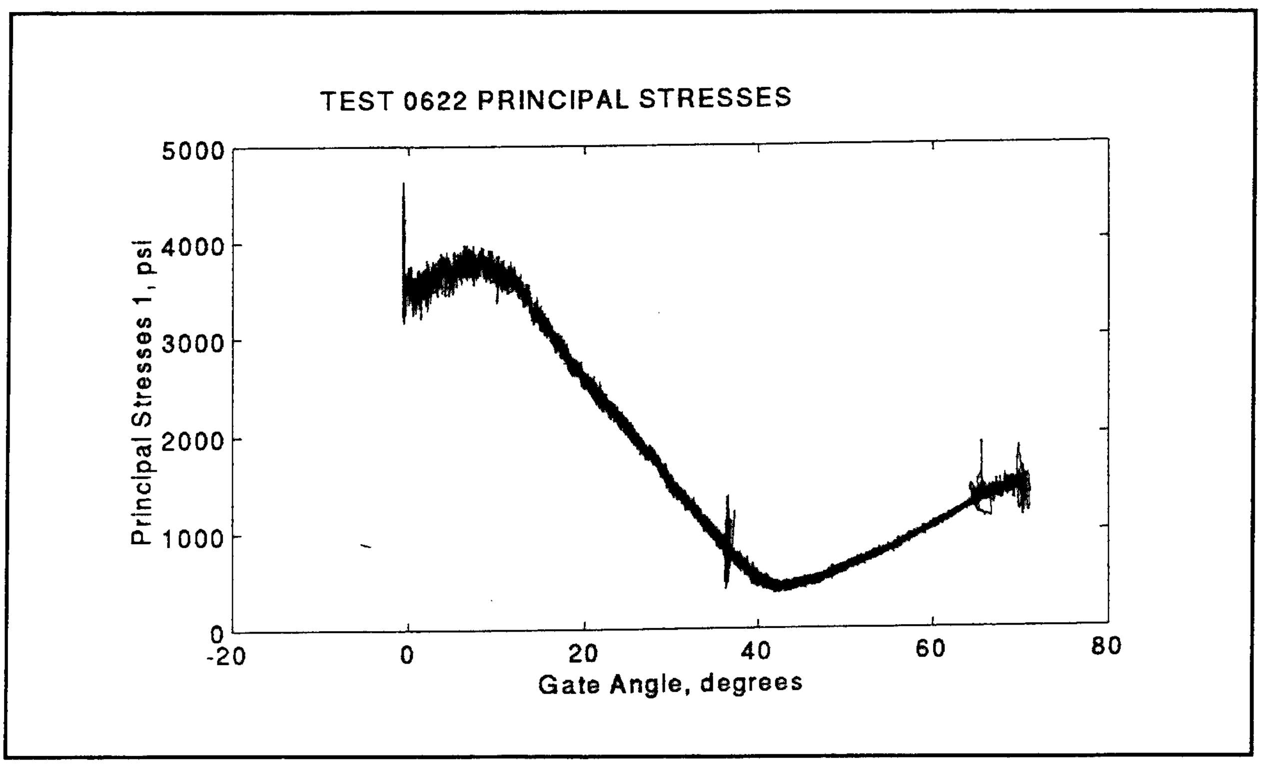

Figure G7. Prototype principal stress 1 vs gate angle for 1-GG down condition

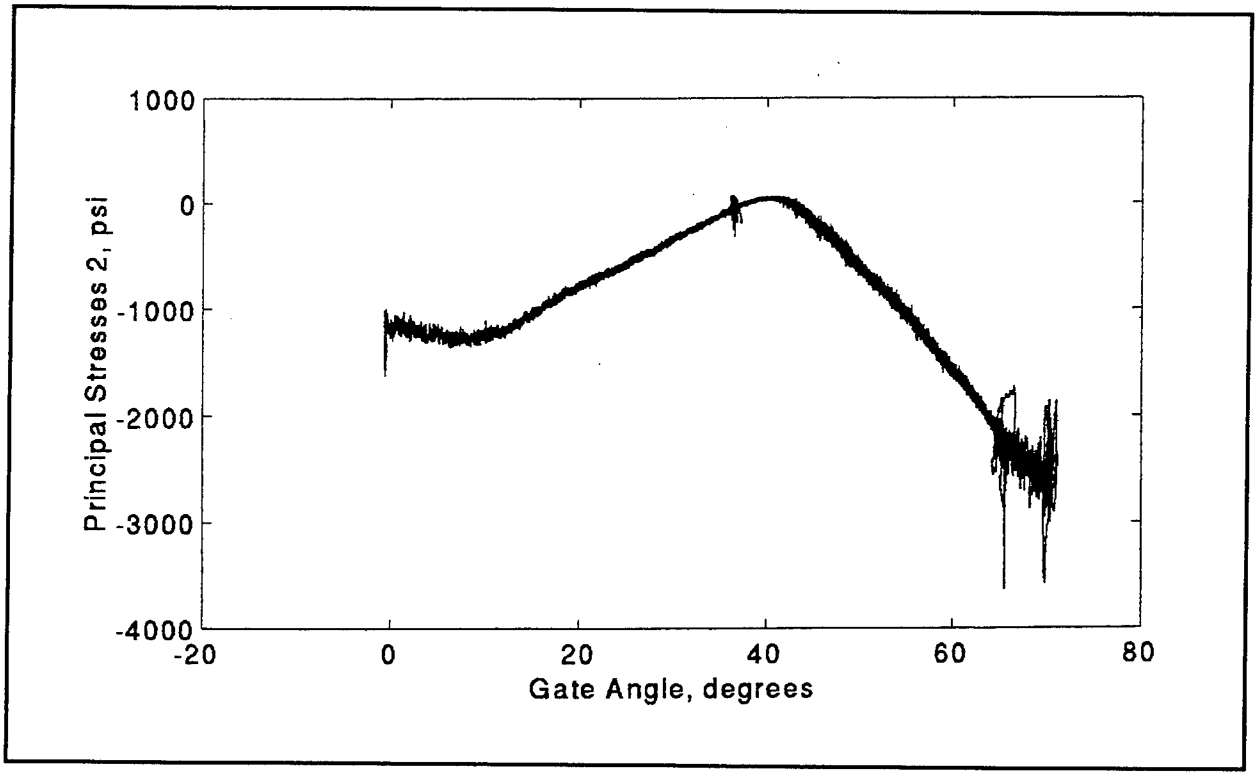

Figure G8. Prototype principal stress 2 vs gate angle for 1-GG down condition

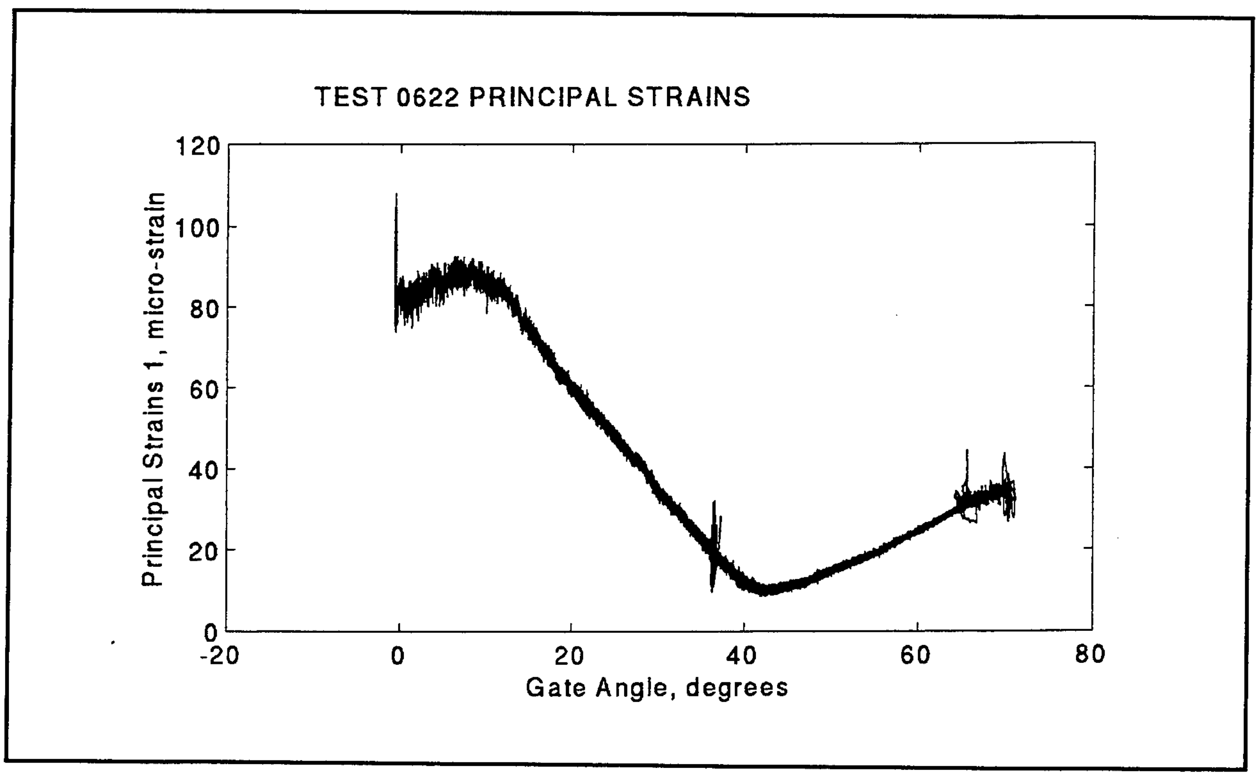

Figure G9. Prototype principal strain 1 vs gate angle for 1-GG down condition

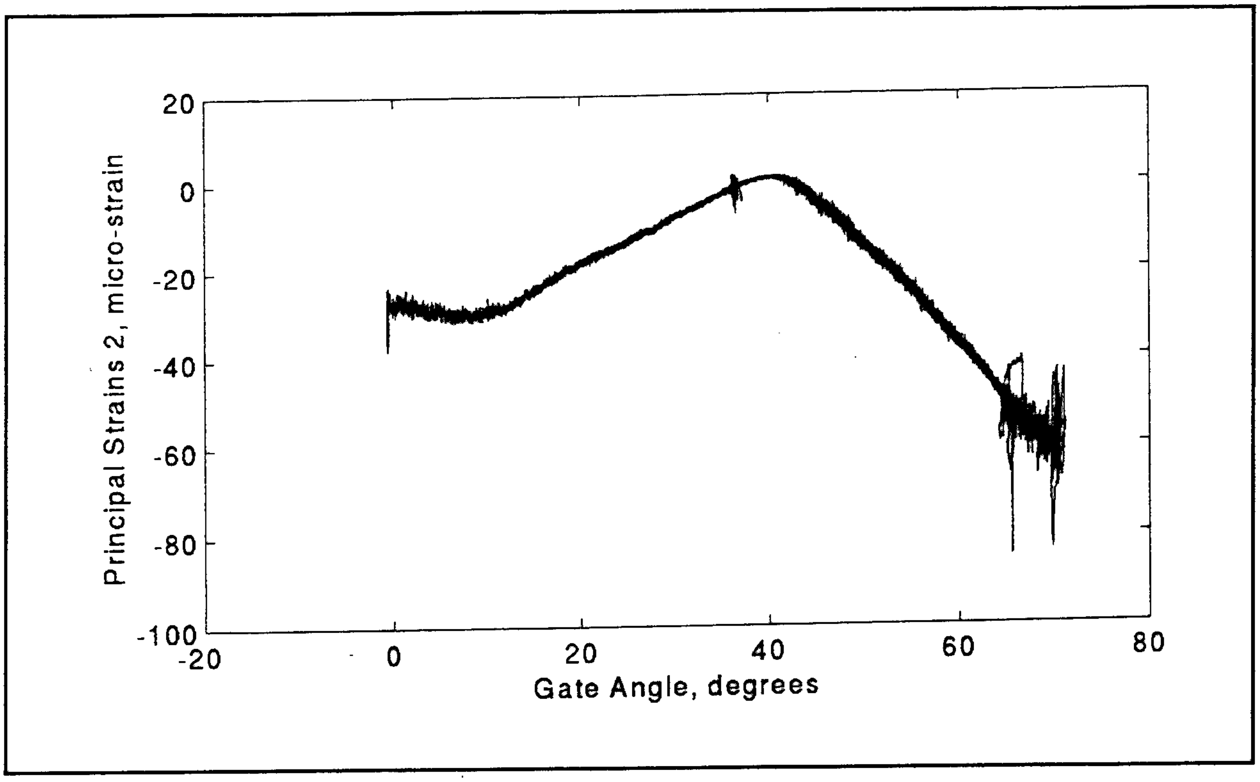

Figure G10. Prototype principal strain 2 vs gate angle for 1-GG down condition

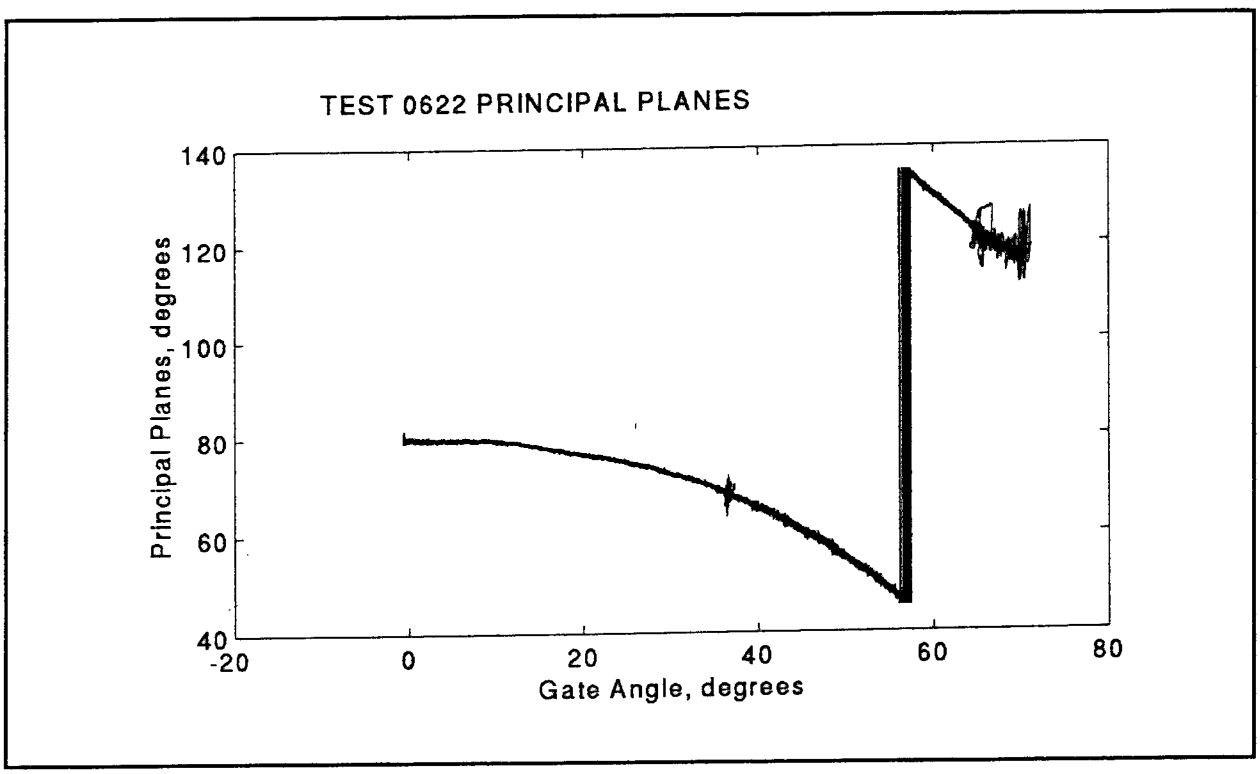

Figure G11. Prototype principal planes vs gate angle for 1-GG down condition

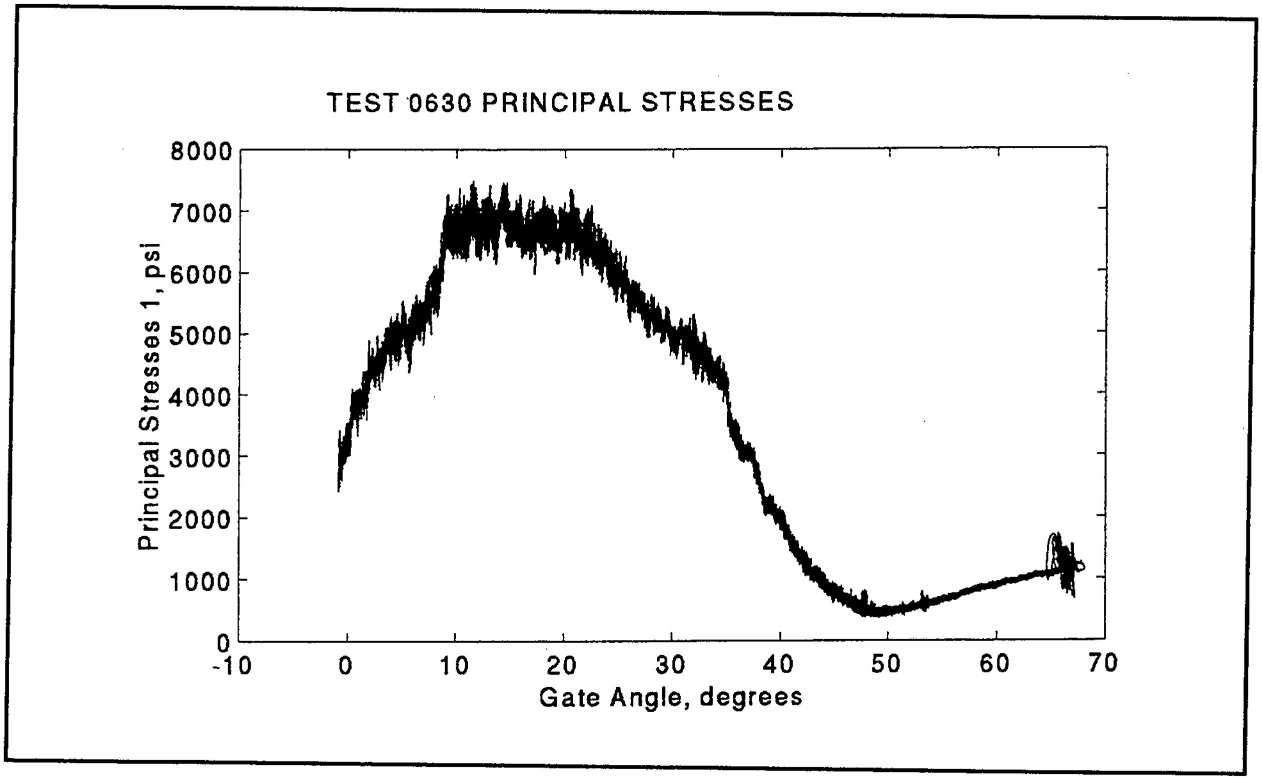

Figure G12. Prototype principal stress 1 vs gate angle for 3-GG up condition

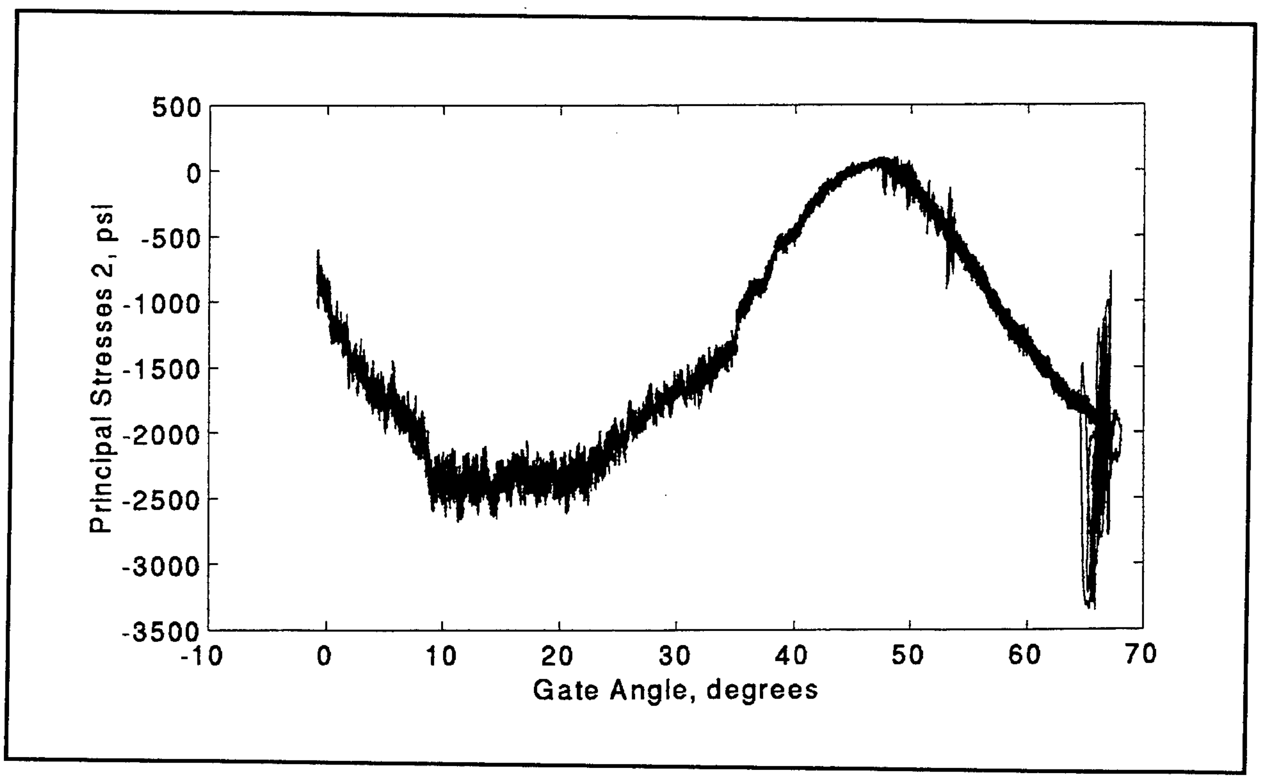

Figure G13. Prototype principal stress 2 vs gate angle for 3-GG up condition

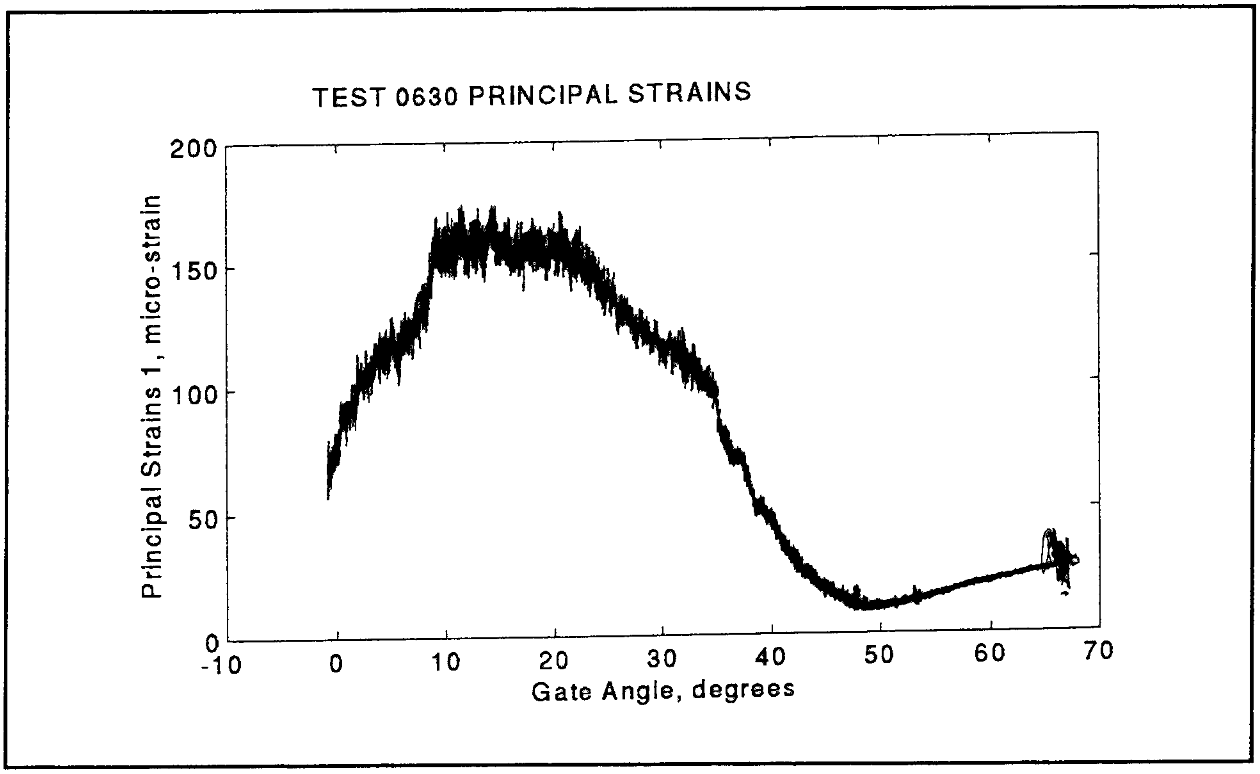

Figure G14. Prototype principal strain 1 vs gate angle for 3-GG up condition

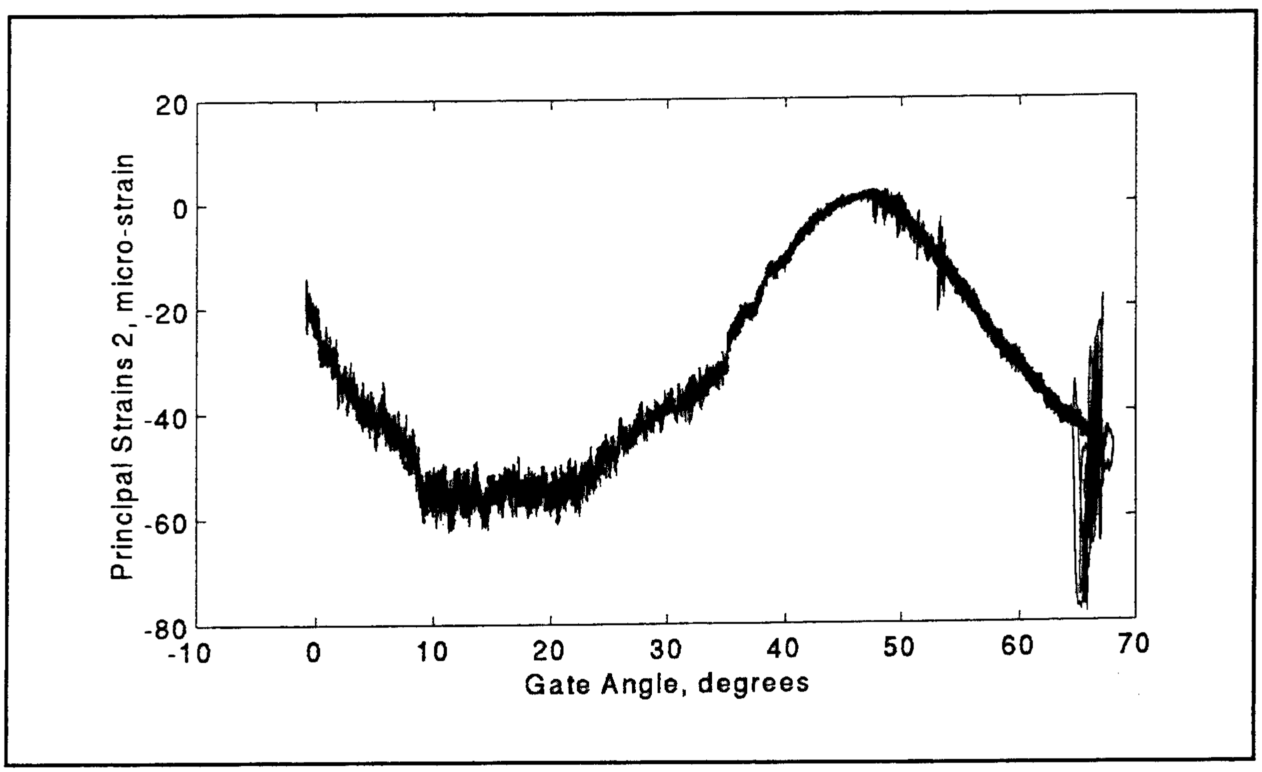

Figure G15. Prototype principal strain 2 vs gate angle for 3-GG up condition

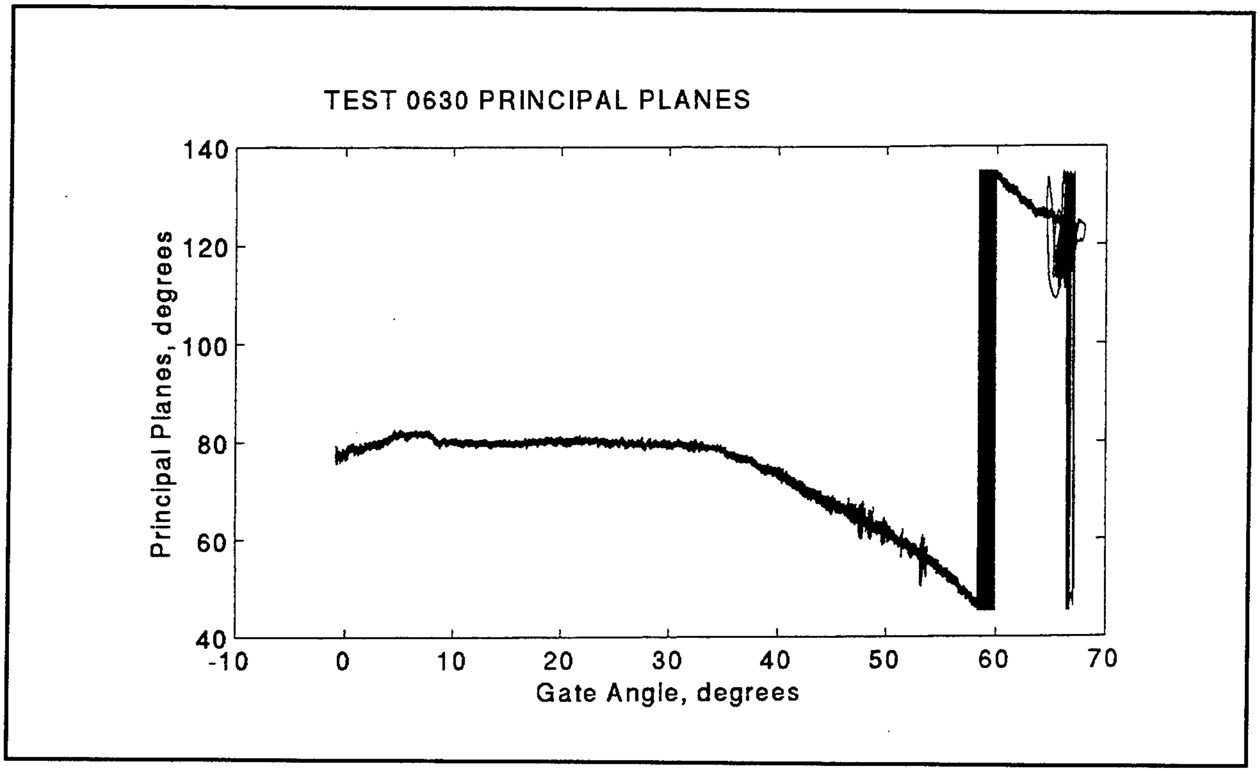

Figure G16. Prototype principal planes vs gate angle for 3-GG up condition

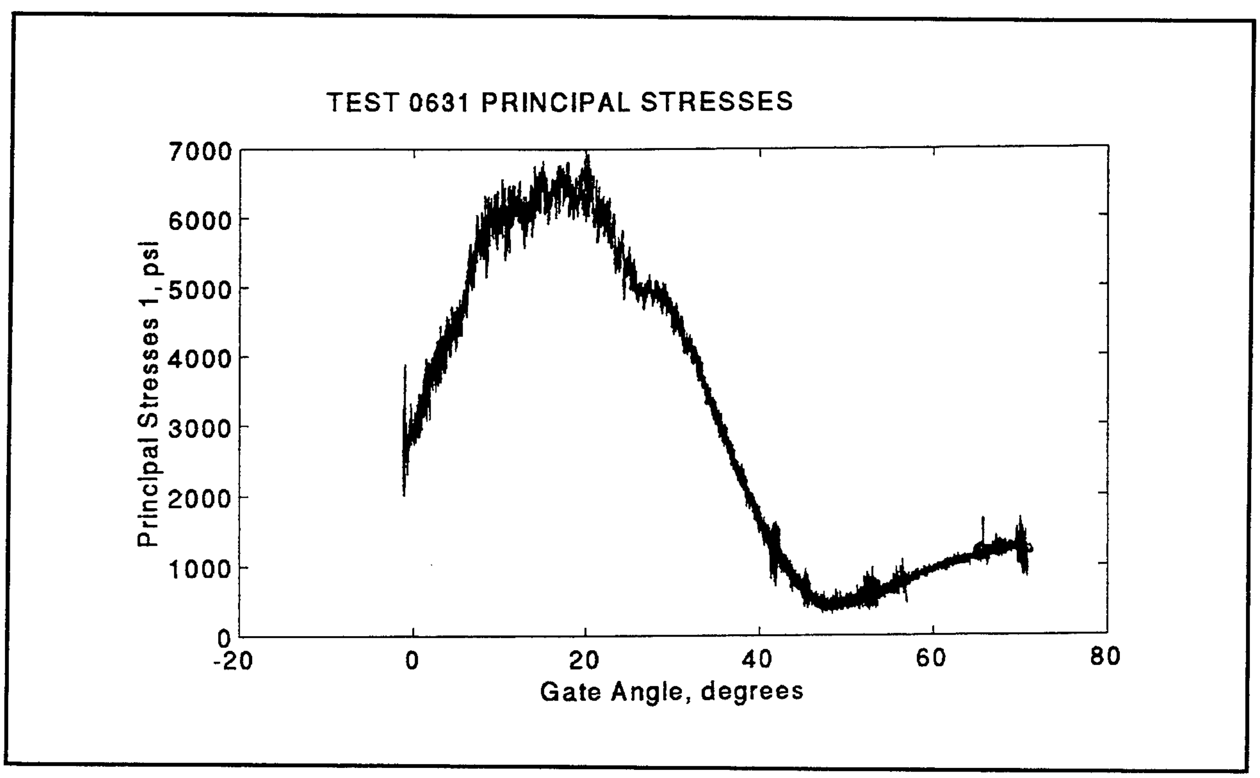

Figure G17. Prototype principal stress 1 vs gate angle for 3-GG down condition

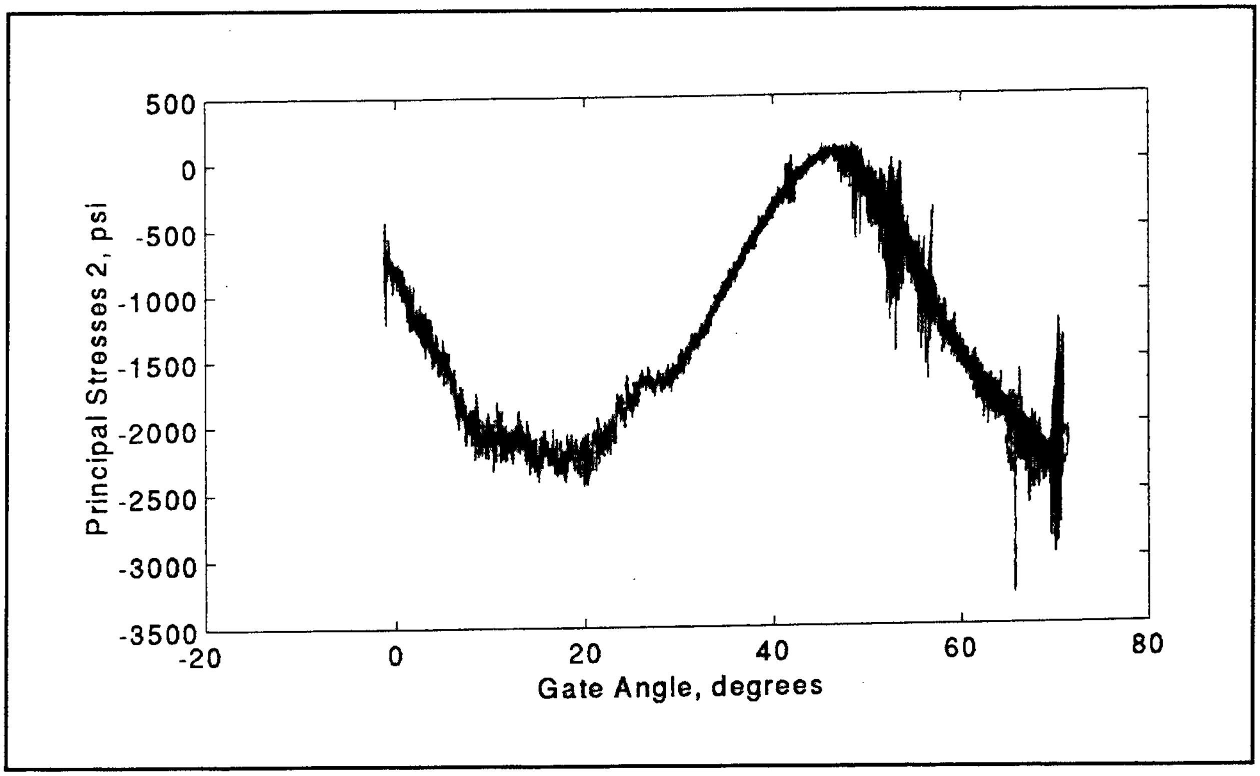

Figure G18. Prototype principal stress 2 vs gate angle for 3-GG down condition

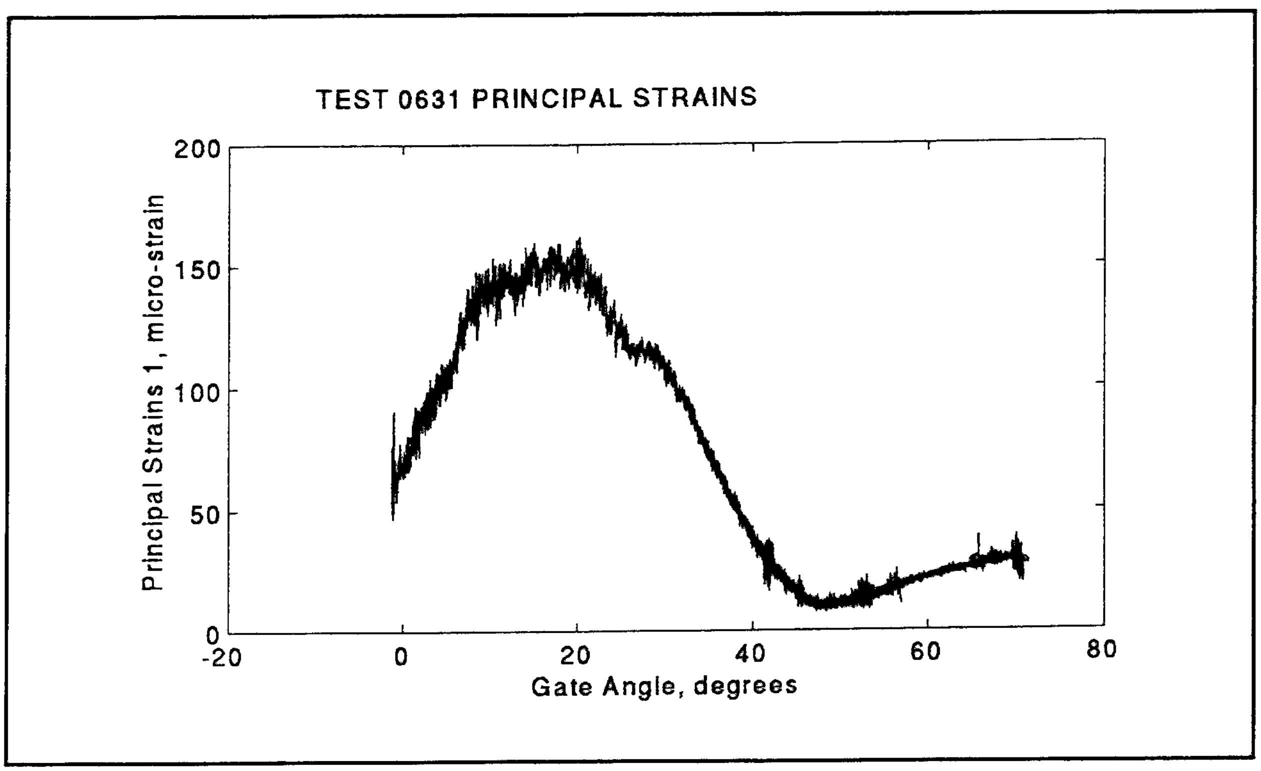

Figure G19. Prototype principal strain 1 vs gate angle for 3-GG down condition

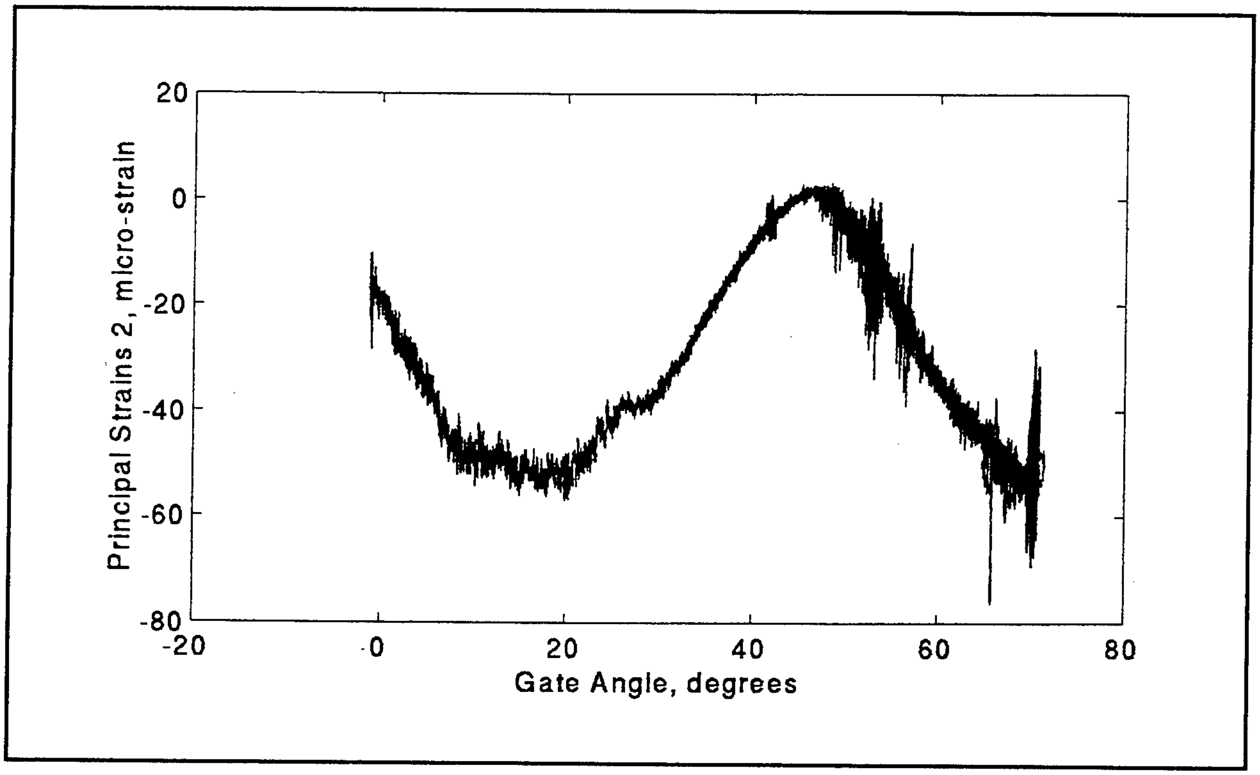

Figure G20. Prototype principal strain 2 vs gate angle for 3-GG down condition

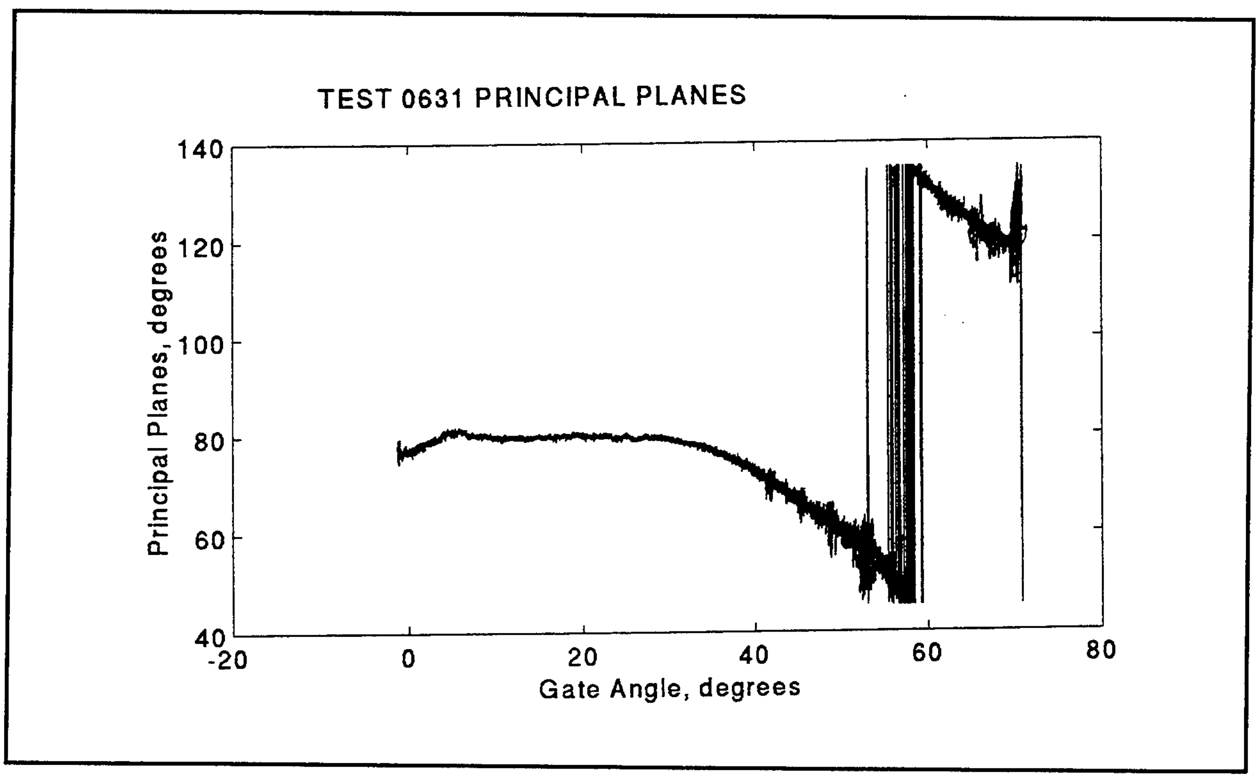

Figure G21. Prototype principal planes vs gate angle for 3-GG down condition

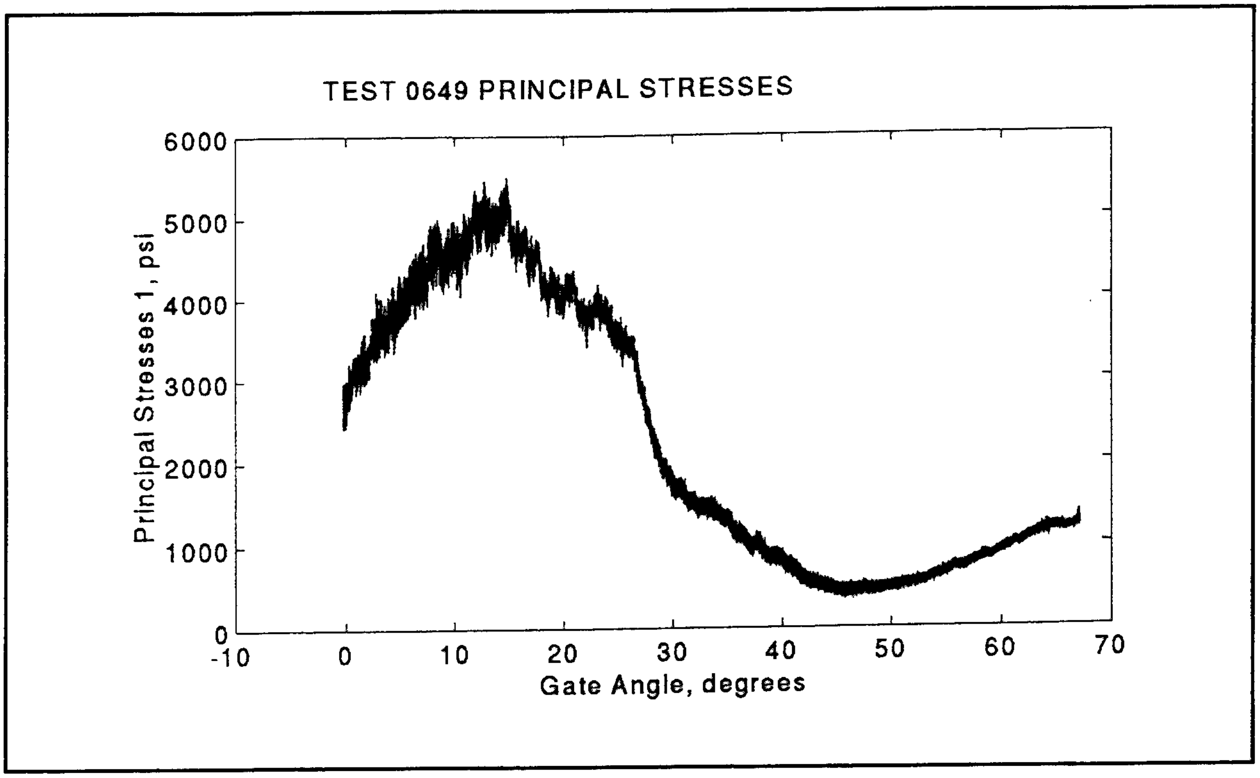

Figure G22. Prototype principal stress 1 vs time for 2-GG (EL) up condition

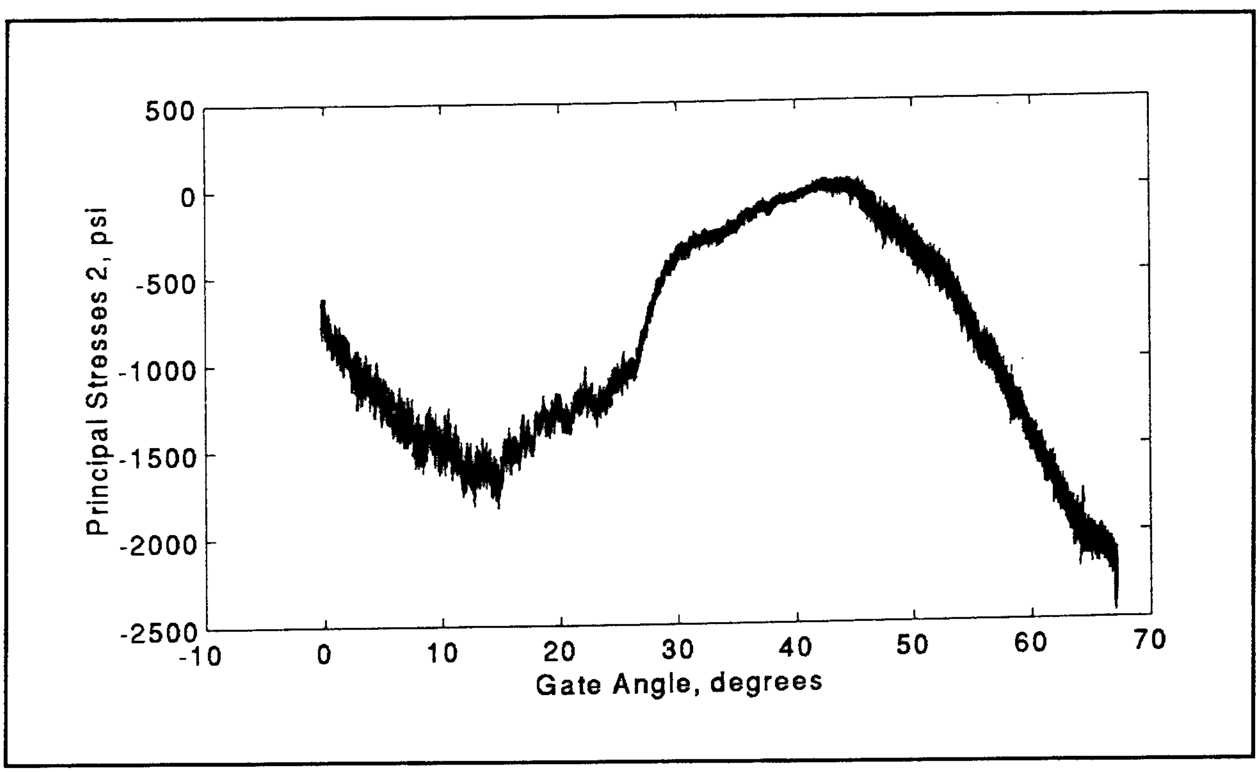

Figure G23. Prototype principal stress 2 vs time for 2-GG (EL) up condition

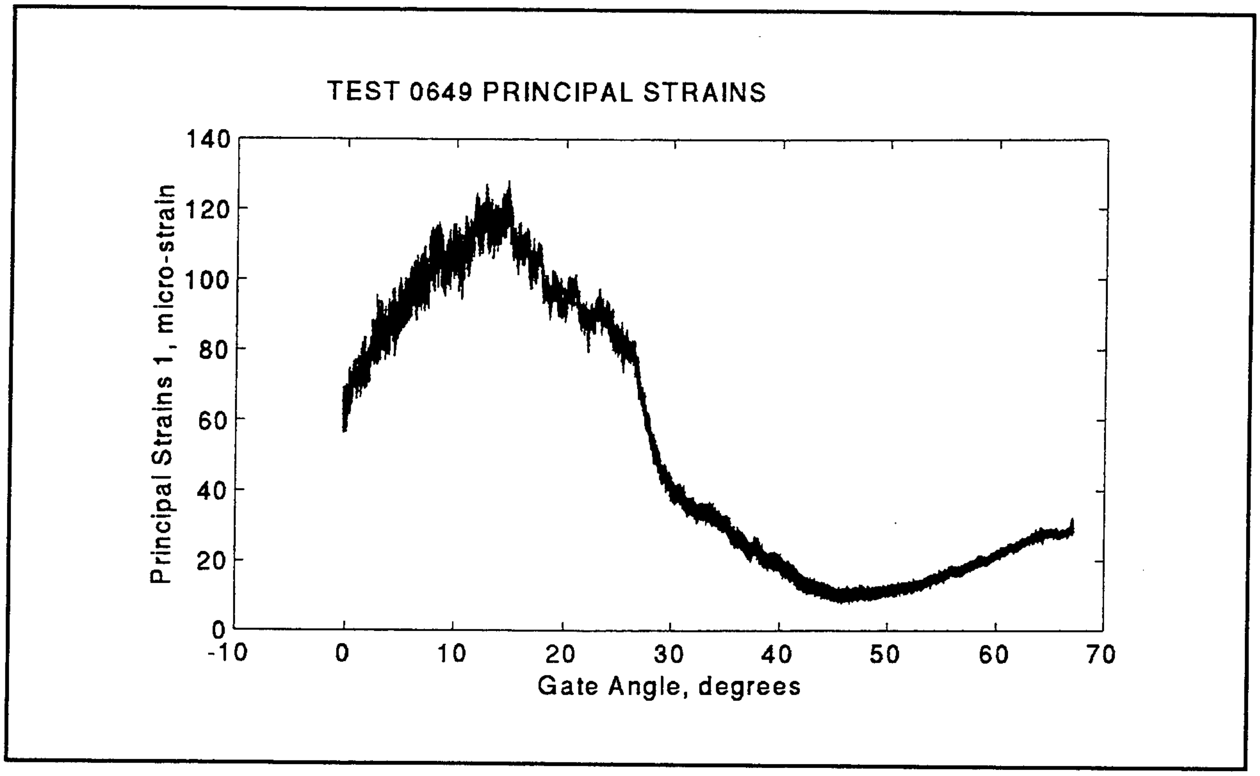

Figure G24. Prototype principal strain 1 vs time for 2-GG (EL) up condition

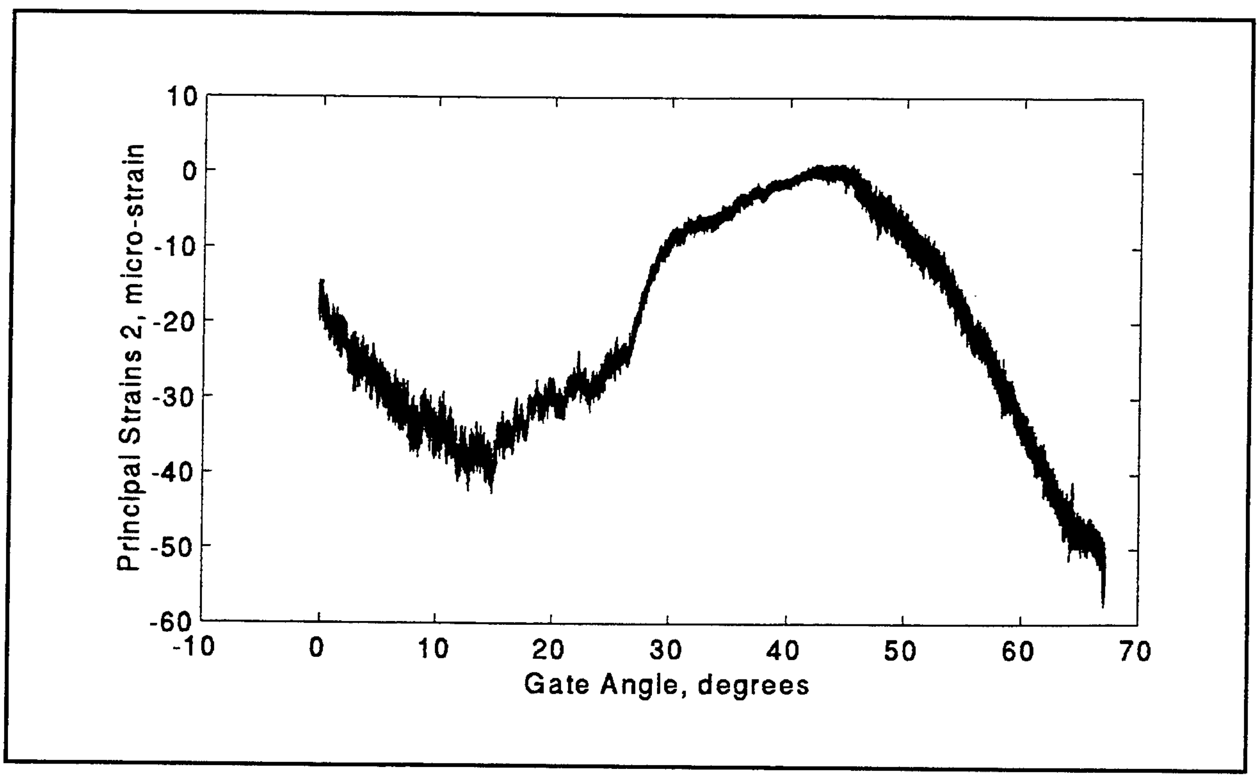

Figure G25. Prototype principal strain 2 vs time for 2-GG (EL) up condition

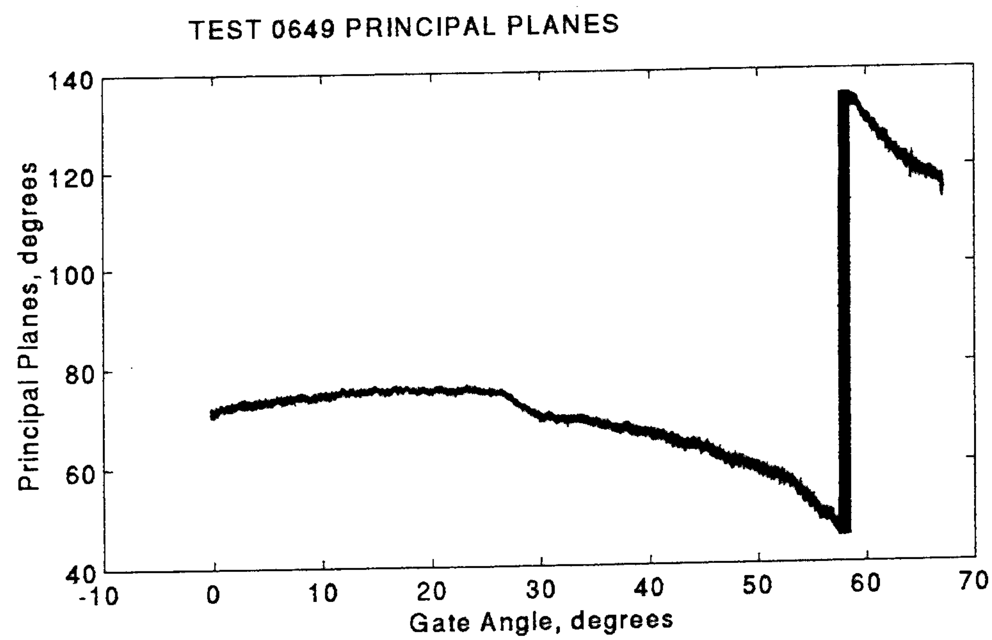

Figure G26. Prototype principal planes vs time for 2-GG (EL) up condition

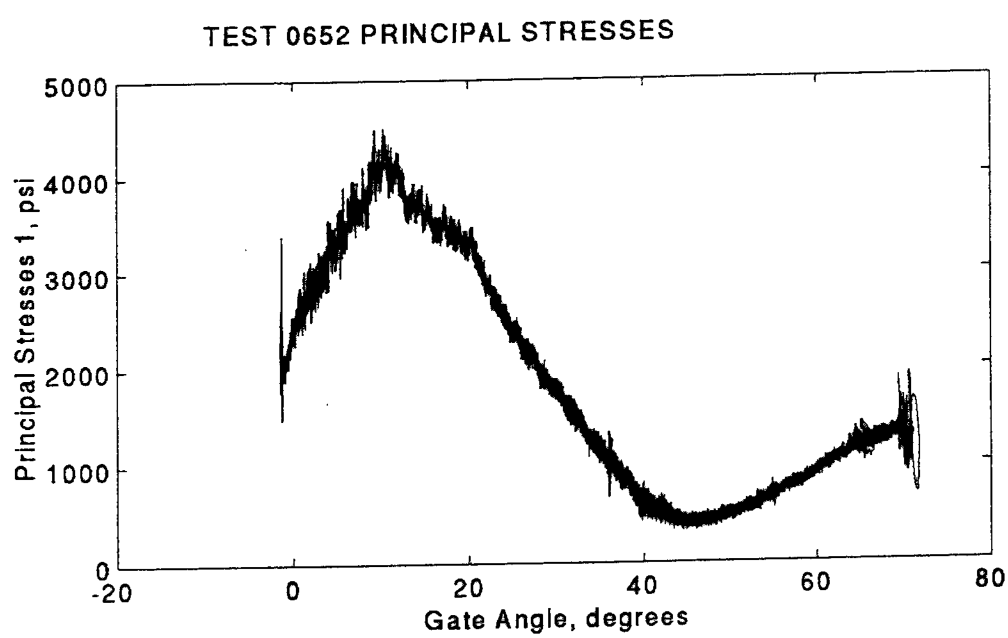

Figure G27. Prototype principal stress 1 vs time for 2-GG (EL) down condition

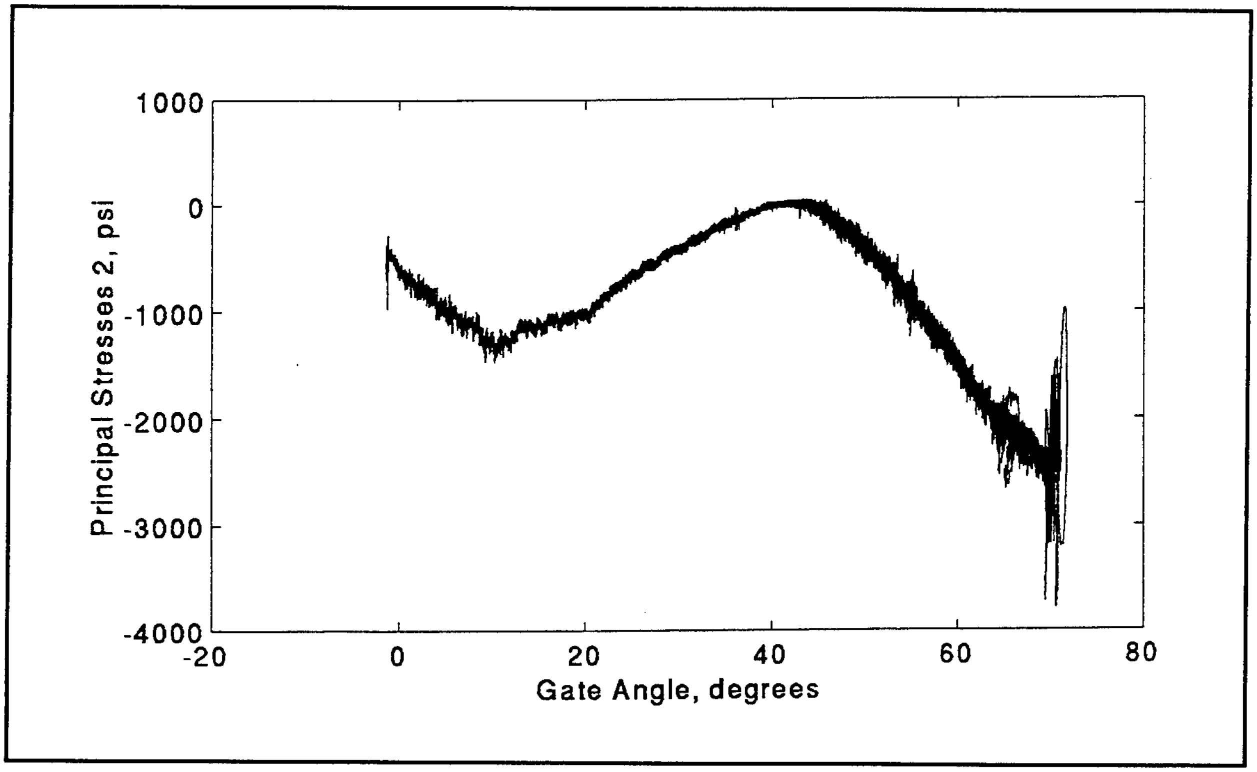

Figure G28. Prototype principal stress 2 vs time for 2-GG (EL) down condition

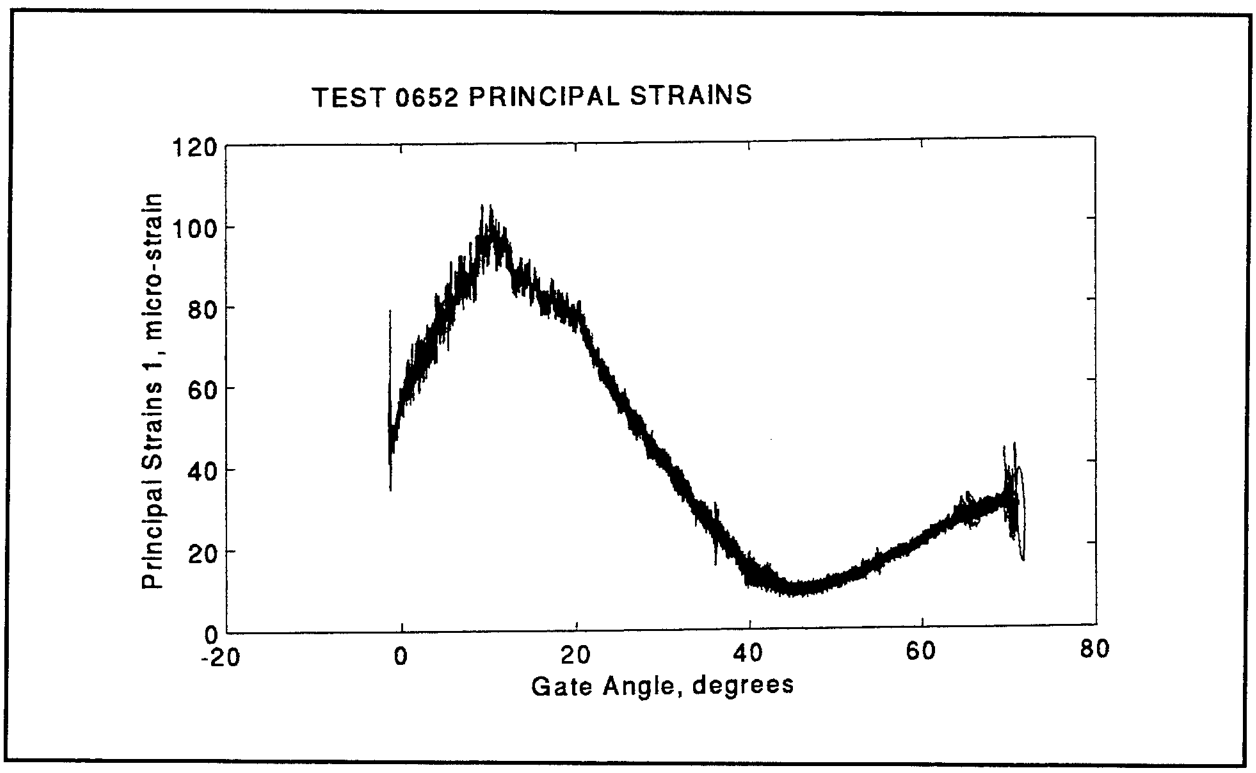

Figure G29. Prototype principal strain 1 vs time for 2-GG (EL) down condition

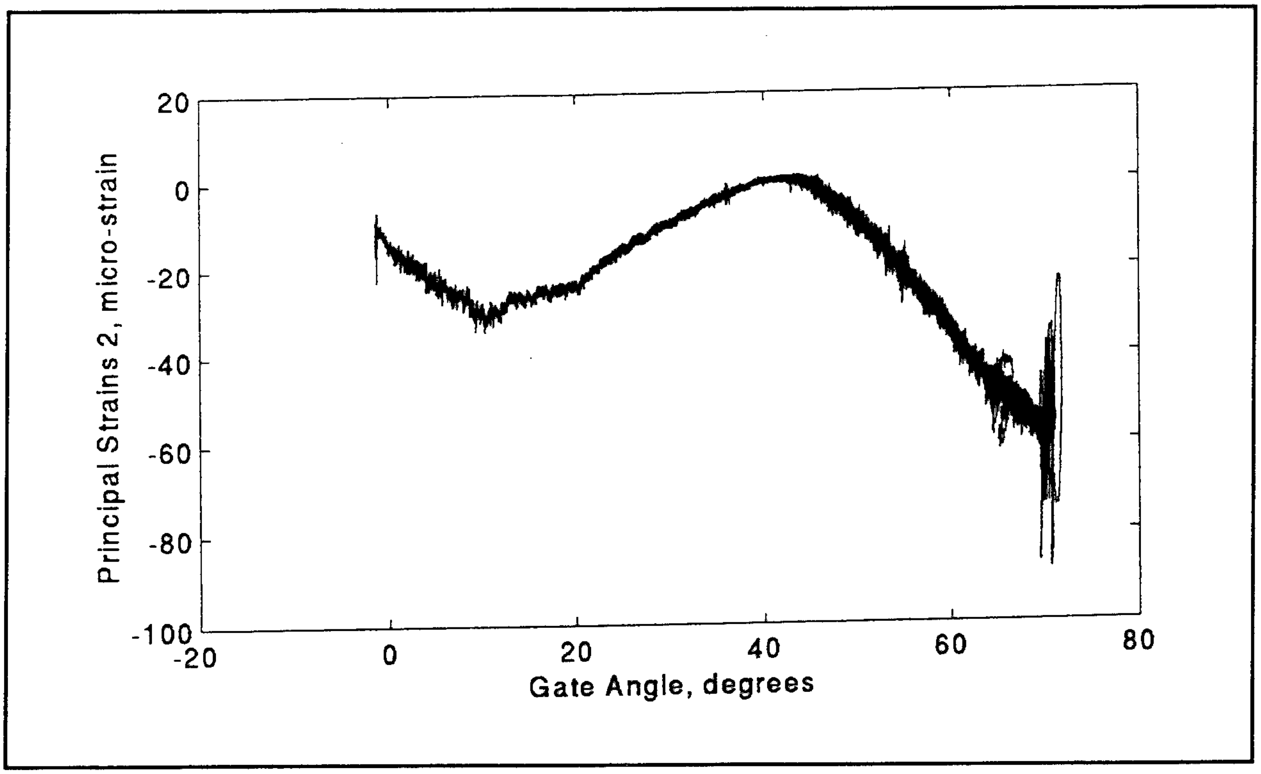

Figure G30. Prototype principal strain 2 vs time for 2-GG (EL) down condition

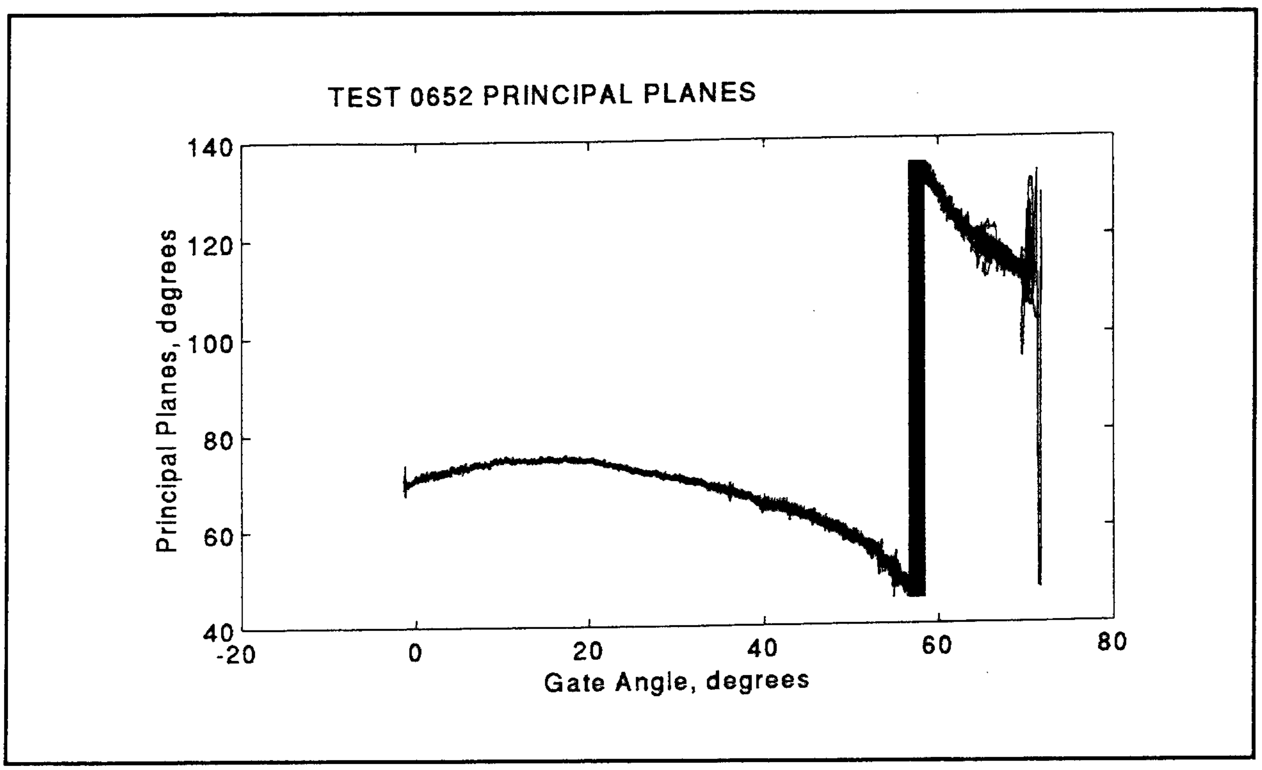

Figure G31. Prototype principal planes vs time for 2-GG (EL) down condition

REPORT DOCUMENTATION PAGE

Form Approved
OMB No. 0704-0188

1. AGENCY USE ONLY *(Leave blank)*

2. REPORT DATE
August 1997

3. REPORT TYPE AND DATES COVERED
Final report

4. TITLE AND SUBTITLE
Experimental Comparison of Prototype and 1:5-Scale Model Wicket Gates

5. FUNDING NUMBERS

6. AUTHOR(S)
Mostafiz R. Chowdhury, Douglas G. Ross, Robert L. Hall

7. PERFORMING ORGANIZATION NAME(S) AND ADDRESS(ES)
U.S. Army Engineer Waterways Experiment Station
3909 Halls Ferry Road, Vicksburg, MS 39180-6199

8. PERFORMING ORGANIZATION REPORT NUMBER
Technical Report SL-97-5

9. SPONSORING/MONITORING AGENCY NAME(S) AND ADDRESS(ES)
U.S. Army Corps of Engineers
Washington, DC 20314-1000
U.S. Army Engineer District, Louisville
P.O. Box 59, Louisville, KY 40201-0059

10. SPONSORING/MONITORING AGENCY REPORT NUMBER

11. SUPPLEMENTARY NOTES
Available from National Technical Information Service, 5285 Port Royal Road, Springfield, VA 22161.

12a. DISTRIBUTION/AVAILABILITY STATEMENT
Approved for public release; distribution is unlimited.

12b. DISTRIBUTION CODE

13. ABSTRACT *(Maximum 200 words)*

Experimental results for the prototype and 1:5-scale physical model were compared to determine the effectiveness of the scaled model in predicting the structural and hydraulic responses of the Olmsted wicket. Limited capabilities of the prototype experiments at the Smithland prototype facility demanded the physical model studies program at the U.S. Army Engineer Waterways Experiment Station in support of the development of an analytical model. A direct correlation of the dry natural dynamic characteristics and the flow-induced structural responses of the prototype and scaled model increased the confidence of the scaled model for further examination of the flow-induced response pattern of the Olmsted dam for various flow and operating configurations.

A very good correlation between the corresponding mode shapes indicated the structural similarity of the prototype and scaled model. Flow-induced time-domain model and prototype responses for identical flow configurations corresponded very well in most cases. Inconsistencies were noted in hinge force data, which was attributed to incorrect placement of hinge force transducers. A time-scale factor was computed to adjust the kinematic dissimilarity of the prototype wicket. An improved correlation of acceleration and pressure data for both prototype and scaled model was obtained in the frequency domain. The composite gate has a much greater vibratory response than the prototype steel gate under similar operating conditions.

14. SUBJECT TERMS

Doppler laser	Scanning
Experimental modal analysis	Simulation
Flow-induced vibration	System

15. NUMBER OF PAGES
232

16. PRICE CODE

17. SECURITY CLASSIFICATION OF REPORT	18. SECURITY CLASSIFICATION OF THIS PAGE	19. SECURITY CLASSIFICATION OF ABSTRACT	20. LIMITATION OF ABSTRACT
UNCLASSIFIED	UNCLASSIFIED		